

Yale University

EliScholar – A Digital Platform for Scholarly Publishing at Yale

Yale Graduate School of Arts and Sciences Dissertations

Spring 2022

Tumor Cell Migration and Interaction with ECM and Stroma in 3D Tissue Models

Chang Liu

Yale University Graduate School of Arts and Sciences, totoroclub.2020@gmail.com

Follow this and additional works at: https://elischolar.library.yale.edu/gsas_dissertations

Recommended Citation

Liu, Chang, "Tumor Cell Migration and Interaction with ECM and Stroma in 3D Tissue Models" (2022). *Yale Graduate School of Arts and Sciences Dissertations*. 626.
https://elischolar.library.yale.edu/gsas_dissertations/626

This Dissertation is brought to you for free and open access by EliScholar – A Digital Platform for Scholarly Publishing at Yale. It has been accepted for inclusion in Yale Graduate School of Arts and Sciences Dissertations by an authorized administrator of EliScholar – A Digital Platform for Scholarly Publishing at Yale. For more information, please contact elischolar@yale.edu.

Abstract

Tumor Cell Migration and Interaction with ECM and Stroma in 3D Tissue Models

Chang Liu

2022

Tumors are often described as "wounds that do not heal". Tumor progression and wound healing both feature sustained proliferative signaling, evasion from immune destruction, cell death resistance, inflammation, angiogenesis, extracellular matrix(ECM) remodeling, and activated cell migration. Unlike normal wound healing which often ends up with restored tissue homeostasis, pathological ECM remodeling is frequently implicated in fibrotic diseases and solid tumors. In addition, the dysregulated ECM signatures are directly associated with poor prognosis and also immunotherapy failure in certain types of cancers. In this dissertation, we used 3D *in vitro* cocultures to understand how tumor cells co-op with stromal/immune components, how ECM remodeling is hijacked, and how ECM architecture impacts tumor progression.

We first investigated the impact from fibroblasts. Fibroblasts are the most abundant cell types in the tumor stroma. The density of cancer-associated fibroblasts(CAFs) has been shown directly correlated with poor prognosis in some types of solid tumors. To uncover potential mechanisms behind the quantitative relationship between CAFs and tumor dissemination, we developed our coculture model by varying the density ratios between normal human lung fibroblasts and breast cancer cells(MDA-MB-231s). We found that fibroblasts increase tumor cell motility and facilitate the transition from confined to diffusive tumor cell motions, indicative of an uncaging effect. Furthermore, the ECM is globally and locally remodeled substantially with the presence of fibroblasts. Moreover, these fibroblast-mediated phenomena are in part dependent on matrix metalloproteinases.

We then investigated the impact from macrophages. In this study, we developed a 3D collagen co-culture system to mimic the melanoma microenvironment and investigate how interactions between melanoma cancer cells, fibroblasts, and macrophages shape the early stages of macrophage immune activity. In this *in vitro* model, we captured the macrophage immunosuppressive transition. Macrophages in the model displayed increased motility and acquired a phenotype that similar to tumor associated macrophages(TAMs) from melanoma tumors. This model may provide a platform for further studies on TAMs targeted immune therapy in melanoma.

In the end, we investigated the impact of ECM architecture in tumor progression. Reconstruction of a biomimetic scaffold is critical in 3D *in vitro* models. Here we introduce

a new type of thick collagen bundles that highly mimic *in vivo* ECM structure. We fabricated this type of thickened collagen bundles by introducing mechanical agitation during the transient gelation process. Thickened collagen patches are interconnected with loose collagen network, highly resembling collagen architecture in human skin scars. This type of thickened collagen bundles promotes tumor cell dissemination. The effect is significantly augmented at the presence of fibroblasts. The application of this type of collagen triggers different morphology and migration behaviors of tumor cells and highlights the importance of mesoscaled architectures.

Overall, this dissertation investigated the roles of stromal and non-stromal components in tumor progression through 3D *in vitro* models. The coculture models established in this dissertation may be further extended to test novel therapeutics targeted at CAFs, TAMs or ECM architecture.

Tumor Cell Migration and Interaction with ECM and Stroma in 3D Tissue Models

A Dissertation
Presented to the Faculty of the Graduate School
of
Yale University
in Candidacy for the Degree of
Doctor of Philosophy

by
Chang Liu

Dissertation Director: Michael Mak, Rong Fan

May 2022

Copyright © 2022 by Chang Liu
All rights reserved.

Acknowledgments

Firstly, I'd like to acknowledge Prof. Rong Fan, who gives me the chance to work and study at Yale and supports me while I am working on this thesis. These 45 days are the best time that I have ever spent at Yale. I will always keep this kindness at the bottom of my heart.

Secondly, I'd like to acknowledge my advisor Prof. Michael Mak. Through Prof. Mak, I realized the key issues in me and what I need to improve on for my next journey. I very much appreciate all the lessons that I learned during my Ph.D. years. I also would like to thank all my committee members, Prof. Michael Murrell, Prof. Xenophon Papademetris, and Prof. Richard Carson, for their kind help and guidance. Thanks!

I thank all my labmates(Xingjian Zhang, Hugh Xiao, Xiangyu Gong, Ryan Nguyen, Alex Rossello), my collaborators(Gabriela Pizzurro and Prof.Kathryn Miller-Jensen), Yale friends, and old friends. It was them who power me through the darkest years in my life.

This thesis is dedicated to my parents and my favorite scientist Thomas Young. I'm grateful that I have the best parents in the world, who give me 100% freedom in pursuing anything I like. I'm glad that I can have the opportunity to see the broader world and develop a broader mind. Also, whenever I am discouraged, Thomas Young always inspires me. I will learn to better harness the "hyperfocus" ability and make it work to the best in a healthy manner. Attached below is one excerpt from Kurt Tucholsky that has touched me since high school, and I hope it can enlighten anybody who accidentally come across this thesis in the future.

I think the ultimate beauty in science is that the piece of knowledge we find may have the chance to transcend time and speak even hundreds of years later, however small that piece of knowledge is. Flesh may fail but spirits and knowledge never. I hope in the future I can focus on providing immediate solutions to urgent issues, and the word that I put down always withstand the test of time.

Es gibt keinen Neuschnee

Wenn du aufwärts gehst und dich hochaufatmend umsiehst, was du doch für ein Kerl bist, der solche Höhen erklimmen kann, du, ganz allein . dann entdeckst du immer Spuren im Schnee. Es ist schon einer vor dir dagewesen.

Glaube an Gott. Verzweifle an ihm. Verwirf alle Philosophie. Laß dir vom Arzt einen Magenkrebs ansagen und wisse: es sind nur noch vier Jahre, und dann ist es aus. Glaub an eine Frau. Verzweifle an ihr. Führe ein Leben mit zwei Frauen. Stürze dich in die Welt. Zieh dich von ihr zurück . . .

Und alle diese Lebensgefühle hat schon einer vor dir gehabt; so hat schon einer geglaubt, gezweifelt, gelacht, geweint und sich nachdenklich in der Nase gebohrt, genau so. Es ist immer schon einer dagewesen.

Das ändert nichts, ich weiß. Du erlebst es ja zum ersten Mal. Für dich ist es Neuschnee, der da liegt. Es ist aber keiner, und diese Entdeckung ist zuerst sehr schmerzlich. In Polen lebte einmal ein armer Jude, der hatte kein Geld, zu studieren, aber die Mathematik brannte ihm im Gehirn. Er las, was er bekommen konnte, die paar spärlichen Bücher, und er studierte und dachte, dachte für sich weiter. Und erfand eines Tages etwas, er entdeckte es, ein ganz neues System, und er fühlte: ich habe etwas gefunden. Und als er seine kleine Stadt verließ und in die Welt hinauskam, da sah er neue Bücher, und das, was er für sich entdeckt hatte, das gab es bereits: es war die Differentialrechnung. Und da starb er. Die Leute sagen: an der Schwindsucht. Aber er ist nicht an der Schwindsucht gestorben.

Am merkwürdigsten ist das in der Einsamkeit. Daß die Leute im Getümmel ihre Standard-Erlebnisse haben, das willst du ja gern glauben. Aber wenn man so allein ist wie du, wenn man so meditiert, so den Tod einkalkuliert, sich so zurückzieht und so versucht, nach vorn zu sehen . dann, sollte man meinen, wäre man auf Höhen, die noch keines Menschen Fuß je betreten hat. Und immer sind da Spuren, und immer ist einer dagewesen, und immer ist einer noch höher geklettert als du es je gekonnt hast, noch viel höher.

Das darf dich nicht entmutigen. Klettere, steige, steige. Aber es gibt keine Spitze. Und es gibt keinen Neuschnee.

Dedication to: Quanfeng Liu, Xiaolan Feng, Thomas Young, my friends, and this
wonderful life

Chapter 1

Introduction: tumor microenvironment

1.0.1 Tumorigenesis is both genetic and stochastic

It has been widely acknowledged that the arise of tumor microenvironment intrinsically comes from genomic instability and accumulative oncogenic mutations. These mutations are inherited, triggered by environmental stress or from DNA replication errors[1]. In this sense, tumorigenesis is both genetic and stochastic. The stochastic side comes from the environmental stress. From the angle of etiology, environmental stress can either comes from physical factors for example radiation, chemicals or from infectious agents such as viruses or bacteria, even fungi. Other factors such as metabolism dysregulation, psychology or age-related degeneration also often elevates the potential risks.

However, the genetic side is even more complicated. Since Brian J Druker first time applied imatinib that targeted Abk1 kinases in chronic myelogenous leukemia in 1996 and achieved great success back then, mapping the genetic cancer dependency has been in the center of stage for years. With ongoing efforts, so far 89 molecule-targeting drugs(in association with 33 types of cancers) have been approved by FDA. Almost 60% of the molecules are targeting enzymes such as tyrosine kinases(27% of total) or transmembrane receptors(12% of total). However, among the 89 approved drugs, 40 drugs are targeted at leukemia, 28 for lymphoma, 27 for breast cancer and 17 for lung cancers. Most of

the cancers have less than 10 available drugs or even none[2]. But how many drugs we need to tackle one cancer? Many. To take chronic myelogenous leukemia for example, the most widely used therapy R-CHOP takes a combination of 5 drugs – rituximab, cyclophosphamide, doxorubicin hydrochloride, vincristine and prednisolone. FDC(fixed-dose combination) tablets are used by pharmaceutical companies to allow cocktail therapy. Hence, we have very limited drugs at hand tackling most of the cancers.

To make things worse, new drug development is extremely long and expensive. One single drug from bench to market normally takes around 10 to 15 years in average including 3-5 years drug screening, pre-clinical toxicity tests, 3 stages of clinical trials and then the final regulatory approval. The cost is about US\$1.8 billion for one new molecule entity[3]. From 2011-2020 period, oncology area consistently had the lowest success transition rate (5.3%) from phase I to approval, with only 5.3% successful transition, which means around 100 drugs that entered clinical trials only 5 drugs pass the approval. Besides, half of the successful drugs that are hematologic and all solid tumors combined account for the other 50% (of the 5.3%). Due to the extreme long development cycle, current drugs in circulation are mostly based on molecule hallmarks investigated back to 10 to 20 years ago. There is a huge time gap between what we know and what we have. For example, the role of MKK4(Mitogen-Activated Protein kinase kinase4) has been intensively investigated around 2007, but so far none MKK4 inhibitor has entered market yet.

While we are extremely short of effective weapons, our recent findings show that our enemies are overwhelmingly strong. In fact, each tumor harbors an average of 3000 mutations compared with normal cells from the same person. Within that pool of mutations, around 120 to 140 “cancer driver” genes have been identified, in which 71 classified as tumor suppressors and 54 oncogenes[4, 5]. In light of the complexity, one recent work[6]has recommended prioritization of 628 targets (92 pan-cancer and 617 cancer-type specific targets)based on analysis from 18,009 genes in 339 cancer cell lines.

There seems to be a beam of hope that we can eventually map out the genetic de-

pendence of all cancers. However, 628 molecule targets prioritized, with each drug costs around \$1 billion and 10 years development cycle. These numbers together still sound terrifying. In fact, my whole Ph.D. is shrouded by these unbelievably daunting and disappointed facts and the doubt whether cancer is curable. And unfortunately tumorigenesis is just a beginning.

1.0.2 Heterogeneity, heterogeneity, heterogeneity

Last chapter summarizes our current exploration in molecular hallmarks and current status in the war against tumor, from a viewpoint of drug development . However, if we zoom in and focus on the tumor niche, the actual battlefield in our body, things are actually beyond the scope of molecular level. Tumor cells are not only able to proliferate without control, evade immune surveillance, and metastasize, they also hijack wound healing process, remodel ECM, induce angiogenesis thus creating an entire microenvironment that recruits, transforms, mobilizes originally innocent stromal cells and reinforce the vicious cycle. Thus, tumor microenvironment is as critical as tumor cells by themselves.

The high involvement of stromal cells lead to the first fact – tumor environment is highly tissue-specific. To take melanoma and breast cancer researched in this thesis for example, melanoma microenvironment involves melanocytes, keratinocytes, dermal fibroblasts whereas breast carcinoma involves luminal cells, adipocytes, myoepithelial cells and breast fibroblasts. Not only the difference exists in the types of stromal cells. In addition, fibroblasts are highly plastic, contextual and heterogeneous and consists of distinct subpopulations[7]. ECM structure and composition is highly organ-specific as well[8]. Therefore, the mechanism established from the observation of one cancer may not be applied to another at all. One classic example is that, breast cancer is intensively investigated and the stiffness of breast tissue is often linked to the poor prognosis of breast cancer. Intensive research with breast cancer cell lines suggest that stiffness triggers epithelial-

mesenchymal transition, promotes cancer cell migration[9]. However, this does not hold true for ovarian cell lines. Breast cancer cell line spread out and migrate faster in rigid substrate[10] meanwhile ovarian cell line stretch out and move more on soft substrate. They also have distinct preferred metastasis sites. Breast cancer cells favor lung, brain and bones. Ovarian cancer cells prefer soft omentum[11, 12].

Tumor microenvironment does not only vary from organ to organ. Even in one tissue, there can be many cancer subtypes that requires varied treatment strategies. Breast cancer can be roughly categorized into subtypes such as luminal A, luminal B, human epidermal growth factor receptor 2(HER) enriched, basal like or triple negative. These subtypes are associated with very distinct patterns of metastasis and prognosis. In Chapter3 and Chapter5, two types of breast cell lines were used and their differences will be addressed in details then.

Not only tumor cells demonstrate highly heterogeneity, fibroblasts[13] and macrophages[14] in TME(tumor microenvironment) are highly plastic as well. Senescent fibroblasts have distinct secretion profile with normal fibroblasts[15]. Normal fibroblasts can be activated in cancer environment and promote cancer metastasis in return[16]. The role of fibroblasts will be extended in next section of chapter1. Chapter3 elucidates how fibroblast facilitate tumor cells leakage by opening ECM.

The population of macrophages are equally, or even more, diverse. In fact, there is a spectrum of macrophages polarizations depending on their molecule signatures[17]. In in vitro macrophage cultures, inactivated bone marrow derived macrophages(BMDM) are annotated as M0, whereas “classically activated macrophages” as M1 and “alternatively activated macrophages” as M2. M1 is associated with anti-tumor and pathogen behaviors and more implicated in tissue damage, multiple sclerosis, stroke and spinal cord injury etc. However, M2 are usually considered as “pro-inflammatory” and excessive M2 usually cause fibrosis or asthma. In the chapter 4 of thesis, we established an in vitro tumor model that recapitulates the entire evolutionary process on how M0, M1 and M2 macrophages all

converge into one M2-like phenotype that resembles macrophages collect from in vivo melanoma. The detailed introduction to macrophages will be covered then.

In addition to cellular component, the ECM structure complexity also compounds many of observations to tumor microenvironment. The densified extracellular matrix (ECM) in tumor niche provides mechanical scaffold support and environmental cues and is tightly associated with tumor progression and metastasis. Thickened collagen fibers in perpendicular alignment with the tumor boundary, termed as “Tumor Associated Collagen Signatures” is found to promote breast cancer cell migration[18], also the malignant breast cancer cell phenotype can be partially reversed by manipulating tumor environment[9]. As a “reservoir” of signaling molecules, the dynamic turnover of ECM is also contributing tumor metastasis by releasing stimulants such as TGF- β [19]. Stiffness or steric structures of ECM can also impact tumor cell behaviors through cytoskeleton associated signaling pathways. As one of the key components in a series of tissues, uncontrolled ECM remodeling can lead to serious pathological conditions such as pulmonary fibrosis, liver cirrhosis etc[20]. From what has been discussed, it is not hard for us to conclude that tumor microenvironment is highly heterogeneous and context-dependent.

1.0.3 Entanglement of chemistry and mechanics

If tumor microenvironment is a battlefield by analogy, we have introduced so far the main types of soldiers researched in this thesis, including tumor cells, fibroblasts, and macrophages and their associated signatures. We also briefly discussed the role of extracellular matrix(ECM), the stronghold seized and even revamped by these soldiers. This section is dedicated to discussing the communication between these “military units” and how they synergistically contribute to the tumor progression. In TME, intensive communications exist between tumor cells-fibroblasts, macrophages-tumor cells and also fibroblasts-macrophages, both biochemically and biomechanically. The interaction between each pair

is summarized as below.

Fibroblast and tumor cells: fibroblasts identified in the TME is usually activated. These activated fibroblasts are called cancer associated fibroblasts(CAFs). CAFs have distinct secretion profiles in comparison with normal human fibroblast. CAFs can produce a series of growth factors or cytokines such as TGF- β , HGF, FGF, NGF, IGF etc. that stimulate cancer cell migration and proliferation. Meanwhile, normal fibroblasts can demonstrate phenotypic features of CAFs with TGF β induction whereas tumor cells have elevated secretion levels of a series of cytokines including TGF β [21]. CAFs can drive cancer cell migration by means of E-cadherin/N-cadherin adhesion[22]and also by tearing open collagen fibers, thus creating space for cancer cells to migrate through[23].

Macrophages and tumor cells: Tumor associated macrophages are highly involved in tumor progression. In the initial stage of tumor formation, macrophages participate as key mediators in chronic inflammation through IFN- γ , IL-6 and TNF- α secretion. In addition, TAM can also secrete growth factors and cytokines that generate a mutagenic environment and promote mutations in normal cells. The mutated cells often recruit other inflammatory cells and exacerbate the inflammation and lead to a vicious cycle[24]. When tumor microenvironment is established, TAM promote directional tumor migration through CSF-1 and EGF, osteonectin(SPARC), cathepsin protease and TGF- β secretion[25]. TAM also participated in angiogenesis by targeting at vascular endothelial cells[?]. TAMs are often associated with immunosuppression in tumor microenvironment. For example, TAMs are able to suppress CD8+ T cell and NK cell functions by secreting Arg-1 (digest L-arginin) , triggering the apoptosis of these cytotoxic cells[26]. TAMs are in the center position of the immunosuppression and extravasation and colonization at secondary metastasis site.

Macrophages and fibroblasts: The interaction of between macrophages and fibroblasts are often intensively researched in wound healing, tissue regeneration. Modeling work has shown that macrophages and fibroblasts can form a stable cell circuit due to local growth factors exchange[27]. However, as tumor environment often hijacked the

wound healing pathway and tissue fibrosis is linked to tumor progression. The interaction between macrophages and fibroblasts is equally important in tumor microenvironment. M2 polarized macrophages promote fibrogenic activities of human dermal fibroblasts in an in vitro tumor model[28]. And also cytokines secreted by macrophages such as TGF- β , IFN- γ , and IL-4 all directly regulate collagen synthesis by fibroblasts. CAFs and TAMs also have been found to interact through CSF1-CSF1R axis in TME[29]. FAP⁺ CAFs can recruited CCR2⁺ myeloid cells by CCL2 secretion[30]. CAFs are also primary source of CXCL14 which stimulates monocyte migration[31]. Mechanically, dynamic fibroblasts can attract macrophages from hundreds of micrometers away in fibrillar collagen[32].

ECM remodeling: Tumor cells, macrophages, and fibroblasts all are ECM remodelers. Tumor cell often remodel local ECM by pulling and aligning collagen fibers. Tumor cell clusters are able to break base membrane by MMPs secretion. M2 macrophages can degrade collagen through a mannose mediated signaling pathway. Specific subpopulation of macrophages are also able to produce collagen[33]. Fibroblasts are highly contractile and fibrogenic and are the main builder of ECM. CAFs are the major player that secrete and modify ECM composition[34] and the primary source of collagen(I, IV, V and VI). CAFs respond to ECM stiffness and remodel collagen by LOX or MMPs related pathways.

1.0.4 Tumor progression and wound healing

Tumors are often described as “wounds do not heal”. Normal acute wound healing in healthy adults usually include rapid homeostasis, inflammation, ECM remodeling, full re-epithelization, angiogenesis and nerve regeneration. Unlike normal wound healing that tissue restores homeostasis, tumor progression usually end up with reactive stroma featured with prolonged inflammation, dysregulated ECM structures, breach of basement membrane and leakage of tumor cells into circulation system.

In fact, recent finding 2.1 have suggested that the hallmarks of cancer are also the

The hallmarks of cancer are also the hallmarks of wound healing

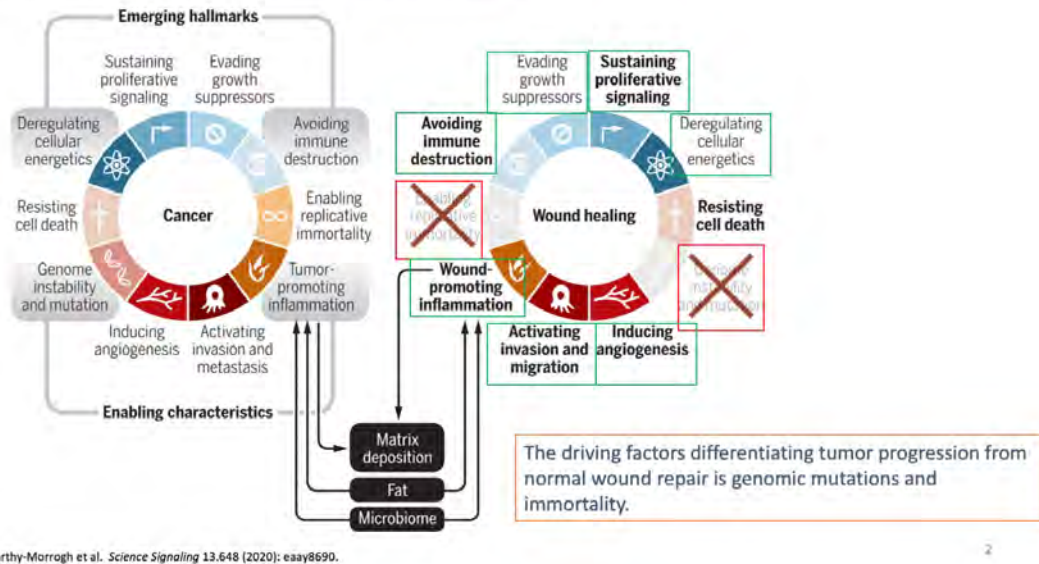


Figure 1.1: The hallmarks of the cancers are also the hallmarks of wound healing

hallmarks of wound healing[35]. Both wound healing and tumor progression involves sustaining proliferative signaling, evading growth factors, avoiding immune destruction, inflammation, resisting to cell death, activated invasion and metastasis. The only driving factors differentiating tumor progression from normal wound repair is the genomic mutations and immortality. It is likely that tumor progression is intrinsically human body's natural response to an immortal population. Under this hypothesis, we can reconstruct the stages of tumor progression based on the normal wound healing process as followed 2.2. In tumor progression, driver mutations initialize the neoplasia. The inflammation may occur as a result of tumor cell populations expansion as a result of local denutrition, hypoxia or necrosis. Fibroblasts were then activated as a result of elevated macrophages infiltration. The activated fibroblasts and expanding cell population soften local tissue and gradual degradation of ECM, which incurs the collective migration of stroma cells moving towards the tumor niche. The mobilization of stromal tissues and continuously activated wound healing pathways trigger the enlargement of tumor and angiogenesis.

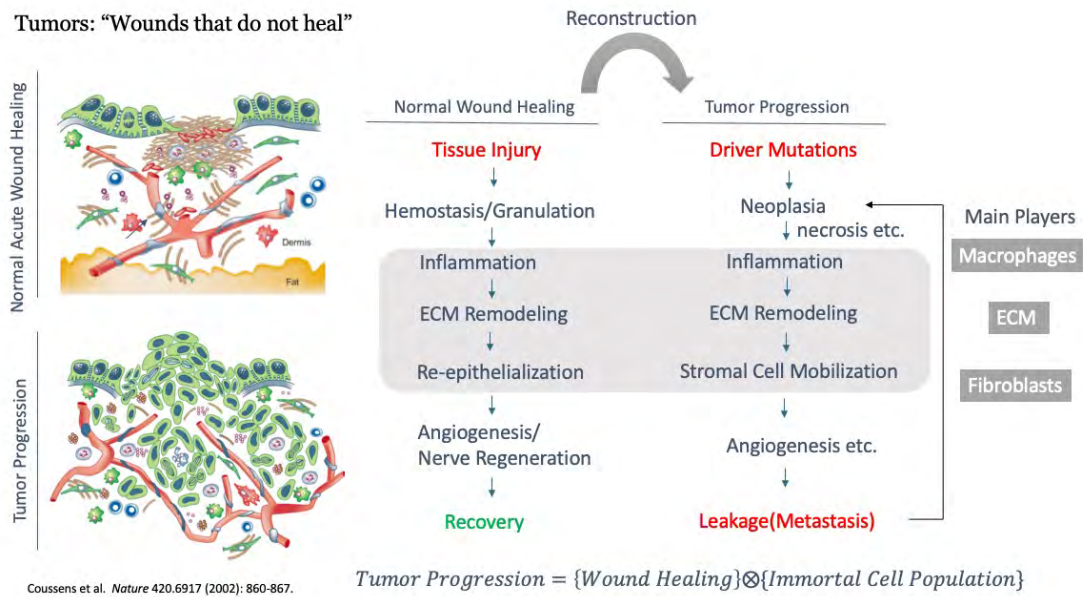


Figure 1.2: The hallmarks of the cancers are also the hallmarks of wound healing

Following this hypothesis, the ideal cancer treatment is to uncouple the hijacked wound healing process and restore the proper tissue homeostasis. Previously, most focus have been on biochemical crosstalk^{2.3} within tumor microenvironment (TME). Here we are more interested in mechanical interactions (TME)^{2.4}. Mechanical interactions on local scale can be categorized into five types including (1) adhesions based collagen fiber binding, usually integrins or syndecans are involved (2) myosin II based fiber alignment and contraction (3) Lysyl oxidase (LOX) based collagen crosslinking (4) MMPs and uPARAP mediated collagen degradation (5) ECM deposition. These interactions usually happen on the cell periphery and have attracted wide attentions. Another type of mechanical interactions, which is termed as paratensile signaling is often less discussed. Previous research has shown that mammary acini (with structural integrity compromised) rapidly disorganize during collagen mediated mechanical interaction [36]. Dynamic fibroblasts can attract macrophages from hundreds of micrometers away through collagen [37]. Most recent research has shown that myofibroblast can activate fibroblasts through paratensile signaling

Shared biochemical crosstalk signatures

- PDGF
- TGF- β
- EGF
- VEGF
- IGF-1
- FGF-7/KGF
- Angiopoietin
- Endothelin
- TNF- α
- IL-1 β
- IL-6
- IL-8
- IL-10
- SLP1
- MCP-1
- MIP-1 α
- MIP-2
- IL-18
- IFN- α/β

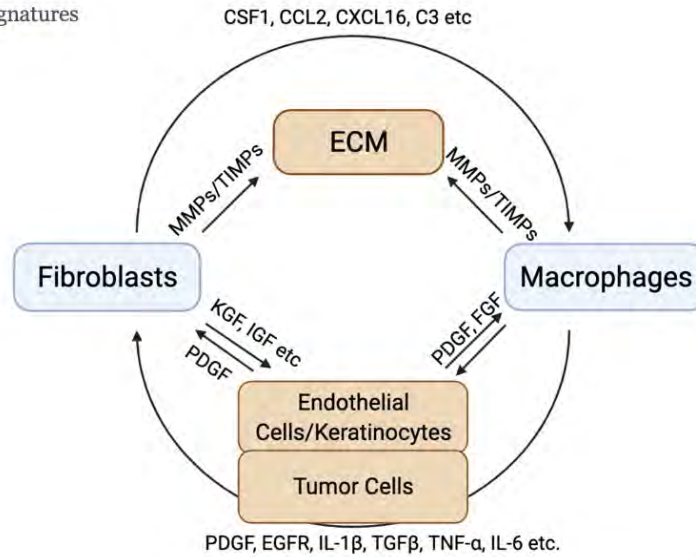


Figure 1.3: **Biochemical crosstalks in tumor niche**

through fibrous matrix mediated transmission[38]. These reports together may suggest the existence of long range force mediated signal transmission. However, when and whether the force mediated signal transmission dominate biochemical interactions are not known.

Based on above challenges faced in anti-tumor therapies and also observations, this dissertation established a series of in vitro tumor models focusing on the role of fibroblasts, macrophages and ECM architecture, in the hope that these observations will lend more insights in novel anti-cancer therapies.

1.0.5 Novelty

Most previous cancer research have been investigating the biochemical interactions of the tumor microenvironment and different therapeutic strategies have been proposed hitherto. However, most of these strategies are based on observations with cancer cell populations cultured in 2D assays. These 2D assays often fail to recapitulate the complicated tumor microenvironment and the interactions between tumor cells with stromal components. In

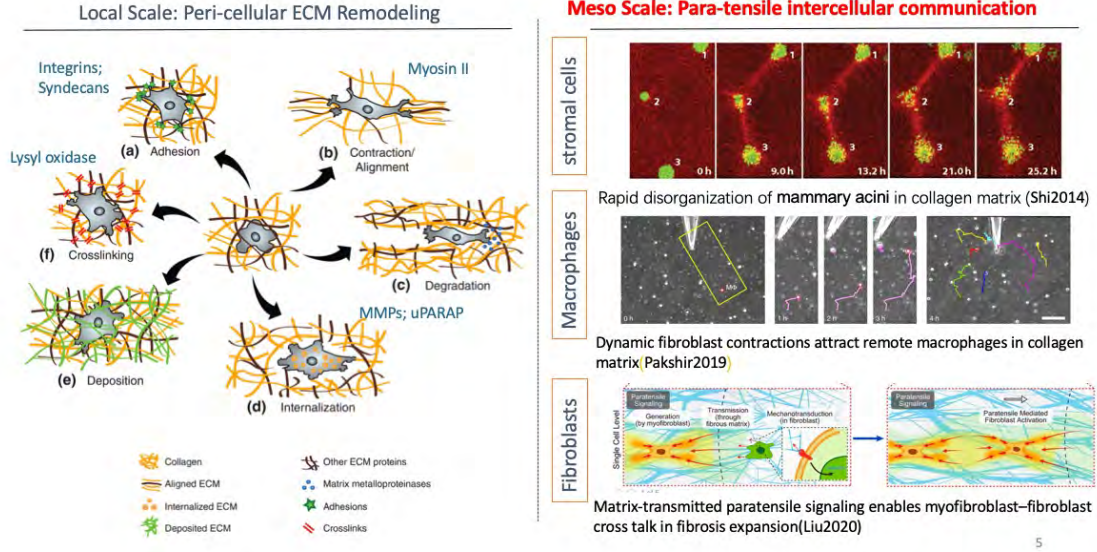


Figure 1.4: **Mechanical crosstalks in tumor niche**

fact, as last chapter suggested, the tumor progression is possibly an immortal cell population convoluted with the wound healing process. In this sense, proper 3D models are necessary to investigate the dynamic tumor progression *in vitro* and advanced cancer therapy should take into consideration of the stromal components and the physical environment. In this dissertation, we developed several 3D models and focused on the major components shared by wound healing and tumor progression including fibroblasts, macrophages and ECM from the mechanical aspect.

Our first project focused on fibroblasts. Cancer associated fibroblasts (CAFs) are associated with poor prognosis of different cancers[39, 40] etc. Previous fibroblast coculture models mainly focused on the biochemical crosstalks between cancer cells and fibroblasts, for example, one has suggested that one type of mechanically active E-cad/N-cad adhesions enable fibroblasts to lead tumor cells out of compact spheroids[22]. However, as a high contractile cell species, fibroblasts can actively remodel ECM by depositing ECM proteins and align fibers and pull collagen nearby and interact with surrounding cells me-

chanically. Therefore, the novelty in our tumor-fibroblast paper is that we investigate the quantitative effect between cancer associated fibroblasts and tumor cells and take on the issue from the aspect of ECM architecture. Our results have shown that the migration of tumor cells (MDA-MB-231s) are fibroblast density dependent. And the main mechanism behind the increased migration in the model is ECM degradation. The inhibitions of MMPs at the right timing rescue the tumor cell dissemination. This paper highlights the importance of proper physical confinement reinforced by ECM and the uncaging effect triggered by the presence of fibroblasts in TME.

Our second project has developed a “tumor-in-a-dish” model that allows the study of the early events of metastatic melanoma. In the model, we captured the phenotypical transition of the macrophages overtime. Previous 3D melanoma models often focus the formation of spherical tumorsphere and establishing a microfluidic platform, for example “skin-on-a-chip”, to mimic melanoma tumor microenvironment[41]. Our model highlights the role of macrophages and also the interaction between macrophages and fibroblasts. Advanced melanomas usually display low infiltration of T cells and high numbers of tumor-associated myeloid cells (TAMs), and the latter correlates with a worse prognosis [42]. TAMs reprogram their functional state as the tumor grows, although the specific mechanisms leading to the accumulation of immunosuppressive TAMs remain unclear. This phenotypic and functional plasticity make TAM-targeted therapies a promising treatment option [43, 44, 45]. In this sense, the novelty in our melanoma model is that we focused on the role of macrophages and tracked the dynamic evolution of macrophages over time. Our data demonstrated the morphological/migration behaviors changes of macrophages along the phenotypical evolution side by side. In this 3D system, the cell components rapidly generated cell circuits that built an environment capable of inducing an immunosuppressive functional signature in the macrophages, as observed *in vivo*. And this model will enable future studies of changes in macrophage-stromal crosstalk in the melanoma TME.

Our 3rd project specifically focused on the architecture of ECM. We established a way to quickly fabricate a type of collagen network (thick collagen patches interconnected by loose collagen fibers) which resembles skin wound ECM architecture by appearance. Many types of thick collagen bundles have been proposed before [46, 47, 48, 49, 50], compared with previous methods, our method has unique advantages. The first thing to note that, this thick collagen scaffold is more than individual bundled collagen fibers. It is a 3D collagen scaffold network that includes thick collagen patches and loose collagen network inter-between, a heterogeneous network features two types of collagen bundles. This coexistence of thick collagen bundles and loose collagen network forms a network which imposes fewer physical constraints, which allows cells to fully spread cell body but also potentially facilitate intercellular communications by means of the loose collagen fibers.

There are several other potential advantages. First, it is created by mechanical agitation, no additional solution or equipment is needed which makes the generation of this collagen scaffold fast and convenient. Secondly, without additional materials introduced, it will not introduce any confounding effect might brought up by the additional of the extra species of chemicals. The only difference between our collagen scaffold with conventional collagen scaffold is the structural difference. The third advantage is, this is a type of collagen scaffold that include thick collagen bundles and loose bundles inter-between, it is more than individual thick collagen bundles created by nanopatterning that is fixed on a substrate. Instead, it is a collagen network that resembles the skin wound environment in 3D. The fourth advantage is that we can seed cells and apply cocultures with this type of scaffold easily as with normal collagen embedment. Our coculture study with this type of thick collagen scaffold demonstrates altered ECM significantly boost fibroblast's promotional effect of tumor cells' migration. The fifth advantage is that the size of thick collagen patches can be modulated by changing mixing duration and frequency. Therefore, this collagen scaffold intrinsically highlights the importance of collagen architecture and we

have provided an easy, fast way of producing such network.

In the end of this dissertation, we included our preliminary results with light-controlled Rho GTPases. Most light activated Rho GTPases studies have been carried out on 2D substrate[51, 52, 53], we applied the method in a fibrillar environment and our exploratory results have shown the role of RhoA, Rac1 respectively in 3D. The function and role of RhoA and Rac1 is displayed in the second last chapter in this dissertation.

Chapter 2

Fibroblast-Mediated Uncaging of Cancer Cells and Dynamic Evolution of the Physical Microenvironment

2.1 Abstract

Stromal cells are prominent in solid tumor microenvironments and contribute to tumor progression. In particular, fibroblasts are common cell types in the tumor stroma that play important roles in remodeling the extracellular matrix (ECM). Here, we perform co-culture experiments with tumor cells and fibroblasts embedded in 3D collagen I matrices. We investigate the impact of fibroblasts on the migratory behavior of neighboring tumor cells and on the evolution of the surrounding ECM. We find that fibroblasts increase tumor cell motility and facilitate the transition from confined to diffusive tumor cell motions, indicative of an uncaging effect. Furthermore, the ECM is globally and locally remodeled substantially with the presence of fibroblasts. Moreover, these fibroblast-mediated phenomena are in part dependent on matrix metalloproteinases.

2.2 Introduction

The solid tumor microenvironment (TME) is highly complex, typically consisting of heterotypic cell populations within a 3D fibrillar extracellular matrix (ECM). The ECM can be dense, particularly in fibrotic tumors often observed in many solid cancer types (e.g. in breast, lung, liver, pancreas)[54]. The dense ECM, which consists of small pores, poses as a biophysical barrier against cell migration[55]. During tumor progression and metastasis, this physical barrier is overcome. Certain canonical mechanisms for overcoming the ECM barrier have been established, including secretion of matrix metalloproteinases (MMPs) by tumor cells to degrade ECM fibers[55, 56] and transition of tumor cells to an amoeboid migratory mode, which relies on cell squeezing through confined spaces via actomyosin-dependent contractile processes[57, 58]. Additional mechanisms are emerging in recent studies. The ECM can be remodeled by cells via mechanical forces due to the viscoplasticity of the matrix material[59, 60, 61, 62]. Stromal cells can also facilitate tumor progression and invasion in a variety of ways[63, 64].

Recent studies have shown that fibroblasts are capable of leading tumor cells out of the primary tumor to initiate dissemination[22], and that this process is associated with adhesions between tumor cells and fibroblasts. However, fibroblasts are capable of performing many additional functions that may contribute to invasion, including remodeling the ECM and generating biophysical cues[65]. Contractile cells can generate locally aligned topographies and ECM stiffening[66, 67], which are known to induce increased tumor invasiveness[68, 69, 70]. Additionally, fibroblasts can degrade the ECM through MMPs, which can create more space for migration[71, 72]. The full effects of fibroblasts on tumor cell behavior and on the spatiotemporal evolution of the TME are not completely elucidated quantitatively.

Here, we investigate the migration profiles of tumor cells with and without the pres-

ence of neighboring fibroblasts inside a 3D ECM. We use MDA-MB-231 breast cancer cells and primary human lung fibroblasts (NHLFs). MDA-MB-231s are metastatic solid tumor cells, and NHLFs represent fibroblasts found in normal stromal tissue. For ECM, we use collagen I, which is one of the most prominent ECM proteins in connective tissues and in the solid tumor microenvironment[73, 74, 75]. As the fibroblast is the most abundant stromal cell type in many solid tumors, and the density of cancer-associated fibroblasts are directly correlated with poor prognosis in solid tumor, by varying the density of fibroblasts in the system and we can first examine the quantitative impact of cell concentration and MMPs in a patho-physiologically relevant setting . Secondly, fibroblasts are highly contractile. To vary the density of fibroblasts allows us to roughly control the the mechanical factors in the system through controlling density of fibroblasts. Thirdly, tumor microenvironment in vivo is packed with dense cellular components where intercellular distance is small. By varying density of cell populations in the system we can modulate the average cell-cell distances and better mimic the tumor microenvironment. We further examined the impact of cell concentration and MMPs. We further examine the global and local remodeling of the ECM in monoculture and co-culture conditions. Our results show that fibroblasts significantly increase the motions of tumor cells, and this originates from a variety of factors. Fibroblasts compact the ECM and alter matrix architecture. Furthermore, the full impact of fibroblasts is dependent on MMPs, which not only influence the migration of tumor cells but also the ECM profile.

Materials and Methods

2.2.1 Cell Culture

MDA-MB-231 cells transfected with Lifeact GFP were a gift from the Lauffenburger lab. They were cultured in DMEM with 10% fetal bovine serum (FBS) and 1% Pen-Strep.

Fibroblasts were primary normal human lung fibroblasts(ATCC, PCS-201-013), and they were cultured in Lonza FGM-2 BulletKit(CC-3132) or RPMI with 10% FBS. Cells were all incubated at 37°C and 5% CO₂.

2.2.2 3D tissue culture experiments

Cells were seeded into 2mg/mL rat tail type I collagen gels (Corning). Briefly, acid solubilized collagen I was neutralized with NaOH and mixed with cells on ice, followed by gelation at 37°C. Cells were seeded at varying concentrations, with 1X indicating 800K cells/mL. Fibroblasts were mixed at 0X to 5X the concentration of cancer cells. For drug studies, GM6001 (20 μ M) was mixed into the collagen gel solution and into the media. For labeled ECM studies, the initial collagen solution was labeled with Alexa Fluor 647 NHS Ester (Succinimidyl Ester) and dialyzed as before[59]. Finally, we coated the surface of the multi-well plates used for imaging with polydopamine to anchor the collagen gel[76, 77].

2.2.3 Image Acquisition

Imaging was performed using a Leica SP8 confocal microscope. For migration studies, we used a 20X 0.75 NA objective.

2.2.4 Image Analysis

Cells were tracked manually or with TrackMate[78] on Image J. Each cell center was calculated by averaging coordinates of corresponding traced cell boundary. Average speed of each cell was calculated as the mean of the absolute value of the net displacement of the cell center over 1hr time intervals. Mean squared displacements were computed with

the following equation[79]:

$$MSD(n) = \frac{1}{N - n + 1} \sum_{i=0}^{N-n} [(x_{i+n} - x_i)^2 + (y_{i+n} - y_i)^2] \quad (2.1)$$

where N indicates the total step number, n indicates the n -th step, x is the x -coordinate and y is the y -coordinate. β was computed by first locally smoothing the MSD profile with a Gaussian-weighted polynomial and then taking the logarithmic derivative of the smoothed MSD over logarithmic time[80], i.e.

$$\beta = \frac{d(\ln(MSD))}{d(\ln(t))} \quad (2.2)$$

Data points of β that are less than zero are considered as noise and discarded. Note that for trajectories-related calculations, 2D trajectories of z -projected cell migration time lapse data were used. ANOVA with Tukey post hoc test was performed for statistical comparisons. * indicates p -values ≤ 0.05 . For quantifying ECM deformation dynamics due to local cell contractions, small fluorescent debris are manually selected for tracking via the following criteria:(1) Debris are well adhered to the matrix instead of to the cell body and are not freely diffusing through the matrix;(2)Neighboring debris show similar movement trend and are moving along gel contraction direction through visual confirmation; (3) Debris appear in more than 80% of the time frames.The trajectories of debris movement and speed/MSD calculation are recalculated in the same way as for cell motions. For pore size measurements, we used the sequential morphological opening method with a disk shape as the incremental structuring element as in previous work.The area change from opening is used to approximate the distribution of pores of specific size. It is important to note that in our experiments, cell density is relatively high. Therefore, in monoculture conditions, we did downsampling by cropping regions without cells into 300X300 pixels. For coculture conditions where cells are occupying most of the gel, we select collagen channels only.

2.3 Results

2.3.1 The set-up of the 3D coculture model

We generate monoculture and co-culture systems in 3D collagen I matrices, and we perform time-lapse imaging and image analysis (Fig.2.1). Under monoculture conditions (tumor cells only), we find that cells appear to be in a more rounded morphology, whereas in co-culture conditions, tumor cells acquire a more extended morphology (Figure2.1c and Figure 2.8). Circularity of MDA-MB-231s drops significantly in the presence of NHLF regardless of GM6001 treatment. The presence of GM6001 in MF conditions can rescue the decrease of circularity on day0. Significant differences are not detected across co-culture conditions. Close proximity and dense mixtures of tumor cells and fibroblasts can be observed at around day4 and 5. In contrast, large round clusters of tumor cells are observed in monoculture conditions. Over time, in monoculture, cell aggregates emerge, whereas in co-culture with fibroblasts, cells tend to occupy more uniformly throughout the matrix(Figure 2.9). However, suppressing MMP activity via GM6001 (a pan-MMP inhibitor) leads to more clumped cells, including in the fibroblast population (Fig.2.2).

2.3.2 Migration tracking of MDA-MB-231 in coculture environment

We track the migration of tumor cells in the 3D ECM with varying concentrations of fibroblasts at day 0 and day 1 after cell seeding. We find that the trajectories and speeds are larger for co-culture conditions (Fig.2.3a and Fig.2.3b). Moreover, this is more apparent in day 1 after cell seeding. In monoculture conditions, trajectories and speeds are relatively small even after 1 day in culture. When MDA-MB-231 cells are cultured with equal amount of MDA-MB-231 by themselves, there is no significant difference in MDA-MB-231 migratory behaviors(Figure 2.10). These results indicate time-dependent evolution of the fibroblast-mediated microenvironment toward a state that facilitates tumor

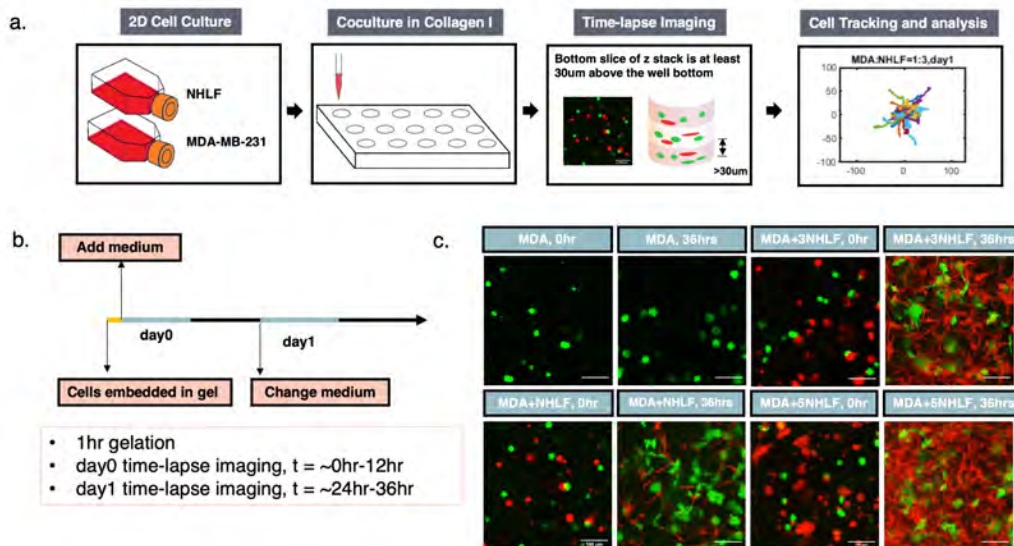


Figure 2.1: **Experiment set-up of the coculture model** a. Pipeline of the experiment setup. b. Diagrams show the timeline of the image acquisition. c. Representative images of MDA-MB-231 (shortened as MDA, shown in green channel) and normal human lung fibroblast (shortened as NHLF, shown in red channel). "MDA" indicates MDA-MB-231 monoculture, "MDA+NHLF" indicates co-culture with initial cell concentration ratio between MDA-MB-231 and NHLF of 1:1; "MDA+3NHLF" indicates co-culture with initial cell concentration ratio between MDA-MB-231 and NHLF of 1:3; "MDA+5NHLF" indicates co-culture with initial cell concentration ratio between MDA-MB-231 and NHLF of 1:5. The scale bar is 100µm.

migration. Moreover, increased cancer cell invasiveness is dependent on fibroblast concentration. More fibroblasts lead to faster cancer cells, but this effect plateaus at relatively high fibroblast concentrations, suggesting saturation of invasion-promoting signals generated by fibroblasts and/or high consumption rate of nutrients due to high cell density, as there is limited nutrient supply in the cell culture well. Alternatively, the limited medium supply of the culture chamber may be another contributing factor to the plateaued effect.

We further investigate the statistical properties of the tumor cell motions. By considering tumor cell mean-squared displacements (MSDs), we find that fibroblasts increase their diffusivity. The magnitude of the MSDs is larger in co-culture conditions in a fibroblast concentration and time dependent manner (Fig.2.4). Additionally, β , the logarithmic

derivative of the MSD, is higher in co-culture conditions (Fig.2.5). β provides insights toward the physical nature of the cell motions. $\beta = 0$ indicates confined motion, characteristic of cells that are caged, and $\beta = 1$ indicates diffusive (unconfined and random) motion. Co-culture conditions enable tumor cells to migrate in a more diffusive manner.

Furthermore, the influence of fibroblasts on tumor migration is dependent on MMPs. Inhibiting MMPs with GM6001 reduces the fibroblast-mediated increases in tumor cell speed, MSD, and β (Figs.2.3,2.4,2.5) However, the co-culture effects are not completely abolished through MMP-inhibition, as shown by the comparisons with tumor cell monocultures, suggesting additional biophysical influences by fibroblasts. Histograms of average speed, average MSD and average β are shown in Figure 2.11, Figure 2.12 and Figure 2.13 respectively.

2.3.3 Global compaction happens to ECM structure over time

We next examine the influence of the cells on the global and local ECM behavior. We find that in co-culture conditions, the matrix is globally compacted over time, as shown by the decrease in whole gel radius (Fig.2.6). This compaction is mediated by fibroblasts, as monoculture tumor cells did not significantly shrink the gel radius. Moreover, this compaction process is dependent on MMPs, as MMP inhibition abrogates the compaction of the gel even in co-culture conditions with relatively high fibroblast concentrations. At the local scale, examined under high resolution confocal microscopy with collagen fibers labeled fluorescently, we find that the architecture of the ECM is drastically different in the presence of fibroblasts, in which rampant remodeling occurs leading increased open spaces (Fig.2.2).

2.3.4 MMPs inhibition is effective suppressing tumor cell invasion

Finally, we investigate whether delayed MMP-inhibition is effective in suppressing tumor cell invasion. We find that if we do not treat co-culture samples with GM6001 at days 0 and 1, thus allowing 2 days for ECM remodeling, and start treatment at day 2, tumor cell motions are not impacted by the drug (Fig.2.7)). This indicates that the ECM is already remodeled sufficiently over 2 days to achieve maximal impact on tumor cell migration. Co-culture samples thus require continuous treatment from initial stages in order to suppress invasion-promoting remodeling of the nominal ECM. The influence of the initial remodeling appear persistent after MMPs are inhibited subsequently.

Discussion

In this study, we demonstrate that fibroblasts mediate increased motility in tumor cells. While this process can be modulated by many factors in the cascade of fibroblast-ECM-tumor cell interactions, our results indicate that MMPs are a major, but not complete, contributing factor. Prior studies have shown that adhesions between tumor cells and fibroblasts are important for fibroblast-mediated invasion[22]. Additionally, fibroblasts can secrete paracrine signaling factors and ECM proteins such as fibronectin, which can increase tumor cell motility[81, 82]. Here, we show that, in dense 3D collagen matrices, these effects may be subsequent and potentially synergistic to the initial impact of MMP-dependent matrix remodeling. Thus, the temporal sequence of stroma-mediated effects is important to consider.

Moreover, in our images, we find that while at times tumor cells are in contact with fibroblasts during their motions, this is not true for all cases. Tumor cells in fibroblast-remodeled microenvironments can move rapidly even when not in direct contact with the fibroblasts themselves, suggesting that the remodeled ECM contains cues that are major

factors that drive invasiveness. Our findings highlight the heterotypic microenvironment as a dynamically evolving space in which stromal cells remodel the ECM and new local cues are progressively being manufactured.

From our MSD results, we find that tumor cells typically migrate in a sub-diffusive manner in 3D ECMs, indicative of confinement. Physically, this is likely due to the dense ECM inducing a caging effect. However, in co-culture conditions, the migration becomes closer to being diffusive (β being closer to 1), particularly with high concentrations of fibroblasts. This suggests that fibroblasts can serve the function of uncaging tumor cells. MMPs are a key mediator of this process. Interestingly, however, even with MMPs inhibited, the presence of fibroblasts can still increase tumor cell movements. This suggests additional factors are involved. In particular, contractile forces from fibroblasts can remodel the ECM, generating alignment cues[67], non-linear stiffening[66, 83], and viscoplastic reorganization[59, 60, 61] – factors that can contribute to tumor invasion[61, 68, 69, 70].

MMPs have been extensively studied, and tumor cells can utilize them to degrade the ECM to facilitate migration[56]. In dense ECMs with pore sizes smaller than the nucleus, MMPs are required for migration[55]. Here, we show that fibroblasts, which are prominent in the solid tumor microenvironment and in many tissues commonly associated with metastatic sites (e.g. lung, liver), can significantly enhance MMP-mediated cancer cell motility. This further implicates the important role of heterotypic microenvironments and cooperative effects in facilitating tumor invasion. Our results suggest that tissues rich in stromal cells and ECM may already be sufficiently conducive to tumor migration even without ECM remodeling by the tumor cells themselves, and that this process may not depend on specialized cancer-associated fibroblasts, as we used normal human lung fibroblasts in this study.

Furthermore, our findings implicate MMPs in the compaction of the ECM. MMPs are traditionally known for their role in matrix degradation. Their potential roles in the mechanical remodeling of the ECM are not well understood. Mechanical remodeling –

ECM deformation and formation of topographical cues – are typically associated with actomyosin and tension mediated processes. Our results show that at the global scale, MMPs mediate the compaction of the whole gel (Fig.2.6), and at the local scale, MMPs facilitate tearing of the matrix and formation of gaps (Fig.2.2). Previous work has shown that mechanical forces generated by cells, particularly dynamic forces, can be used to recruit ECM toward cells in a mechanically irreversible manner, as ECM bonds can break under tension[59, 62]. Our findings suggest that MMPs can facilitate this process, contributing to ECM compaction and tearing by locally weakening the ECM and making it more susceptible for mechanical remodeling.

Finally, the reliance of tumor invasion on MMPs in dense ECMs is time-dependent, as inhibition of MMPs after 2 days of co-culture without initial inhibition does not reduce tumor cell migration. This indicates that on the time-scale of hours to days, the ECM can be irreversibly remodeled by stromal cells into an invasion promoting microenvironment. Thus, MMP-inhibition treatments may only be effective at the very early stages of tumor progression or at the earliest time points when tumor cells reach secondary sites. This also suggests that pre-emptive MMP-inhibition may suppress new sites from promoting further tumor invasion.

2.4 Conclusions

The dense ECM can mechanically restrict cell invasion. Stromal cells, particularly fibroblasts, can facilitate tumor invasion via both MMP dependent and independent mechanisms. In the presence of fibroblasts, the microenvironment is dynamic, evolving toward an invasion-promoting state that is highly distinct from that of the nominal reconstituted ECM in vitro. New local ECM architectures emerge, with features that are conducive to cell invasion. MMPs contribute to the microenvironment remodeling process, not only through matrix degradation but also through facilitating local and global ECM mechanical

reorganization. Overall, our results support that modulating regulators of ECM remodeling, particularly stromal cell-mediated activities, is critical toward controlling tumor invasion.

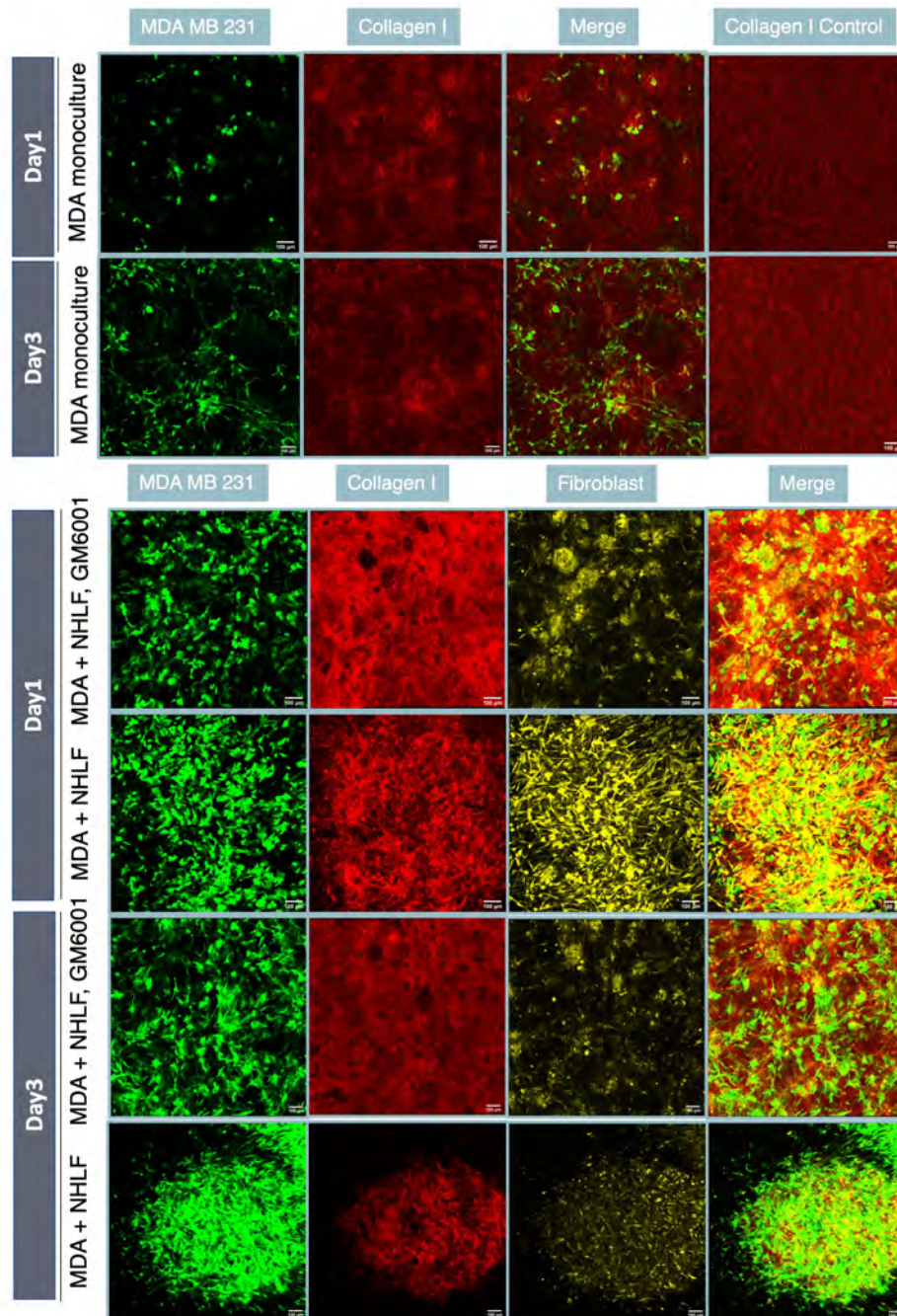


Figure 2.2: **Comparison of the spatial environment over time** Comparison of the spatial environment of the MDA-NHLF coculture at day 1 and day3, with and without GM6001 treatment ($20\mu\text{M}$). In MDA-MB-231 monoculture, collagen bundling or thickening mostly occurred on the peripheral region near MDA cells, as shown in images from row 1 and row 2. At day1 in MDA-NHLF coculture, with $20\mu\text{M}$ GM6001 treatment, the collagen gel remained intact and fibroblasts were trapped in the middle of gel. In conditions without GM6001 treatment, fibroblast filled up the whole gel space evenly. At day3, with GM6001 treatment, the collagen gel collapsed to the middle. "MDA+NHLF" indicates co-culture with initial cell concentration ratio between MDA-MB-231 and NHLF of 1:1. Scale bar is $100\mu\text{m}$.

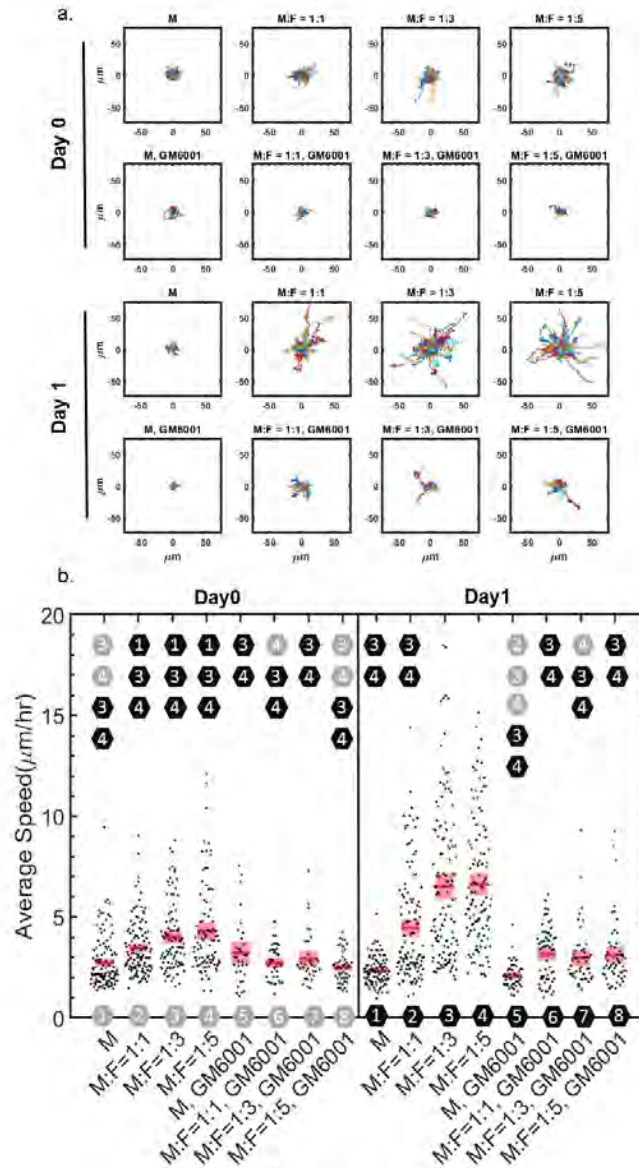


Figure 2.3: **MDA-MB-231 invasion is NHLF density dependent** a. Overlaid trajectories from each condition truncated at 180min. M indicates MDA-MB-231, and F indicates NHLF. The ratio indicates the initial seeding concentration ratio of MDA-MB-231 to NHLF cells. GM6001 indicates 20 μm GM6001 treatment. b. Average speed of MDA-MB-231 cells from different conditions. Red line indicates the mean value and pink boxes indicate the 95% confidence interval. Each condition is number coded as indicated by the hexagon along x axis. Gray hexagons indicate day0, black hexagons indicate day1, GM6001 indicates 20 μm GM6001 treatment. One way ANOVA was performed to show the difference across all conditions. The numbers floating on top of each bar indicate conditions which are significantly different ($p < 0.05$) from the corresponding condition. Tukey's honest significant difference criterion is used in post-hoc analysis. Histogram data are shown in Figure 2.11.

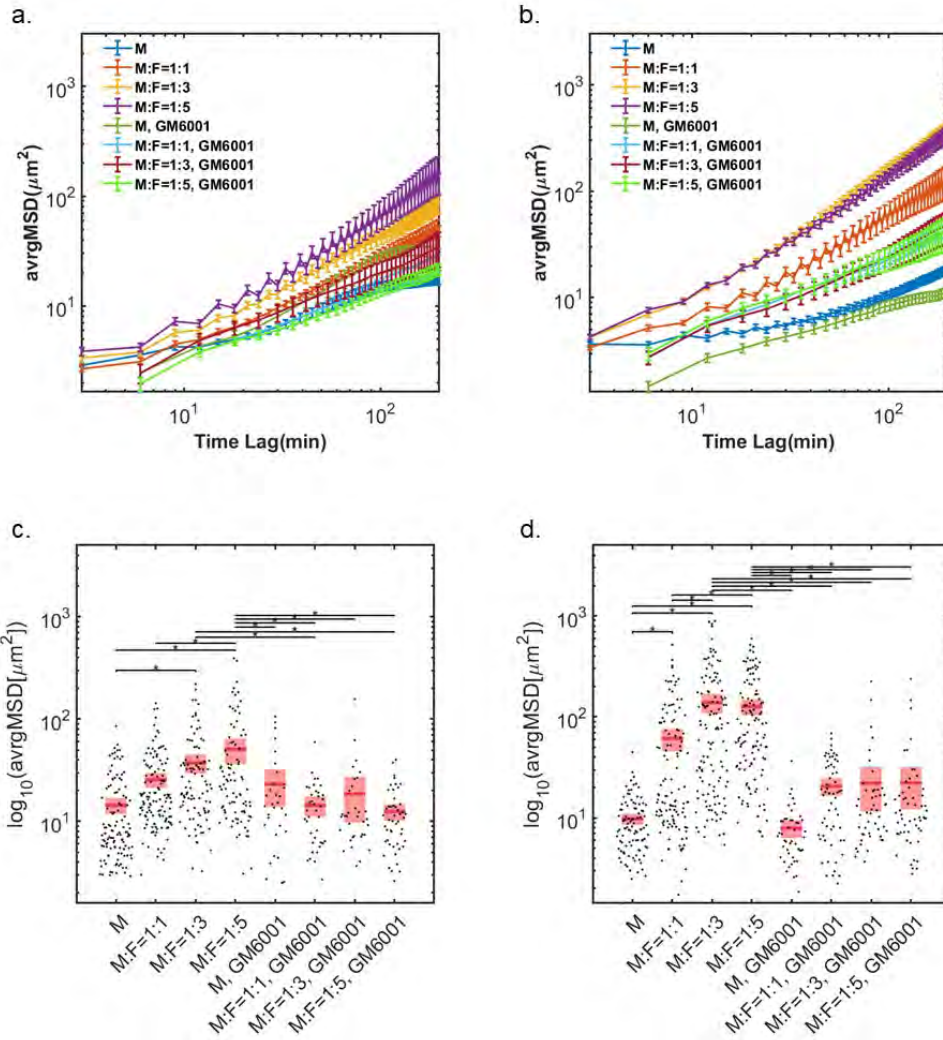


Figure 2.4: **MDA-MB-231 invasion is NHLF density dependent** a. Average MSD at day0, error bar in SEM; b. Average MSD at day1, error bar in SEM; c. MSD taken at the 90min time interval, day0; d. MSD taken at the 90min time interval, day1. M indicates MDA-MB-231 and F indicates NHLF. The ratio indicates the initial seeding concentration ratio of MDA-MB-231 to NHLF cells. Red line indicates the mean value and pink boxes indicate the 95% confidence interval. One way ANOVA was performed to show the difference across all conditions. * indicates the two compared conditions are significantly different ($p < 0.05$). Histogram data are shown in Figure 2.12.

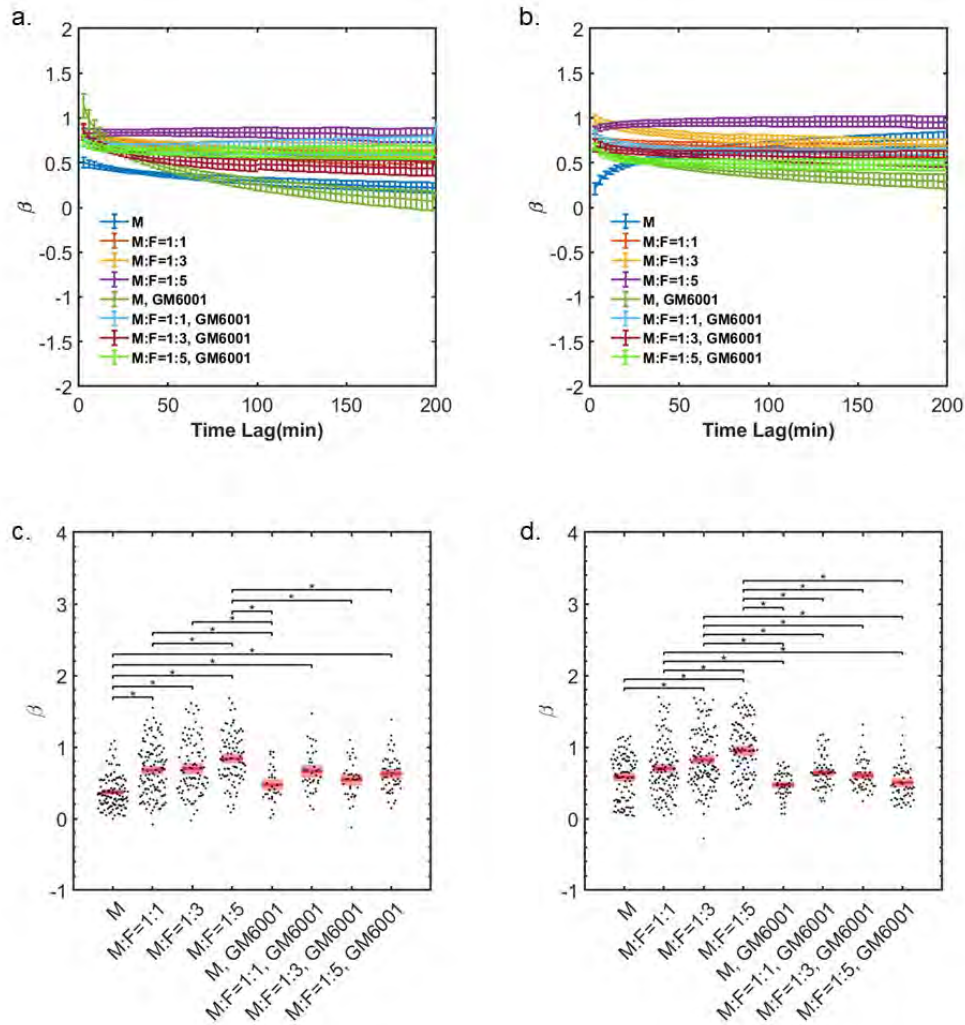


Figure 2.5: **MDA-MB-231 invasion is NHLF density dependent** a. Average beta at day0, error bar in SEM; b. Average β at day1, error bar in SEM; c. β taken at the 90min time interval, day0; d. β taken at the 90min time interval, day1. M indicates MDA-MB-231, and F indicates NHLF. The ratio indicates the initial seeding concentration ratio of MDA-MB-231 to NHLF cells. Red line indicates the mean value and pink boxes indicate the 95% confidence interval. One way ANOVA was performed to show the difference across all conditions. * indicates the two compared conditions are significantly different ($p < 0.05$). Histogram data are shown in supplementary information Figure 2.13.

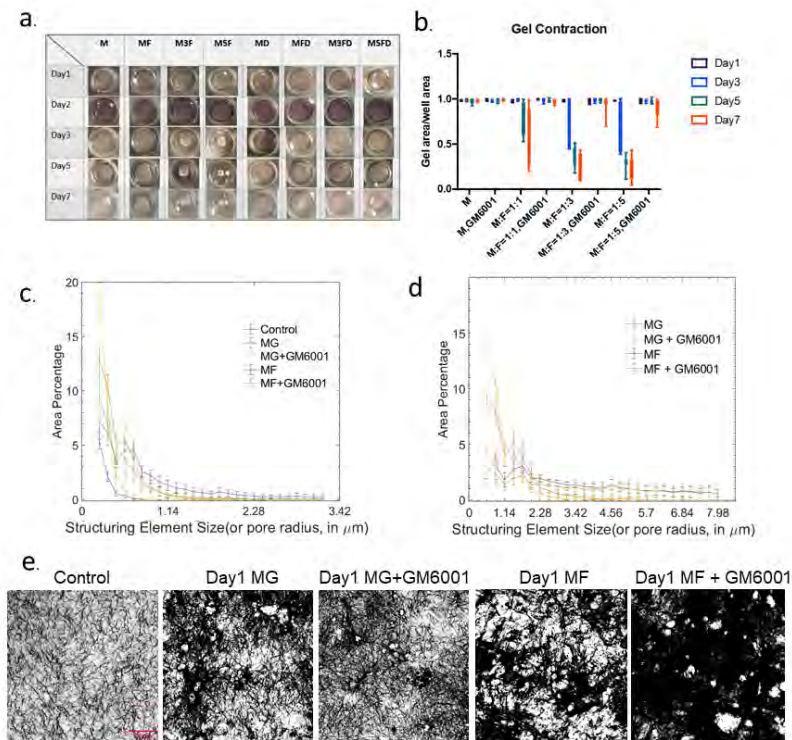


Figure 2.6: Global gel compaction in the coculture system a. Gel contraction recorded longitudinally from day1 to day7. "M" indicates MDA-MB-231 monoculture, "MF" indicates initial seeding concentration between MDA-MB-231 to NHLF is 1:1; "M3F" indicates initial seeding concentration between MDA-MB-231 to NHLF is 1:3; "M5F" indicates the initial seeding concentration between MDA-MB-231 to NHLF is 1:5; "MD" indicates MDA-MB-231 monoculture with $20\mu\text{M}$ GM6001 treatment; "MFD" indicates an initial seeding concentration ratio of 1:1 between MDA-MB-231 to NHLF with $20\mu\text{M}$ GM6001 treatment; "M3FD" indicates an initial seeding concentration ratio of 1:3 between MDA-MB-231 to NHLF with $20\mu\text{M}$ GM6001 treatment; "M5FD" indicates an initial seeding concentration ratio of 1:5 between MDA-MB-231 to NHLF with $20\mu\text{M}$ GM6001 treatment; b. Quantification of gel contraction. The ratio indicates an initial seeding concentration between MDA to NHLF in each condition. Data from at least triplicates are averaged, and in each repeat there are duplicate wells for each condition. Error bars in SEM. c and d. Pore size distribution on day0(c) and day1(d). Around 5 to 12 images (around 1000×1000 pixels) from two replicates were used for the quantification. The existence of NHLF contributes to the erosion of collagen scaffold and lead to larger hole size overall. GM6001 inhibits ECM erosion and breakage, consistent with the global gel compaction trend. e. Binarized collagen images before pore size measurement. Similar to control conditions, day1 MDA monoculture generally has more small pores visually than coculture conditions, consistent with quantification shown in d.

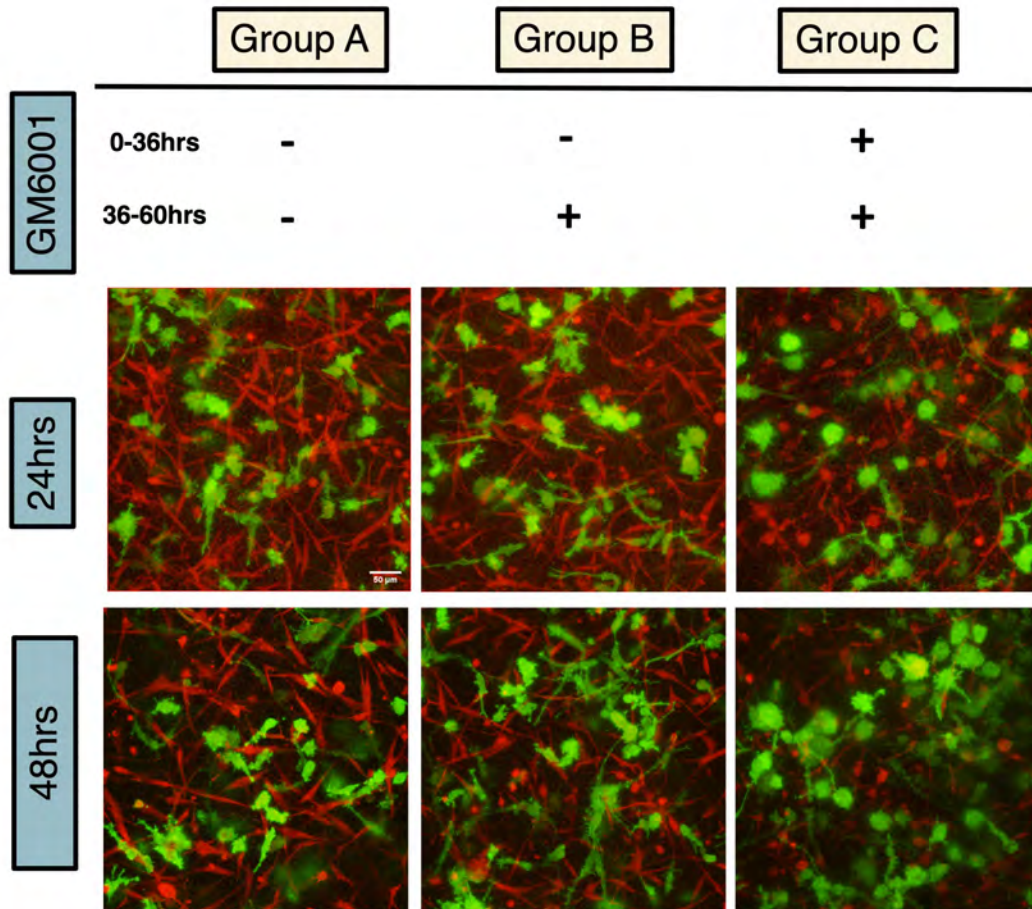


Figure 2.7: **Only GM6001 added early not late inhibits MDA migration** Addition of GM6001 into MDA-NHLF coculture system after day1 did not inhibit MDA migration compared with GM6001 addition since cell embedding, indicating the mechanism of GM6001 inhibition is through inhibiting collagen remodeling induced by NHLF. In Group A, GM6001 was not present throughout the experiment. In Group B, GM6001 was added at 36hrs after gelation. In Group C, GM6001 was added at 0hr during cell embedding. The bottom images show morphology of MDA-MB-231 cells at 24hrs and 48hrs after gelation. The initial seeding density of MDA-MB-231 is 800K/ml and NHLF is 2400K/ml. Scale bar is 50 μ m.

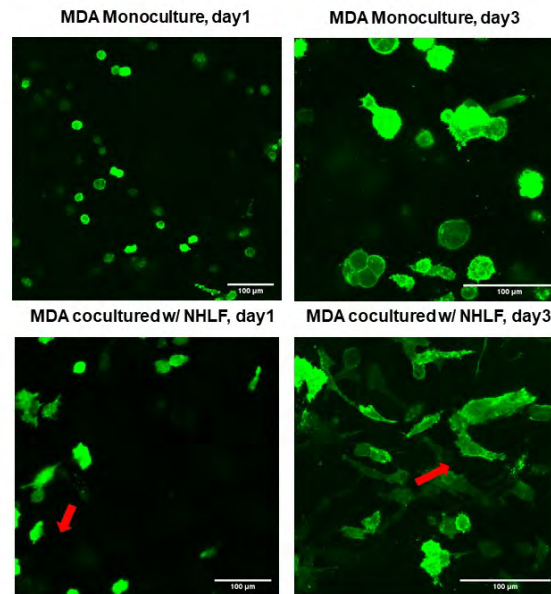


Figure 2.8: MDA-MB-231 morphology in long term culture. Scale bar is 100 μ m.

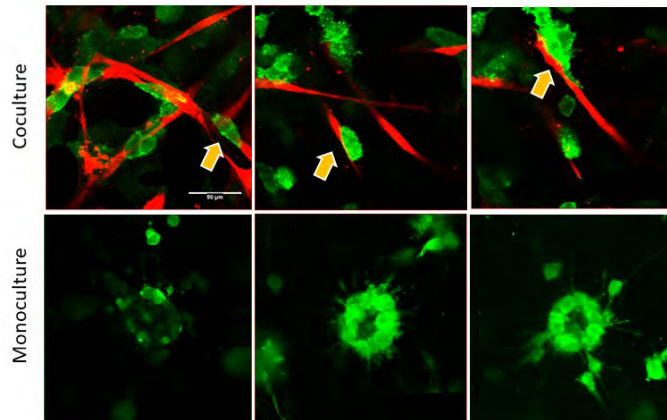
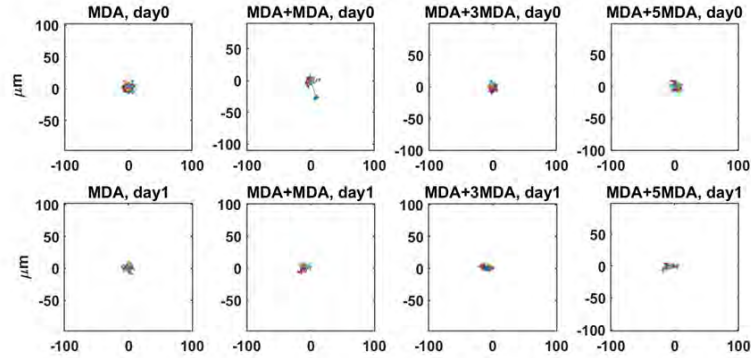
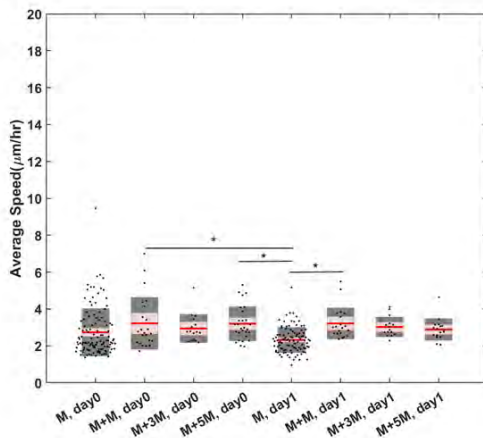


Figure 2.9: MDA-MB-231 (green) in close contact with NHLF (red) can be seen in coculture conditions (top row). In monoculture, petal-like structure can be seen after around \sim 4-5 days post cell embedment. Scale bar is 50 μ m.

a.



b.



c.

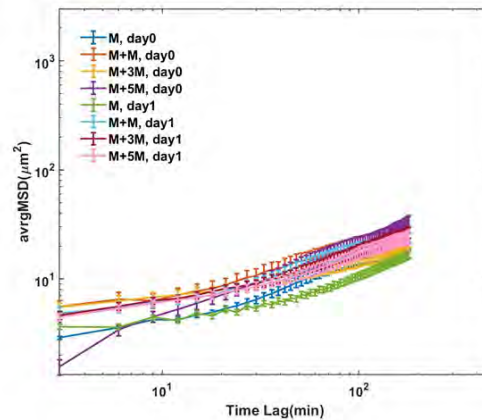


Figure 2.10: When NHLFs are replaced with MDA-MB-231 cells, differences in cell concentration in monoculture conditions appear to have low impact on cell migration, relative to coculture conditions. a: Overlaid trajectories truncated at 180min; "MDA" indicate 1X MDA-MB-231 monoculture, "MDA+MDA", "MDA+3MDA", "MDA+5MDA" indicate 2X, 4X and 6X MDA-MB-231 monoculture respectively. b: Average speed, "MDA" is shortened as "M" for brevity. Raw data points are overlaid with gray boxes which indicate +/- one standard deviation and pink boxes which indicate the 95% confidence interval; One way ANOVA was performed to show the difference across all conditions. * indicates the two compared conditions are significantly different ($p < 0.05$). Tukey's honest significant difference criterion is used in post-hoc analysis. c: Average MSD, errorbar in SEM.

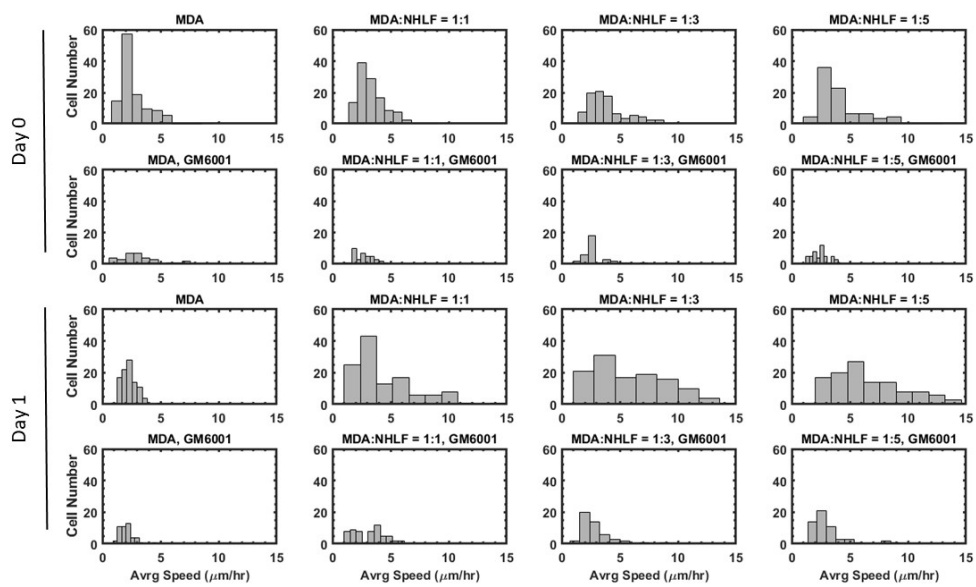


Figure 2.11: Histogram of Average Cell Speed, X axis: average speed. Y axis: number of cells.

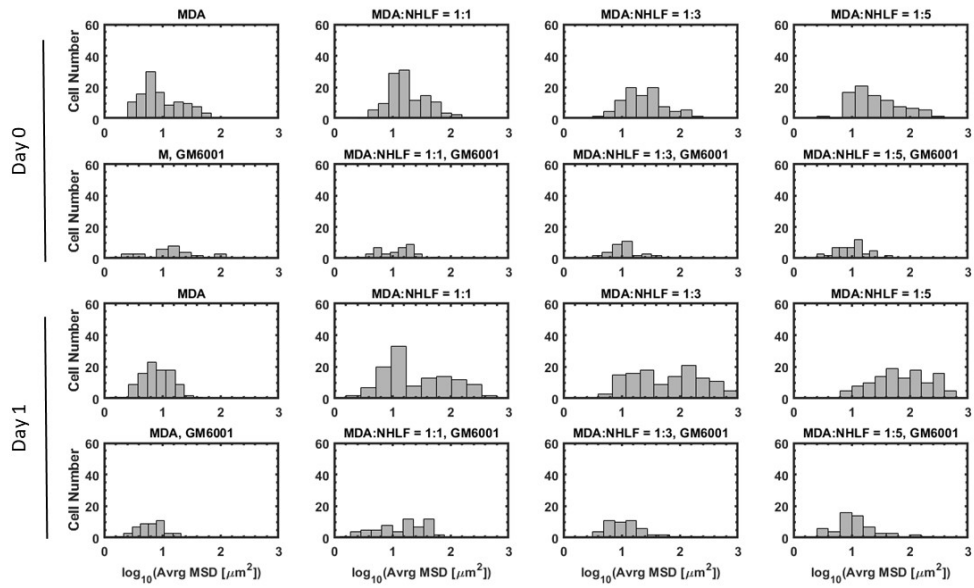


Figure 2.12: Histogram of $\log_{10}(\text{averageMSD})$, X axis: $\log_{10}(\text{averageMSD})$. Y axis: number of cells.

2.5 Future Directions

In this study, MDA-MB-231 cell line is investigated. However, in my other unpublished data, such as Hela, Mel624, they do not show significantly increased migration when in coculture with NHLF.

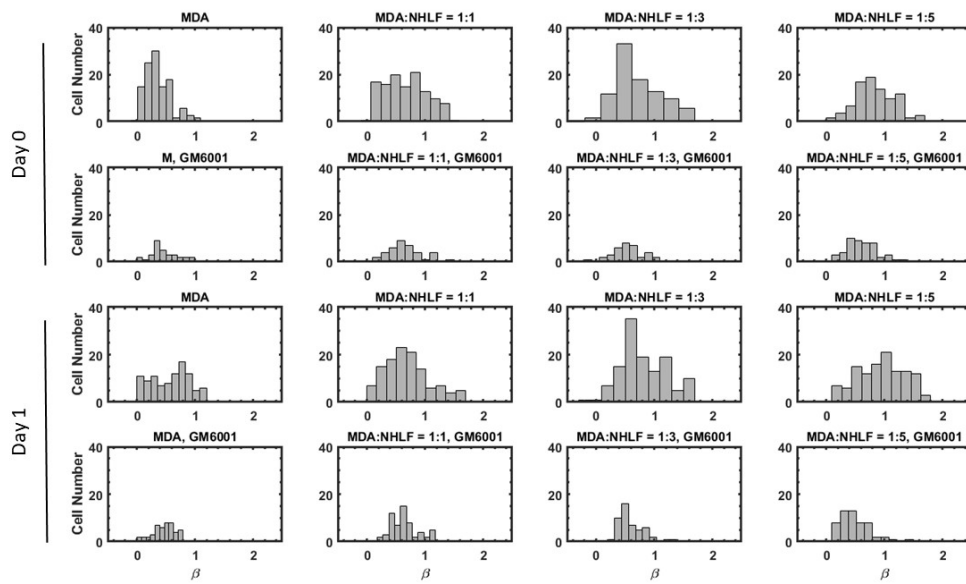


Figure 2.13: Histogram of β , X axis: β . Y axis: number of cells.

Chapter 3

3D Model of the Early Melanoma Microenvironment Captures Macrophage Transition into a Tumor-promoting Phenotype

3.1 Abstract

Tumor immune response is shaped by the tumor microenvironment (TME), which often evolves to be immunosuppressive, promoting disease progression and metastasis. An important example is melanoma tumors, which display high numbers of tumor-associated macrophages (TAMs) that are immunosuppressive but also have the potential to restore anti-tumor activity. However, to therapeutically target TAMs, there is a need to understand the early events that shape their tumor-promoting profile. To address this, we built and optimized 3D *in vitro* co-culture systems, composed of a collagen-I matrix scaffolding murine bone-marrow-derived macrophages (BMDMs), YUMM1.7 melanoma cells, and fibroblasts to recreate the early melanoma TME and study how interactions with fibroblasts and tumor cells modulate macrophage immune activity. We monitored BMDM behavior and interactions through time-lapse imaging and characterized their activation

and secretion. We found that stromal cells induced a rapid functional activation, with increased motility and response from BMDMs. Over the course of seven days, BMDMs acquired a phenotype and secretion profile that resembled late melanoma TAMs. Overall, the direct cell-cell interactions with the stromal components in a 3D environment shape BMDM transition to a TAM-like immunosuppressive state. Our systems will enable future studies of changes in macrophage-stromal crosstalk in the melanoma TME.

3.2 Introduction

The immune response against tumors is conditioned by the tumor microenvironment (TME), which is often highly immunosuppressive and depleted of effector cells[84]. In the TME, cells communicate via direct contact and a network of secreted signals established early during tumor development. Non-tumor cell types within the milieu co-evolve with tumor cells, disrupting tissue homeostasis while favoring disease progression and metastasis[85]. Thus, cell-cell interactions between immune cells, tumor cells, and other support cells play an active role in shaping the immune environment in tumor progression and responses to immunotherapy[86].

Melanomas are very aggressive tumors and frequently lethal, but they have been particularly responsive to immune checkpoint inhibitors aimed at boosting T cell function, specifically through PD-1 and CTLA-4 blockade [87, 88]. On the other hand, advanced melanomas usually display low infiltration of T cells and high numbers of tumor-associated myeloid cells (TAMs), and the latter correlates with a worse prognosis [42]. TAMs and cancer-associated fibroblasts (CAFs) are key players in the TME, with a context-dependent role and providing support for both tumor and immune cells[86, 89]. TAMs reprogram their functional state as the tumor grows, although the specific mechanisms leading to the accumulation of immunosuppressive TAMs remain unclear. This phenotypic and functional plasticity make TAM-targeted therapies a promising treatment option[43, 44, 45].

However, current available data is not sufficient to explain or predict treatment outcomes, since the immune activity in the TME is an emergent property of many interacting cell populations[90].

In recent years, the biomechanical interactions within the TME have been of interest since this interplay can induce and regulate specific functional phenotypes of its components. Cells in the TME are embedded in an extracellular matrix (ECM), which has a complex and evolving composition and structure and mediates a series of dynamic physical interactions between tumor and stromal cells[91]. Collagen structure can modulate TAM polarization and changes in macrophage morphology have suggested different functional phenotypes, such as higher expression of Arg-1, CD206 and YM-1[92]. Higher collagen density usually correlates with higher numbers of immunosuppressive macrophages and the reinforced confinement can down-regulate pro-inflammatory cytokine secretion[93, 94]. Increased collagen stiffness can regulate immune cell spreading, motility and response to treatment[95, 96]. Fibroblasts are key remodelers of the ECM, through secretion of ECM proteins, proteolysis via metalloproteinases, and force-mediated ECM reorganization[97, 98]. Dynamic forces in the ECM have a role in initiating and guiding macrophage migration. As the major source of contractile forces, fibroblasts cue and recruit macrophages from hundreds of micrometers away[38].

Intercellular signaling between TAMs and other cell types is central to establishing and maintaining an immunosuppressive TME and is a critical target to reestablish an effective TME immune response[99, 100]. Although TAMs have been associated with resistance to checkpoint inhibitors treatment[101], targeting TAMs through the combination of CD40 agonist and CSF1R inhibitor induces a new pro-inflammatory TAM subpopulation that leads to a change in the TME and T-cell dependent tumor control[99]. Determining how TAMs communicate with other cell types in the melanoma TME is needed to develop more effective methods to target the network of extracellular signals[102, 103].

Studying all these variables in dynamic *in vivo* environments can be challenging when

trying to identify individual contributions to TME evolution. Recent studies have demonstrated that organotypic melanoma cultures outperform 2D assays when studying TME-imprinting mechanisms and closely resemble tumor growth as observed in human lesions while supporting cell survival and function[104, 105]. The use of 3D cultures may accelerate the identification of predictive and/or prognostic markers and the development of effective combination therapies[106]. *Ex vivo* systems that incorporate key features of the native TME and model the dynamic response to checkpoint inhibitors can facilitate efforts in precision immuno-oncology.

Our work recapitulated the evolution of the dynamic interactions in an *in vitro* 3D co-culture model. In this model, we have demonstrated how profiles of cytokines evolve over time and also how phenotype, morphology, and migration of macrophages change longitudinally, providing insights on early cell-cell interactions in the melanoma microenvironment.

3.3 Materials and Methods

3.3.1 Animals

Female C57BL/6J mice 6–8 weeks of age were purchased from Jackson Laboratories. Mice were housed according to the standard housing conditions of the Yale Animal Resources Center in specific pathogen-free conditions. Mice were left to acclimate for one week before use. All animal experiments were performed according to the approved protocols of the Yale University Institutional Animal Care and Use Committee.(Credited to my collaborator Gabriella Pizzurro)

3.3.2 Cell Lines

Yale University Mouse Melanoma (YUMM) and YUMM exposed to radiation (YUM-MER) cell lines, both WT and GFP⁺, were kindly provided by Marcus Bosenberg, Yale University [107, 108]. 3T3 MEFs WT (CRL-2742) was acquired from ATCC. 3T3MEF-tdTomato cells were previously generated in the lab using a tdTomato vector transfection (0036VCT, Vectalys, Takara) and selected for stable expression of the fluorescent protein, according to manufacturer's instructions. Cells were grown in DMEM/F12 media supplemented with 10%FBS, 1% NEAA, 2 mM L-glutamine and 1% sodium pyruvate. 3T3 MEFs were treated with 10ng/ml TGF- β 1.

3.3.3 BMDM Culture

Bone marrow-derived macrophages were generated as previously described[109]. Briefly, bone marrow was extracted from the hind legs of the mouse with a syringe. After red blood cell lysis with ammonium-chloride-potassium lysis buffer (Lonza), cells were incubated for 4h at 37°C with 5% CO₂ in a non-tissue culture (TC)-treated plastic petri dish with BMDM media (RPMI supplemented with 10% FBS, 100 U/ml penicillin, 100 μ g/ml streptomycin, 1% sodium pyruvate, 25mM HEPES buffer, and 50 μ M 2-mercaptoethanol). After 4h, the non-adherent cells were transferred to a new petri dish and incubated with BMDM media + 20ng/ml macrophage-colony stimulating factor (M-CSF; Peprotech). After 3 days, an additional 10ml of BMDM media + 20ng/ml M-CSF was added to the plate. After a total of 6 days, BMDMs were harvested in PBS+5mM EDTA with gentle scraping, and the cells were ready for further use.(Credited to Gabriella Pizzurro)

3.3.4 BMDM Polarization

BMDMs were plated non-TC treated multi-well plates (Falcon) at a density of 100,000 cells/cm² and cultured in BMDM media + 20ng/ml M-CSF. For polarization, cells were stimulated for 24h with 100ng/ml LPS (Invivogen) and 10ng/ml IFN- (Peprotech) for M1 profile, or 20ng/ml IL-4 (Peprotech) for M2 profile.(Credited to Gabriella Pizzurro)

3.3.5 Tumor Studies and Sample Processing

Female C57BL/6J mice were anesthetized with isoflurane and intradermally injected with 3.5×10^5 tumor cells in both flanks. Mice were monitored every other day for tumor growth. Tumor volume was assessed measuring with caliper tumor length (L) and width (W) and calculated as $0.52 \times L \times W^2$. At the designated timepoints, mice were euthanized in a CO₂ chamber and tumors were resected and weighted for processing. Briefly, tumors were first cut with scissors and then chopped with razor into 1mm³ pieces. They were transferred to a tube with 10ml of digestion buffer (1X PBS Ca⁺Mg⁺ containing 0.1mg/ml DNase I, Roche 05401127001, and 0.82mg/ml Collagenase IV, from *C. histolyticum*, Sigma-Aldrich C1889) and incubated at 37°C in shaker for 30 min. Samples were vortexed, filter in 40μm cell strainer and placed on ice. Cells were washed and resuspended in ACK lysis buffer at RT for 5 min. Samples were filtered and washed again, resuspended and counted.(Credited to Gabriella Pizzurro)

3.3.6 Immunostaining, Flow Cytometry and Cell Sorting

For flow cytometry, we used the following antibodies and dyes (clone, cat): CD45 AF700 (30-F11, 103128), CD45 PercP (30-F11, 103132), CD11b BV421 (M1/70, 101236), F4/80 PerCP (BM8, 123126), CSF1R BV605 (AFS98 , 135517), Ly6C BV711 (HK1.4, 128037), Ly6C AF488 (HK1.4, 128022), Ly6G AF647 (1A8, 127610), iNOS AF488 (CXNFT, 53-

5920-82), CD40 PE (3/23, 124609), CD86 PE-Dazzle594 (GL1, 105042), MHCII APC-Cy7 (M5/114.15.2, 107628), CD206 PE-Cy7 (C)O68C2, 141720), Arg1 APC (A1exF5, 12-3697-82), and Live/Dead eFluor506 (423101) Biolegend. For phenotype analysis, at the day for processing, cells were obtained from the tumors, as previously described, or retrieved from the collagen gel by digestion with Collagenase (Advanced Matrix 5030) following the manufacturer's manual. Single-cell suspensions were stained in FACS Buffer (PBS 2% FBS). Briefly, cells were incubated with FcBlock 1/200 (anti-CD16/CD32, eBiosciences) for 20 min at 4°C. Cells were washed and then incubated with the antibody mix for extracellular markers. For intracellular staining, we used the CytoFix/CytoPerm and Perm/Wash Buffer kit (BD, 554714), according to manufacturer's instructions. Cells were then incubated with the antibody mix for intracellular markers. Samples were re-suspended in 500 μ L PBS and were analyzed on a LSRFortessa (BD Biosciences). For analysis, samples were gated for singlets and live cells. Macrophages were gated on CD11b⁺F4/80⁺ (low and high) population. For TAM sorting, single-cell suspensions from tumors were prepared as described above, and stained without fixing. TAMs were processed in a FACS Aria instrument (BD Biosciences) and sorted as CD45⁺CD11b⁺Ly6G⁻, Live⁺, and singlets. For sorting cells from the 3D coculture, single cells suspensions were sorted from Live⁺ cells: GFP⁺YUMM cells, CD45⁺CD11b⁺ BMDMs and negative selection for 3T3MEFs. (Credited to Gabriella Pizzurro)

3.3.7 Multiplex Protein Secretion

For monitoring the evolution of the microenvironment in the 3D cultures, 100 μ l were collected from the media in each well at indicated timepoints. For all the rest of different samples types, cells were plated at a density of 1x10⁶/ml in cell culture plates and incubated supernatants from *in vitro* and *ex vivo* cultures were collected, centrifuged for removing cell debris and kept at -80°C until further processing. They were then submitted to Eve

Technologies Corp (Calgary, Alberta, Canada) to perform a Mouse Cytokine/Chemokine Array 44-Plex (MD44) assay, which is based on color-coded polystyrene beads combined with a dual-laser and a flow-cytometry system for sample acquisition and analysis. All detected analytes were within the dynamic range of the standard curves of each analyte, observing no saturation in the samples analyzed. For data analysis purposes, those presenting an out of range (OOR) measurement below the parameter logistic standard curve were systematically replaced with the lowest value obtained for a particular analyte, as per suggestion of the company. The data were then either natural log-transformed or converted to z-scores to aid in visualization. Samples were visualized and hierarchically clustered using the clustermap function from the Seaborn module in Python. (Data analysis credited to Gabriella Pizzurro)

3.3.8 Single-cell Secretion Assay and Analysis

The single-cell secretion profiling experiments were performed as previously described[110]. TAMs were loaded into the PDMS microwells in BMDM media, and exposed to the flow-patterned antibody array slide for Chi3l3, MMP9, IGF-I, IL-10, CCL17, CCL22, CCL2, CCL3, CCL5, IL-27, IFN-1, CXCL1, TNF- α , IL-6, IL-12p40, and analyzed as previously described. For visualization, single-cell secretion data were embedded in two-dimensional space with Potential of Heat diffusion for Affinity-based Transition Embedding (PHATE)[111]. This dimensionality reduction algorithm better preserves the nonlinear progressions and branching that describe the spectrum of continuous phenotypes expected in single-cell data from a single cell type. To investigate functional heterogeneity, cluster analysis of the single-cell secretion data was accomplished with PhenoGraph[112], which is an unsupervised, graph-based clustering method developed to identify subpopulations in high-dimensional single-cell data. Extracted clusters were analyzed using custom scripts written in Python. PHATE and PhenoGraph are both available as publicly available

software packages in Python.(Credited to Gabriella Pizzurro, Amanda F. Alexander and Kathryn Bridges)

3.3.9 Histology and Immunofluorescence

Tumor samples were fixed in formaldehyde and paraffin-embedded. Hematoxylin/Eosin (HE)staining was performed on tumor slices. Immunohistochemistry for EGFR was performed on tumors slices and counterstained. Fibroblast density was calculated as area per High-Power Field (HPF). For immunofluorescence on 3T3MEFs, cells were plated onto round, poly-L-lysine-coated glass coverslip in 24-well plates. YUMM conditioned media (CM) was generated by culturing cells to 100% confluency and then replacing media for FBS-free RPMI. CM was collected after 48h, fractioned and kept at -80°C. Cells were left unstimulated, or treated with 5ng/ml TGF- β 1 (Peprotech) or YUMM conditioned media, for 24h. Then cells were fixed in methanol, stained with anti-SMA AF488 (ab184675, Abcam) and anti-FAP (ab28244, Abcam) overnight at 4°C. Then they were incubated with Goat anti-Rabbit PE and Hoechst. Coverslips were mounted and analyzed in a fluorescent microscope.(Credited to Gabriella Pizzurro, Alice Huang)

3.3.10 Stained Collagen Pulling Assay

Rat tail type I collagen(Corning) was labeled with Alexa Fluor 647 NHS Ester (Succinimidyl Ester) and dialyzed as before[113]. The CM was then made by diluting thawed supernatants 1:2 with fresh culture media. In the assay, 3T3MEFs (tdTomato) were embedded in 1.5mg/ml stained collagen at a density of 600K/ml. Conditioned medium or normal medium(control group)was added after 1h gelation at 37°C and replaced daily. Confocal tilescan imaging was taken on day5.

3.3.11 Proliferation Assay

Once BMDMs were differentiated and stimulated, they were stained with 5uM CFSE (Molecular probes, Life Technologies) in PBS. In brief, cells were washed, resuspended with the CFSE solution to 2×10^6 /ml and stained for 10 min at 37°C, plus 5 min on ice. Then equal volume of complete media was added, and left for 5 min at room temperature. Cells were then centrifuged at 1500rpm for 5 min, resuspended in fresh media and counted for subsequent use. Analysis of CFSE assay was performed using FlowJo software (TreeStar).(Credited to Gabriella Pizzurro)

3.3.12 Spheroid Assay

BMDMs, 3T3 MEFs and YUMM cells were first stained with CellTracker™ Deep Red Dye(C34565), CellTracker™ Orange CMTMR Dye(C2927), and CellTracker™ Green CMFDA Dye(C7025) respectively at 37°C incubator for 45min, then washed in fresh medium and resuspended in 2% Matrigel (Corning 354230). Resuspended cell solutions were aliquot in agarose gel-coated 96 well plates with a fixed density of 12K BMDMs, 1K YUMM cells, and 3K 3T3 MEFs per well. The cell-loaded plates were centrifuged with 1000g for 10min and then kept in 37°C, 5% CO₂ incubator. Spheroids were collected on day4 and embedded in 1.5mg/ml rat tail type I collagen (Corning CB354249) for further study.

3.3.13 3D Cell Culture

BMDMs, 3T3MEFs, and cancer cells were harvested and seeded in neutralized 1.5mg/ml rat tail type I collagen (Corning CB354249) as previously described[114]. Complete growth medium was added after 1h gelation at 37°C incubator. The 3D coculture was maintained in 37°C, 5% CO₂ with medium changed every 1-2 days. Unless other noted,

BMDMs, 3T3 MEFs and cancer cells were seeded at a density of 2400K/ml, 200K/ml and 200K/ml respectively. At the day for processing, cells were retrieved by digestion with collagenase (Advanced Matrix 5030), following the manufacturer's instructions.

3.3.14 Collagen Quantification

In the collagen quantification assay, BMDMs, 3T3 MEFs and cancer cells were seeded at a density of 2400K/ml, 600K/ml and 200K/ml, respectively, in a 96 well plate. Only half of the medium was changed daily and was gently added in a dropwise manner to minimize the pipetting disturbance to the collagen. On day3 and day7, the 96 well plates were frozen and kept at -80°C immediately after medium removal. Fresh tumor samples were collected on day7 and day14 and kept frozen at -80°C after mass and volume measurement. Collagen was measured using the SirCol Collagen Assay Kit (Accurate CLRS1111). Both *in vitro* culture and tumor samples were thawed right before the assay and processed according to manufacturer's instructions. To note, after acid extraction, tumor samples were first filtered by 100um cell filter and then centrifuged at 5000g for 10min to remove residual undigested debris. The total collagen in the supernatants were measured and used to represent the total soluble collagen in the tumor sample.

3.3.15 Confocal Imaging

Confocal imaging (Leica SP8, 20X0.75NA objective) was performed to track 3D culture along time. For these experiments we used GFP⁺ melanoma cells. BMDMs were stained with CellTracker Deep Red Dye (C34565) and 3T3MEFs with CellTracker Orange CMTMR Dye (C2927) at 37°C incubator for 45min before coculture. Alternatively, 3T3MEFs tdTomato were used for imaging. 12h time-lapse or tile scan images were collected on day0, day1, day3, day5, and day7 for macrophage migration and morphology analysis.

3.3.16 Confocal Image Analysis

Macrophage migration was tracked with TrackMate on Fiji. Cell center was defined by averaged coordinates of traced cell boundary on a projected image, and average speed was calculated as the mean of the absolute value of the cell net displacement every 1hr time intervals. Mean squared displacements were computed with the following equation:

$$MSD(n) = \frac{1}{N - n + 1} \sum_{i=0}^{N-n} [(x_{i+n} - x_i)^2 + (y_{i+n} - y_i)^2] \quad (3.1)$$

where x and y indicate x and y coordinates, n indicates the n-th step and N total step number. For morphology analysis, high resolution XYZ tile scan imaging was collected longitudinally. Imaging tiles were merged and projected before segmentation. Macrophage compactness, circularity and elongation index was calculated by following equations in MATLAB respectively:

$$compactness = \frac{4 * pi * Area}{Perimeter^2} \quad (3.2)$$

$$circularity = \frac{4 * pi * Area}{ConvexPerimeter^2} \quad (3.3)$$

$$elongation = \frac{width_{boundingbox}}{length_{boundingbox}} \quad (3.4)$$

In the tumor-macrophage distance measurement, xy coordinates of cell center were tracked by TrackMate while z coordinate was decided manually by identifying the slice with the highest intensity pixels and clearest cell boundaries. To calculate 3D distance at each time point is cumbersome, hereby we use the cell position at the beginning of imaging (immediately after 1h gelation) to represent the paired 3D distance. Average speed of macrophages was calculated with the same way as above-mentioned by deriving the planar net displacement per hour. To properly define the close and far macrophages, each paired macrophage-tumor distances was ranked from smallest (close to tumors) to largest (far from tumors). The average speed of the fifteen closest macrophages (i.e. close

macrophages) and the fifteen farthest macrophages(i.e. far macrophages) was calculated by taking the mean of the macrophage distances in each group.

3.3.17 Statistical Analysis

Unless other noted, one-way ANOVA or two-way ANOVA was used with post-hoc comparisons in Prism9. Pearson correlation coefficients were calculated for each pairwise combination of samples using the pearson function from the scipy.stats module in Python. These results were visualized with Matplotlib's matshow function. For far-close tumor-macrophage distance comparison, one tailed t-test was performed to compare the average speed of close and far macrophages.

3.4 Results

3.4.1 *In vitro*-polarized BMDM phenotypic and functional profiles are distinct from TAM profiles

To study the early events in the melanoma TME that shape the TAM tumor-promoting profile, we proposed to build a 3D *in vitro* culture system using the Yale University Melanoma Model (YUMM) 1.7, which has genetic changes common to human melanomas, including BRAFV600E, Pten^{-/-}, and Cdkn2^{-/-} [107, 108]. In order to have a benchmark for our model of melanoma TAMs *in vitro*, we first isolated TAMs from YUMM1.7 murine tumors on days 7, 10 and 16 and characterized their phenotypic and functional profiles. The melanoma TAMs from YUMM1.7 (Y) and YUMMER1.7 (YR) tumors showed an overall similar phenotypic profile when contrasted against peritoneal macrophages isolated from the same mice, with slight variations across timepoints (Figure3.4.a). However, these melanoma TAMs displayed a heterogeneous phenotype, clustering into multiple subsets expressing a combination of markers canonically associated with opposed polarization

states. When we isolated TAMs from the tumor and cultured *in vitro*, they quickly lost this complexity and became a more homogeneous population (Figure 3.4.b).

We next generated BMDMs with different polarization states (M0, M1 and M2), which we proposed to use to model TAMs in our *in vitro* co-cultures, and we compared their characteristics to the melanoma TAMs. Specifically, we measured expression of CD11b, F4/80, Ly6C, CSF1R, iNOS, CD40, CD86, MHCII, Arg1 and CD206 expression by flow cytometry. When we used principal component analysis (PCA) to visualize the expression of M0, M1, and M2 BMDMs versus TAMs isolated from melanomas, we found that TAMs showed an intermediate state (Figure3.1.a). Interestingly, we also found that TAMs had a stronger association determined by the stage of the tumor, early (day 7) or late (day 14), than with the tumor from which they were isolated. When the single-cell FACS data was visualized using UMAP, we found that *in vitro*-polarized BMDMs had a more consistent expression of canonical markers and were more tightly clustered than the TAMs, which appeared to be composed of subpopulations with a mixed expression of M1- and M2-associated markers (Figure3.1.b-c).

We also defined functional aspects of the melanoma TAMs in the TME through their secretion profiles. Again using PCA to visualize the population-level secretion program for each group, we observed that TAMs occupied a distinct functional state from M0, M1, and M2 BMDMs, and these differences increased over time (Figure3.2.d). Analysis of the cytokine and chemokine (C/C) secretion levels showed that TAMs secrete a broader number of C/Cs than BMDMs with well-defined polarization states (Figure3.2.e), and displayed more variance between samples (Figure3.5.c). TAMs isolated from day 14 tumors were more active secretors than those from day 7 tumors.

To further dissect the functional subsets of melanoma TAMs, we studied their single-cell secretion using a multiplex panel for M1/M2-like profiling in an in-house micro-well device, developed in our lab (Figure3.6.d, [115]) and previously used to characterize BMDMs and TAMs [99, 110]. We found that approximately 60% of TAMs isolated

from these melanoma tumors were not actively secreting any of the measured proteins (Figure3.6.e), similar to previous observations[99]. When we compared secretion from BMDMs polarized *in vitro*[110] to melanoma TAMs, we found that TAMs displayed a secretion profile that placed them between the M1 and M2 *in vitro*-defined profiles (Figure3.2.f, Figure3.3.g). We identified functional clusters within these TAMs, which aligned into two activation axes, one having an M2-like profile and another one with a mixed pro-inflammatory one (Figure3.3.h, Figure3.6.f). TAMs from both melanoma tumors exhibited similar profiles of secretion, with single-cell functional sub-clusters heterogeneity (Figure3.6.g-h).

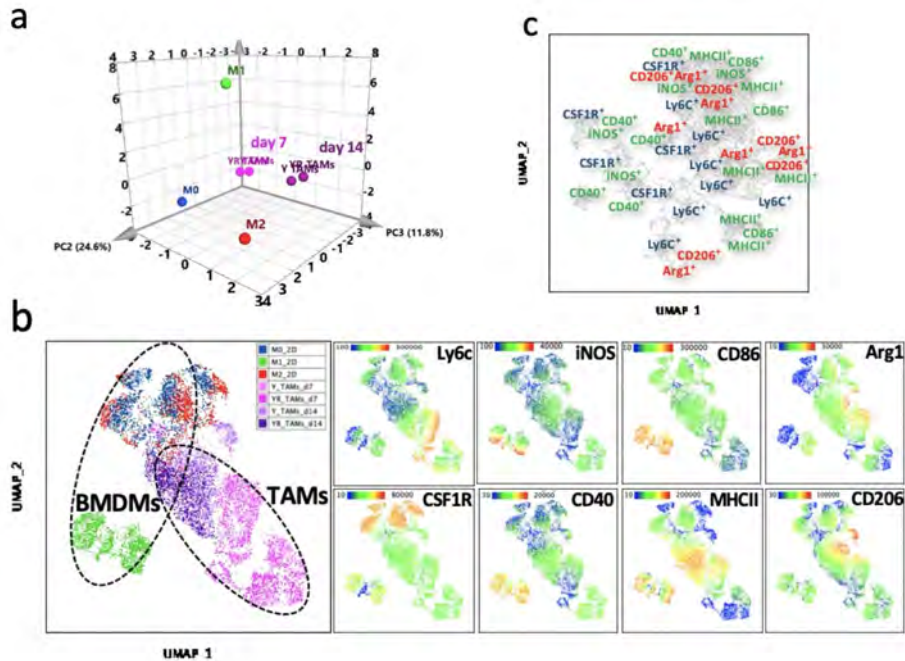


Figure 3.1: **Characterization of the phenotype and functional profile of melanoma TAMs.** a. Phenotypical profile of melanoma TAMs. Principal component analysis (PCA) of the phenotype of *in vitro* stimulated BMDMs compared to TAMs from YUMM and YUMMER early (day 7) and late (day 14) tumors. This phenotypical characterization was assessed by flow cytometry using a panel of 10 markers and then combining the percentage and MFI of those parameters for the PCA analysis. For BMDMs n=5, TAMs n=4/5. b. UMAP plots containing representative FACS single-cell data from a. Left, sample annotation. Right, detailed panels with heatmaps showing the expression of different markers used for analysis. c. UMAP visualization with superimposed annotation of markers expressed in different regions of the phenotypic space in YUMM d14 tumors.

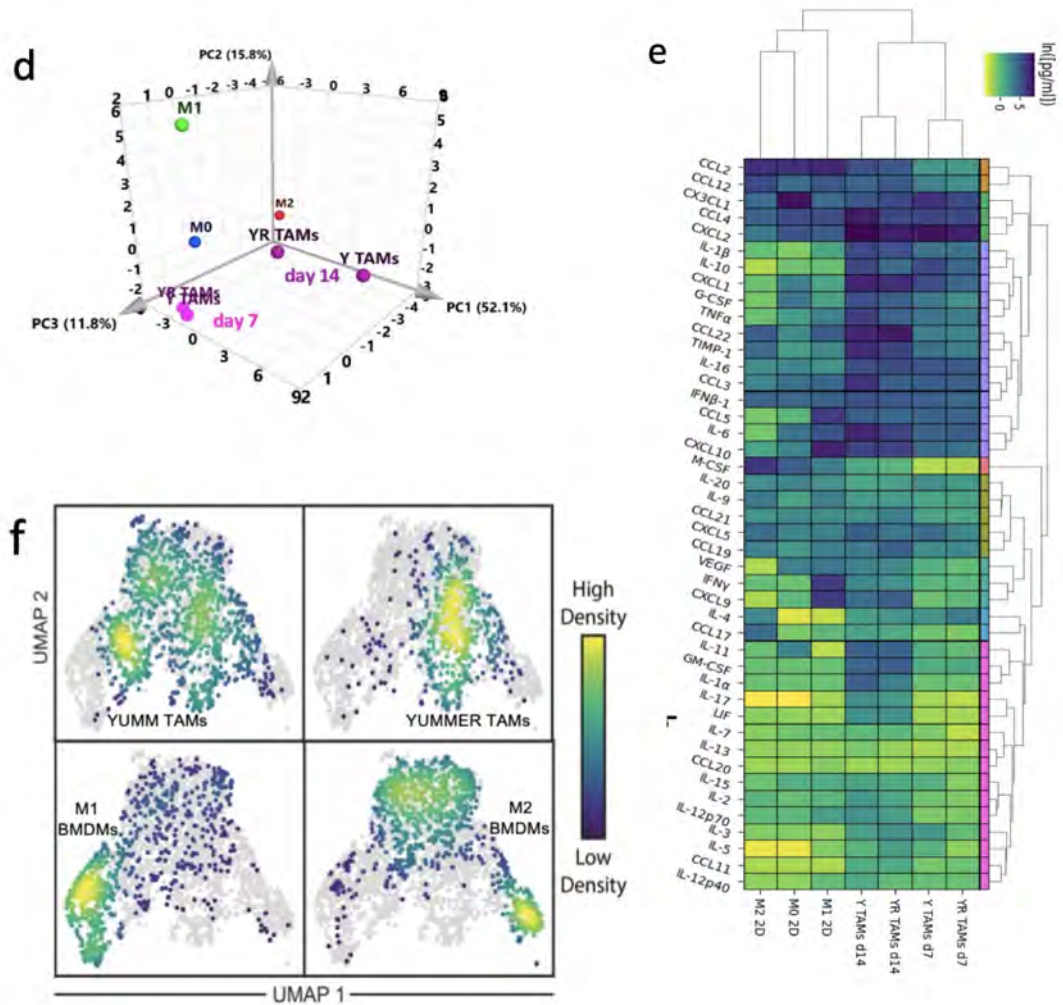


Figure 3.2: **Characterization of the phenotype and functional profile of melanoma TAMs.** d. Functional profile of melanoma TAMs. PCA of the bulk secretion of *in vitro* stimulated BMDMs compared to TAMs from YUMM and YUMMER early and late tumors. e. Hierarchical clustering analysis of the secretion profile of Y and YR TAMs at early and late timepoints compared to BMDM reference polarized states. f. UMAP visualization of single-cell secretion profiles combining Y and YR TAMs with *in vitro* polarized BMDMs into M1 or M2.

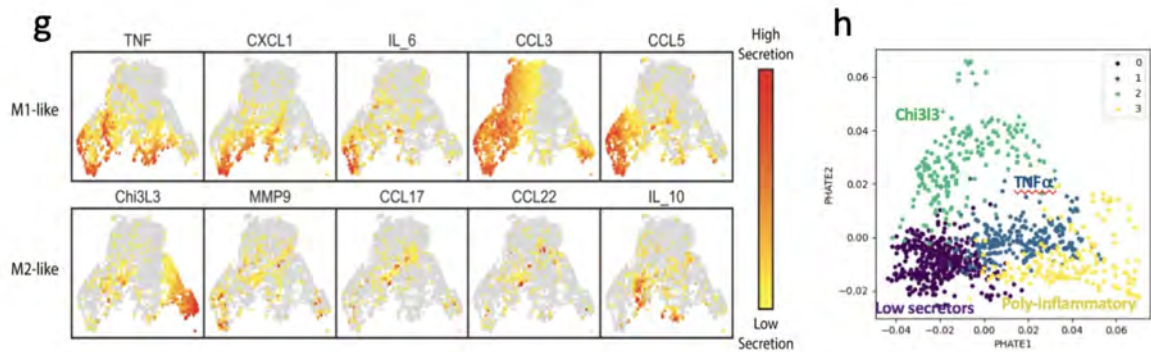


Figure 3.3: **Characterization of the phenotype and functional profile of melanoma TAMs.** g. Detail of the protein secretion associated with and M1- or M2-like function and distribution between conditions. h. Annotation of the TAM functional clusters from YUMM and YUMMER tumors, in the PHATE plots, showing the generation of a pro-inflammatory axis on the first component and a Chi3L3 immunosuppressive axis on the second component.

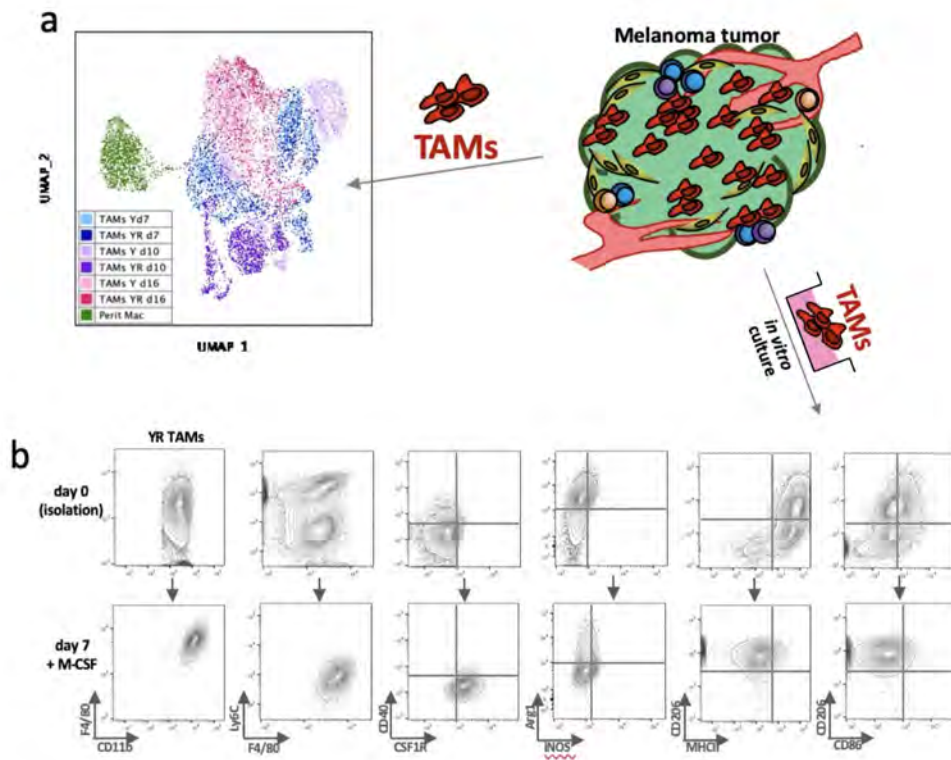


Figure 3.4: **Characterization of the phenotype and functional profile of melanoma TAMs.** a. We assessed melanoma TAM phenotype evolution by flow cytometry. Y and YR TAMs were processed at different timepoints (days 7, 10 and 16) and combined in a UMAP space for visualization. Peritoneal macrophage sample was added as a reference/control. b. Representative characterization of the phenotypic changes TAM undergo after isolation from the tumor and subsequent culture in in vitro 2D conditions for 7 days.

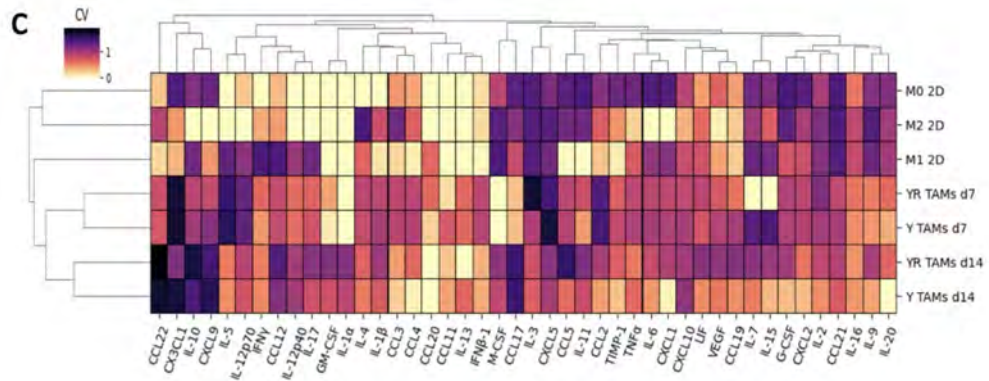


Figure 3.5: **Characterization of the phenotype and functional profile of melanoma TAMs.** c. Heatmap showing the variation of each measured protein across conditions.

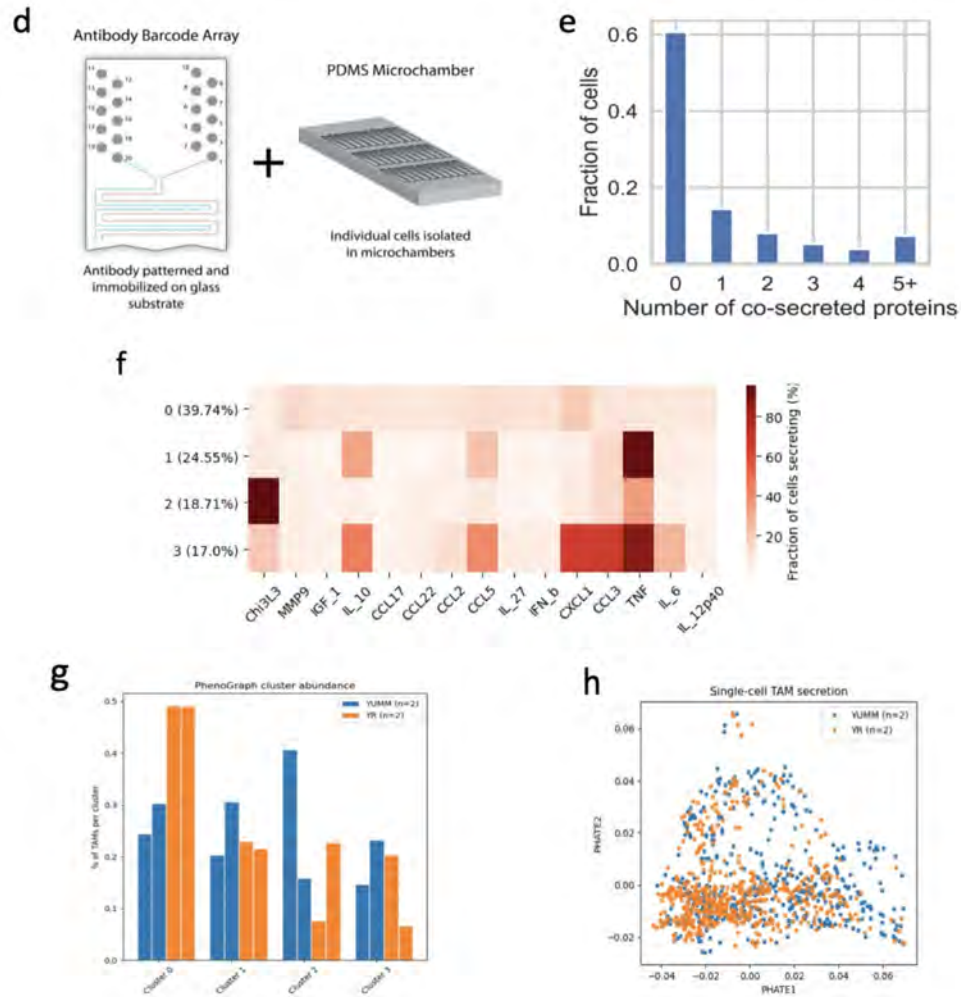


Figure 3.6: **Characterization of the phenotype and functional profile of melanoma TAMs.** d. Single-cell barcode chip device components for detecting multiplexed individual cell secretion. e. Fraction of individual melanoma TAMs from d14 tumors secreting different amount of proteins, showing high percentage of quiescent cells. f. Phenograph clustering analysis of the single-cell secretion profile of Y and YR TAMs and classification into functional clusters. g,h. Analysis of single-cell TAM secretion and detected clusters, comparing Y and YR TAMs across different clusters.

3.4.2 3D collagen cultures with BMDMs generate dynamic systems appropriate to model the early melanoma TME

In addition to melanoma cells, YUMM tumors contain fibroblasts, immune and endothelial cells, and ECM. When these melanoma cells are injected into mice, they come in contact with the dermal components and infiltrate through the collagen structure (Figure 3.7.a). Between day 5 and day 7, fibroblast infiltration changes from being evenly distributed across different regions of the tumor to being isolated in the periphery (Figure 3.7.b, Figure 3.10.a). At this timepoint, YUMM melanoma tumors were established and consistently continued to grow, but there was also a significant increase in tumor volume after a week of this event (Figure 3.7.c left, Figure 3.10.b). To determine if this change in fibroblast infiltration is associated with a significant change in the composition and interaction with the ECM, we quantified the soluble collagen present within the tumor structure of this melanoma model between days 7 and 14. In YUMM tumors, the collagen concentration significantly decreased (from $6.9 \pm 0.1 \mu\text{g}$ collagen per mg of tumor to $5.5 \pm 0.8 \mu\text{g}$ collagen per mg tumor; Figure 3.7.d). During the early days, tumor cells are growing in direct contact with the dermal structure, fibroblasts and the immune infiltrate, which is primarily made up of innate immune cells, mainly macrophages [107, 116]. Therefore, it was in our interest to understand the interactions and supporting role of fibroblasts in generating conditions that lead to tumor-promoting macrophages and favor tumor growth.

We first examined spheroids comprised of different combinations of macrophages, fibroblasts and melanoma cells. The cell structure and adhesiveness of the spheroids changed depending on their composition. BMDMs failed to form spheroids when cultured alone, but were able to incorporate into spheroids when combined with other cell types (Figure 3.10.c, Figure 3.8.e). The spheroids comprising BMDMs and YUMM cells (M0+Y) were loose, hollow cell clusters with macrophages interspersed. Adding fibroblasts to the BMDMs (M0+F) generated more solid spheroids but with indistinct bound-

aries from which cells escaped over time. Notably, spheroids with BMDMs, YUMM cells and fibroblasts (M0+Y+F) exhibited distinct features, forming solid, dense spheroids with well-defined smooth boundaries (Figure 3.8.e), resembling the compact structure of *in vivo* YUMM tumors [116]. These results support the critical role of melanoma-fibroblast-macrophage interactions in establishing the growing tumor. However, imaging these structures is difficult due to the high cell density, and so in order to study early cell-cell interactions, we proceeded to develop the 3D collagen cultures.

To recapitulate the melanoma TME *in vitro*, and study the early interactions between macrophages and stromal cells, we generated 3D cultures in 1.5mg/ml type-I collagen gels (Fig 2f). We combined YUMM cells with the 3T3-MEF fibroblast cell line and BMDMs, and analyzed the cocultures for up to 7 days. For the cell lines used, we compared different seeding densities for optimal growth in this 3D environment, and we selected 6×10^5 3T3MEF/ml and 2×10^5 YUMM/ml. We set the initial ratio in our cocultures of BMDM:Fibroblast:YUMM to 12:3:1 (Figure 3.11, Figure 3.12). In this coculture setting, unstimulated BMDMs (M0) displayed a distinct change in morphology and behavior depending on cell distributions in local areas of the gel. Macrophages in close proximity to YUMM or fibroblasts are generally longer and display extended protrusions, with their cell body aligned along the direction of the accompanying cells, and reaching for direct contact (Figure 3.9.f, Figure 3.11.d). Macrophages farther away from other cell populations are mostly round and small, with a morphology similar to monocultured macrophages. This suggests that macrophages are influenced by other cell types in the 3D collagen cocultures.

Furthermore, we observed collagen alignment and thickening in the gels, colocalizing spatially with the fibroblasts, suggesting that they might be pulling collagen bundles and altering the landscape of ECM over time (Figure 3.9.h).

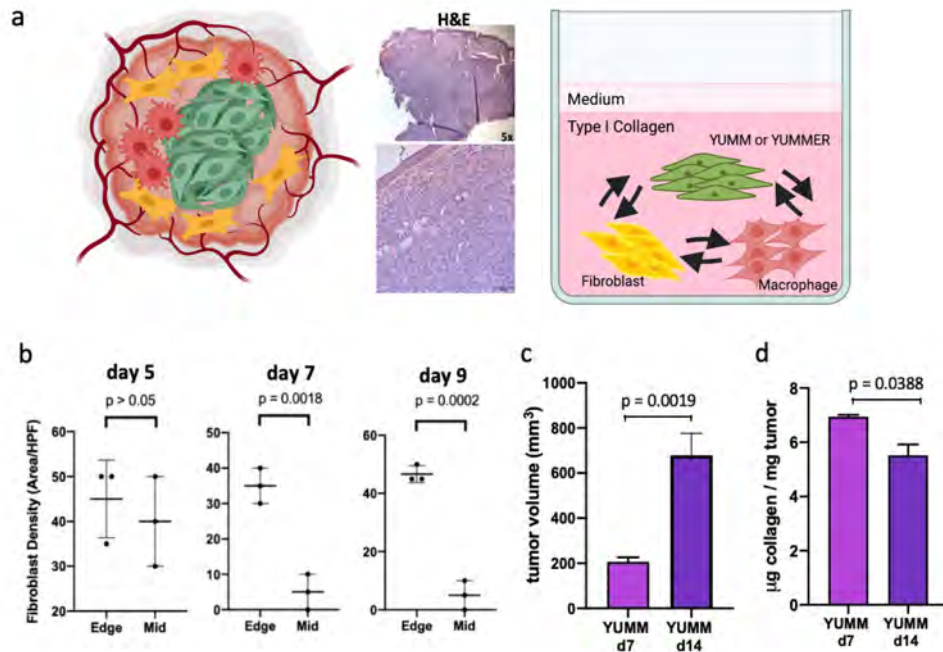


Figure 3.7: Mimicking the early melanoma TME with a 3D co-culture system. a. Characterization of YUMM tumors. Schematic representation of the melanoma microenvironment (TME), HE staining of tumors showing the intradermal tumor structure, infiltrating the whole dermal compartment and the subcutaneous space (d7 n=5, d14 n=6). b. Quantification of EGFR⁺ fibroblast density in two regions of the tumor, the middle (Mid) and the Edge. In this melanoma model, fibroblasts are evenly distributed in across regions of early tumors but, after day 7, they are rapidly segregated to the edge. c. Change in tumor volume between d7 and d14 in YUMM (n=6). d. Quantification of soluble collagen in YUMM tumors (d7 n=2, d14 n=4).

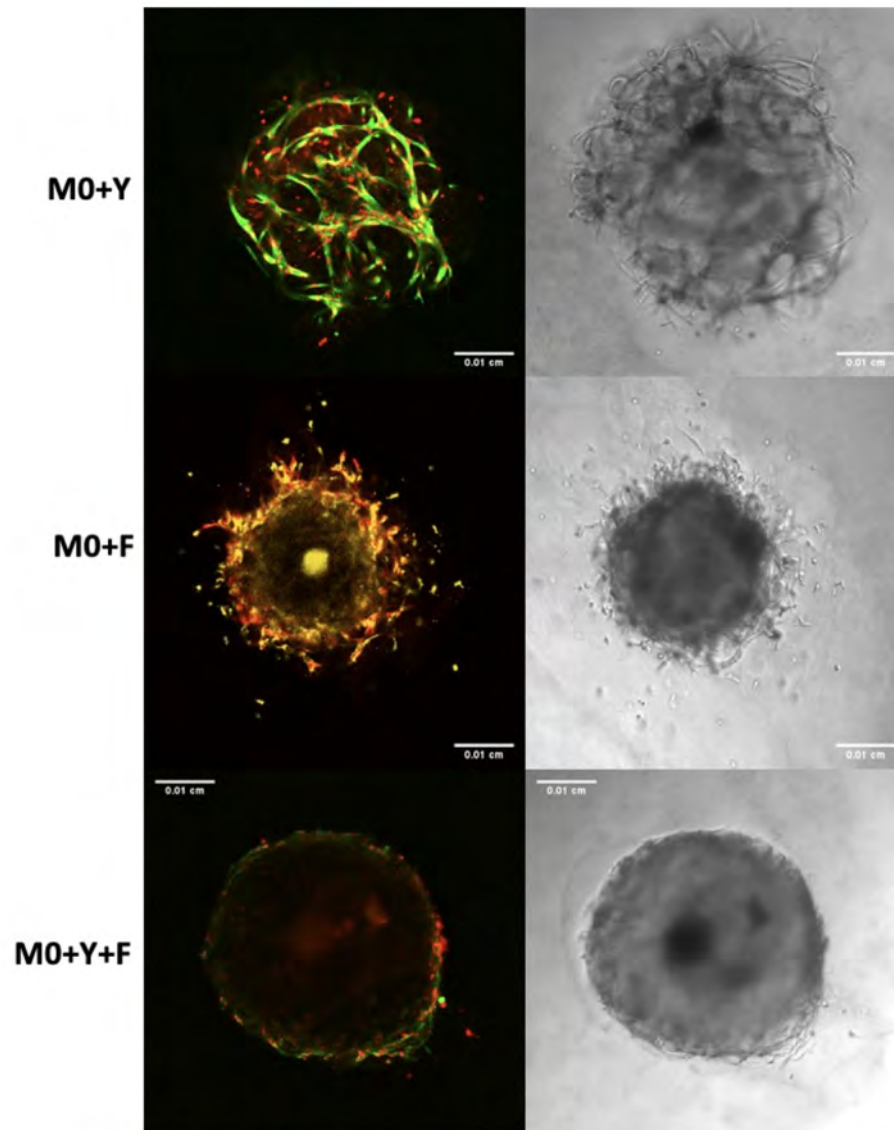


Figure 3.8: **Mimicking the early melanoma TME with a 3D co-culture system.** e. Schematic of the proposed translation of the melanoma TME into a 3D collagen cultures for *in vitro* analysis, combining BMDMs with YUMM cells and fibroblasts. After a few days in these cultures, BMDMs show different activation states, depending on their and presence of other cells.

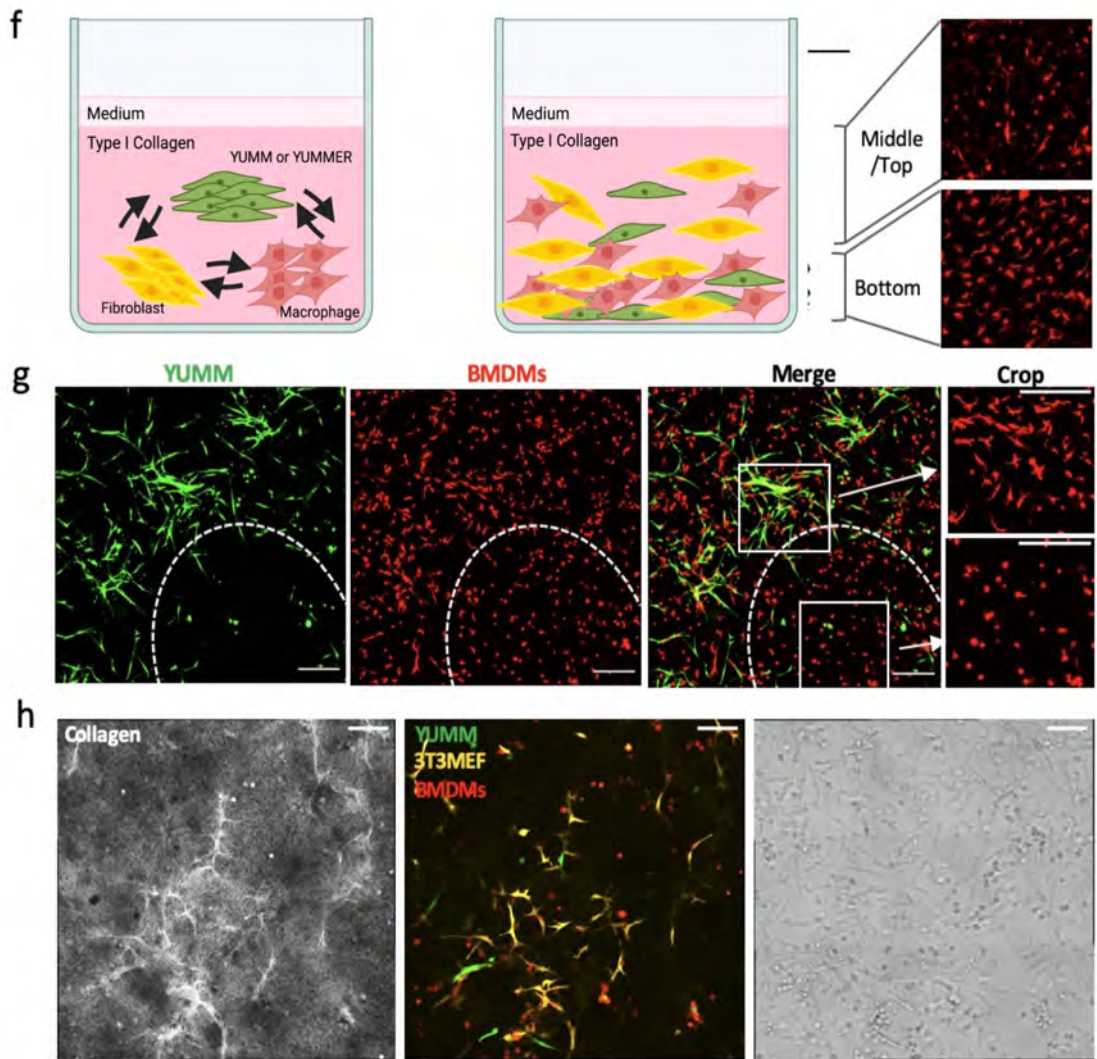


Figure 3.9: Mimicking the early melanoma TME with a 3D co-culture system. f. Representative image of a YUMM/BMDM 3D culture seeded as a single cell suspension of the cells. The white ellipse delineates an area where macrophages located further away from YUMM cells. Inserts on the right are cropped areas delineated by the dotted squares. Zoomed-in images of how macrophages differ in morphology as soon as 24h after starting the coculture, Scale bar in $200\mu\text{m}$. g. Representative images of collagen remodeling at 48h post gel embedding. Scale bar in $100\mu\text{m}$. h. Representative confocal imaging of spheroids seeded in collagen after 4 days, containing unstimulated BMDMs (M0) and combined with the other components of the system. Initial cell seeding number M0: 24×10^3 /well, YUMM: 2×10^3 /well. Fibroblast: 6×10^3 /well, in $10\mu\text{l}$ gel. Scale bar are $100\mu\text{m}$.

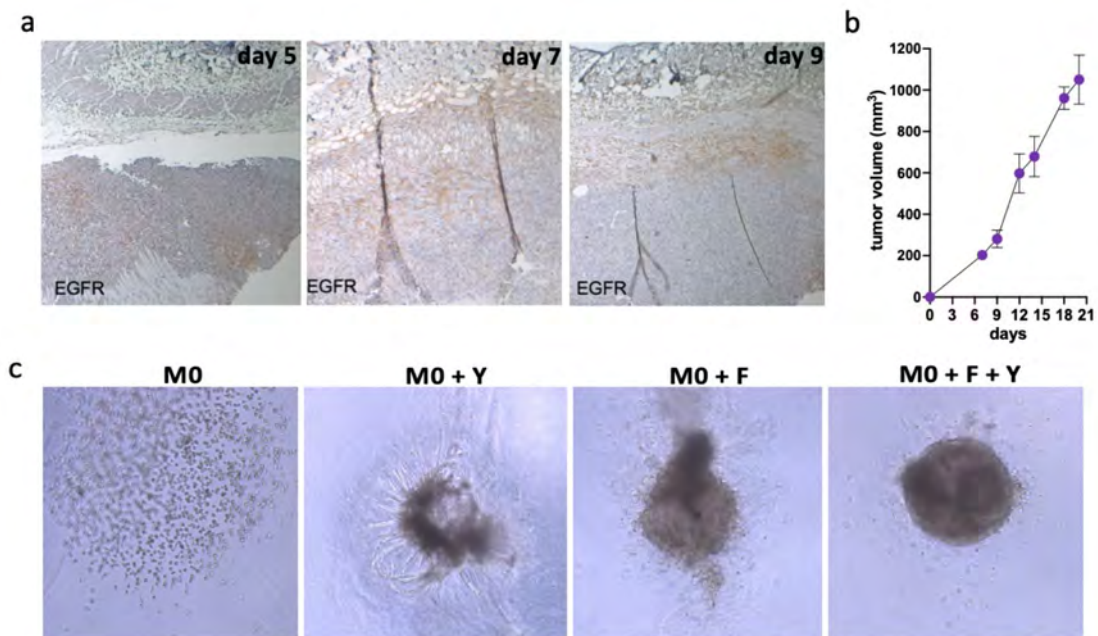


Figure 3.10: **Mimicking the early melanoma TME with a 3D co-culture system.** a. Representative images of fibroblast staining on YUMMER tumors. To locate and quantify fibroblasts in melanoma tumors at early time points, we performed immunohistochemistry staining for EGFR⁺ cells. After day 7, fibroblasts became segregated to the edge and this distribution was sustained over time. b. Growing curve, expressed in tumor volume (mm³), of YUMM tumors, injected in B6 immunocompetent mice (n=6). c. Representative spheroids generated in Matrigel prior to embedding into collagen-I for further culture.

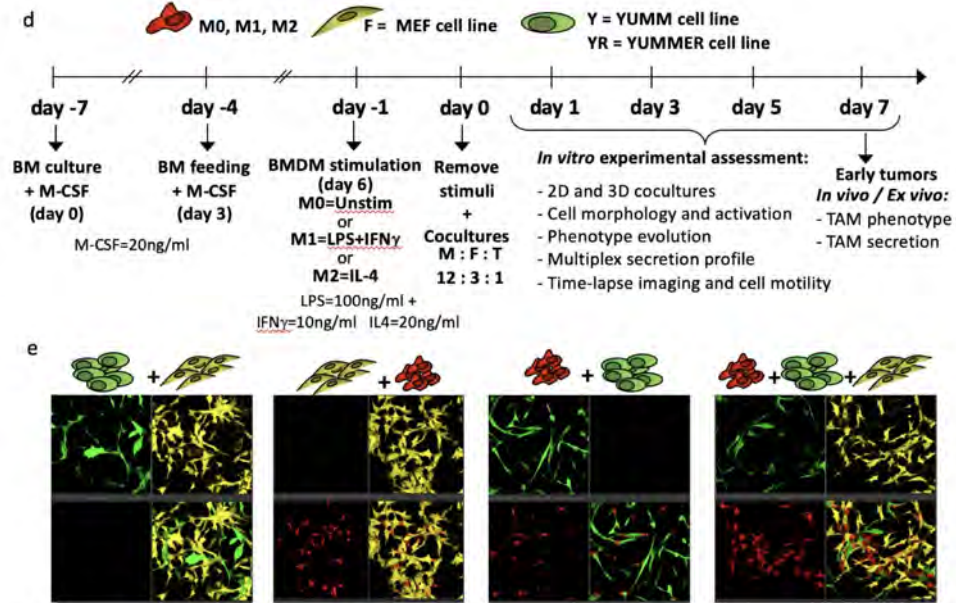


Figure 3.11: **Mimicking the early melanoma TME with a 3D co-culture system.** d. Description of the timeline of the 3D coculture experiments. e. Representative confocal images of coculture combinations of the 3 components. Cocultures were prepared using single cell suspensions, with GFP⁺ YUMM cells, tdTomato⁺3T3-MEFs and Deep-red dye⁺ BMDMs.

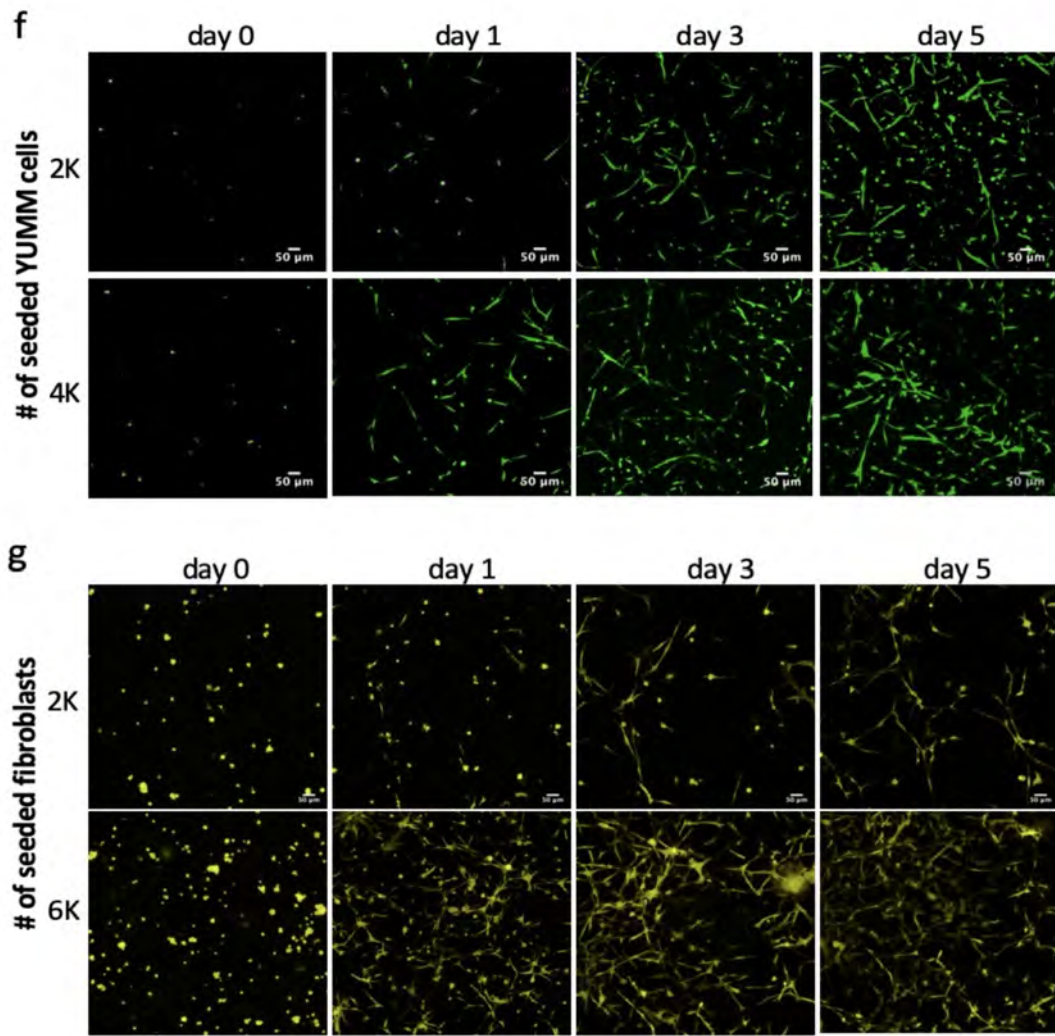


Figure 3.12: **Mimicking the early melanoma TME with a 3D co-culture system.** f. Timeline of 3D culture of GFP⁺ YUMM cells in collagen-I with different starting seeding cell density. g. Timeline of 3D culture of tdTomato⁺ 3T3MEF cells in collagen-I with different initial cell seeding densities.

3.4.3 3D collagen culture reveals progressive macrophage-stromal interactions leading to cell activation

Once we determined the optimal density and conditions for each cell type in the 3D collagen-I environment, we characterized the composition of the coculture at different timepoints. Starting with a composition containing 75% BMDMs (12M:3F:1Y ratio), we observed a rapid increase in the tumor cells and fibroblasts in the first 24h, most likely due to their higher proliferation rates. By day 3, the macrophages made up less than 20% of the total culture, while the tumor cells and fibroblasts significantly increased in number, comprising more than 80% of the culture system (Figure 3.13.a). This ratio was sustained over time, showing similar proportions after a week (Figure 3.13.a). We next characterized the health and proliferation of macrophages as a function of other cells in the cocultures. BMDMs cultured alone in the collagen-I matrix, in complete media but without M-CSF or polarizing cues, remained viable for the first 24h, but did not survive past day 3 (Figure 3.13.b). However, the presence of either fibroblasts or tumor cells within the culture significantly increased their survival, with fibroblasts slightly more efficient than tumor cells at maintaining the viability of the BMDMs (Figure 3.13.b, day 3 time point). Consistent with viability, the proliferation of macrophages in the 3D cocultures gradually increased over time, and by day 7, most of the BMDMs had undergone at least one division cycle (Figure 3.13.c). The presence of fibroblasts induced increased macrophage proliferation as early as day 3, and also supported a larger fraction of highly proliferative macrophages (Figure 3.13.d). Increased BMDM viability and proliferation in 3D cocultures with tumor cells and fibroblasts was observed with all polarization states (Figure 3.16.a-b).

We also examined how 3T3MEF fibroblasts were affected in the co-cultures with macrophages and tumor cells. This fibroblast cell line expressed several receptors and adhesion molecules commonly found in primary fibroblasts and CAFs, including PDGFR, TGFRI, VCAM1 and Podoplanin, but exhibiting heterogeneity in the population level

(Figure 3.16.d). 3T3MEF fibroblasts in the 3D cocultures showed secretion profile different from basal state and TGF-1 stimulation. Their interaction with the BMDMs and tumor cells in the collagen-I matrix induced increased production of GM-CSF, G-CSF, IL-6, CCL2, CCL3, CCL4 and CCL12, and reduction of IFN-1, LIF, VEGF, CCL17, CXCL5 and CX3CL1 (Figure 3.14.e). We found that 3T3MEFs appeared to be activated by signals from the 3D TME. YUMM-conditioned media alone induced activation of these fibroblasts, observed by morphological changes, upregulation of -SMA and FAP expression. These fibroblasts were active secretors and contractile in a collagen-I environment for several days, even if alone in the cocultures (Figure 3.15.f, Figure 3.12).f

To study how the cell components of the 3D culture dynamically interact with the matrix, we quantified the soluble collagen in each condition over time. The presence of different cell types in the cocultures led to distinct changes in the collagen-I ECM. There was a significant overall loss of soluble collagen between day 3 and day 7 across all conditions, indicating ECM remodeling and collagen degradation (Figure 3.15.g). The polarization state of BMDMs (M0, M1 or M2) did not impact the total soluble collagen present in the 3D cocultures in the evaluated timepoints (Figure 3.16.d). Overall, we conclude that fibroblast activation in the cocultures was accompanied by the remodeling of the ECM, similar to what we observed in tumors (Figure 3.7.c).

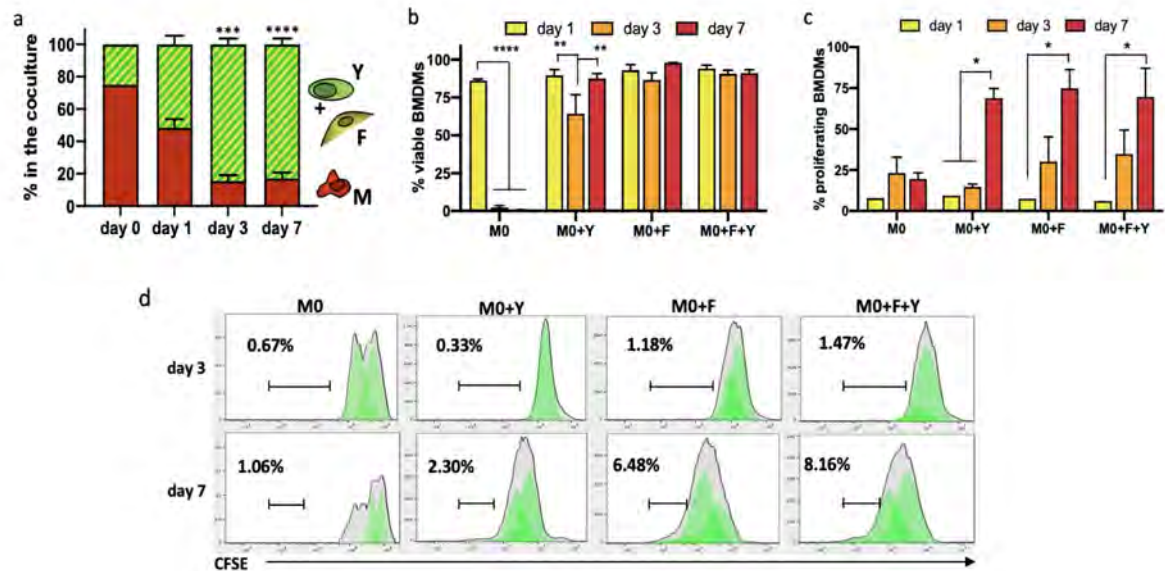


Figure 3.13: **Rapid functional cell activation after early interactions in the 3D melanoma TME.** a. Evolution of the composition of cell types in 3D cultures over time, starting from a 12:3:1 M-F-Y ratio (d1 n=4, d3 n=5, d7 n=8). b. M0 BMDM survival in 3D cultures over time. Viability of macrophages was assessed after being cultured alone or in combination with the other cell components, at d1, d3 and d7 (n=3). c. M0 BMDM proliferation in 3D cultures overtime. We analyzed cell divisions of macrophages after CFSE staining, and considered in the proliferating fraction all cells that had undergone at least one division cycle (n=2). d. Representative histograms of macrophage proliferation from all the coculture conditions, gates are highlighting the high proliferative subpopulations (over 2 divisions at each timepoint).

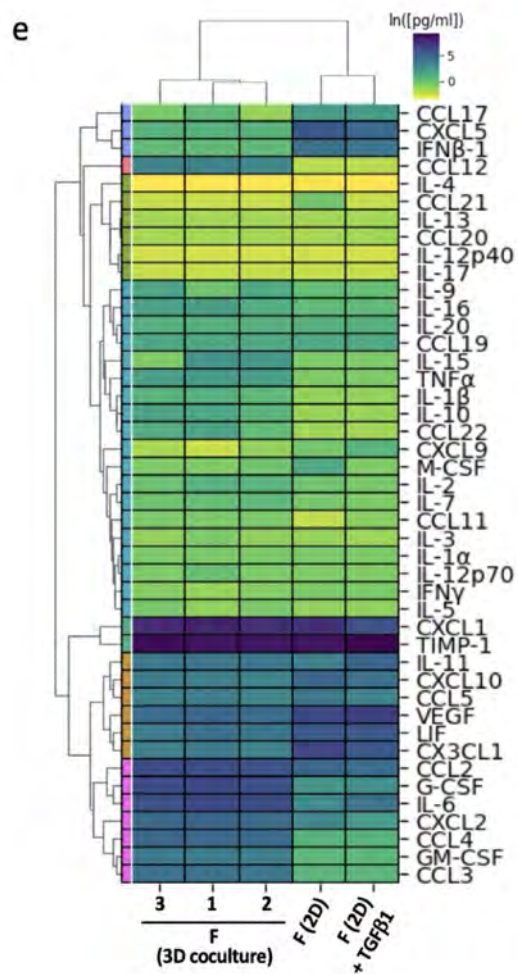


Figure 3.14: **Rapid functional cell activation after early interactions in the 3D melanoma TME.** e. Hierarchical clustering of 43-plex secretion profile analysis of 3T3MEF fibroblasts. We compared secretion in resting cells with TGF- β 1 stimulation and fibroblast from 7d 3D cocultures.

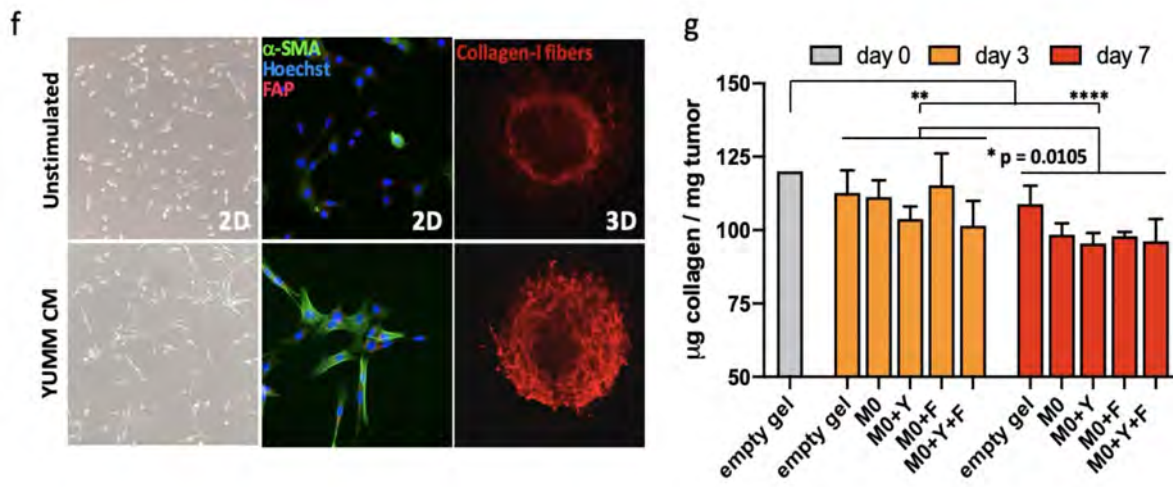


Figure 3.15: **Rapid functional cell activation after early interactions in the 3D melanoma TME.** f. Activation of the 3T3-MEF cell line by YUMM melanoma cells. Fibroblasts were stimulated with YUMM conditioned media (CM), and we observed morphological changes under the light microscope and activation through expression of α -SMA. When cultured in 3D cultures, we assessed fibroblast functional activation in a stained collagen pulling assay. g. Quantification of total soluble collagen-I in the M0 3D cultures, at d3 and d7, compared to the initial collagen-I added in each. A control well with no cells was kept as a control of the quantifiable soluble collagen-I (n=4). * $p < 0.05$, ** $p < 0.01$, *** $p < 0.001$, **** $p < 0.0001$.

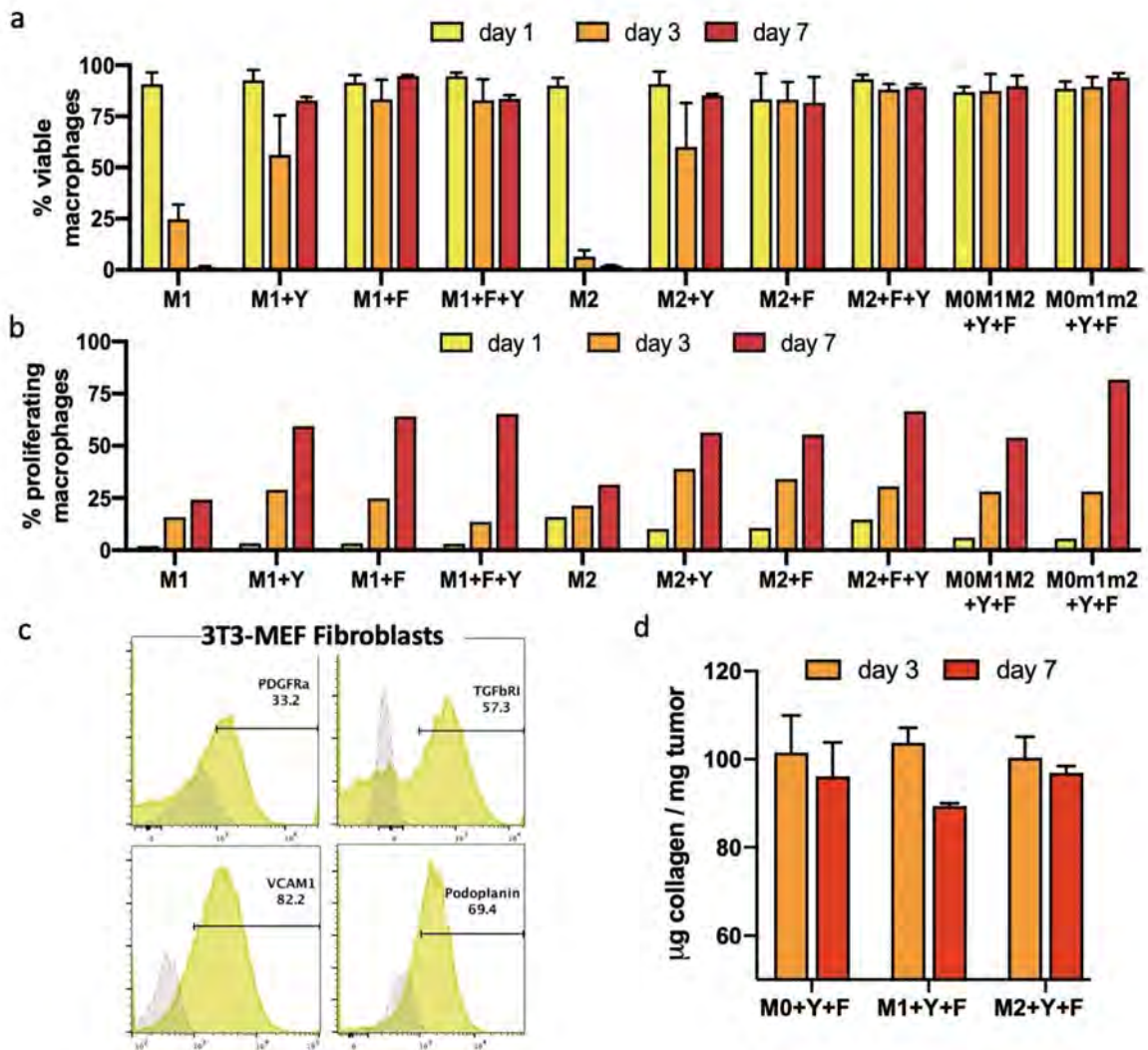


Figure 3.16: **Rapid functional cell activation after early interactions in the 3D melanoma TME.** a. Survival of polarized BMDMs in 3D cultures over time. Viability of macrophages was assessed after being cultured alone or in combination with the other cell components, at d1, d3 and d7 (n=2). b. Proliferation of polarized BMDMs in 3D cultures overtime. We analyzed cell divisions of macrophages after CFSE staining, and considered in the proliferating fraction all cells that had undergone at least one division cycle. In M0M1M2, polarized BMDMs were mixed in equal parts in the same culture. In M0m1m2, polarized BMDMs were mixed in ratio 4:1:1 in the same culture. c. Representative histograms of FACS characterization of 3T3MEF fibroblast marker expression. d. Comparison of total soluble collagen-I in M+F+Y 3D cocultures with different initial polarization states at d3 and d7 (n=4). *p<0.05.

3.4.4 BMDMs undergo rapid major changes in morphology and motility in response to melanoma cells in the 3D *in vitro* TME

We next explored the biomechanical activation of BMDMs in 3D cocultures that could be associated with functional changes in these cells. We quantified parameters related to the size, shape and motility of the BMDMs in 3D cocultures over time, in response to the presence of tumor cells and/or fibroblasts in the culture. Regarding morphology, we characterized the BMDM compactness (i.e., the degree of protrusive structures that add to the total cell body area) and circularity (i.e., the degree of the cell shape approximating to a circle; see Methods). Most M0 BMDMs are round, with high compactness index. However, when exposed to tumor cells or fibroblasts, the morphology of BMDMs change significantly during the first 3 days, and was sustained thereafter (Figure 3.17.a). In coculture conditions, macrophages elongate and generate protrusive dendrites, although BMDMs from M0+Y+F cocultures demonstrate a slightly higher frequency of ‘star-like’ morphology and relatively lower compactness (Figure 3.19.a-c). The circularity and elongation of macrophages exhibited similar distribution in coculture conditions in the first several days (Figure 3.17.b). More heterogeneity in cell shape was observed in coculture versus monoculture conditions.

The average speed of macrophage migration in 3D cocultures with fibroblasts and tumor cells increased over time; in contrast, the average speed of macrophages in monocultures remained low (Figure 3.17.c, Figure 3.18.d). This demonstrates that the presence of melanoma cells and/or fibroblasts, provided cues not only to maintain macrophage survival but also to promote activation and migration. Macrophages in M0+Y and M0+Y+F generally show similar levels of motility, as shown by their average displacement within the 3D gels (Figure 3.17.e). Of note, BMDMs in the M0+Y condition migrate around the culture slightly more than the M0+Y+F condition on day 7, as seen both by average speed and displacement (Figure 3.17.c,e).

We observed high synchronicity between individual macrophage behavior in the cocultures combining melanoma cells and fibroblasts. Initial activation for the first 24h induced a non-directional, oscillatory movement in the BMDMs. Then, most macrophages acquired a spindle-like shape on day 3, with a ‘scouting mode’ on, moving faster and longer distances. Finally, they transitioned into a more stationary state, with star-like morphology on day 7 (Video S1 - see published paper supplementary information). We did not observe significant differences in morphology when starting the cocultures with pre-polarized BMDMs (i.e., M1 or M2; data now shown); overall, they showed similar migration behaviors to M0, in both monoculture and cocultures (Figure3.19.c, Figure3.20.d).

To determine if the activation of macrophages in the 3D environment is dependent on the relative distance to the tumor cells, we tracked the speed of each macrophage relative to its initial distance from a tumor cell (Figure3.18.f-g). We found that the average speed of macrophages initiated within 100μ of a tumor cells was significantly higher than for macrophages that started further away (Figure3.18.h,j). However, proximity to a tumor cell did not guarantee high macrophage mobility. Overall, we conclude that the presence of tumor cells and fibroblasts have a strong effect on macrophage motility in the co-cultures.

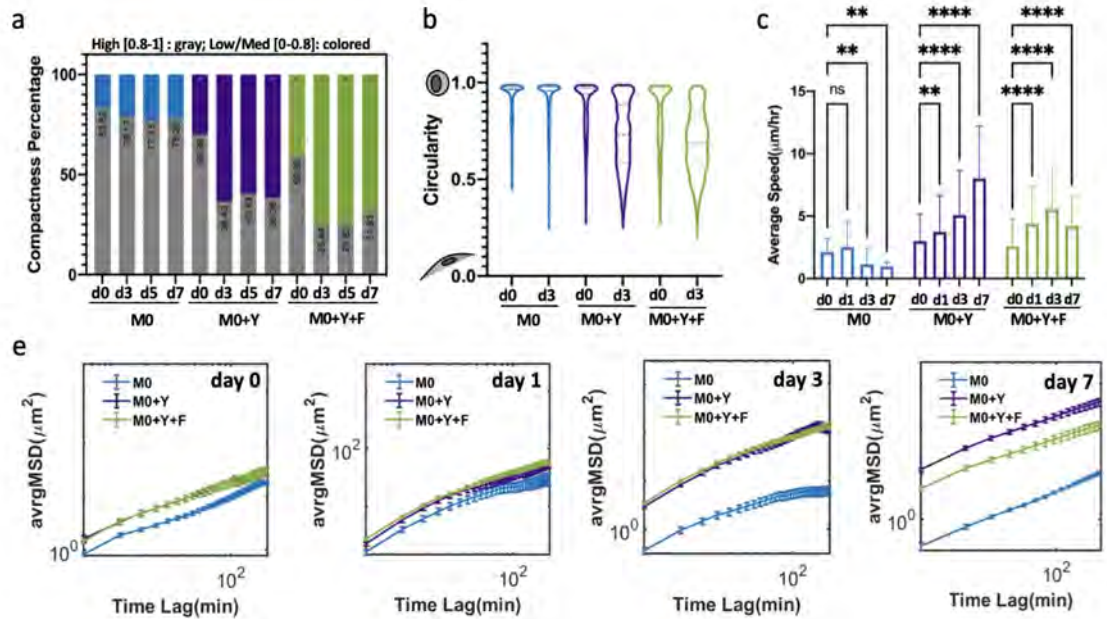


Figure 3.17: **Significant morphology and motility changes in BMDM activation in 3D co-cultures over time.** a. Generation of cell protrusions in M0 BMDMs across multiple days exposed to different 3D environments. Compactness was calculated as described in the methods. Cells were first classified into two categories, low/medium compactness [0-0.8] and high compactness [0.8-1]. For each condition and time, proportion of cells in each category were calculated and plotted as percentages of total. Gray bar, high compactness [0.8-1], colored bar, low/med compactness [0-0.8]. b. Violin plots showing the early changes in BMDM morphology in different 3D environments. Circularity index was calculated as described in MM. c. Average migration speed of macrophage, data shown as Mean +/- SD. e. Average mean square displacement (MSD) of M0 BMDMs across multiple days exposed to different 3D environments. data shown as Mean +/- SEM.

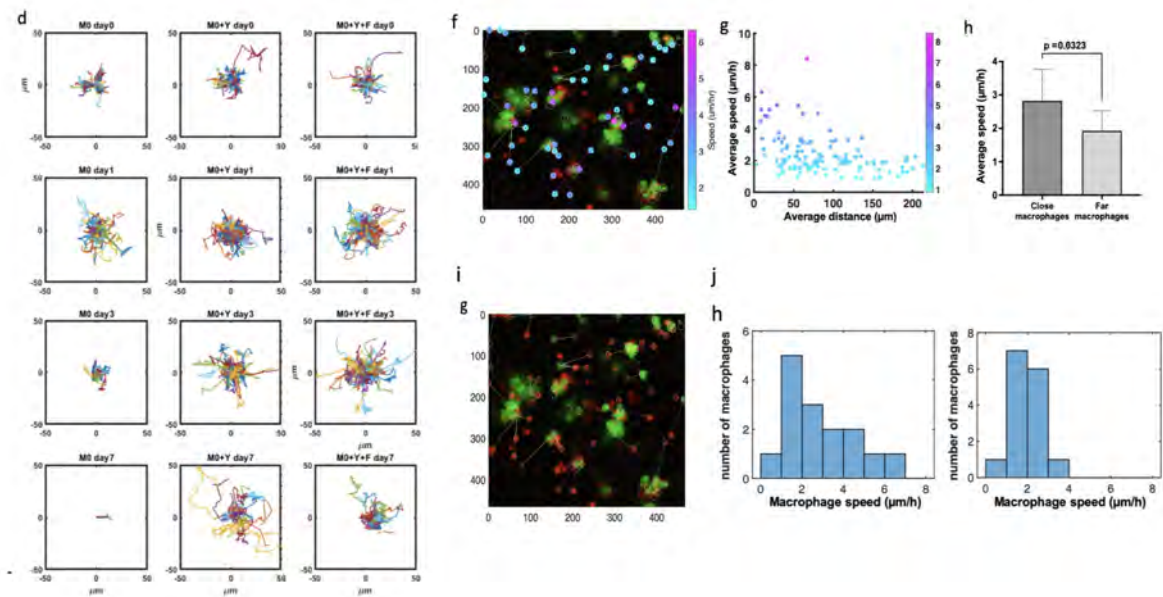


Figure 3.18: Significant morphology and motility changes in BMDM activation in 3D co-cultures over time. d. Overlaid migration trajectories of M0 BMDMs in different 3D environments, at different timepoints. f. Representative image of calculation of distance between macrophages and the closest tumor cell at early timepoint (day 1). Overlaid data on individual average speed of the BMDM. g. Scatter plot of M0 BMDMs average speed vs distance to the closest YUMM cell after 24h of 3D coculture. h. The bar plots compare the average speed of the top 15 closest and top 15 farthest macrophages from the nearest YUMM cell at day0. i. Representative image of the initial stage of M0+Y 3D coculture used to identify macrophages and locate and calculate their distance in x,y,z to the closest tumor cell. j. Histograms of the average speed of M0 BMDMs either closest to (left) or farthest from (right) tumor cells.

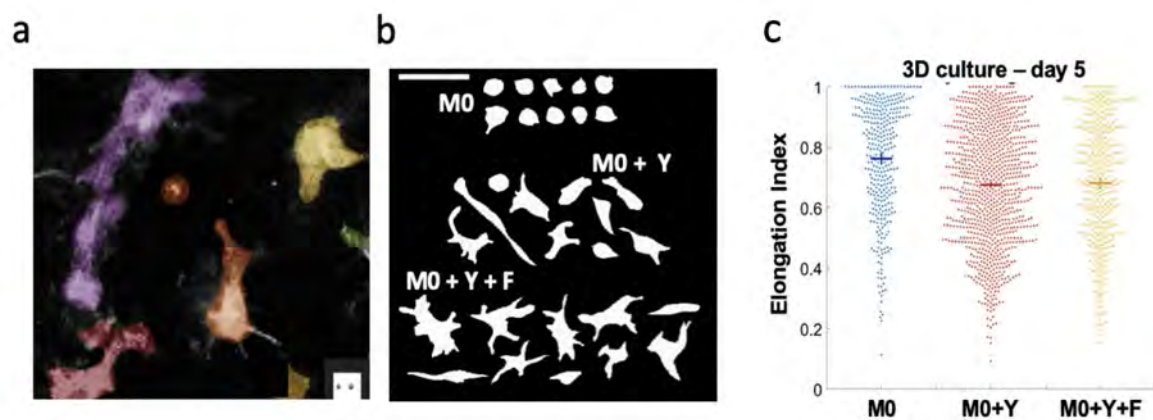


Figure 3.19: **Significant morphology and motility changes in BMDM activation in 3D co-cultures over time.** a. Representative image to demonstrate segmentation performance. b. A summary of representative macrophage morphology in each condition, 36h post gel embedding. Scale bar is $100\mu\text{m}$. c. Comparison of the elongation index of macrophages at day 5 in different 3D environments. The elongation index is defined as the width/length ratio of the maximum bounding box of macrophage.

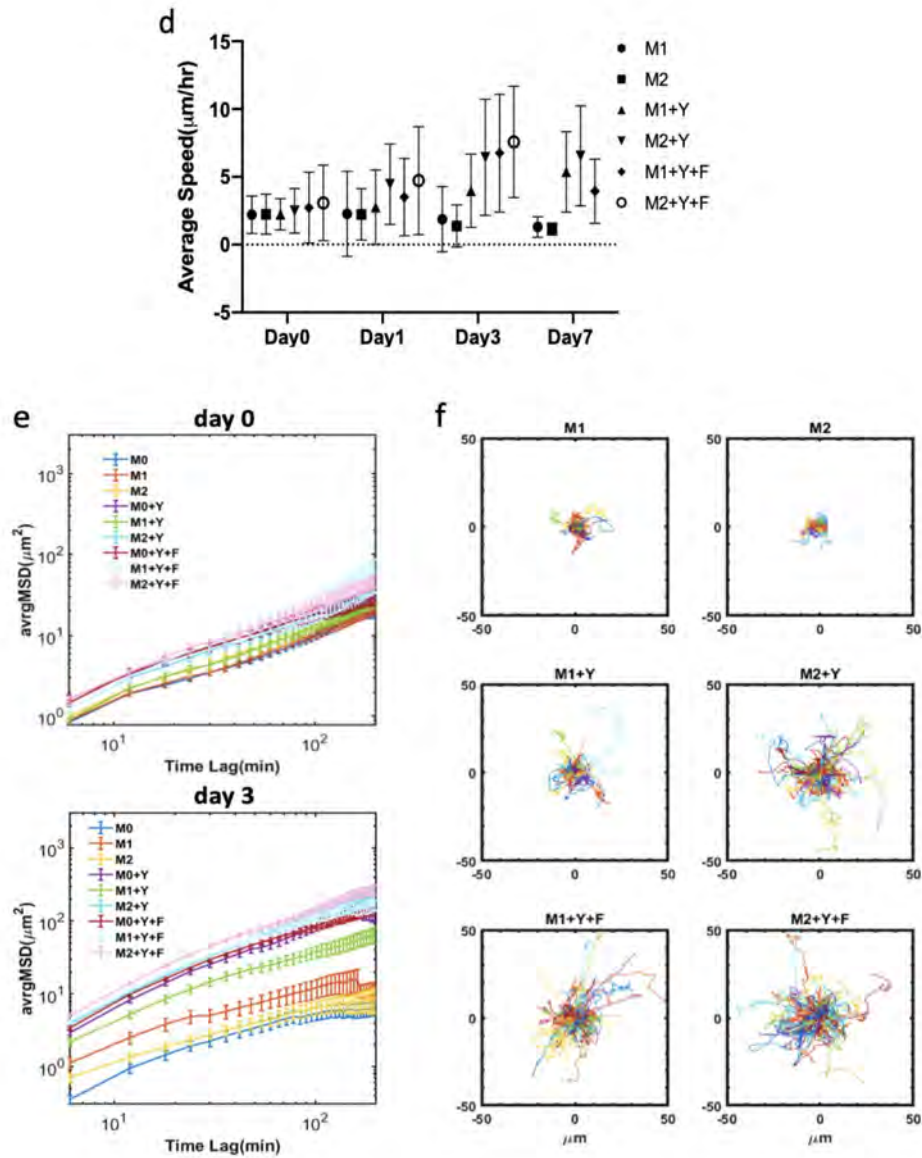


Figure 3.20: **Significant morphology and motility changes in BMDM activation in 3D co-cultures over time.** d. Average speed of M1 and M2 BMDM 3D cultures from day 0 to day 7. Data shown as Mean \pm SD. e. Average MSD of unstimulated and polarized BMDMs (M0, M1 and M2) at the initiation of the 3D cultures and at day 3. Data shown as Mean \pm SEM. f. Overlaid migration trajectories of polarized BMDMs (M1 and M2) at day 3.

3.4.5 BMDMs in the *in vitro* 3D TME show an immunosuppressive transition into a melanoma TAM-like profile

The parameters analyzed above, including cell-cell direct interactions, forces transduced by the 3D matrix and motility, and the membrane-bound or secreted cues, suggested that macrophages would be influenced by these coculture conditions. Therefore, we evaluated how macrophages evolve in the cocultures over time. We were particularly interested in assessing the plasticity of their phenotype as the culture progressed, and determining which initial polarization state (M0, M1, or M2) would most resemble TAMs isolated directly from the melanoma TME.

We first assessed the phenotype of M0 BMDMs in the 3-cell coculture (M0+Y+F) conditions using multiplexed flow cytometry. When we visualized these measurements using UMAP, we observed diverse subpopulations of ‘3D TAMs’ that evolved over time (Figure 3.21.a), with a fraction of BMDMs acquiring expression of Arginase-1 (Arg-1), CD206 and F4/80. After 7 days of coculture, the phenotypic profile of the M0 BMDMs evolved to look more similar to the average phenotype of the melanoma TAM profile in early (day 7) tumors, as analyzed by PCA (Figure 3.21.b). When analyzing 3D cocultures with BMDMs cultured with only one other cell type (i.e., with fibroblasts or tumor cells), we found that it was the fibroblasts that favored the M0 BMDM transition, observing a larger fraction positive for Arg-1 by day 7 (19% vs. 13%; Figure 5c). When all three cell types were combined, there was a more dynamic evolution of the phenotype. Initially a small fraction of M0 BMDMs acquired iNOS expression, which was not observed after day 1, while rapidly acquiring Arg-1 expression (both iNOS⁺ and iNOS⁻ at day 1), and increasing towards day 3, as compared to the 2-component cultures (Figure 3.21.c).

Interestingly, when BMDMs were pre-polarized with an M1 or M2 phenotype, they exhibited different trajectories in their temporal phenotypic evolution in the co-cultures that were distinct from the mono-cultures, but were also less similar to the TAMs than BMDMs

initialized in an M0 state, as analyzed by PCA (Figure 3.24.a). A more detailed examination of their evolution revealed that BMDMs retained characteristics of their starting states up to day 3; and between days 3 and 7, BMDMs started expressing complex phenotypes with mixed M1/M2 markers regardless of their initial starting state (Figure 3.24b-c). Interestingly, M1 BMDMs showed a strong dependence on the polarizing cues to maintain their profile, as evidenced by their rapid loss of iNOS expression in the co-cultures. In contrast, M2 BMDMs exhibited a stronger commitment to their induced phenotype, with increasing expression of Arg-1 in the co-cultures (Figure 3.24.d).

We further examined cocultures initialized with a mix of BMDM polarization states, as might be expected to occur in a more complex tissue at the point of tumor initiation. As shown previously, YUMM TAMs exhibited a mixed M1/M2 profile, though not as clearly polarized as reference BMDMs (Figure 3.1a-c, Figure 3.22.d). Starting with different M0:M1:M2 ratios in the macrophage fraction of the cocultures generated by day 7 more diverse '3D TAM' populations (Figure 3.22.d). Mixed BMDMs in the cocultures maintained characteristics of their initial states through day 3, and seemingly evolving independently from one another. However, by day 7, the BMDMs were expressing mixed M1/M2 markers similar to the M0 BMDMs evolved in the cocultures (Figure 3.24.d, Figure 3.25.e).

Finally, to evaluate how closely our '3D TAMs' resembled more advanced tumor stages, we compared BMDMs initialized in either the M0 state or in a mix of M0:M1:M2 states, followed by evolution in the 3D cocultures, and compared them to d7 and d14 melanoma TAMs. We chose to compare both time points since we observed heterogeneity between TAM samples collected at the same timepoint and we had observed a dynamic TAM phenotype *in vivo* (Figure 3.1.a). We observed that '3D TAMs' initialized in either the M0 or the mixed state evolved towards TAMs isolated from YUMM tumors, as analyzed by PCA (Figure 3.23.e). Interestingly, when examining the heterogeneity of the TAMs using UMAP, we found that '3D TAMs' clustered slightly closer to

d14 YUMM TAMs, displaying the expression of a combination of immunosuppressive and pro-inflammatory markers (Figure3.23f-g, Figure3.26.f). In addition, it appeared that BMDMs initialized in a mix of states clustered closer to YUMM TAMs than a pure M0 culture (Figure3.26.g). Overall, we conclude that co-cultures with tumor cells and fibroblasts shape BMDM phenotypic profiles regardless of initial state, but initializing with a mix of M0:M1:M2 BMDMs, and to a lesser extent with M0 BMDMs, leads to a phenotype most similar to TAMs from YUMM/ER tumors.

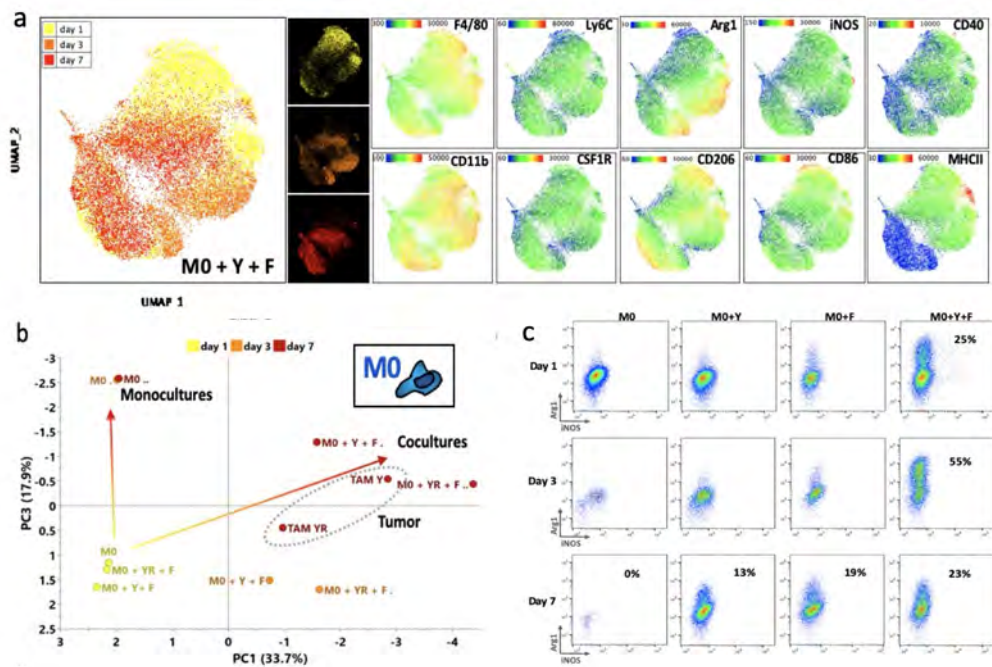


Figure 3.21: Evolution and modeling of BMDM phenotype into a TAM-like state.
a. Analysis of unstimulated BMDM (M0) phenotype over time in 3D cocultures. UMAP clustering showing macrophages from the M0+F+Y coculture at d1, d3 and d7 combined. Heatmaps provide detailed distribution of marker expression, highlighting different subpopulations and evolution over time. b. PCA analysis of M0 BMDM phenotype trajectory over time in 3D cultures, compared to day 7 melanoma TAMs. c. Representative dot plots of M1/M2 markers iNOS/Arg1 in M0 BMDMs as monocultures and different combinations of macrophage 3D cocultures, and their evolution over time.

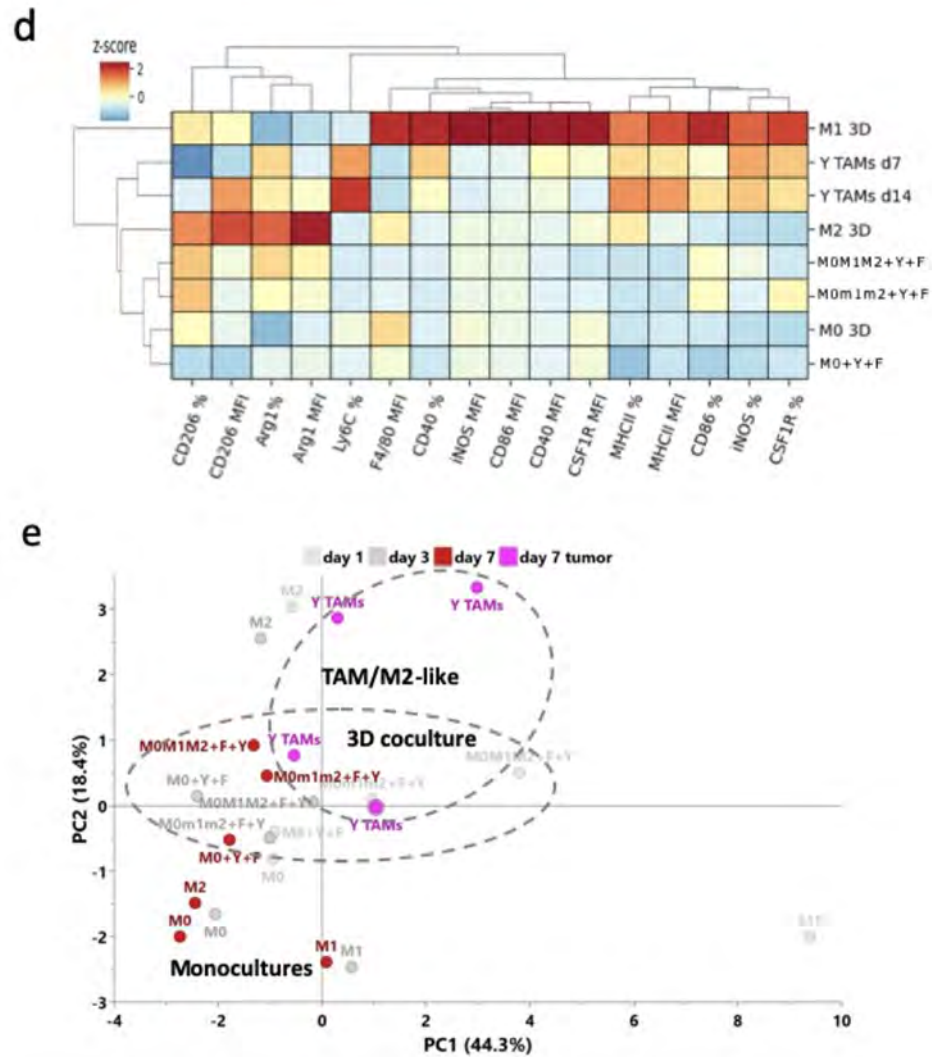


Figure 3.22: **Evolution and modeling of BMDM phenotype into a TAM-like state.** d. Hierarchical clustering of marker z-score of macrophages from polarized BMDM profiles, 3D cocultures at d7 and early (d7) and late (d14) melanoma tumors. e. PCA analysis of macrophage phenotype over time in 3D cocultures. Highlighted in color, M0 3D monocultures and cocultures and TAMs, collected at day 7. Dashed circles delineate the phenotypic space by sample type, showing partial overlap between the YUMM TAMs and *in vitro* ‘3D TAMs’.

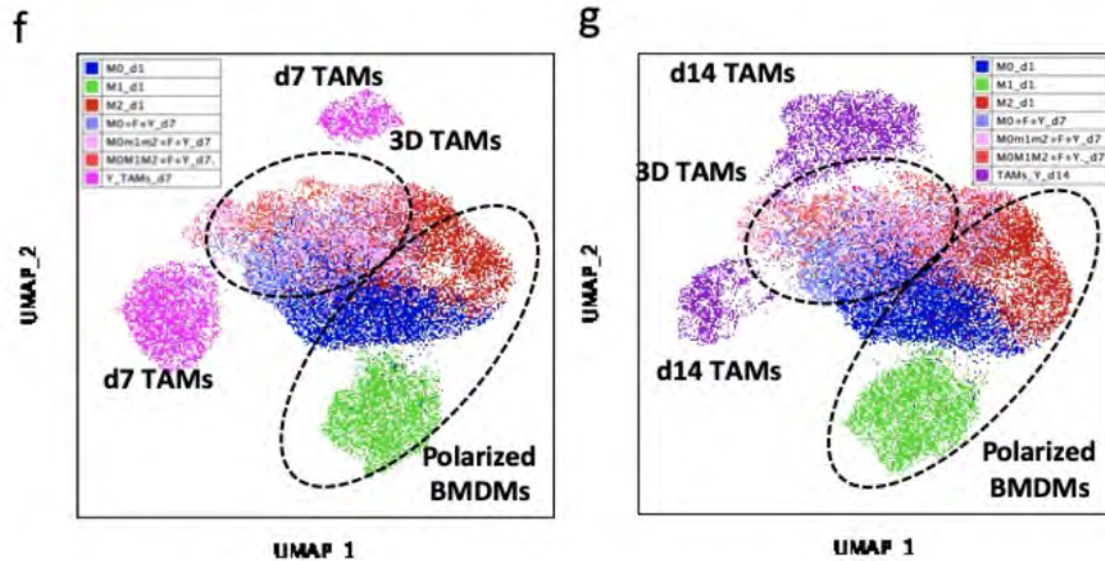


Figure 3.23: **Evolution and modeling of BMDM phenotype into a TAM-like state.** f. UMAP clustering of macrophages from 3D mono- and cocultures and early (d7) melanoma tumors, comparing single-cell phenotype. g. UMAP clustering of macrophages from 3D mono- and cocultures and late (d14) melanoma tumors, comparing single-cell phenotype. In M0M1M2, polarized BMDMs were mixed in equal parts in the same culture. In (1) M0M1M2, polarized BMDMs were mixed in equal parts in the same culture. In (2) M0m1m2, polarized BMDMs were mixed in ratio 4:1:1 in the same culture. In (3) M0+Y+F.

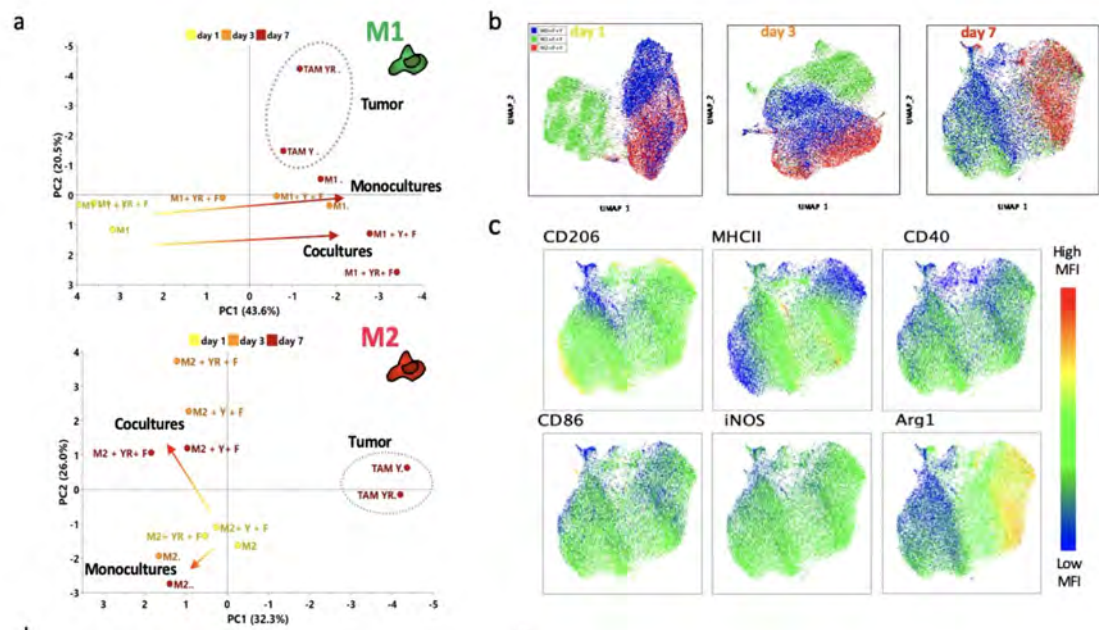


Figure 3.24: **Evolution and modeling of BMDM phenotype into a TAM-like state.**a. PCA analysis of pre-polarized macrophage phenotype trajectories over time in 3D cultures, compared to day 7 melanoma TAMs. b. UMAP clustering visualizing the plasticity and evolution of the macrophage phenotype in 3D cocultures, starting from different pre-polarized states (M0, M1 or M2). c. Heatmaps with details of the marker expression at day 7, starting from different pre-polarized states.

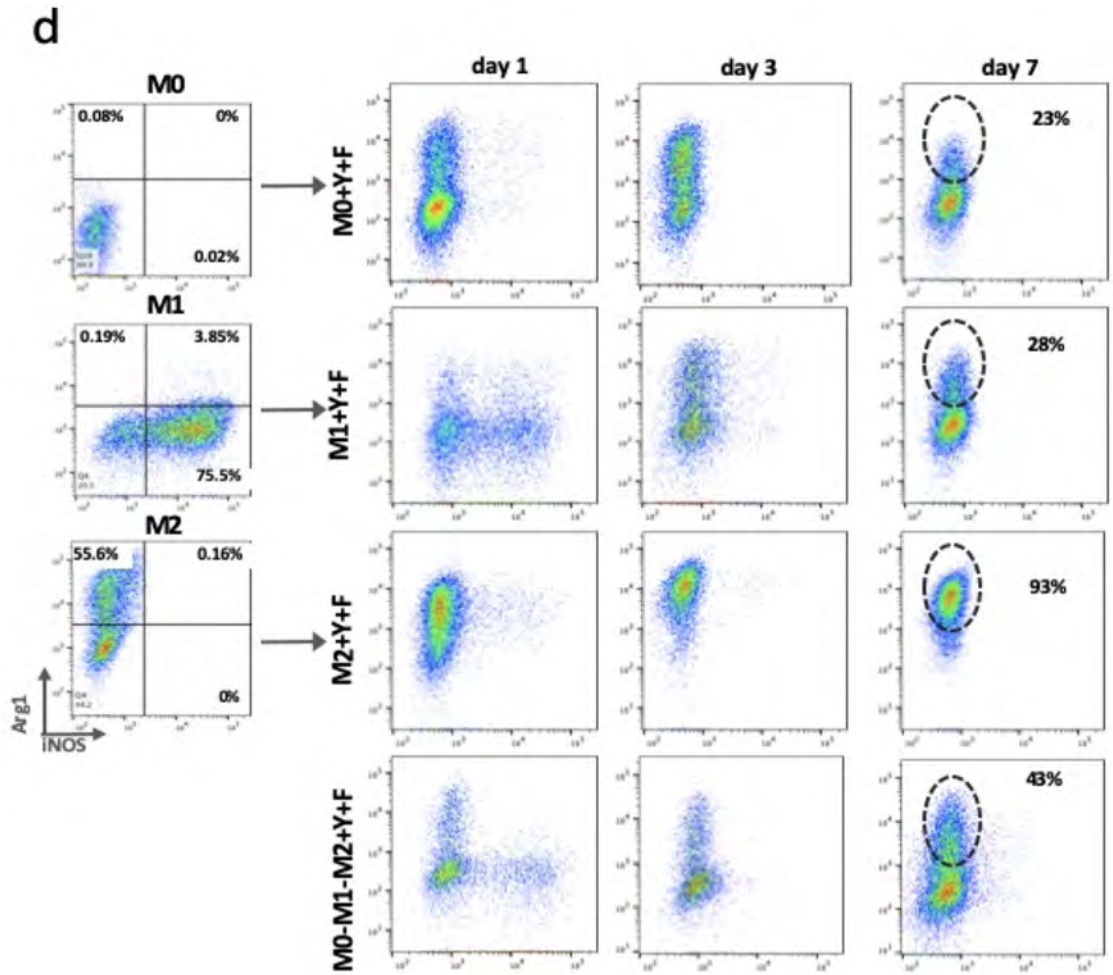


Figure 3.25: **Evolution and modeling of BMDM phenotype into a TAM-like state.**
 d. Representative dot plots of M1/M2 markers iNOS/Arg1 in the pre-polarized BMDMs before coculture, and their evolution in the coculture with YUMM and fibroblasts.

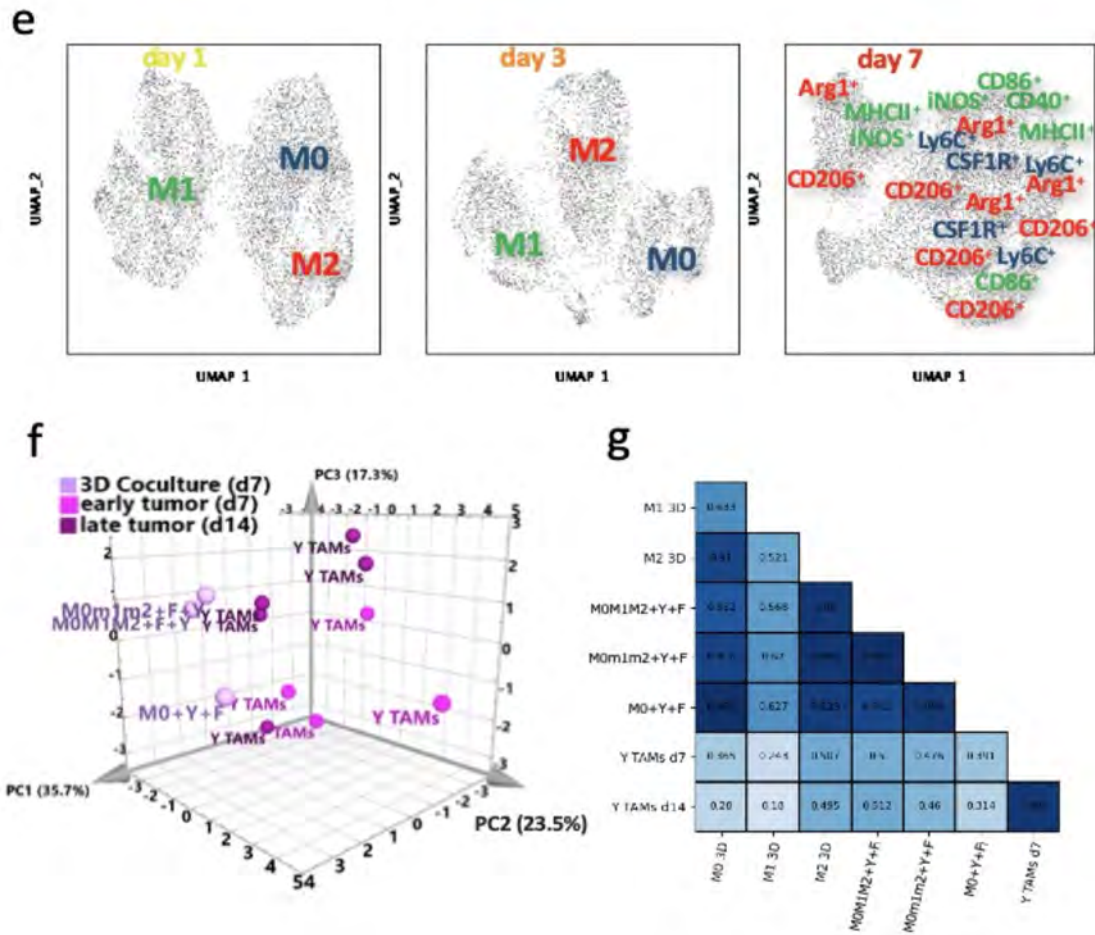


Figure 3.26: **Evolution and modeling of BMDM phenotype into a TAM-like state.**
 e. UMAP clustering visualizing the plasticity and evolution of the macrophage phenotype in 3D cocultures, starting from a mix of pre-polarized states (M0+M1+M2). At day 1 and day 3, sub-clusters were labeled according to their leading phenotype. At endpoint at day 7, the plot has superimposed annotations of the main markers expressed in different regions. f. PCA analysis comparing d7-coculture macrophage phenotype to d7 and d14 melanoma TAMs. g. Pearson correlation. In M0M1M2, polarized BMDMs were mixed in equal parts in the same culture. In M0m1m2, polarized BMDMs were mixed in ratio 4:1:1 in the same culture.

3.4.6 BMDMs in the *in vitro* 3D TME acquire a sustained mixed M1/M2-like functional profile resembling melanoma TAMs

Lastly, we evaluated the secretion profile induced in BMDMs evolved in the 3D TME cocultures as a measure of the potential effector functions of ‘3D TAMs’ and the other cell components. We analyzed cocultures containing all the cell types but varied the initial composition of polarized BMDMs (i.e., M0, M1, M2, or mixed). After 7 days in the 3D cocultures, we extracted and sorted the three cell types, cultured them to collect their conditioned media and then analyzed the secreted C/Cs with a multiplexed immunoassay (Figure3.27.a). We observed that ‘3D TAMs’ secreted higher levels and a broader range of C/Cs on the panel, as compared to tumor cells and ‘3D CAFs’. Some of these secreted proteins were shared with the ‘3D CAFs’, such as CXCL1, VEGF, G-CSF and GM-CSF. The tumor cells secreted few C/Cs on the panel, including exclusive secretion of IL-11, and shared secretion of CX3CL1, LIF and TIMP-1 with the fibroblasts (Figure3.27.b).

Similar to the results from our phenotypic analysis, the 3D TME shaped the BMDM secretory profile to resemble the one observed in melanoma TAMs. PCA analysis of the secretion profile showed a transition path similar to our phenotypic analysis, in which secretion was initially aligned with polarized BMDMs, but then transitioned to a more complex state resembling TAMs from YUMM tumors (Figure3.28.c). Coculturing BMDMs with tumor cells and fibroblasts in 3D conditions induced a secretion profile that exhibited a similar pattern to TAMs, with some of these complex M1/M2 features, after only 7 days (Figure3.28.d, Figure3.29.e). When looking in detail at the multiplexed secretion, the 3D TAMs secreted TNF- α , IFN- β 1 and CXCL10, as well as IL-10, CCL17 and CCL22. This 3D TAM profile correlated with the standard M2-like profile, to a similar degree as TAMs (Figure3.29.f). But the cocultures established with BMDMs that were M2 pre-polarized only, rapidly changed the production of these cytokines over time (Figure3.30.b). However, not all the networks from the melanoma TME were reproduced *in*

vitro. Supernatant from whole YUMM tumors contained a significant number of shared cytokines/chemokines, but also contained IL-1 β , IL-2, IL-4, IL-9, IL-17, CCL20, CCL21, among others, which were not observed in the cocultures and so were most likely produced by other components not included *in vitro*, like T cells or endothelial and lymphatic cells (Figure3.30.c).

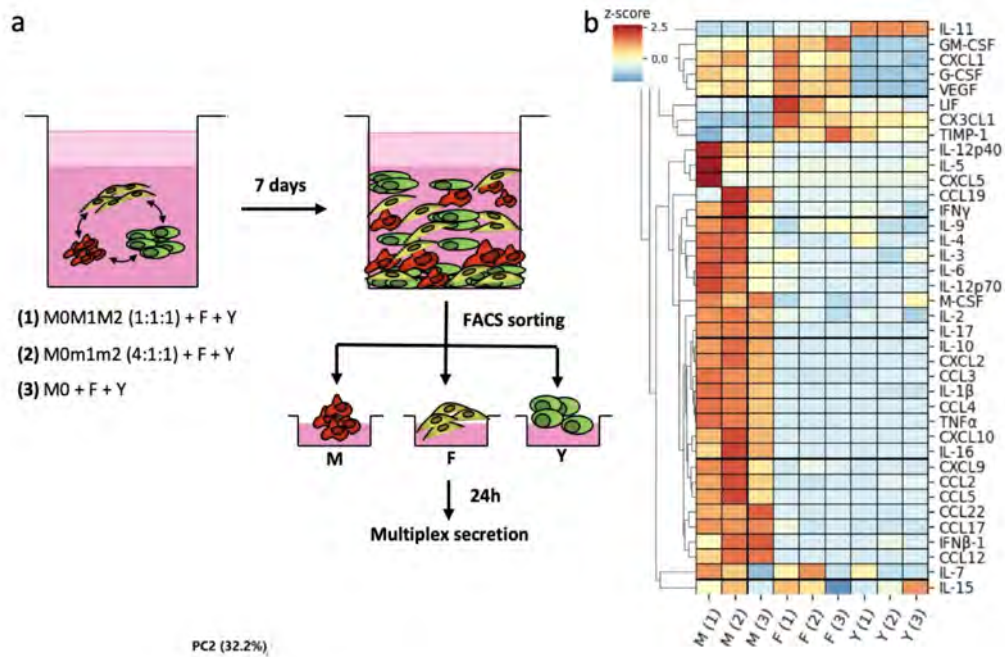


Figure 3.27: **BMDM transition into an immunosuppressive TAM-like functional profile after 7 days of 3D co-culture.** a. Schematic representation of the isolation of components after 3D coculture for secretion profiling combining BMDMs with fibroblasts and YUMM cells. b. Heatmaps with z-scores for all the proteins studied in all three fractions.

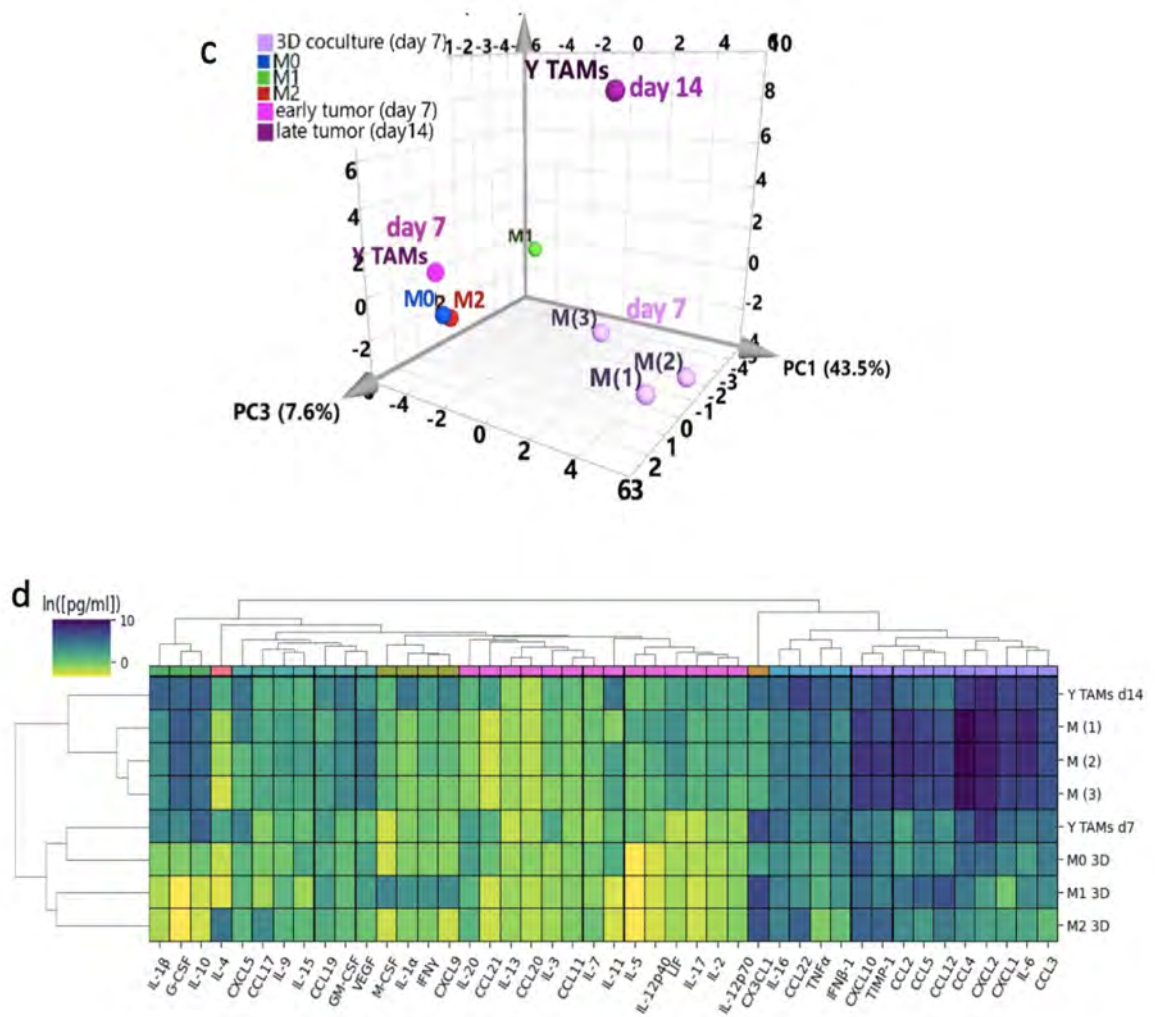


Figure 3.28: **BMDM transition into an immunosuppressive TAM-like functional profile after 7 days of 3D co-culture.** c. Functional profile of ‘3D TAMs’ compared to melanoma TAMs. PCA of the bulk secretion of macrophages from 3D cocultures, *in vitro* stimulated BMDMs and TAMs from YUMM early and late tumors. d. Hierarchical clustering of 43-plex secretion profile analysis of ‘3D TAMs’ and Y TAMs at early and late timepoints compared to 3D BMDM reference polarized states.

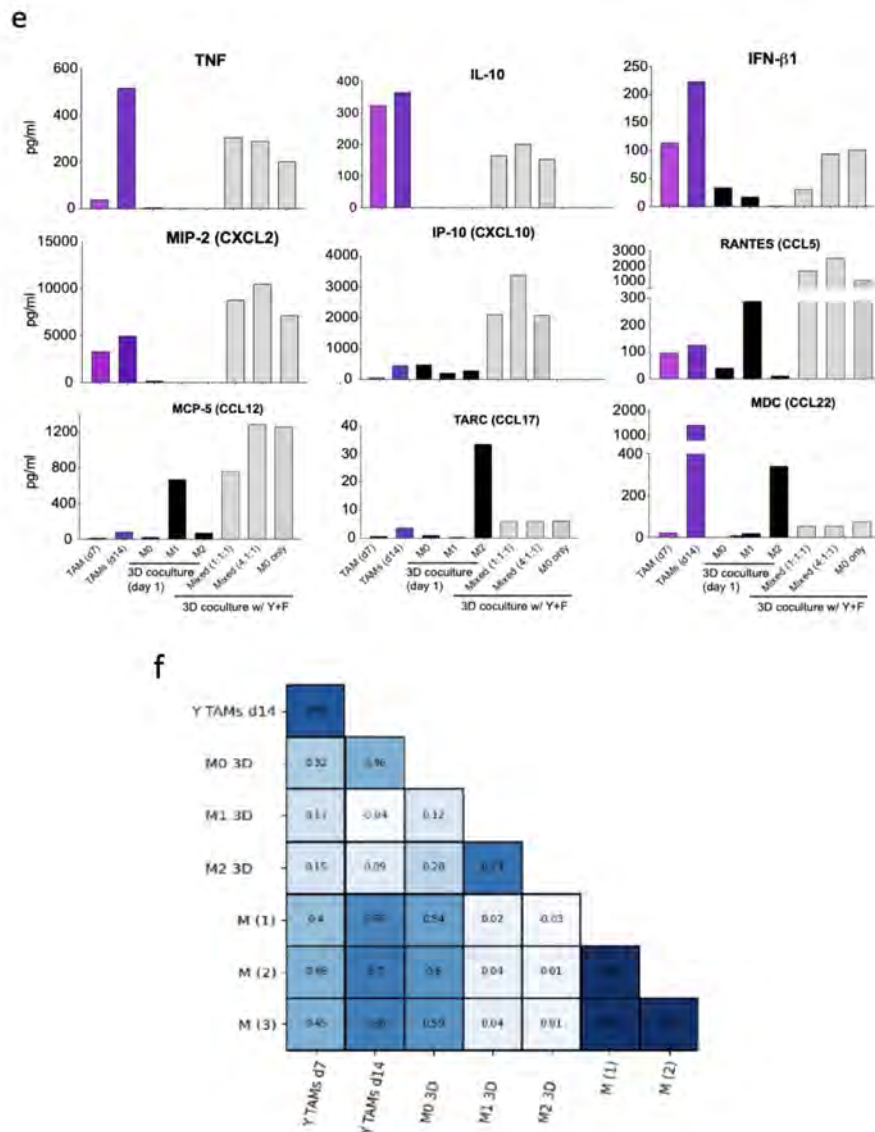


Figure 3.29: **BMDM transition into an immunosuppressive TAM-like functional profile after 7 days of 3D co-culture.** e. Bar graphs with the absolute concentration of secreted cytokines/chemokines in sorted macrophages from 3D cocultures at day 7, and compared with polarized reference BMDMs and early and late Y TAMs. f. Pearson correlation. (1) In M0M1M2, polarized BMDMs were mixed in equal parts in the same culture. In M0m1m2, polarized BMDMs were mixed in ratio 4:1:1 in the same culture.

3.5 Discussion

It is increasingly clear that *in vitro* macrophage polarization protocols do not recapitulate the complex macrophage phenotypes observed *in vivo* [117, 118]. Single-cell approaches have provided a more complete look into macrophage heterogeneity in tumor infiltrates [119, 120], with surrounding cells and cues that influence their behavior and shape their functional response [91, 121, 122]. Developing experimental models to study TAMs *in vitro* is not as simple as inducing a cell program through a signaling pathway, especially when the definition of polarization state, especially for ‘M2-like, has been expanding over the years to fit the pathophysiology of the macrophages [123]. TAMs in the YUMM model were no exception, with strong heterogeneity and an evolving profile over time. Single-cell analysis showed that individual TAMs indeed had a mixed M1/M2 phenotype, with co-expression of markers such as CD206 and MHCII, while the secretion profile revealed an interesting pattern with a high proportion of resting cells and the remaining cells aligned with either a pro-inflammatory or an immunosuppressive axis.

Interestingly, we also found that TAM heterogeneity is lost when isolated and cultured *ex vivo* in 2D conditions, emphasizing the need for TME signals to maintain their identity. In recent years, 3D cultures in hydrogels, including collagen [124, 125], have provided valuable tools to accelerate tumor studies and TME modeling [106, 105]. In the present study, we developed a 3D collagen co-culture system to mimic the melanoma TME and investigate how interactions between melanoma cells, fibroblasts, and macrophages shape the early stages of macrophage immune activity leading to such complex phenotypes. At this early timepoints, immune infiltration in the tumors is primarily from myeloid lineages, with tissue-resident and newly-recruited components. While our 3D system does not recapitulate all influential immune components, such as dendritic cells [126], there is strong evidence that macrophages play a key role in generating a pro-tumoral niche [86, 90].

Here, we found that with a relatively simple 3-cell type reconstruction of the TME, we were able to capture a macrophage immunosuppressive transition and see them acquire a phenotypic and functional profile similar to that of TAMs isolated directly from growing melanoma tumors.

The 3D 3-cell type reconstruction of the TME provided survival, proliferation and activation cues to the macrophages, building evident cell circuits with the fibroblasts, as described before [127]. However, by starting with extreme polarization state profiles (M0, M1, and M2), we identified different trajectories in which the macrophages evolved their phenotypic and functional profiles. In an effort to recreate a starting point that would ultimately lead to the melanoma TAM-like state, we generated conditions in which macrophages expressed markers and secreted factors associated with both M1 and M2 polarization (Figure 5). Interestingly, just like our 3D TAMs, M2 macrophage profile partially correlated with the overall TAM phenotypic profiles, reinforcing the traditional idea of their categorization as immunosuppressive. However, detailed analysis of the markers indicates that there still was mismatch on M1-associated markers. With this 3D TME, we were able to generate a stable system that generated and combined most of this M2-like immunosuppressive features with M1-like parameters, and was sustained over time.

Evidence from our work showed that adding fibroblasts to macrophage+tumor cells limits macrophage migration after day 3, most likely related to ECM remodeling. It remains to be studied whether this has an impact in the dynamics *in vivo*. When YUMM tumors start to grow exponentially after day 5 and 7, they may be leaving fibroblasts physically excluded in the periphery, with a higher ratio of tumor cell to fibroblast, in line with our measured reduction of total collagen per tumor mass. This newly-formed surrounding fibroblast belt could provide a compact tumor structure, as we have seen in the *in vitro* YUMM spheroids, and potentially generate a physical barrier with additional immunosuppressive signals to the arriving T cells [128].

From the time-lapse imaging in our 3D coculture system, we observed several significant trends in macrophage behavior over time. First, we found that the average speed of macrophage migration increased inversely with the distance to the closest YUMM melanoma cell (Figure 4). A previous study suggested that dynamic fibroblast contractions can recruit macrophages when cocultured in fibrillar collagen[38]. YUMM cells likely activate macrophages in a similar way by dynamically contracting surrounding collagen. Second, we observed that macrophages in the cocultures increased their average speed and became more stellate-like over time, which might be in part due to dynamic changes in the collagen environment. Both macrophages and fibroblasts are highly active in remodeling collagen [129, 130, 131]. In addition, macrophages are plastic and respond to material surfaces or collagen architecture by adopting different shapes[92, 132, 133]. Macrophage shape has been linked to phenotype, as elongation of macrophages without external cytokine stimulation was shown to induce markers of M2 polarization [92]. In our system, we also observed that elongation of macrophages was associated with an M2-like evolution. Direct contact with neighboring tumor cells and/or fibroblasts through integrins can also shape macrophage phenotype[134]. Importantly, by day 5, macrophages in the 3D cocultures resembled the morphology of TAMs observed via intravital imaging [101, 135].

In addition to biomechanical cues, it is likely that BMDMs in the cocultures are responding to biochemical cues in the microenvironment. Fibroblasts and macrophages create a stable circuit in tissues through the exchange of growth factors[127]. In our cocultures, we observe fibroblasts secreting several growth factors, including G-CSF and GM-CSF that could account for the viability and proliferation of macrophages in the cocultures, in addition to their own production of M-CSF[136]. In addition, we see fibroblasts secreting fractalkine/CX3CL1, which has been implicated in anti-cancer responses[137]. Macrophages evolved in the cocultures secrete pro-inflammatory cytokines associated with an M1 polarization state (e.g., TNF- α , IL-6, and CCL3), as well as factors more

commonly associated with an M2 phenotype (e.g., CCL17, CCL22, and IL-10). This reflects what we have measured from TAMs isolated from *in vivo* tumors[99].

As discussed above, this is a closed system, which is limited to the original components used to set up the culture and is further limited in the total time the culture can be monitored without collapsing. In this 3D TME, we are able to evaluate local responses of macrophages and fibroblasts to addition of perturbations to the system. Possible next steps would include to sequentially incorporate other cell types in the 3D TME, as shown recently[105], and also capture some features of this dynamic transition in live tumors and interaction with other tissue structures and cell types, using lineage and functional reporters [138, 139]. Live-tumor experiments would also allow us to understand better the dynamics of exclusion of fibroblasts. During this first 7 days, melanoma cells interact with fibroblasts and macrophages to build and establish their immunosuppressive, tumor-promoting TME.

3.6 Conclusions

We have developed an *in vitro* 3D collagen model of cell-cell interactions that shape immune activity in the early melanoma TME. In this *in vitro* model, stromal cells induced increased motility and response from macrophages, and macrophage acquired a phenotype and functional profile that resembled TAMs from melanoma tumors. Our systems will enable future studies of changes in macrophage-stromal crosstalk in the melanoma TME.

Chapter 4

Self-Assembly of Mesoscaled Collagen Architectures and Applications in 3D Cell Migration

4.1 Abstract

3D *in vitro* tumor models have recently been intensively investigated as they can recapitulate key features in the tumor microenvironment. Reconstruction of a biomimetic scaffold is critical in these models. However, most current methods focus on modulating local properties (e.g. micro- and nano-scaled topographies), without capturing global scaled (millimeter) or mesoscaled (intermediate scales from micrometer to millimeter) features. Here we introduce a novel, simple and reproducible method of modulating type I collagen-based ECM scaffolds by disrupting the gelation process. Collagen scaffolds fabricated with this method are thickened and wavy at a larger scale while featuring global softness. Thickened collagen patches are interconnected with loose collagen network, highly resembling collagen architecture in human skin scars. This type of thickened collagen bundles promotes tumor cell dissemination. The effect is significantly augmented at the presence of fibroblasts. The application of this type of collagen triggers different morphology and migration behaviors of tumor cells and highlights the importance of mesoscaled architec-

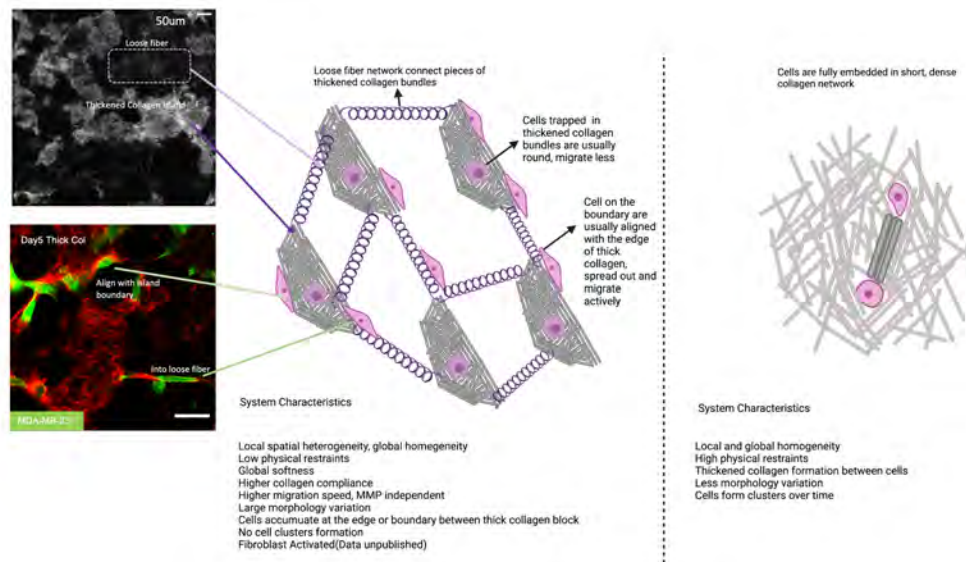


Figure 4.1: **Graphic Abstract**

tures. In addition, our method paves new ways of collagen architecture modification by mechanical agitation during fibrillogenesis and gelation.

4.2 Introduction

Tumors are often described as "wounds that do not heal"[140]. Tumorigenesis is tightly associated with chronic tissue damage and repair processes[141]. The hallmarks of tumors are highly overlapped with those of wound healing[35]. Cancer and wound healing both feature sustained proliferative signaling, evasion from immune destruction, cell death resistance, inflammation, angiogenesis, ECM remodeling, and activated cell migration[35]. However, cancer cells harbor high genome instability and immortality which intrinsically differentiate the morbid tumor progression from normal wound healing[35, 6].

During the scar formation of mechanically injured tissue, blood clot consisting of red blood cells, platelets, and extracellular matrix molecules are first formed, followed by recruitment of neutrophils, monocytes, and ensuing inflammation. Meanwhile fibroblasts

are activated into myfibroblasts and increase ECM deposition. Continuous ECM generation and crosslinking(wound closure), re-epithelization and angiogenesis are the last stage of wound healing before tissue restores original homeostasis[142].

The progression of solid tumor and fibrotic diseases are highly tissue-dependent and more complicated than normal scar formation. Pathological ECM remodeling[143, 144] is usually implicated in liver carcinoma[145], breast cancer[68], melanoma[91] and lung cancer[146]. The dysregulated ECM signatures are directly associated with poor prognosis and also immunotherapy failure[147].

3D *in vitro* models are useful for mimicking specific aspects of the tumor microenvironment(TME) and study the dynamic ECM evolution. Previous work on reconstructing the tumor ECM *in vitro* primarily focused on individual local parameters, such as pore size, fiber diameter[148, 149, 150, 151], stiffness[152], viscoelasticity[61], collagen alignment[153, 154] or microarchitecture of the collagen[46, 47, 48]. However these models usually focus on sub-micrometer topographies and mechanics, lack of global architectural similitude(milliliter scale) to *in vivo* ECM structure.

Here we introduce a new type of thick collagen bundles that highly mimic *in vivo* ECM structure, especially similar to human skin scars[155, 156]. Different from most previous efforts in modulating collagen structures through buffer condition[149], glycation[152], nanopatterning[157], stretching[153], mixing different gels[49], we fabricate a novel type of thickened collagen bundles by introducing mechanical agitation during the transient gelation process. *In vivo* fibrillogenesis often involves integrins, fibronectins and tight cellular regulation. *In vitro* fibrillogenesis, on the other hand, driven by the self-assembly of proteins[158].

By disrupting *in vitro* fibrillogenesis through mechanical agitation, we create collagen bundles that are thickened and curly, with clustered collagen patches interspersed within a loosely connected collagen network. From here on, we will refer to this material state as "thick collagen". This type of collagen imposes less steric restraints. MDA-MB-

231, MCF10A and mel624 cells migrate significantly faster in thickened collagen versus normally gelled collagen(generated without applying external mechanical disturbance). MCF10A acini develop invasive strands in thick collagen. The enhanced migration is not hindered by MMP(matrix metalloproteinases) inhibition. Additionally, this type of collagen is locally dense but globally soft. It provides local spatial heterogeneity (inside the patch versus on the boundary) but global homogeneity(similar size of thick collagen patches and interspacing). Our thick collagen bundles can be easily prepared and bulk produced(tested up to milliliters scale). It has the potential to be widely applied in *in vitro* wound, tumor metastasis, and stem cell differentiation related 3D models. It also opens new ways of collagen structure modification and *in vivo*-like ECM architecture mimicry through mechanical fibrillogenesis disruption.

4.3 Materials and Methods

Cell Culture

MDA-MB-231s(Lifeact GFP) were a gift from the Lauffenburger lab. They were cultured in DMEM(Gibco™11965092) with 10% FBS(Gibco™ 16000-044) supplemented with 1% penicillin-streptomycin(5,000U/ml, Gibco™15070-063). Normal human lung fibroblasts(ATCC, PCS-201-013) were cultured in Lonza FGM-2 BulletKit(CC-3132) or RPMI1640(Gibco™11875-093) with 10% FBS and 1% Pen-Strep. Mel624 cells were maintained in DMEM(Gibco™11965092) supplemented with 10% FBS, 1% Pen-Strep, 1% Sodium Pyruvate(Gibco™11360070), and 1% Hapes buffer(americanbio,AB06021-00100).Cells were all maintained at 37°C and 5% CO₂.

MCF10A maintenance and acini formation

MCF10As (ATCC, CRL-10317TM) were cultured with MCF10A growth medium which includes DMEM/F12(GibcoTM, 11330-032) supplemented with 5% horse serum (GibcoTM 16050122), 20 ng/ml EGF, 0.5 mg/ml hydrocortisone(Sigma H-0888), 100 ng/ml cholera toxin(Sigma C-8052), 10 ug/ml insulin(Sigma I-1882) and 1% penicillin-streptomycin(5,000U/ml, GibcoTM15070-063). To produce MCF10A acini, 24 well plates were first coated with a thin layer of pre-thawed Matrigel(Corning 354230) and then kept in incubator for 30 minutes to allow Matrigel gelation. Around 5K to 10K MCF10A single cells were then seeded on top of the Matrigel and maintained with MCF10A assay medium in 37°C, 5% CO₂ incubator until day4. MCF10A assay medium has the same components with MCF10A growth medium but with 2% horse serum and no EGF. MCF10A maintenance and acini formation protocols are adopted from the Brugge lab[159]. Cell recovery solution(Corning354253) was used to extract MCF10A acini from Matrigel following manufacturer's protocol. Briefly, MCF10A acini(in Matrigel) were first washed with ice cold PBS 3 times followed by 1hr ice incubation in cell recovery solution. Then MCF10A acini were spun down and washed in ice cold PBS for 3 times at 70g for 2 minutes in pre-chilled centrifuge. Washed MCF10A acini were seeded in normal or thick collagen for further study.

3D tissue culture in normal collagen

Acid solubilized collagen I(Corning354249) was first neutralized with NaOH and then diluted with suspended cells(or acini) to a final concentration of 2 mg/ml or 1mg/ml(MCF10A study) on ice. Culture media were added after 1hr gelation at 37°C. For labeled ECM studies, the initial collagen solution was labeled with Alexa Fluor 647 NHS Ester (Succinimidyl Ester)and dialyzed as before[60]. To note, the surface of the multi-well plates used for imaging were all pre-coated with polydopamine to anchor the collagen gel[77, 81],

including thick collagen gels.

3D tissue culture in thick collagen

Acid solubilized collagen I(Corning354249) was neutralized with NaOH in the same way as in normal collagen preparation mentioned above(step 1 in Fig.1D). Then the solution was kept still in room temperature for around 6.5 to 7.5 minutes (step 2) to allow initial nucleation. In step 3, wide-bore tips were used to gently pipette up and down the collagen while warming up the gel with fingertips. Mixing is stopped when the collagen solution becomes cloudy. The turbidity of the cloudy thick collagen after complete gelation (without adding medium or PBS) at A405 should fall around 0.4 to 0.5. The cloudy collagen solution can be directly mixed with cells(acini) and aliquoted into polydopamine coated wells followed by 1hr gelation at 37°C. Alternatively, the cloudy collagen solution can be kept on ice for up to 30 minutes before mixing with cells. In this way, the cell mixing step needs to be prolonged accordingly before aliquoting(i.e., the longer the ice incubation, the longer the cell mixing is needed to retain collagen clusters). To note, over mixing will result in collapsed(non-cohesive) scaffold. The other steps are the same with standard 3D tissue culture. In all cell seeding experiment, 2mg/ml thick collagen was used unless otherwise noted.

Migration inhibition drug assay

Drugs were reconstituted and stored following manufacturers' recommendations and diluted in culture media to working concentrations. Specifically, 20 μ M pan-MMPs inhibitor GM6001(Abcam, ab120845), 30 μ M ROCK inhibitor Y27632(Abcam, ab144494), 10 μ M Cdc42 inhibitor ML141(Calbiochem@217708), 50 μ M Formin inhibitor SMIFH2(Abcam,ab218296), 50 μ M Arp2/3 inhibitor CK666(Abcam, ab141231), 100 μ M Rac1 inhibitor NSC23766, 20 μ M Rac1 inhibitor EHT1864(Cayman 17258) were used. Fresh media mixed with spe-

cific drug were prepared right before experiment and replaced daily. In the drug assays, at least two independent experiments were performed with at least two replicates (technical duplicates) in each experiment.

Turbidimetry

The microplate reader was first pre-heated to 37°C. For normal collagen measurement, acid solubilized collagen was neutralized and diluted to 2 mg/ml as above-mentioned. Ice-cold collagen solution was aliquoted into 96 well plates (80 μ l per well) and absorbance at 405nm (A405) was tracked every minute for 20 minutes. For thick collagen measurement, after following the standard thick collagen protocol to step 4(without ice incubation), thick collagen solution was aliquoted into 96 well plates(80 μ l per well) and readouts of A405 were recorded every minute for 20 minutes.

Immunostaining

Culture media were first removed and then the gels were rinsed 3X gently with 1XPBS. Cells were then fixed with 4% formaldehyde for 30min and permeabilized by 0.3% Triton X-100 for another 30min. After fixation and permeabilization, cells were blocked with 1% BSA followed by primary antibody incubation(1:200), 3X PBS wash and secondary antibody incubation(1:500) supplemented by Hoechst stain(1:2000) and Alexa Fluor™ 647 Phalloidin(Invitrogen™ A22287, 1:200). Fluorescence imaging were acquired within one week after immunostaining.

Imaging

Imaging was performed using a Leica SP8 confocal microscope. Time-lapse imaging(XYZT mode) was taken with a 20X objective(0.75 NA), with time interval set to 3 minutes or 6 minutes and z-step size set to 2 μ m. Day0 time-lapse imaging was acquired between

around 0hr to 12 hrs post embedding cells into gels. Day1 time-lapse imaging was acquired between around 24hrs to 36hrs post gel-embedding. Overview tilescan images were taken at day1, day2 or day5 respectively.

Image Analysis

To track cell migration, XYZT data were first reduced in dimensions by conducting standard deviation projection along the z-axis. The XYT data were then processed by TrackMate in Fiji and produced cell trajectories. Trajectories were exported to MATLAB to calculate average speed and mean squared displacement. Average speed specifically refers to the mean of the absolute value of the net displacement of the cell center per hour. Mean squared displacements were computed with the following equation[79]:

$$MSD(n) = \frac{1}{N - n + 1} \sum_{i=0}^{N-n} [(x_{i+n} - x_i)^2 + (y_{i+n} - y_i)^2] \quad (4.1)$$

In this equation, N is the total step number, n is the n-th step, x,y are the x,y coordinates respectively. For morphology analysis, z projected tilescan images were segmented and analyzed by in-house MATLAB codes. Segmentation performance was validated, with wrong segmentation manually corrected or removed. For difficult automatic segmentation data such as the Y27632 treated condition, manually tracked data were supplemented. The definitions of elongation, compactness, sphericity and shape variance were described in Fig.4B. A custom ImageJ script was used to derive the colocalization of the Yap/Taz signal in the nucleus and cytoplasm.

Rheometry

An Anton Parr Shear Stress Rheometer was used for mechanical characterization of collagen gels with the 25-mm parallel-plate geometry and a 500 μ m gap. To prevent slip

between the gel and the plate, no. 1 25-mm cover glasses (VWR) used for the top plate and a 40 mm cover glass were chemically treated with polydopamine and attached to each plate of the rheometer with double-sided tape (3M 666). The rheometer was then zeroed and calibrated. The temperature of the system is preset and maintained at 37°C. Around 300 μ L collagen was pipetted onto the rheometer, the gap was set to 500 μ m, and the sample was kept in a custom made humidity chamber to prevent evaporation. After at least 60 minutes of gelation, gels were immersed in PBS and allowed to sit for at least 15 minutes before taking measurements. Then the shear modulus was measured at 2% strain and at 0.1Hz. The shear modulus was determined and analyzed using custom Python scripts.

Scanning Electron Microscopy

The collagen sample is placed in 4% PFA for 1 hour at room temperature. We then soak the sample twice in PBS for 10 minutes each. This is followed by two 10 minute ddH₂O washes. We then put the sample through a graded ethanol + H₂O wash for 10 minutes each in this order: 30% EtOH, 50% EtOH, 66% EtOH, and 100% EtOH. We then put the sample through a graded ethanol + HMDS wash for 10 minutes each in this order: 30% HMDS, 50% HMDS, 66% HMDS, and 100% HMDS. Samples were then placed on aluminum foil and allowed to dry in the fume hood overnight. Subsequently, the samples were mounted on a support with carbon tape and covered with a 8 nm layer of iridium with a sputter coater. The samples were then imaged with a scanning electron microscope.

Statistical Analysis

Sampling and statistical analyses of various results plots are indicated in their corresponding figure caption. For shear modulus, unpaired t-test is performed. For statistical comparisons in drug studies, one-way ANOVA with post-hoc Tukey HSD test was performed. * indicates p-values < 0.05. ** indicates p-value < 0.01. *** indicates p-value < 0.001, ****

indicates p -value < 0.0001 . # indicates current condition is significantly different ($p < 0.05$) with every other condition unless otherwise annotated.

4.4 Results

4.4.1 Thickened collagen better mimics in vivo ECM architecturally

The first feature of thickened collagen bundles is their high resemblance to in vivo ECM in appearance [156, 155, 160] as shown in Figure 4.2 and Figure 4.3. Thickened collagen bundles appear much long and curly compared with the short, dense collagen network conventionally gelled (i.e., normal collagen). Collagen bundles within each patch are aligned and impose limited physical restraints. In addition, these thickened collagen patches are connected by inner between loose collagen fibers. These thin fibers are sometimes invisible in reflectance imaging, but polystyrene beads can attach with them and indicate the existence of such a network. Cells can be seeded, maintained, and mechanically supported in this 3D collagen network as in normal collagen. Though thick collagen patches vary in size, orientation, and microstructure which provide local spatial heterogeneity for individual cells, each patch is homogeneously dispersed and separate by the loose collagen network judging from the overview tile scan imaging (Figure 4.4).

The generation of thickened collagen bundles is easy and reproducible (Figure 4.5). Ice cold neutralized rat tail Type I collagen is first kept at R.T. for 6.5min, then warmed up by fingertips while stirred gently by wide-bore pipette tips until turbidity approaches around 0.4-0.5 (Figure 4.9.A). The whole process takes approximately 20min. This method can be applied to different concentration of collagen at any volumes larger than 100ul. Different patterns can be created to mimic varied in vivo ECM architecture (Figure 4.9.D).

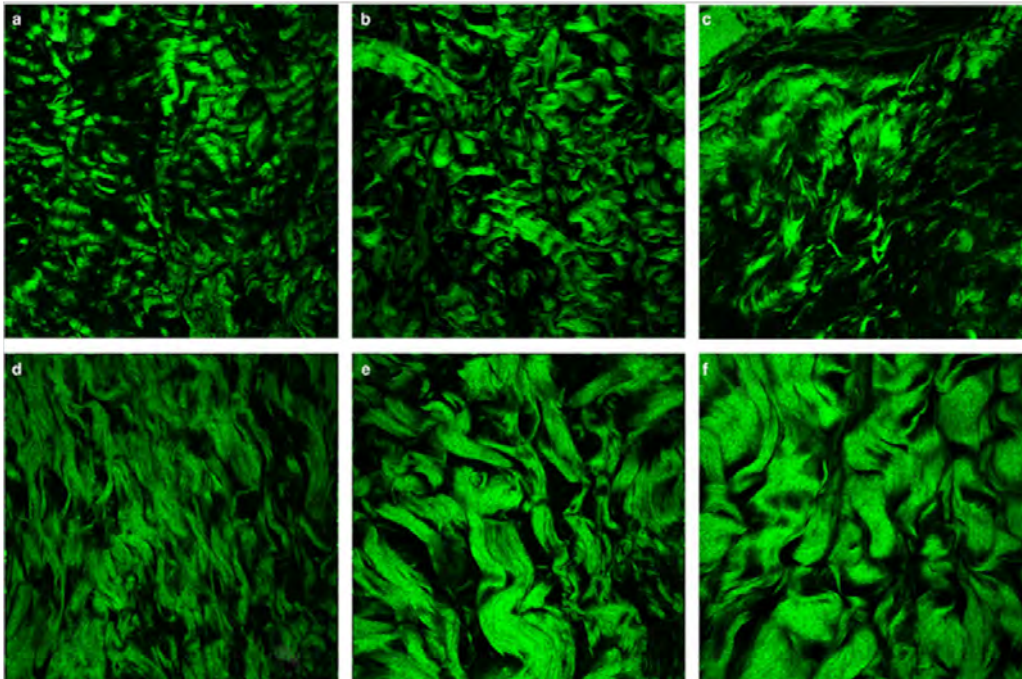


Figure 4.2: **Representative collagen second-harmonic generation (SHG) images from human scars** (a – e) Representative collagen second-harmonic generation (SHG) images from human scars of 2, 4, 8, 15, and 21 years of age after wound. f : Collagen SHG image of normal skin sample from a healthy volunteer aged 29 years who had no scar lesions. [155]

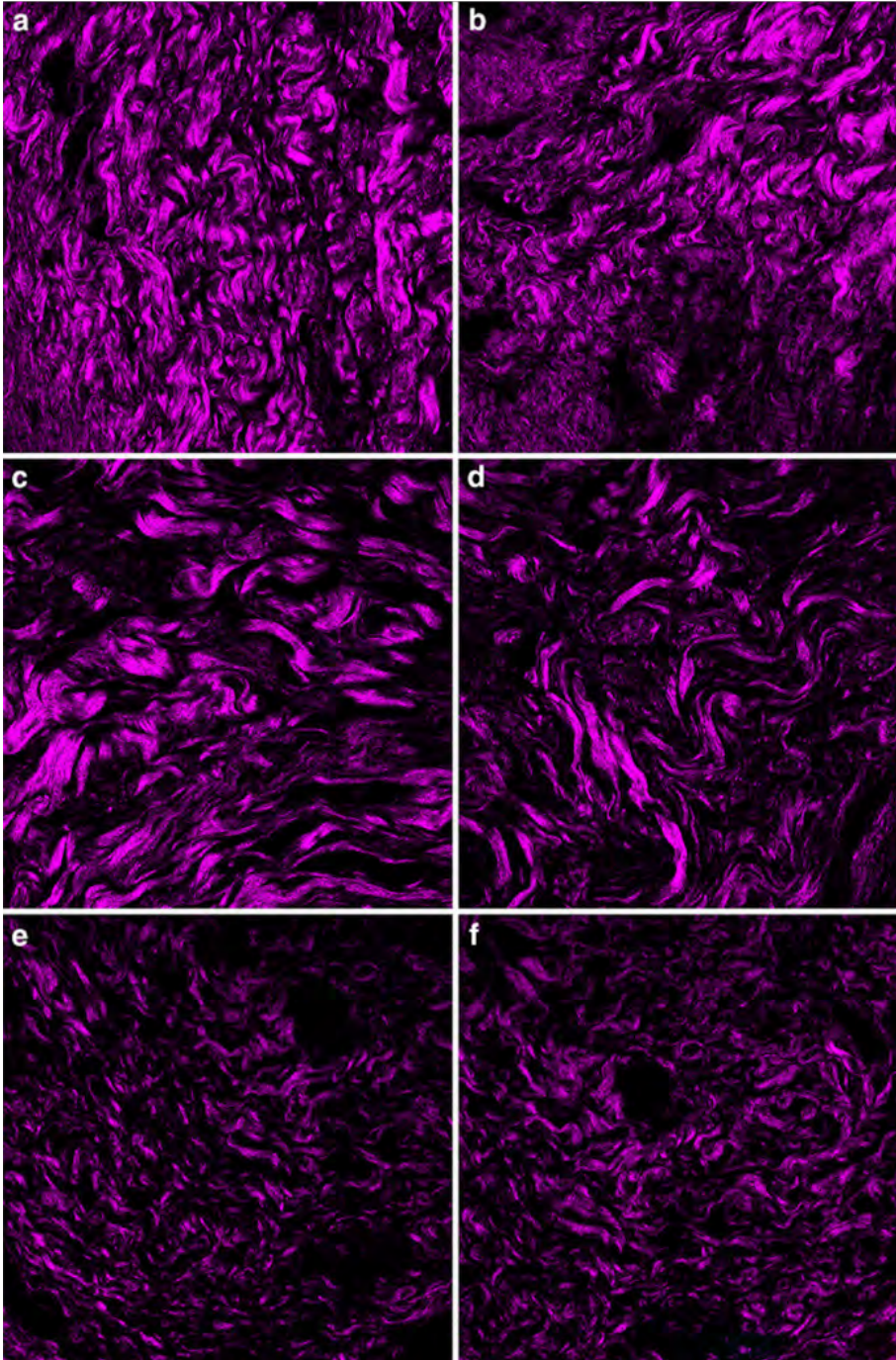


Figure 4.3: **Second-harmonic generation (SHG) images of collagen of ex vivo samples of healthy human skin and the skin of patients with classical and vascular type Ehlers–Danlos syndrome (EDS) in a horizontal view.** a, b Normal human skin. c, d Patient 1, classical EDS. e, f Patient 2, vascular EDS. g, h Patient 3, vascular EDS. The detected SHG signal is shown in violet color. The size of the images is $150 \times 150 \mu\text{m}^2$. i Integrated optical density (measured by ImageJ software) of the SHG signals is displayed in an arbitrary unit, which correlates with the amount of unimpaired collagen. [156]

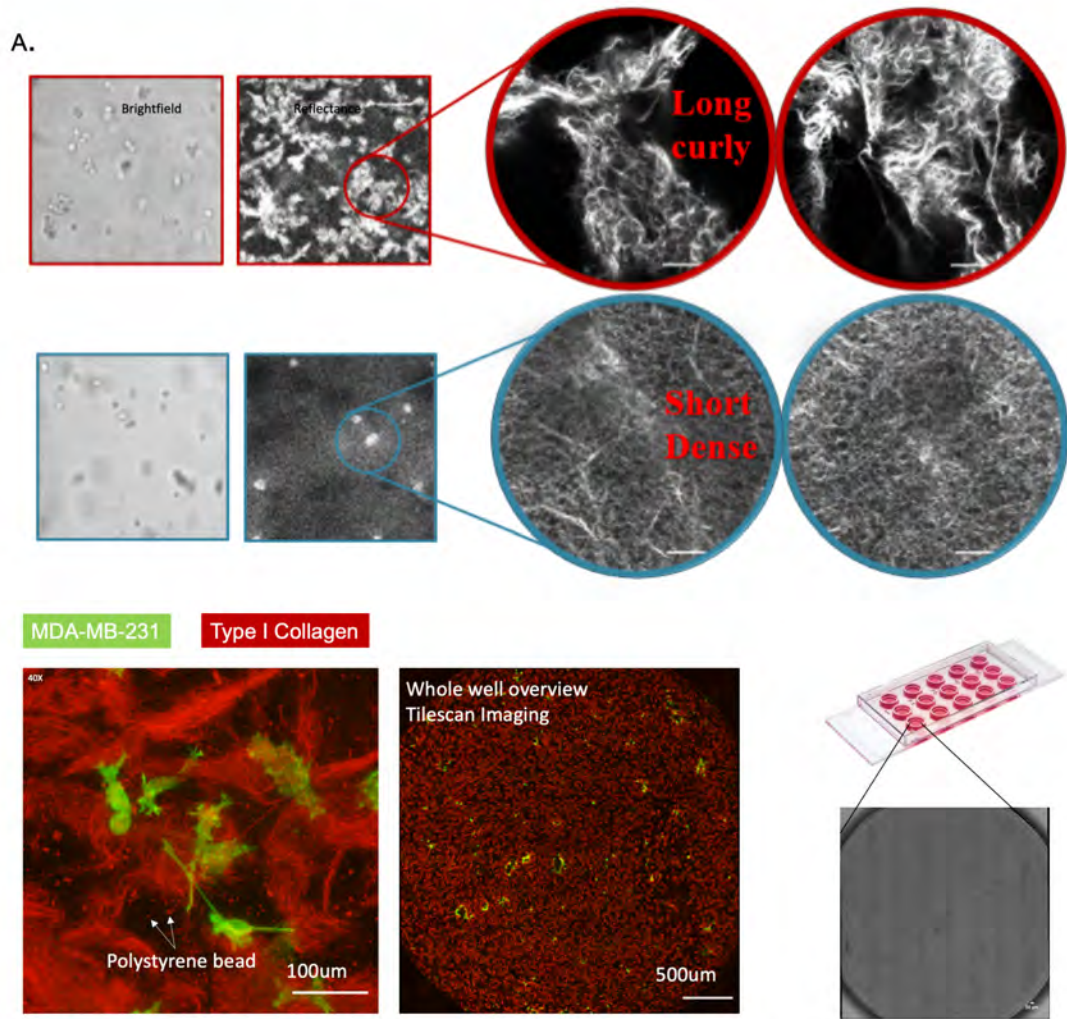


Figure 4.4: **Thickened collagen better mimics in vivo ECM architecturally.** (A) Structural differences of thick collagen bundles versus normal collagen. MDA-MB-231 cells(life-act) seeded in thick collagen bundles respond to the local architectural heterogeneity, demonstrating an invasive phenotype. Thick collagen bundles vary in length and size but are holistically homogeneous in an overview tilescan imaging.

B.

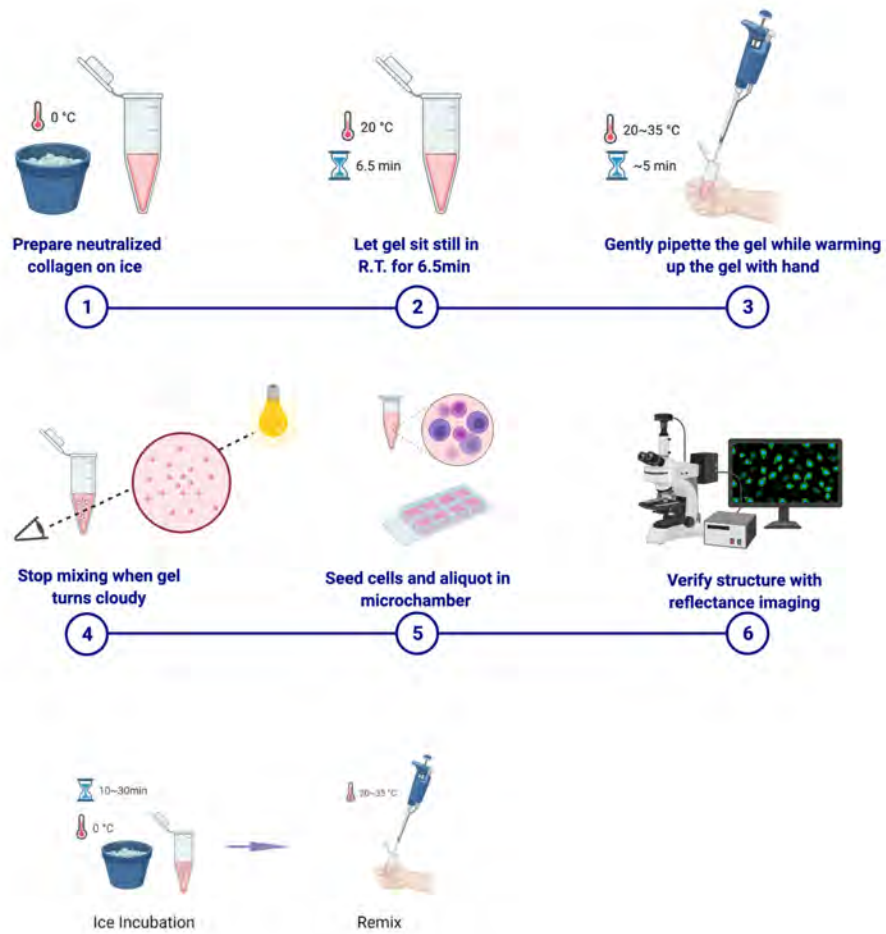


Figure 4.5: **Thickened collagen better mimics in vivo ECM architecturally.** (B) Simplified step-by-step protocol of creating long and thick collagen via collagen fibrillogenesis intervention.

4.4.2 Thickened collagen structure can be tuned by temperature and mixing.

Fibrillogenesis is an indispensable part of ECM remodeling and is heavily implicated in different pathological conditions such as tumor metastasis, fibrotic disease etc. In vivo fibrillogenesis is complex and often involves integrins, fibronectins and tight cellular regulation. In vitro fibrillogenesis, on the other hand, is often simple entropy-driven self-polymerization of collagen monomers[158]. In vitro fibrillogenesis of animal derived collagen such as rat tail type I collagen or bovine dermal collagen are widely used in current fibrillar collagen based 3D models.

Previous studies have delineated in vitro fibrillogenesis into three steps: nucleation, linear growth and lateral growth[161, 162, 163]as schematized in Figure4.6.A. The thickening of individual fibril is often reflected as the lag phase in the typical turbidimetry curve[163, 151]. However, the growth of visible particle-like structure is directly associated with the sigmoid phase from our observation and confirmed by another study[164]. Besides, this particle-like(visually) structure or the thickened collagen patch(microscopically) is not thermally stable and may disassemble upon ice incubation(Figure4.7.B,Figure4.9.B&C). Similar observation has been noticed before that collagen precipitation can dissolve upon pH[165]or temperature change[166, 163] and it was suggested that the temperature-related fibril instability may be governed by entropy[166]. It is highly likely that erosion of thickened collagen bundles upon ice incubation may subject to the same mechanism. Temperature tuning in fibrillogenesis has been used by some study to control collagen pore size[151].

In addition to temperature, we also notice that the frequency and strength of remixing (the specific mixing step between step4 and step5 as annotated in Figure4.7.B) are equally critical in tuning the average size of collagen patches. The size of the final collagen patches grow linearly with the degree of mixing. However, over mixing often result in an ultra-

fragile collagen network that collapses upon PBS addition(data not shown).

Thus, we hypothesized that the formation of these thickened collagen bundles comes from the uneven entanglement(aggregation) of collagen fibers due to external disturbances during in vitro fibrillogenesis. Hypothetically, heating up the gel gradually with fingertip results in faster assembly of outmost layer of collagen fibril. Heating up while mixing hence homogenize the distribution of these early gelation core(thickened collage islands) in the biphasic solution. The imbalanced early assembly is further augmented at 37°C later which result in the patches of thickened collagen bundles. SEM imaging Figure4.8.E shows thick collagen patches, the loose fibers(indicated by the red arrows)extend out from the patch, and the large void space on the boundary of each patch suggesting reduced steric restraints in thick collagen bundles.

4.4.3 MDA-MB-231 located on the boundary of thick collagen patch is more invasive

MDA-MB-231 is a triple-negative basal type cancer cell line derived from breast adenocarcinoma. This cell line is highly aggressive and metastatic, featuring low-claudin(reduced cell-cell contact) and overexpression of ECM remodeling related proteases (COL3A1, COL6A1/2/3, MMP2/14, FN1,FBN1), mesenchymal associated markers(VIM, MSN), and tumor favoring signals(TGFB1, TGFBR2, AXL)[167].

In in vitro 3D models, MDA-MB-231 cells are highly sensitive to collagen alignment[168, 169], stiffness[170, 161] and steric hinderance such as pore size[170, 150, 55]. In vivo these tumor cells also preferentially metastasize to the bones, brain and lungs[171, 172, 173].

Our thick collagen system is characterized with reduced physical hinderance but global softness(unpublished rheometry data) and local thickened fiber bundles. When seeded in thick collagen, MDA-MB-231 react immediately during day1 after gel embedment. In

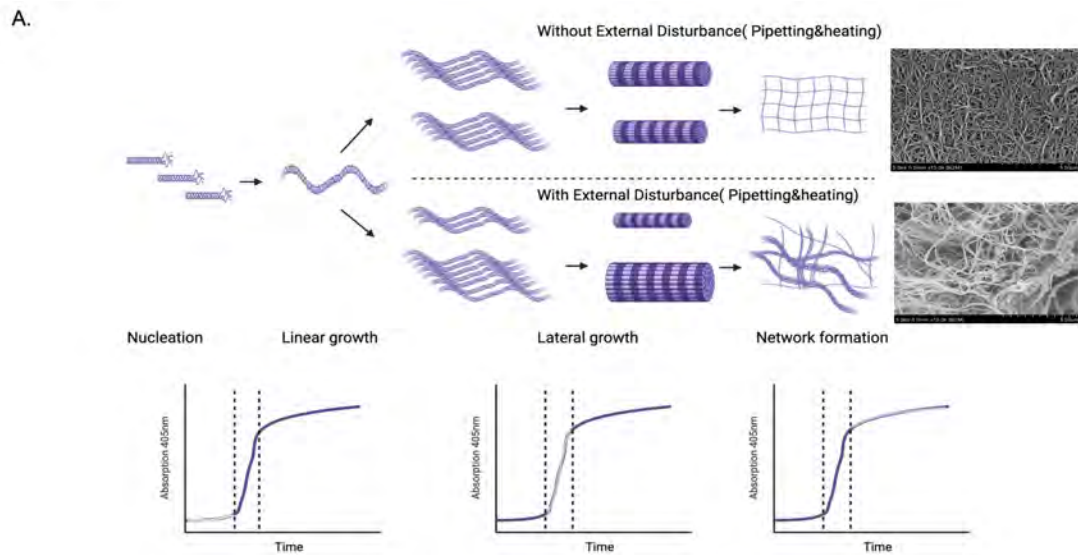


Figure 4.6: **Thickened collagen structure can be tuned by temperature and mixing** (A) Schematic diagram demonstrates how external disturbance in the collagen lateral growth stage triggers the formation of thick collagen bundles. (B) After thick collagen is formed, ice incubation decreases the overall granularity of the thick collagen system. (C) Reflectance imaging shows that ice incubation between step4 and step5 (before complete gelation at 37°C) reduces the size of collagen bundles. (D) The frequency and strength applied in mixing thick collagen bundles before step5 controls the size of collagen bundles. (E) Scanning electron microscope images of normal collagen versus thick collagen bundles

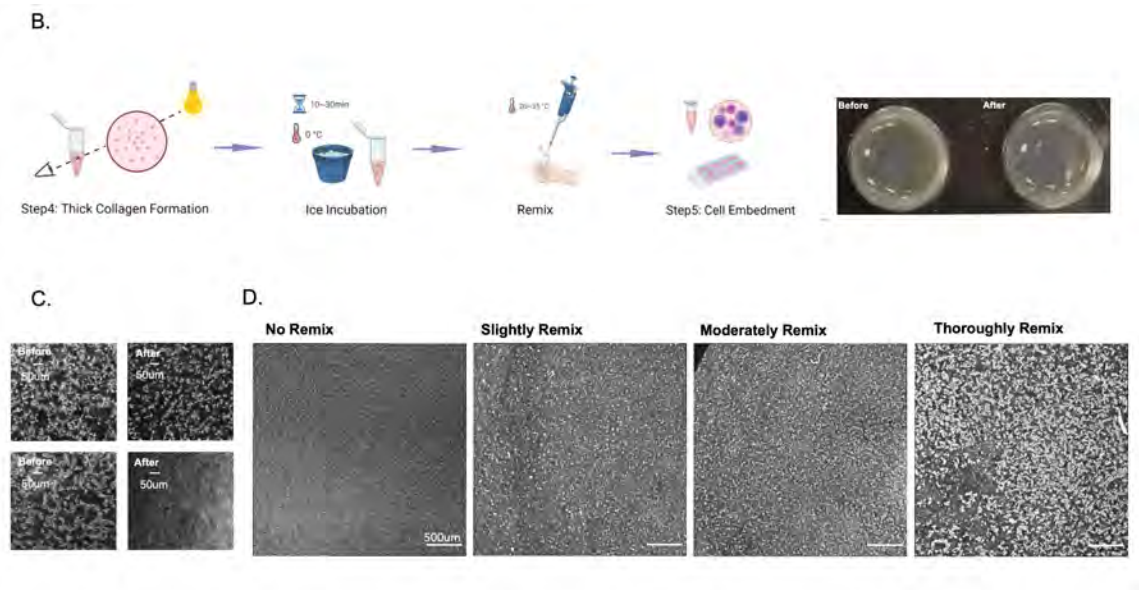


Figure 4.7: **Thickened collagen structure can be tuned by temperature and mixing** (B) After thick collagen is formed, ice incubation decreases the overall granularity of the thick collagen system. (C) Reflectance imaging shows that ice incubation between step4 and step5 (before complete gelation at 37°C) reduces the size of collagen bundles. (D) The frequency and strength applied in mixing thick collagen bundles before step5 controls the size of collagen bundles. (E) Scanning electron microscope images of normal collagen versus thick collagen bundles.

E.

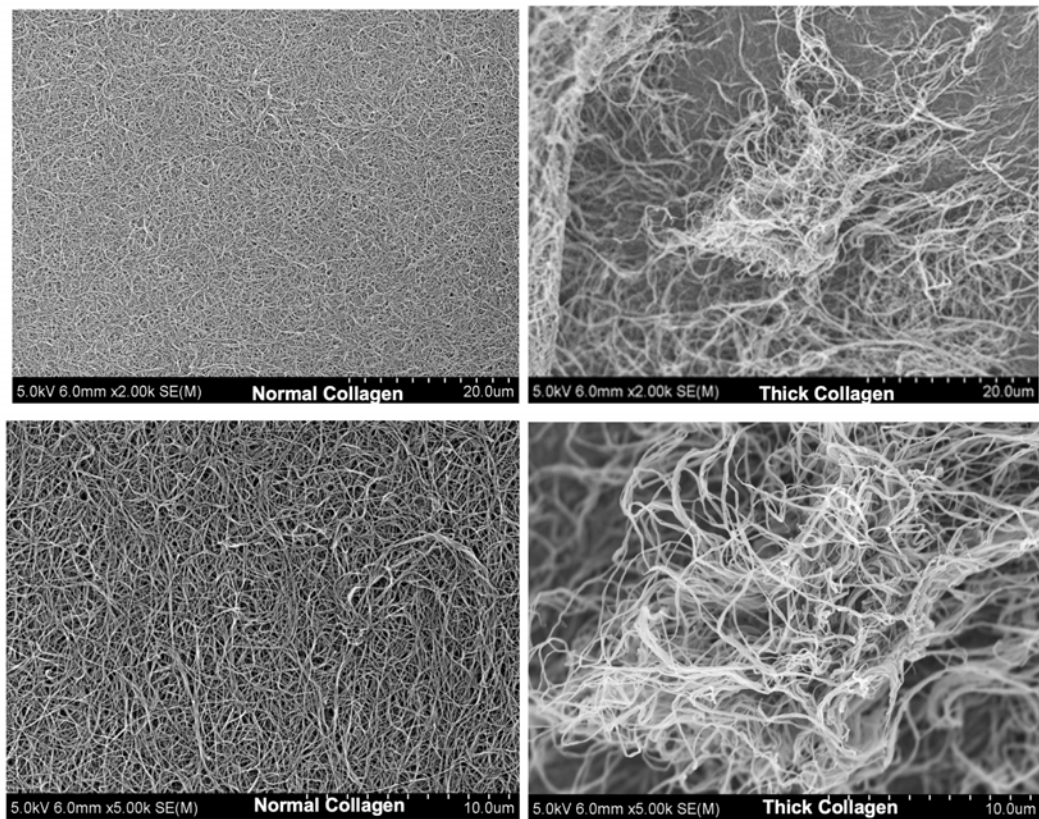


Figure 4.8: **Thickened collagen structure can be tuned by temperature and mixing (E)**
Scanning electron microscope images of normal collagen versus thick collagen bundles.

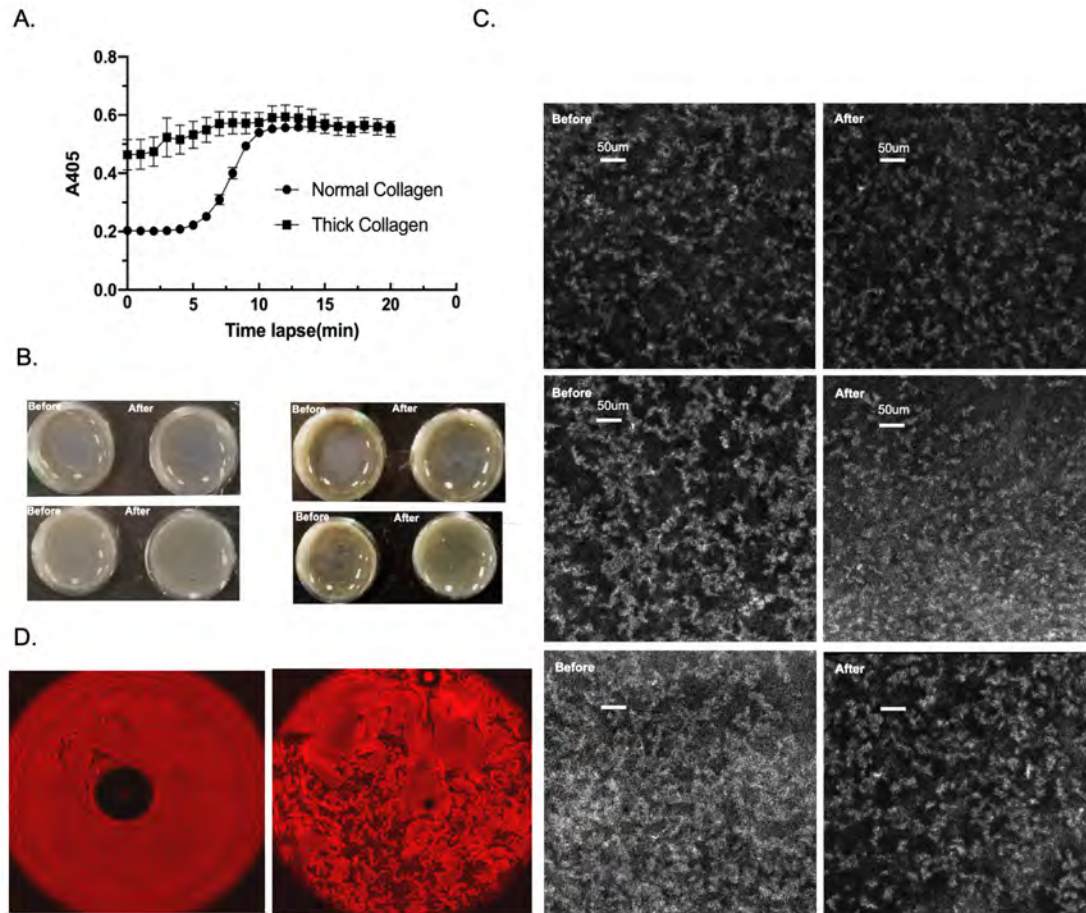


Figure 4.9: **Thickened collagen structure can be tuned by temperature and mixing** (A). Turbidity of thick collagen and normal collagen at A405. Error bar is in SEM. (B). Additional photos demonstrate the disassembly of thick collagen bundles before and after ice incubation (C). Confocal reflectance imaging verified shortened collagen bundles before and after ice incubation. (D). Other types of collagen architecture can be generated by the manipulation of 4mg/ml collagen.

long term culture (up to day 5), MDA-MB-231 seeded in normal collagen mostly grow into spherical cell clusters whereas cells seeded in thick collagen remain individual and rarely cell clusters are found (Figure 4.10.A, Figure 4.13.A). This observation can be further supported by our overview whole-well tile scan imaging (Figure 7.A and Figure 7.B). Overall, MDA-MB-231 in thick collagen demonstrate higher invasiveness (Figure 4.11.B), average speed (Figure 4.11.C&E, Figure 4.11.E) and persistence (Figure 4.11.D) compared with cells in normal collagen on day 0 and day 1 (Figure ??C). Though we didn't collect time-lapse imaging after day 1, but from the day 5 clustering results (Figure 4.10.A), the faster migration of MDA-MB-231 in thick collagen should last at least up to day 5.

In addition, MDA-MB-231 cells often demonstrate two distinct morphological phenotypes depending on the position of MDA cells in thick collagen patch. MDA-MB-231 perching on the boundary of thick collagen bundles often are highly stretched, "spindle-like", reaching out to nearby collagen patch (Figure 4.12.E, Figure 4.14.B-left) whereas MDA-MB-231 trapped in the center of thick collagen patch are more spherical (similar to cells in normal collagen (Figure 4.12.F-H)). In coherence with morphological disparity, MDA-MB-231 on the boundary display higher migration speed than cells in the middle of thick collagen.

Interestingly, our finding echoes with one intravital imaging study of breast cancer [174]. This study identified two subpopulations of tumor cell phenotypes and their multiparameter classification links the driving factor of these two subpopulations to their relative loci in the TME. This study also concluded the importance of spatial heterogeneity of TME.

4.4.4 Drug treatment trigger different cell morphology patterns in thick collagen versus normal collagen

To investigate the molecular mechanism behind the elevated invasiveness of MDA-MB-231 cells, pan-MMPs inhibitor GM6001 (20uM), potent selective Cdc42 inhibitor ML141 (10uM),

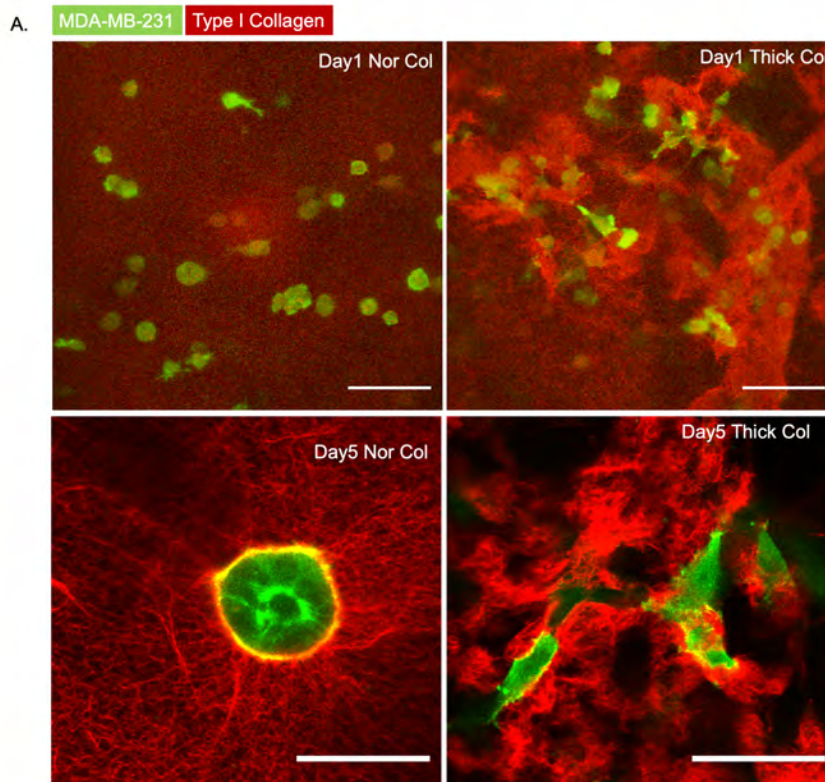


Figure 4.10: **MDA-MB-231 located on the boundary of thick collagen patch is more invasive**A). MDA-MB-231(lifeact-GFP) cells seeded in normal Type-I collagen versus thick collagen. MDA-MB-231 cells seeded in thickened collagen bundles do not form cell clusters and maintain an invasive phenotype throughout the culture.

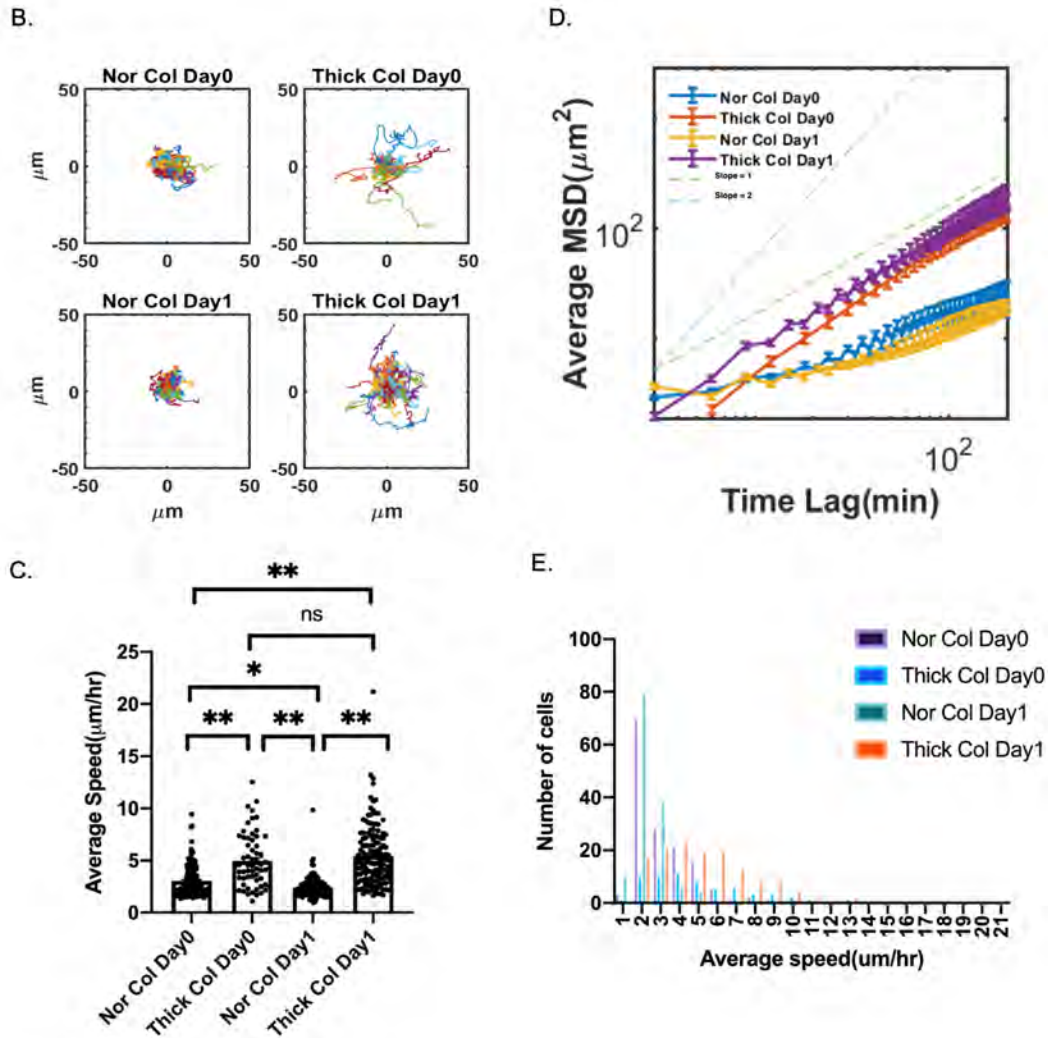


Figure 4.11: **MDA-MB-231 located on the boundary of thick collagen patch is more invasive** (B). MDA-MB-231(lifeact-GFP) seeded in thick collagen bundles migrate more actively than normal collagen on day0 and day1. (C). Average speed of MDA-MB-231(lifeact-GFP) between normal versus thick collagen on day0 and day1. (D). Average mean squared displacement of MDA-MB-231(lifeact-GFP) between normal versus thick collagen on day0 and day1. (E) Histogram of average speed, in supplementary to Figure4.11.C.

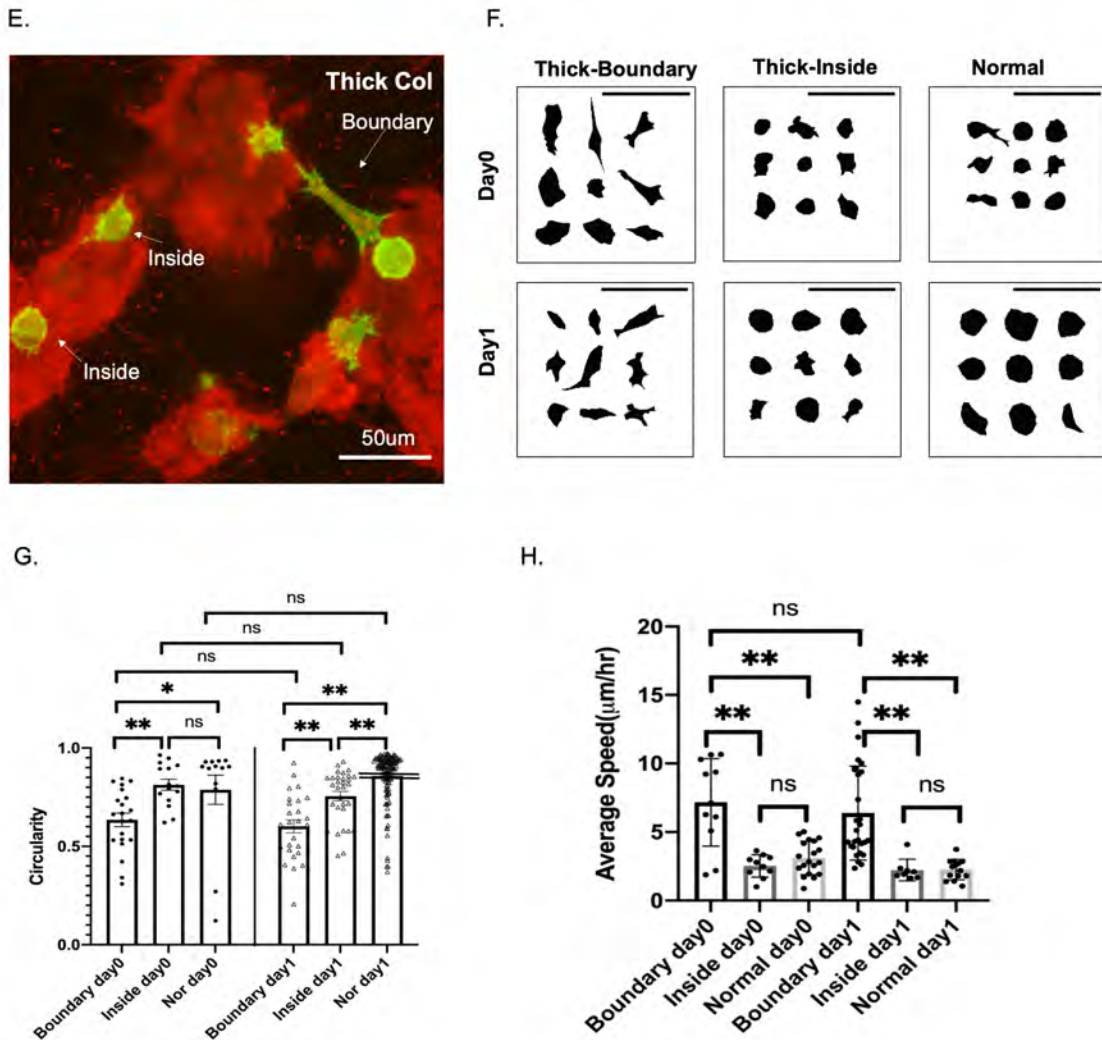


Figure 4.12: **MDA-MB-231 located on the boundary of thick collagen patch is more invasive** (E). Representative image demonstrates the distinct behavior of MDA-MB-231(lifeact-GFP) along gel boundary versus trapped in the middle of the thick collagen. The beads trapped between the gel patches indicate the existence of loose connecting fiber but are invisible to reflectance microscopy. (F). Summarized morphology of MDA-MB-231(lifeact-GFP) in different conditions. Thick-Boundary: on the boundary of thickened collagen patch; Thick-Inside: in the middle of thickened collagen patch; Normal: normal collagen. (G). Average speed of MDA-MB-231(lifeact-GFP) located on the boundary versus cells found trapped in the middle of gel. (H). Circularity of MDA-MB-231(lifeact-GFP) located on the boundary versus cells found trapped in the middle of gel.

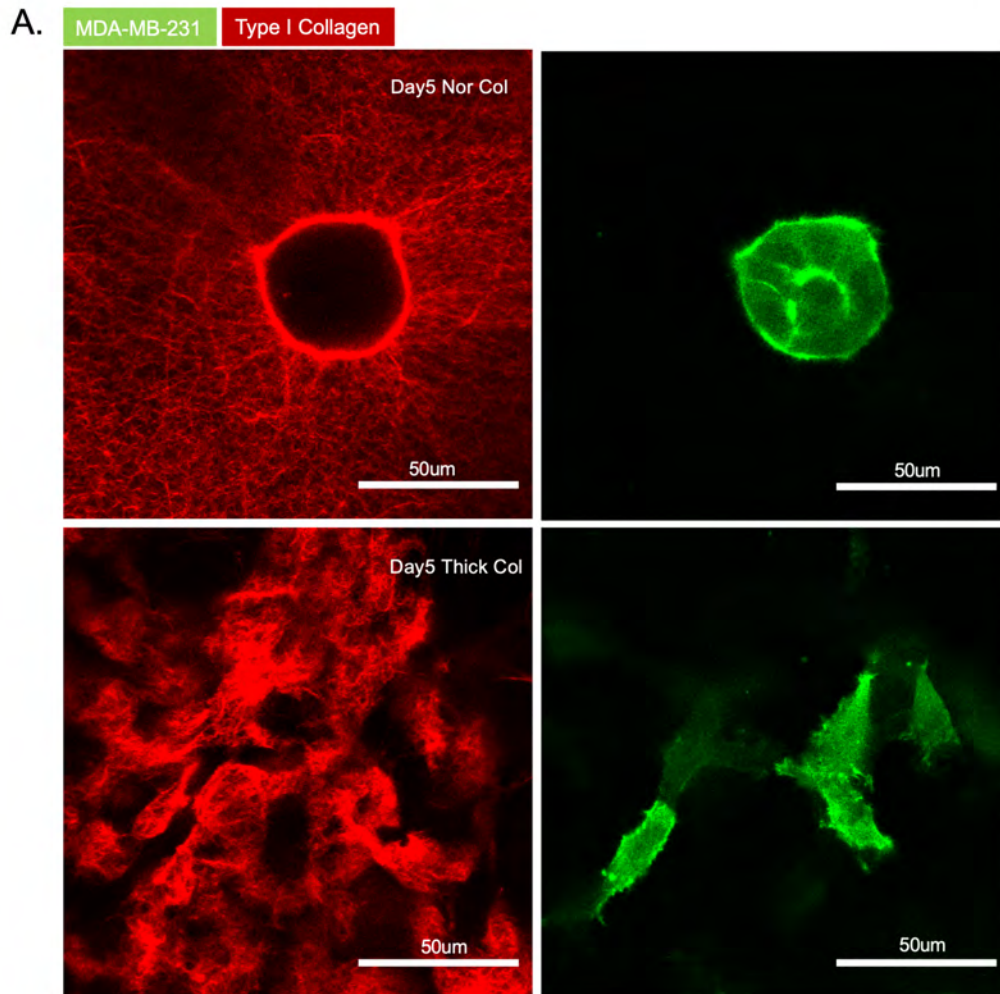


Figure 4.13: **MDA-MB-231 located on the boundary of thick collagen patch is more invasive (A).** Zoomed-in view of MDA-MB-231(lifeact-GFP) on day5 in normal collagen and thick collagen.

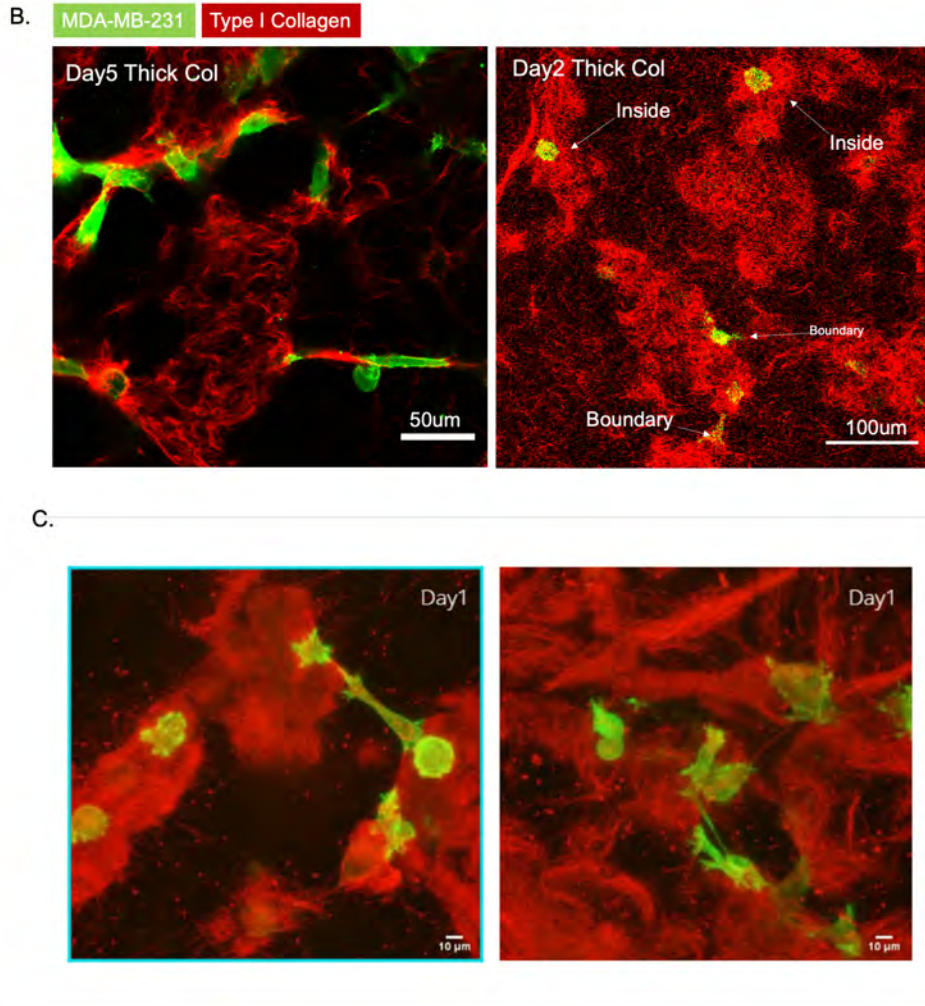


Figure 4.14: **MDA-MB-231 located on the boundary of thick collagen patch is more invasive** (B). Left: Most MDA-MB-231(lifeact-GFP) locate on the boundary of thick collagen patches on day5. Right: the criterion we used to differentiate middle vs boundary cancer cell. (C). Representative videos of MDA-MB-231(lifeact-GFP) in thickened collagen bundles on day1(40X). See videos in published paper.

ROCK inhibitor Y27632(30uM), Arp2/3 inhibitor CK666(50uM), formin inhibitor SMIFH2(50uM), Rac1 inhibitors NSC23766(100uM) and EHT1864(20uM) were introduced into the culture.

GM6001, ML141 and EHT1864 showed similar morphology patterns with DMSO control group in both normal collagen and thick collagen(Figure4.15 and Figure4.16) indicating that the governing factor of cell morphology is collagen architecture instead of drug treatment. On the other hand, Y27632, CK666, SMIFH2 and NSC23766 treated cells demonstrate distinct and unique morphology compared with control. MDA-MB-231 display similar morphology in normal collagen and thick collagen. This suggest that the driving factor in these groups are drugs instead of architecture. The architecture induced morphology feature has been summarized in Figure4.12.F, therefore will not be repeated again. Hence this part will focus on drug dominating morphology patterns.

To note, each of the observed intriguing pattern is directly associated with inhibitors' function. Y27632 is potent and selective ROCK inhibitor. ROCK mediates actomyosin based cell contractility via regulating retrograde flow of actin from protrusive structures[175]. The loss of ROCK hence halts the recycle of actin from the protrusions and lead to the extremely long protrusions. Also neurocytes upon Y27632 or H1152 treatment also generate extended protrusions[176]. Interestingly, cell body in normal collagen are usually round whereas cell body in thick collagen are slightly elliptical as indicated by the round/elliptical dotted circle in Figure4.16. This may suggest that the alignment of cell body in response to collagen architecture may not be entirely abolished without presence of ROCK.

Though both CK666 and SMIFH2 are nucleator inhibitors but they trigger total different morphologies. CK666 inhibits Arp2/3 whereas SMIFH2 inhibits formins. Arp2/3 is the nucleator that initializes actin branching and is closely associated with lamellipodia. Upon Arp2/3 inhibition, MDA-MB-231 in both normal collagen and thick collagen are much elongated and stretched compared with other conditions. This phenomenon may

suggest that Arp2/3 as a branching nucleator may contribute to the thickness and stability of the actin meshwork near cell periphery. In the absence of Arp2/3, formins dominated actin network are unidirectionally aligned and lead to the extreme polarization of cell body. However, SMIFH2 treated cells are completely round, deprived of any cell periphery fluctuations and lack of F-actin accumulation around cell membrane(indicated by red arrows on Fig4.B). This may suggest that appropriate function of formins-based are prerequisite of Arp2/3. Recently finding[177] also showed that contractile cells rely on more on formin and FAP signaling pathway whereas low traction environment initiate dendritic like protrusions that depends more on Arp2/3.

NSC23766 has shown similar effect with SMIFH2 but discernible differences still can be told in fluorescence imaging(Figure4.16). NSC23766 treated cells are smaller than most other drug treated groups without proliferation and expansion on day2. Similar effect has been noted in other work that CLL cells under treatment with NSC23766 have reduced proliferation[178]. In addition, SMIFH2 treated cells lack of F-actin accumulation on the cell periphery but such F actin accumulation in NSC23766 treated cells are clear(red arrows Figure4.16). NSC23766 and EHT1864 are Rac1 inhibitors but generate distinct morphological response in MDA-MB-231 cells. The possible explanation is discussed in following section.

The quantification of MDA-MB-231 population in each group agrees with above findings(Figure4.17; Figure4.18). In conditions(GM6001/ML141/EHT1864/DMSO) governed by collagen architecture, cell population demonstrate almost identical distribution regardless onto whichever morphology index the data is projected onto(as indicated by red dotted arrows in Figure4.17). A specific subpopulation of MDA-MB-231 cells (as indicated by yellow arrows)responding to the architectural change and contribute to the morphology profile shift from normal collagen to thick collagen.

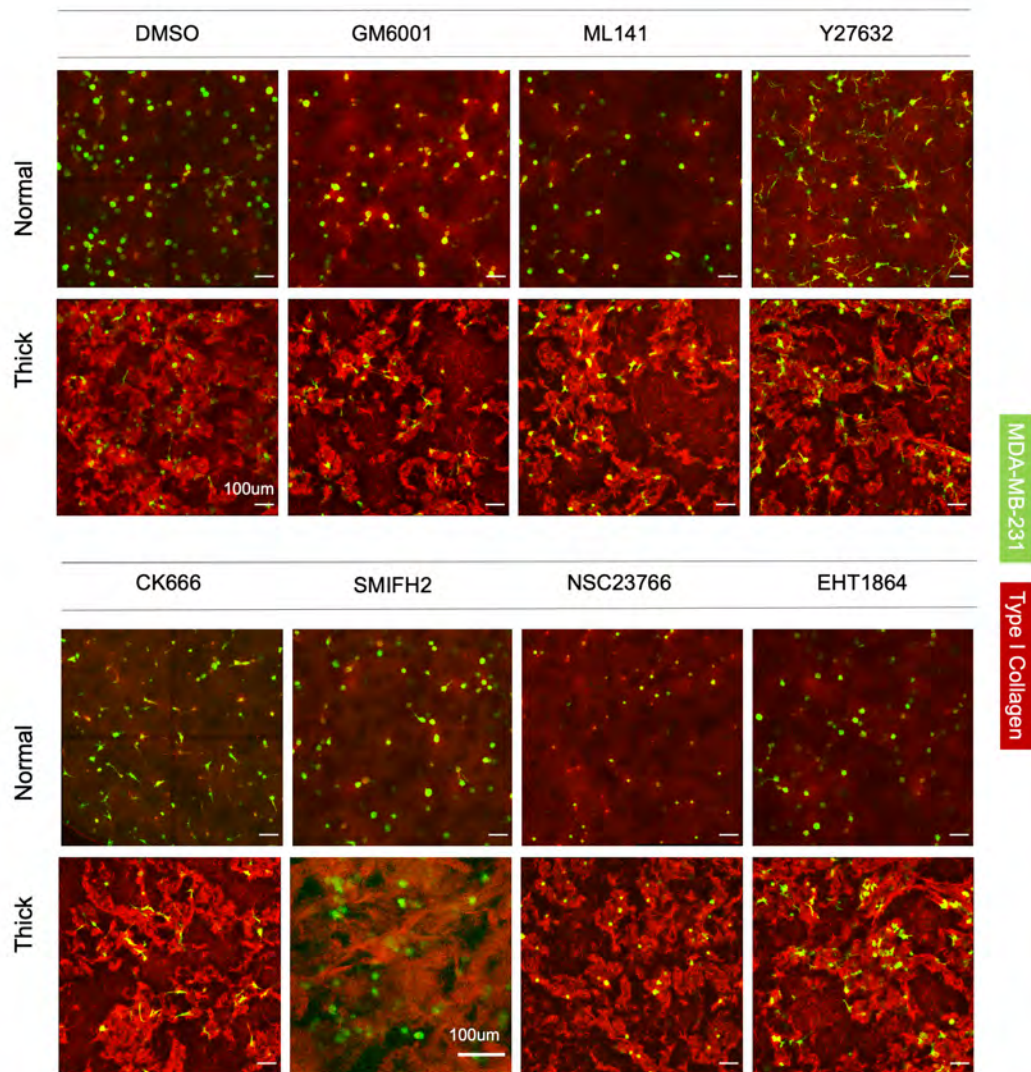


Figure 4.15: **Drug treatment trigger different cell morphology patterns in thick collagen versus normal collagen (A).** Morphology of MDA-MB-231(lifeact-GFP) under drug treatment on day2.

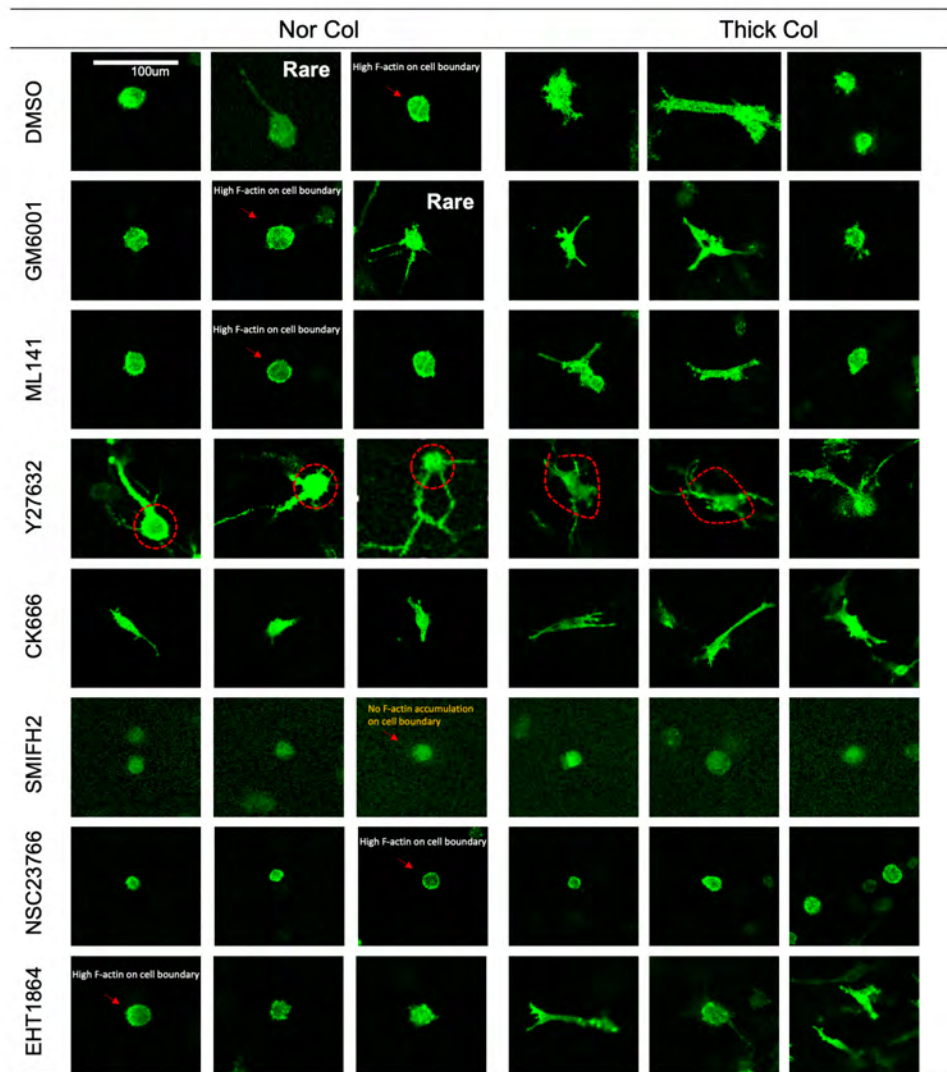


Figure 4.16: **Drug treatment trigger different cell morphology patterns in thick collagen versus normal collagen (B).** Summarized morphology of MDA-MB-231(lifeact-GFP)under drug treatment on day2.

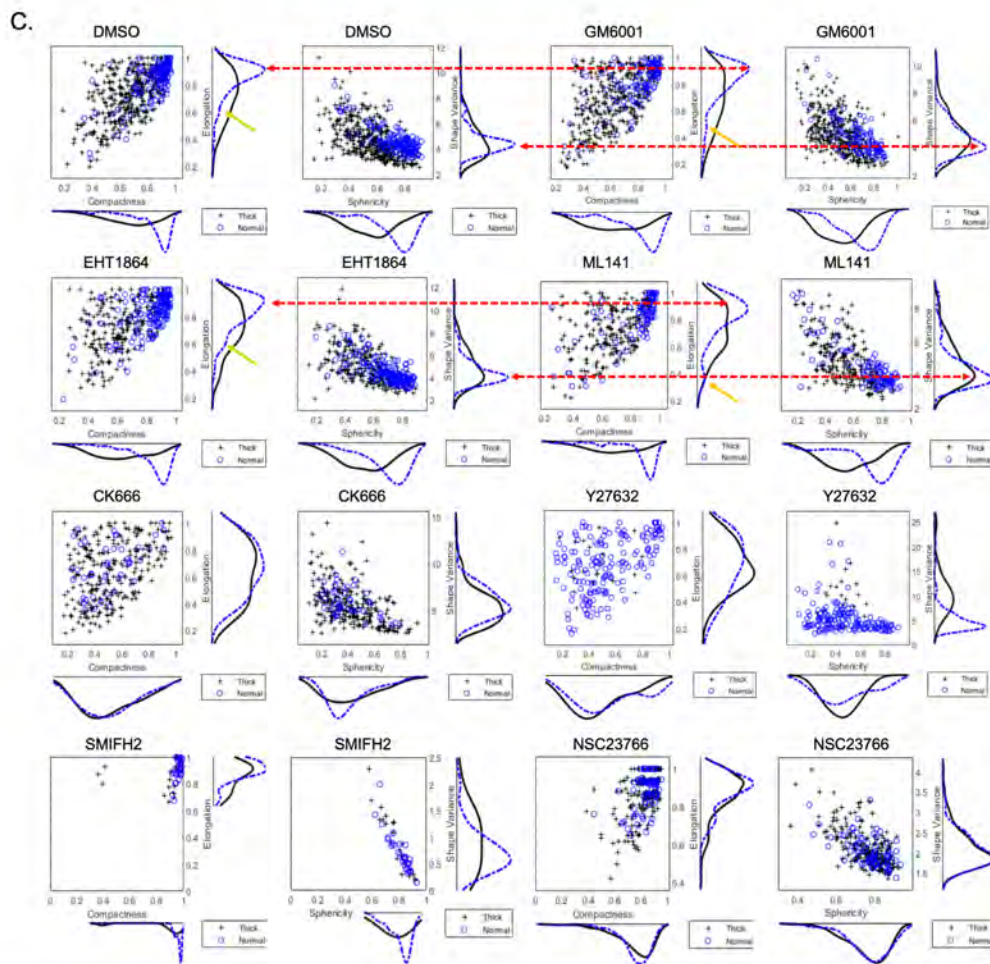


Figure 4.17: **Drug treatment trigger different cell morphology patterns in thick collagen versus normal collagen (C).** MDA-MB-231(lifeact-GFP) population distribution when projected on the axis of elongation index, compactness index, shape variance, and sphericity. See the definition and calculation of these four indexes in the materials and methods section and also Figure4.19.B. ;See the normalized sphericity at Figure4.19.C;See the segmentation performance at Figure4.20

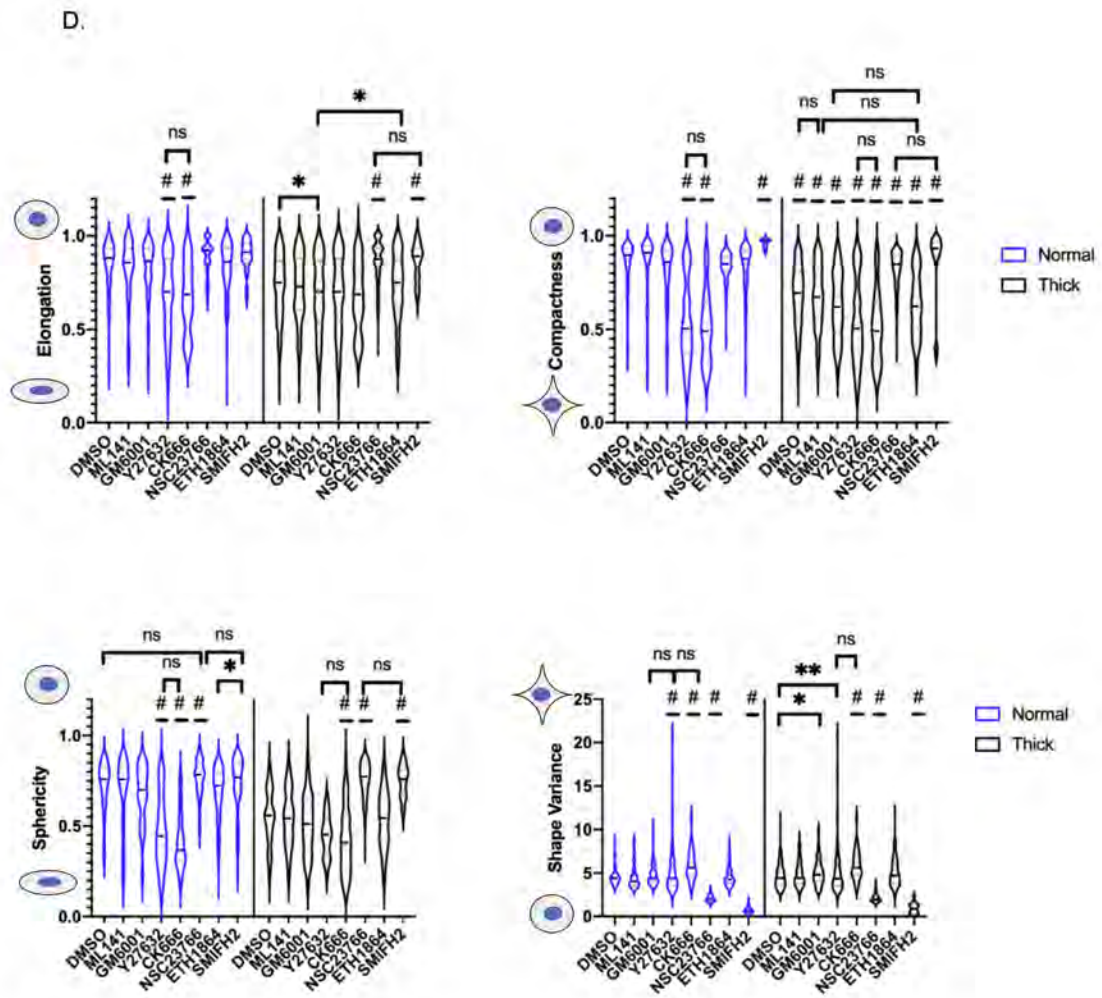


Figure 4.18: **Drug treatment trigger different cell morphology patterns in thick collagen versus normal collagen (D).** Violin plot of morphology index of each condition on day0 and day1.

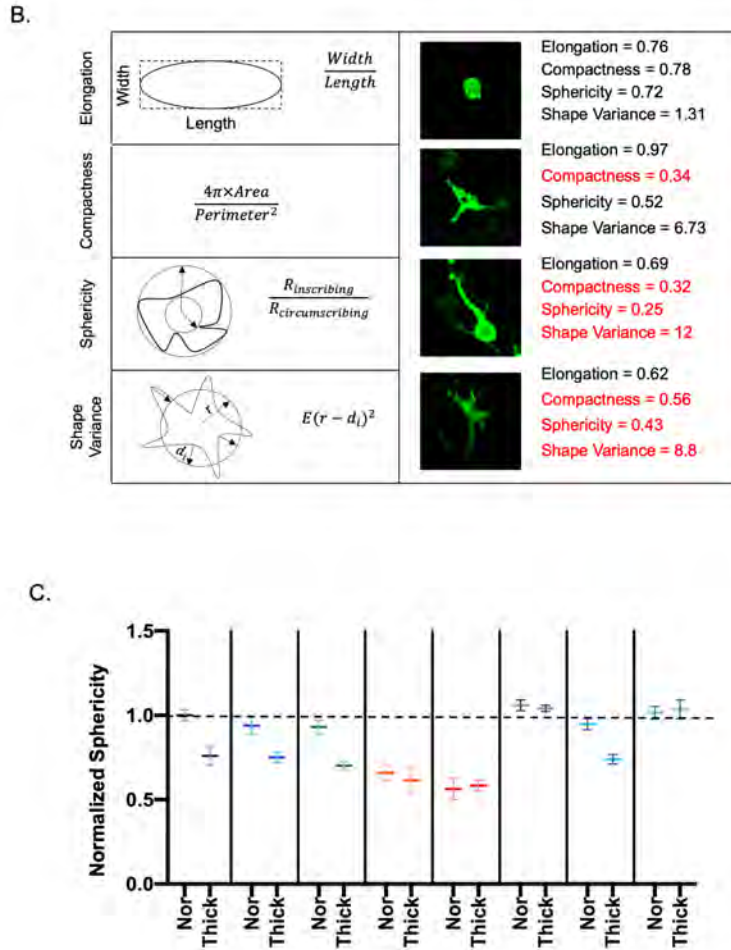


Figure 4.19: **Drug treatment trigger different cell morphology patterns in thick collagen versus normal collagen** (A). Brightfield channel images in supplementary to Fig4.A. (B). Illustration of the morphology index used. (C). Normalized sphericity of MDA-MB-231(life-act) across all drug conditions.

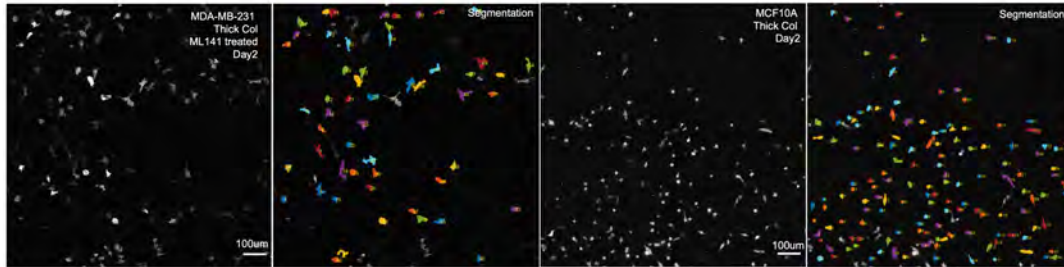


Figure 4.20: **Drug treatment trigger different cell morphology patterns in thick collagen versus normal collagen (D).** Performance of imaging segmentation.

4.4.5 Fast migration of MDA-MB-231 in thick collagen requires coordinated contractility and protrusions but not MMPs

Apart from morphology signatures, we also tracked cell migration. Firstly, MDA-MB-231 with GM6001 treatment in thick collagen migrate as actively as DMSO control, and much more actively than cells in normal collagen. The fast migration of tumor cells in thick collagen are MMP-independent in the absence of steric restraint. Besides MMPs, we also noticed that Y27632, NSC23766 and SMIFH2 reduced MDA-MB-231 migration significantly (Figure 4.21, Figure 4.22, Figure 4.23). This suggests that actomyosin mediated contractility by RhoA/ROCK and formin-based actin nucleation is necessary for effective cell migration in thick collagen. However the interpretation of NSC23766 is compounded by the ineffective performance of another Rac1 inhibitor ML141. Both NSC23766 and EHT1864 potently inhibit serum of PDGF induced lamellipodia formation [179, 180]. NSC23766 binds directly with Rac1 and block the interaction between GEF Trio or Tiam [179]. EHT1864 also binds with Rac1 but in an allosteric inhibition manner, by inhibiting gua-

nine nucleotide association. It has been noted that CLL cells under treatment with NSC23766 have reduced proliferation[178], our results demonstrate similar halt of cell proliferation. EHT1864 on the other hand has not shown similar proliferation inhibition. And also EHT1864 block PDGF-induced lamellipodia formation, though was blocked completely, LPA or bradykinin can still trigger cytoskeleton rearrangement by RhoA and Cdc42, respectively[180] on the presence of EHT1864. These together may suggest that the high activity of cells in thick collagen is likely to be associated with cell cycle or cell proliferation-related cell migration.

On the other hand. ML141, one of the Cdc42 inhibitor did not show significant inhibition. There were not much research available of ML141 on MDA-MB-231 studies, however one study on [181]demonstrates that human pancreatic cancer cells PANC-1 move significantly faster in aligned matrix fiber irregardless of ML141 treatment and also NSC23766's inhibit cell movement irregardless collagen fiber orientation. This echos our finding. Interestingly, even though ML141 is uable to inhibit MDA-MB-231 or pancreatic cancer cells. It is able to inhibit ovarian cancer cell line such as OVCA429 or SKOV3ip in a dosage dependent manner in 2D. And there is a unique difference between ovarian cell line with MDA-MB-231[11, 12]that MDA-MB-231 prefer stiff substrate whereas metastatic ovarian cancer cell line prefer compliant substrate. This finding together may suggest that, MDA-MB-231's preference towards stiffness may be associated with Rac1 whereas MOCC's preference is determined by ML141.

4.4.6 Non-metastatic MCF10A pick up invasive phenotype in thick collagen

In contrast with MDA-MB-231 cell line, MCF10A is an immortalized noncancerous breast epithelial cell line that established in labs. MCF10A lack of the potential to form tumors and metastasize in nude mice[182]. When culture in 3D reconstituted basement mem-

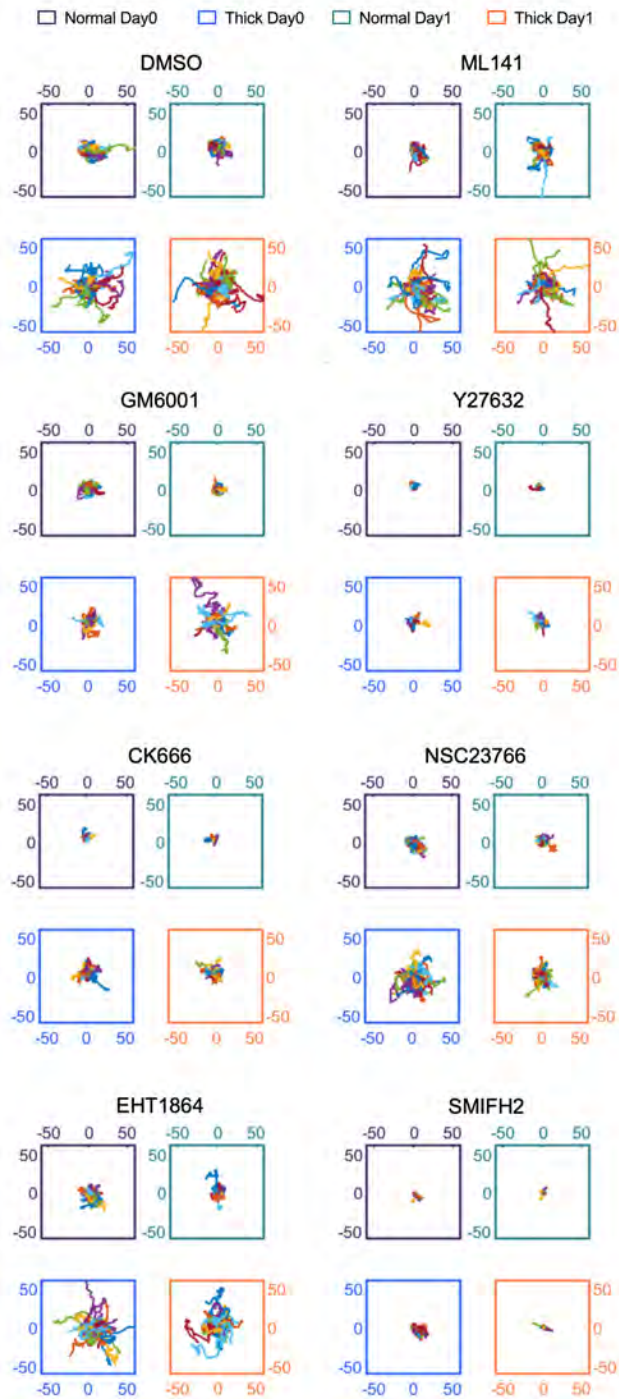


Figure 4.21: **Fast migration of MDA-MB-231 in thick collagen requires coordinated contractility and protrusions but not MMPs** (A). Overlaid trajectories of MDA-MB-231(lifeact-GFP) in thick collagen versus normal collagen on day0 and day1.

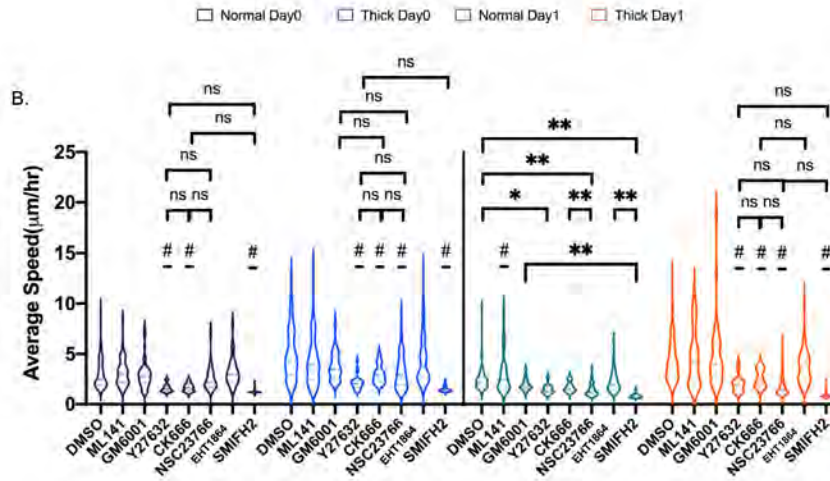


Figure 4.22: **Fast migration of MDA-MB-231 in thick collagen requires coordinated contractility and protrusions but not MMPs** (B). Average speed of MDA-MB-231(lifeact-GFP) in thick collagen versus normal collagen on day0 and day1.

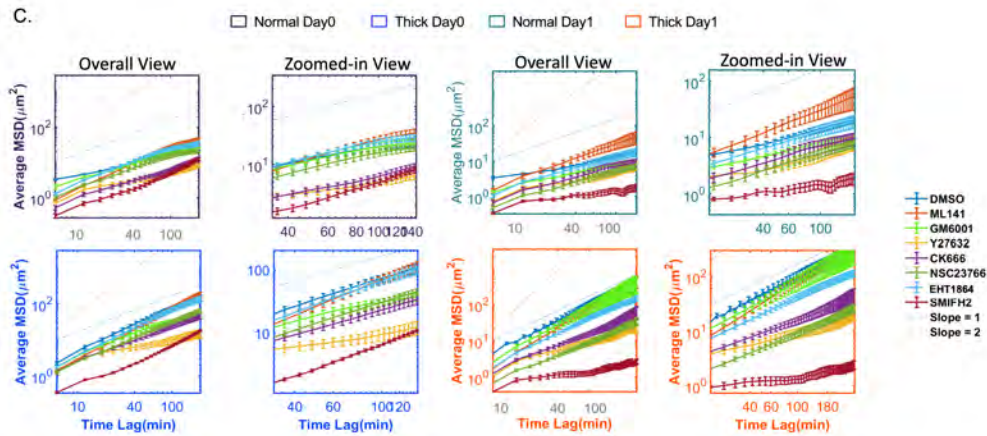


Figure 4.23: **Fast migration of MDA-MB-231 in thick collagen requires coordinated contractility and protrusions but not MMPs** (C). Average mean squared displacement of MDA-MB-231(lifeact-GFP) in thick collagen versus normal collagen on day0 and day1. Error bar is in SEM.

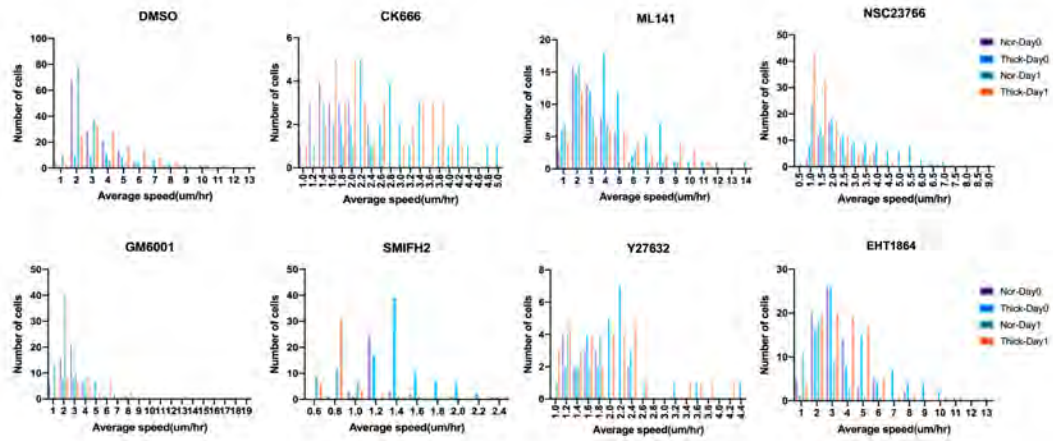


Figure 4.24: **Fast migration of MDA-MB-231 in thick collagen requires coordinated contractility and protrusions but not MMPs** Histograms of average speed in supplementary of Figure4.22.B.

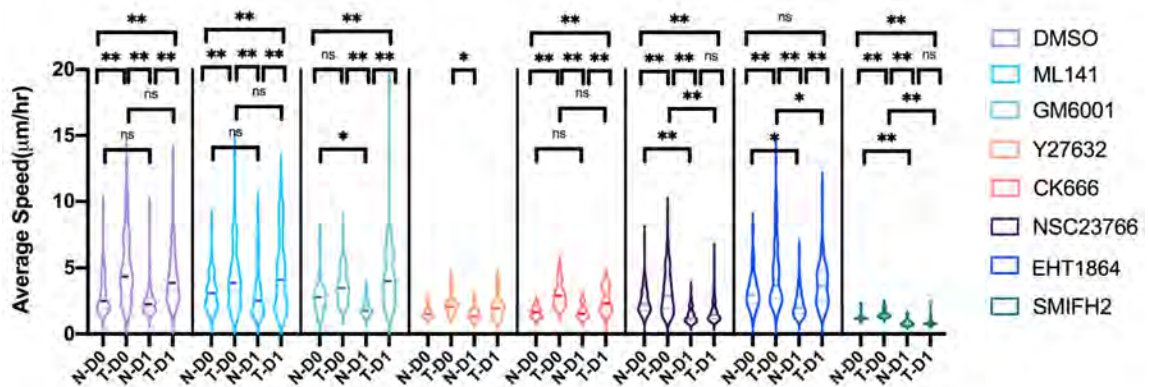


Figure 4.25: **Fast migration of MDA-MB-231 in thick collagen requires coordinated contractility and protrusions but not MMPs.** (A). Rearranged violin plot of average speed in supplementary to Figure4.22.B.

brane, MCF10A undergo differentiation and growth arrest and develop into acinar structures that recapitulate many features of normal breast epithelial cells. MDA-MB-231 and MCF10A are usually deemed as two poles of epithelial-mesenchymal transition.

MCF10A single cells demonstrate respond to thick collagen as well, though not as dramatic as MDA-MB-231(Figure4.26.A). Higher number of MCF10A cells in thick collagen are elongated and less spherical and compact, resembling a mesenchymal cell type. In contrast to MDA-MB-231's irregular protrusion patterns (as indicated by shape variance distribution in Figure 4.12.F) induced by thick collagen architecture, MCF10A single cell only transition from round to more elliptical without producing any protrusions(as indicated by the highly concentrated distribution of shape variance in Figure4.26.B and Figure4.26.C). Also, MCF10A is not only sensitive to thick collagen architecture but also influenced by collagen density(Figure4.26.C).

In consistence with the morphological transition, MCF10A have increased invasiveness in thick collagen as shown in Figure4.27.EF. MCF10A migrate significantly faster(Figure4.26.E) and persistent (Figure4.26.F) in thick collagen than 1mg/ml or 2mg/ml collagen.

Surprisingly, MCF10A acini when seeded in thick collagen also demonstrate significant morphology change compared with normal collagen. Invasive branches shoot out from the acini and pull the collagen patches nearby dramatically(Figure4.28.G). In contrast, MCF10A acini seeded in normal collagen are more quiescent and less collagen pulling is manifest. MCF10A acini generate protrusive cell strands in response to mechanic force has been documented by previous study[36].

Collagen pulling is not limited to MCF10A acini but also observed in single cell. In our whole-well overview tilescan imaging(Figure4.29.H,Figure4.30). Morphological change happens is universal across entire well accompanying the collapse and detachment of the thick collagen bundles from the well wall.

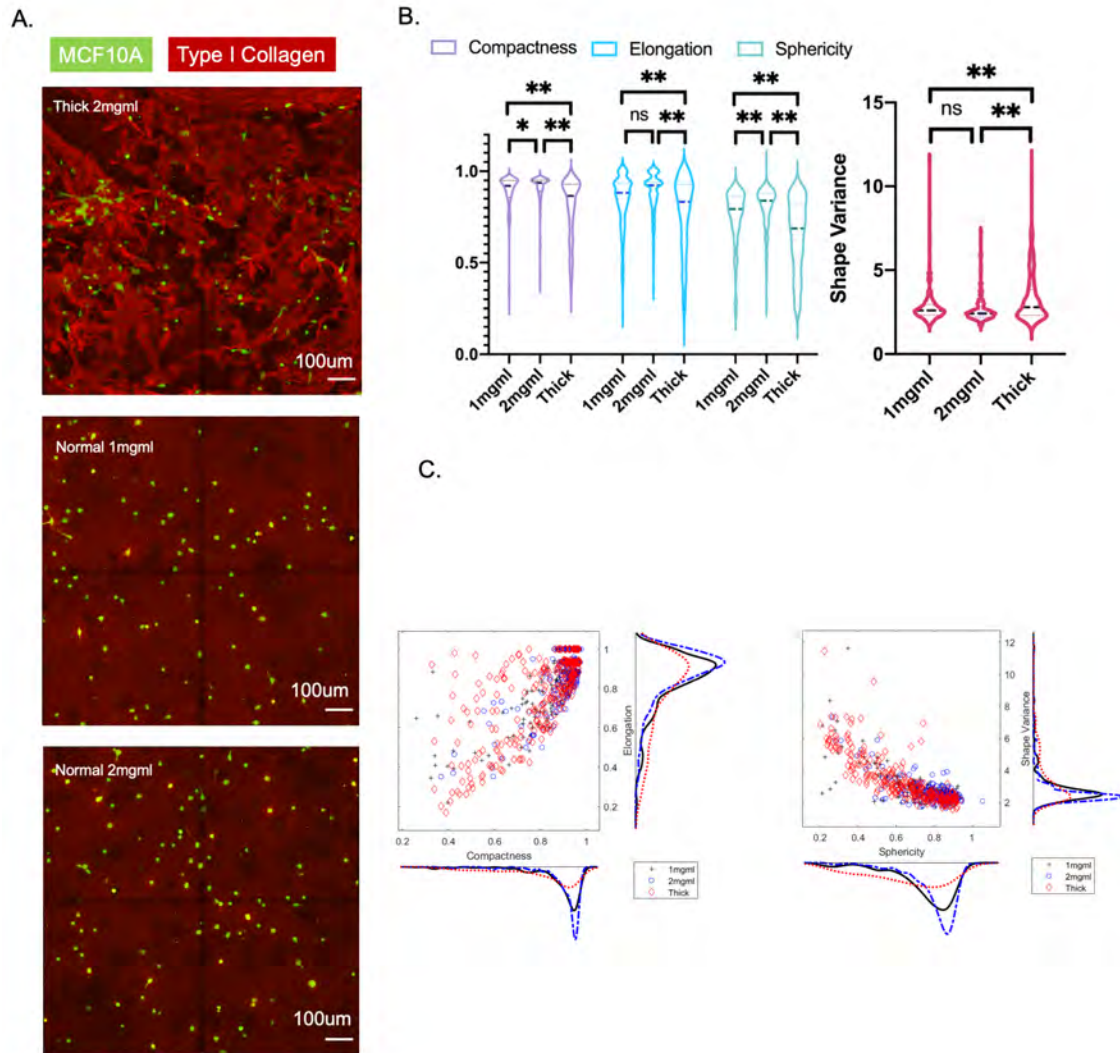


Figure 4.26: **Non-metastatic MCF10A pick up invasive phenotype in thick collagen** (A). Projected confocal imaging of MCF10A in thick collagen, 1mg/ml and 2mg/ml normal collagen. (B). Compactness, elongation, sphericity, and shape variance index of MCF10A in different conditions. (C). MCF10A cell population distribution is projected on the axis of elongation, compactness, shape variance, and sphericity.

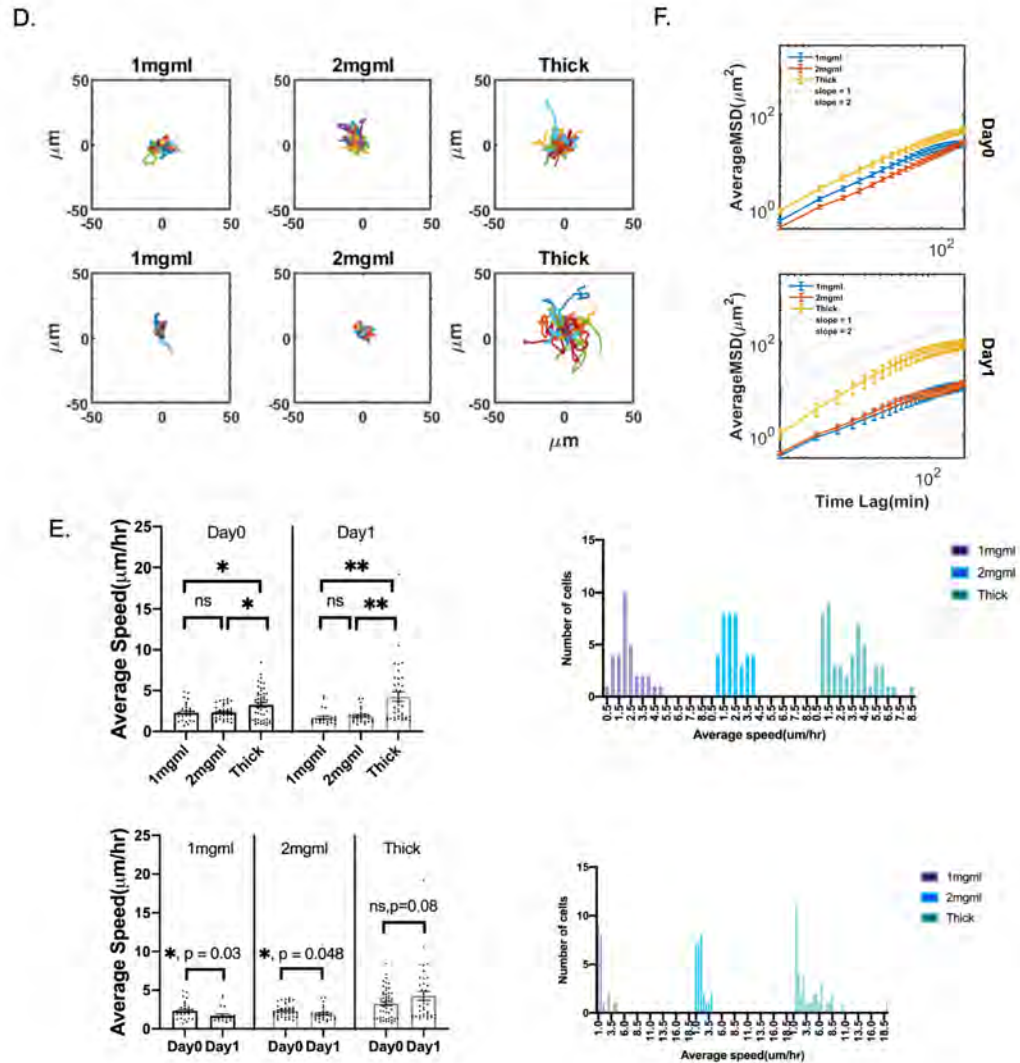


Figure 4.27: **Non-metastatic MCF10A pick up invasive phenotype in thick collagen** (D). Overlaid migration trajectories of MCF10A on day0 and day1. (E). Average speed of MCF10A on day0 and day1. (F). Average mean squared displacement of MCF10A on day0 and day1.

G.

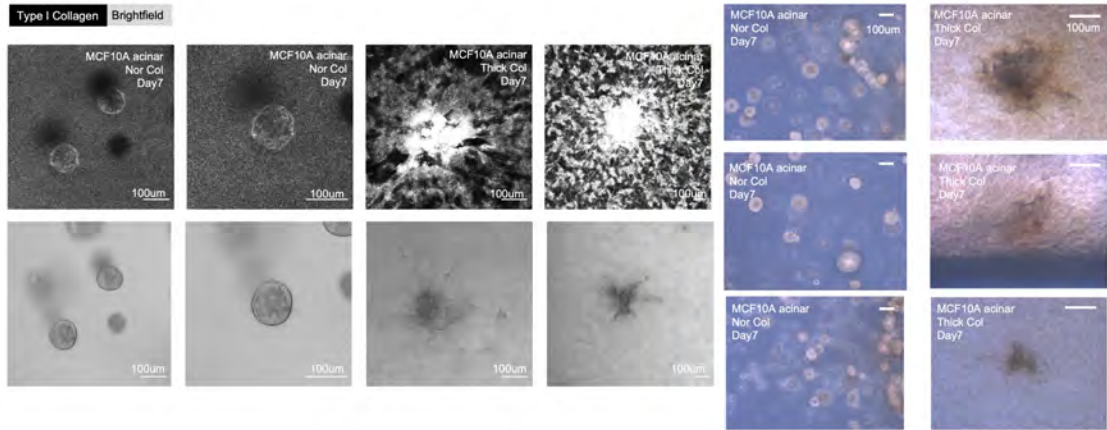


Figure 4.28: **Non-metastatic MCF10A pick up invasive phenotype in thick collagen (G).** Day4 old MCF10A acinar in normal versus thick collagen on day7(3 days after collagen embedding). Reflectance imaging is shown to demonstrate collagen thickening as a result of MCF10A acinar contraction.

4.4.7 Molecular signatures underlie MCF10A transition

To elucidate the molecular mechanism underpin the MCF10A transition in thick collagen, immunofluorescence imaging of E-Cad(unpublished data), N-Cad(unpublished data), YAP/TAZ, vinculin, pMLC was collected.

YAP/TAZ is a sensitive mechanosensor and its relative nuclear/cytoplasmic localization is regulated by substrate rigidity[183]. YAP/TAZ accumulate more in nucleus when cell stretch out on substrate of high rigidity and more in cytoplasm when cells are in confinement or less spread out.

Our YAP/TAZ quantification indicate that both MCF10A single cells and MCF10A clusters, MCF10A have higher nucleus/cytoplasm ratio in thick collagen versus normal collagen(Figure4.31.A), consistent with existence of the highly stretched MCF10A clusters in thick collagen. However, the nucleus/cytoplasm ratio among all conditions are close to 1, also in agreement with rheometry data(not published).

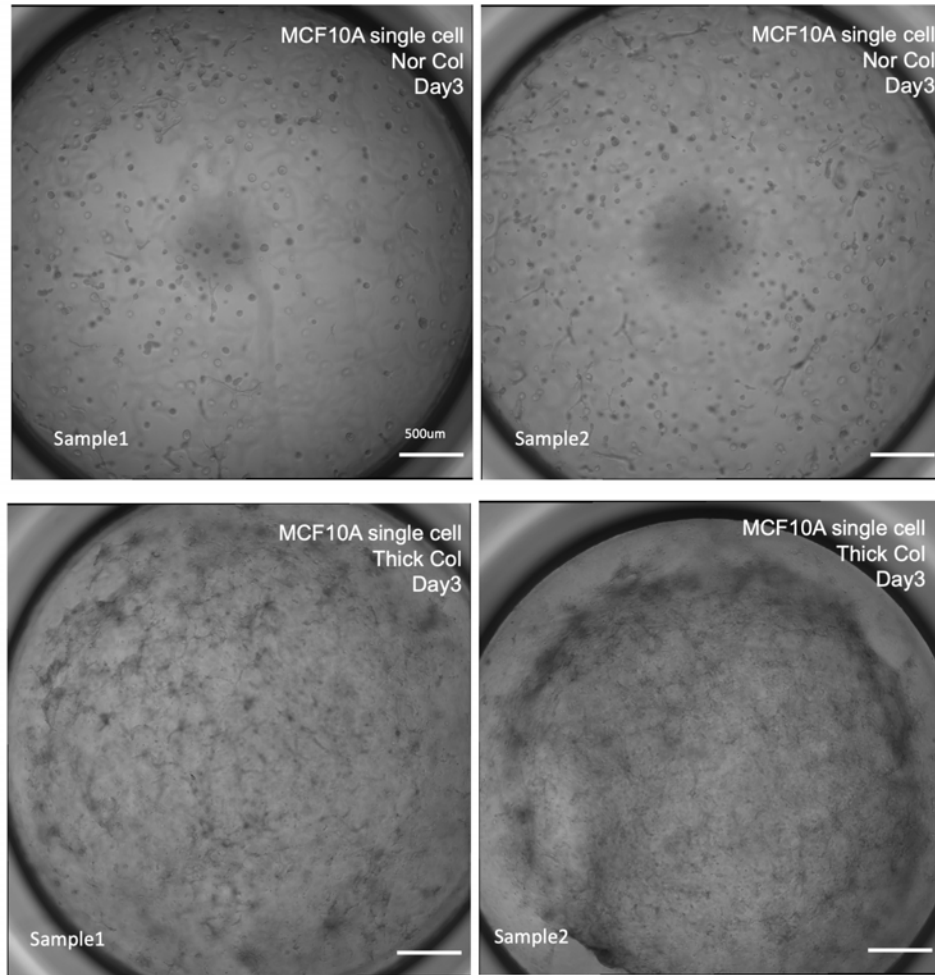


Figure 4.29: **Non-metastatic MCF10A pick up invasive phenotype in thick collagen (H).** MCF10A single cell seeded in normal collagen developed into round or extended cell clusters on day3. MCF10A single cells seeded in thick collagen manifest an invasive phenotype, and almost no round cell clusters can be observed. In addition, the global contraction of thick collagen network happens.

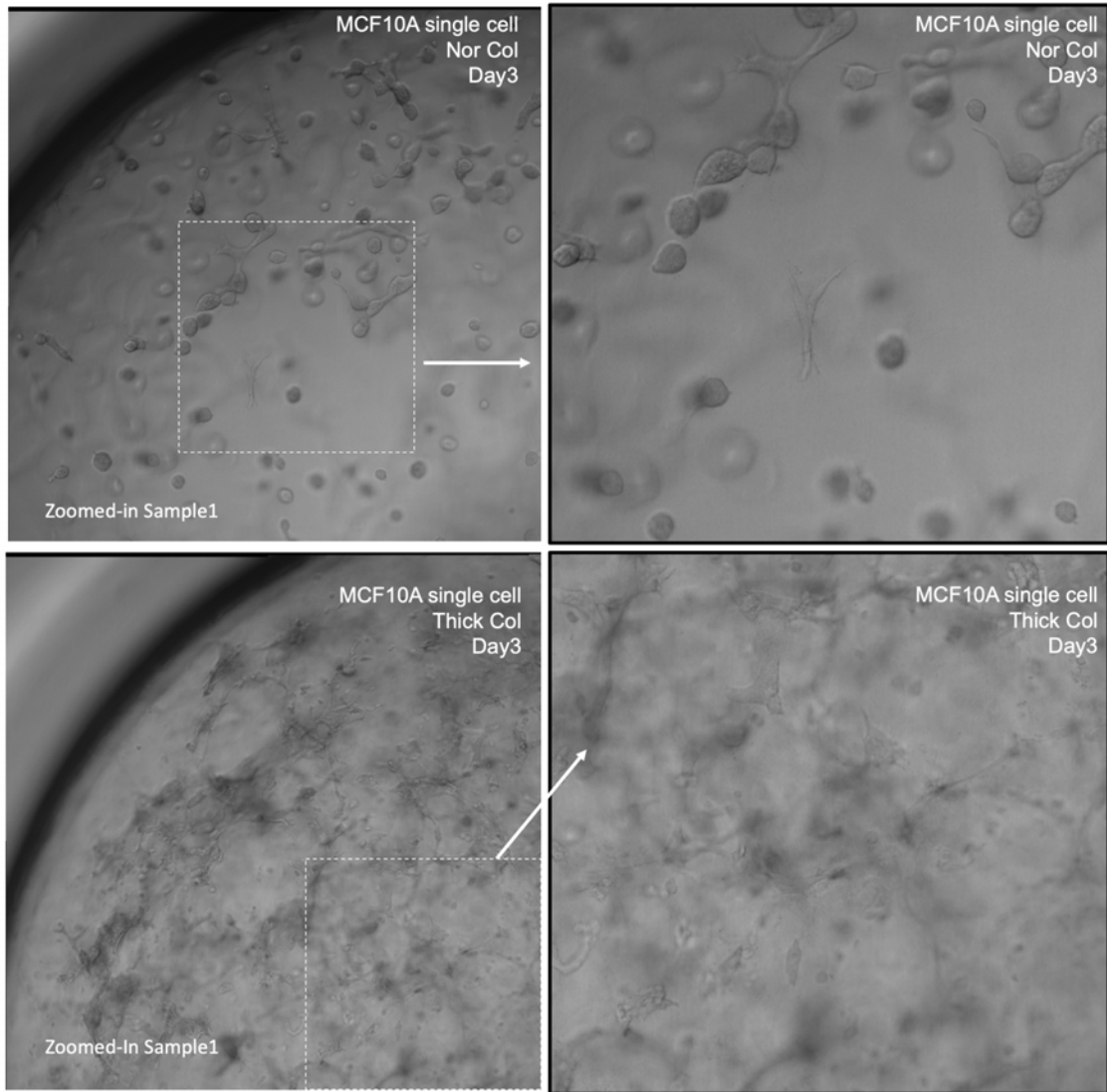


Figure 4.30: **Non-metastatic MCF10A pick up invasive phenotype in thick collagen**
Zoomed-in view of Figure 4.29

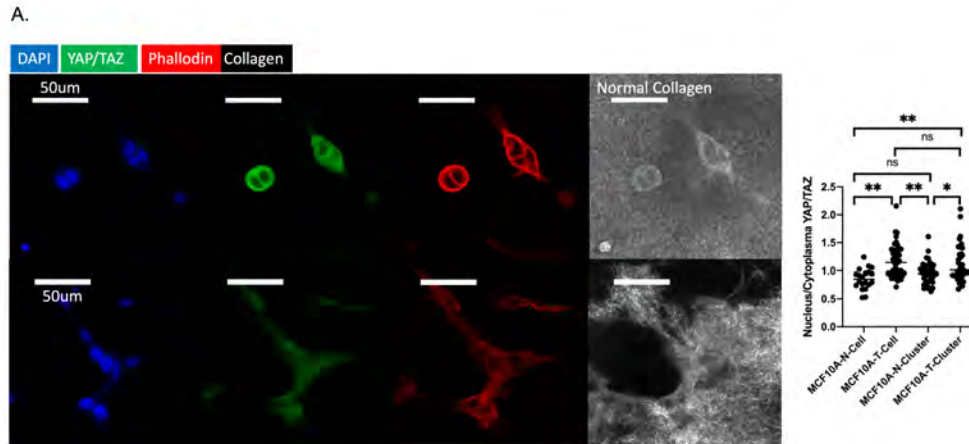


Figure 4.31: **Molecular signatures underlie MCF10A transition** (A). YAP/TAZ localization in MCF10A single cell and clusters at day4.

Vinculin is a frequent marker for both intercellular and cell-ECM adherens. Vinculin is highly expressed in MCF10A clusters in both collagen conditions. In the invasive strand from MCF10A cell cluster, vinculins (dot-like structure as indicated by the red arrow, Figure4.32.B) are found colocalized with collagen pulling. This indicate the collagen pulling observed in Figure4.29 and Figure4.30 is linked to focal adherens.

pMLC is a direct marker for cell actomyosin based contractility. Figure4.33.C demonstrate that in thick collagen where large gel patch contraction happens, increased pMLC can be observed. This indicate the collagen pulling observed in Figure4.29 and Figure4.30 is linked to cell contractility.

4.5 Discussion

In this work, we introduced a fast and reproducible protocol that allows manipulating mesoscale architecture without additional devices or mixing different gel species. The introduction of the this type of thick collagen has opened several windows and also highlight several important directions in near future. The first window that is opened is the

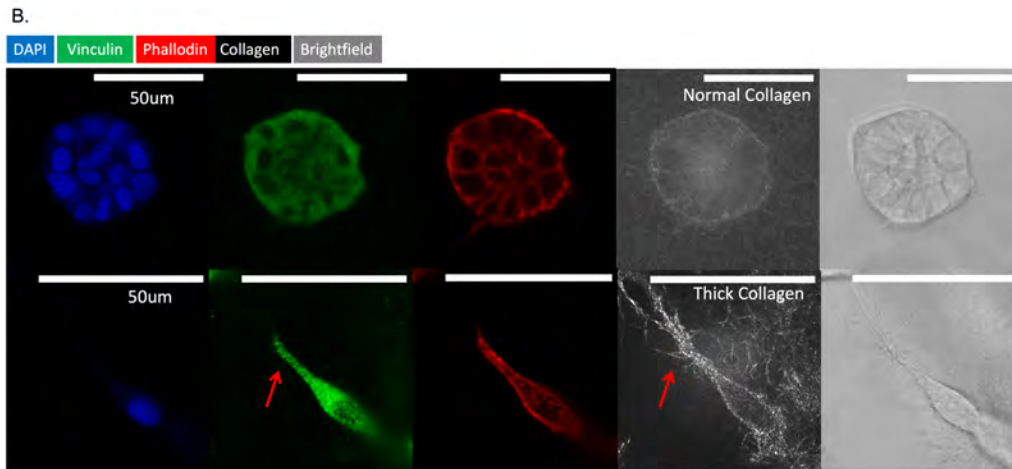


Figure 4.32: **Molecular signatures underlie MCF10A transition (B)**. Immunofluorescence staining of vinculin in normal versus thick collagen. The red arrow indicates the colocalization of vinculin and collagen pulling. Quantification of colony expansion among all six conditions, "MG_NorCol_12hrs" indicates MDA-MB-231(lifeact-GFP) in normal collagen post 12hrs gel embedment. "MG_ThickCol_12hrs" indicates MDA-MB-231(lifeact-GFP) in thick collagen post 12hrs gel embedment. "MG_F_ThickCol_12hrs" indicates MDA-MB-231(lifeact-GFP) cocultured with NHLF in thick collagen post 12hrs gel embedment. The other three conditions are the same except for data taken at 36hrs post gel embedment.

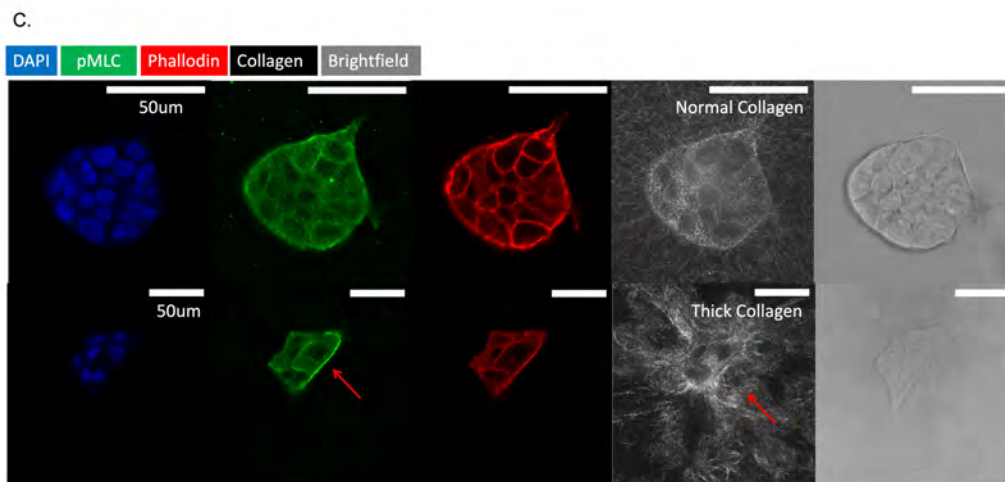


Figure 4.33: **Molecular signatures underlie MCF10A transition (C)**. Phosphorylated-MLC staining in normal versus thick collagen. The red arrow indicates the colocalization of phosphorylated-MLC with the collagen pulling(alignment).

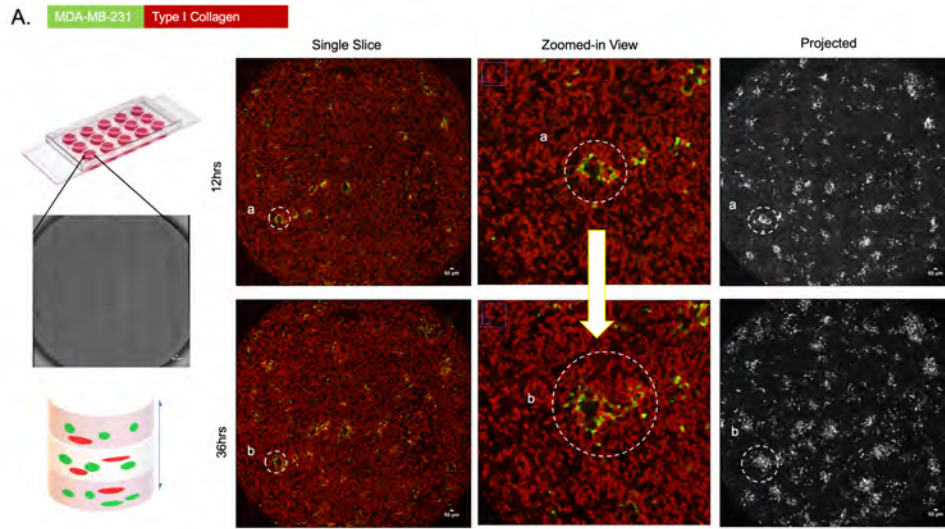


Figure 4.34: **Thick collagen applied in MDA-MB-231 and NHLF coculture (A).** The fast invasion of MDA-MB-231(lifeact-GFP) in an overview tilescan imaging. The tilescan imaging tracks the expansion of each single cell colony along time. MDA-MB-231(lifeact-GFP) fast "diffuse" along thick collagen bundles from 12hrs post gel embedment to 36hrs post gel embedment.

modulation of collagen properties through fibrillogenesis intervention. Fibrillogenesis not only can be tuned by temperature, buffer pH but also by external stirring force. Actin-polymerization not only can be modulated chemically but also mechanically. Intriguingly, the thickened collagen bundles formed under external mechanic shearing demonstrate high similitude with in vivo ECM architecture, especially dermal collagen. We also proposed a hypothetical mechanical model (Figure 4.39) that may explain the elevated activities for cells cultured in thick collagen. In this model, we propose that local thick collagen may provide local stiffness that help anchor cell body while long distance force transmission is mediated by force fiber. In this way, the intercellular mechanosensing stimulates cell migration.

The second window opened by thick collagen is the readjusted view on MMPs in tumor microenvironment. Most previous reports of tumor cell migration in 3D collagen are based on conventionally gel collagen, which result in an emphasis of collagen degradation

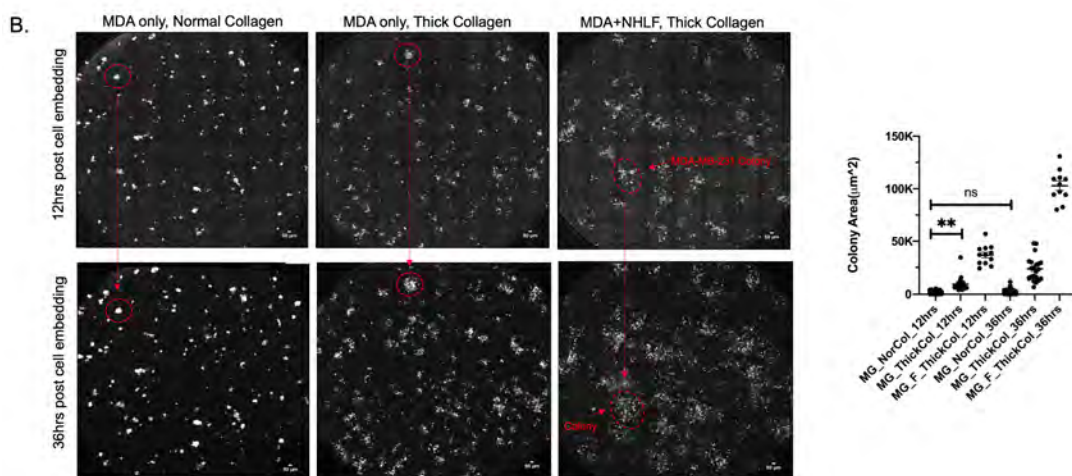


Figure 4.35: **Thick collagen applied in MDA-MB-231 and NHLF coculture (B).** The projected entire well tilescan imaging at 12hrs and 36hrs post gel embedment. The same ROI were taken that allows accurate track of colony expansion in 24hrs. In MDA-MB-231+NHLF coculture condition, MDA-MB-231 and NHLF were seeded at 200K/ml and 50K/ml, respectively.

and proteolytic behaviors in tumor migration[55, 184, 185, 186]. Some work demonstrated that[69]aligned collagen matrix can induce MMP-independent invasion. Some work notice that physical limits or steric restraints[48, 154] of collagen greatly impacted cell behavior. In our scenario, the independence of MMPs of cell migration may partially arise from the reduced physical restraints. Interestingly, our result once again agrees with intravital work[174] that the migration of breast tumor is MMP independent. This may evidence the land-sliding failure of MMP inhibitors in clinical trials[187].

More importantly, thick collagen, instead of normal collagen, help to differentiate and augment drugs' subtle impacts in cell morphology. In normal collagen, GM6001,ML141, SMIFH2, NSC23766, EHT1864 appear to exert exactly the same effects on cell morphology(all cells are round) due to the compounding effect of physical restraints. However, MDA-MB-231 cells in thick collagen clearly fall into two subgroups: GM6001/ML141/EHT1864 versus SMIFH2/NSC23766(Figure4.22.B). GM6001/ML141/EHT1864 all fail to inhibit

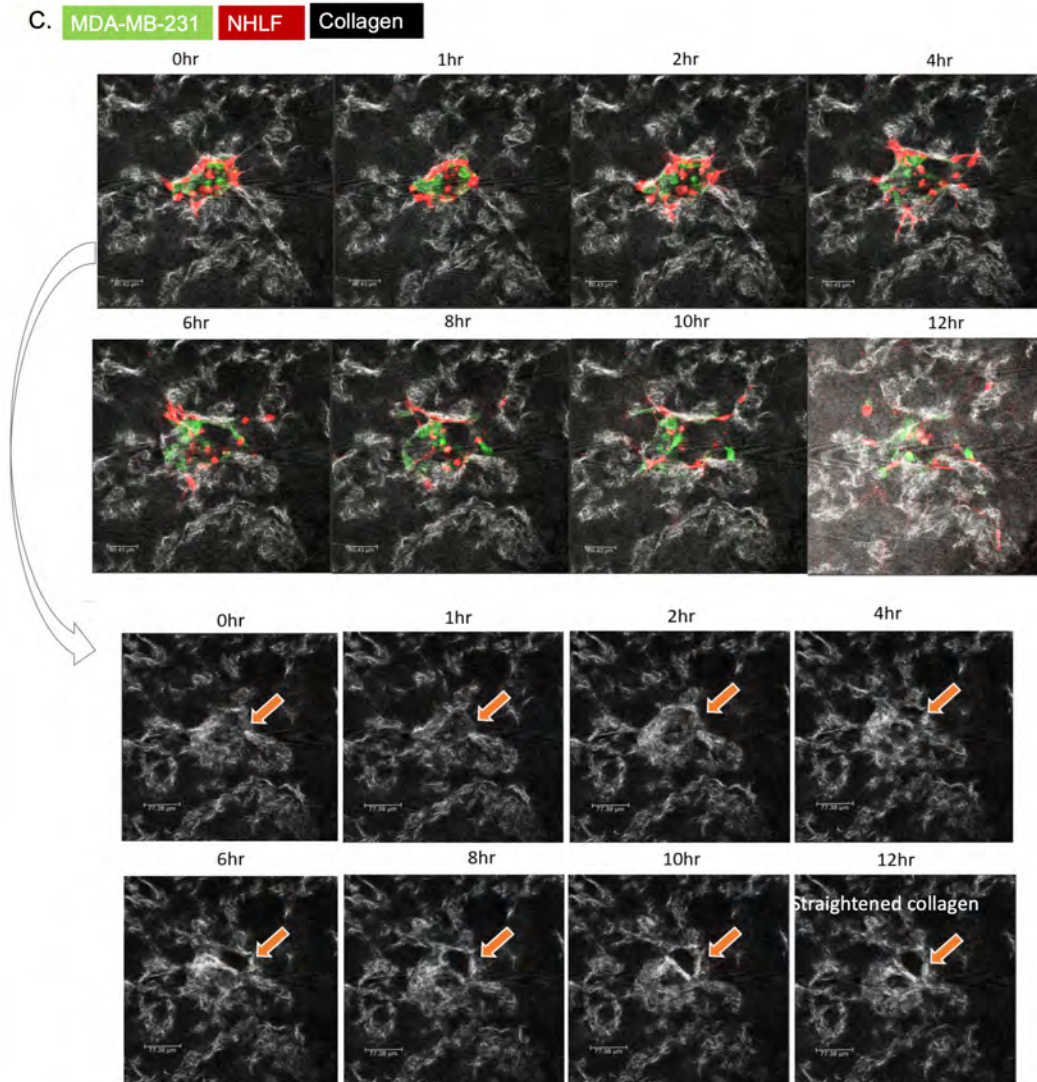


Figure 4.36: **Thick collagen applied in MDA-MB-231 and NHLF coculture (C).** Both NHLF and MDA-MB-231(lifeact-GFP) spread out fast in the first 12hrs after gel embedment. NHLFs pull and align thick collagen bundles, result in straightened collagen bundles.

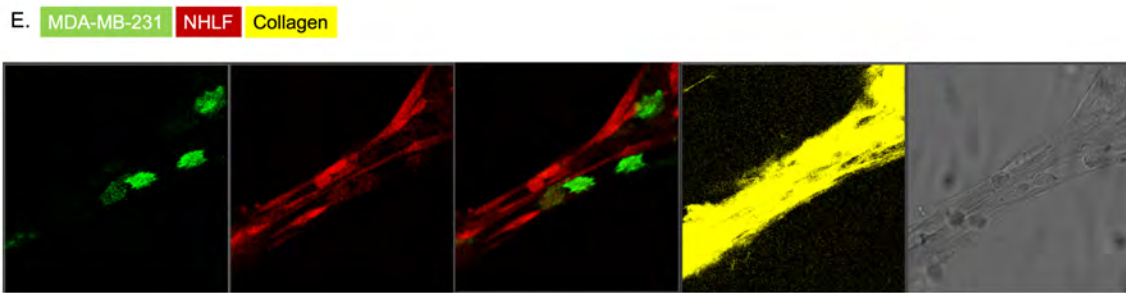


Figure 4.37: **Thick collagen applied in MDA-MB-231 and NHLF coculture (E)** Long and thick collagen bundles can be formed when a high density of NHLFs are present(600K/ml). In addition, fast MDA-MB-231 (lifeact-GFP) migration can be observed along this highly stretched "collagen bridge".

the protrusive structures and elongation of cell body whereas NSC23766, SMIFH2 abolish membrane ruffling completely. However, NSC23766 and SMIFH2 treatment result in similar morphology but discernible differences still can be told in fluorescence imaging(Figure4.22.B). NSC23766 treated cells are smaller than most other drug treated groups without proliferation and expansion on day2. SMIFH2 treated cells lack of F-actin accumulation on the cell periphery. In addition, we notice that morphology distribution of DMSO, GM6001, EHT1864, ML141 treated cells are almost identical regardless of which morphology index the data are projected onto. As collagen architecture is the driving factor in these groups. We highly speculate that there is a specific subpopulation of MDA-MB-231 cells responding to the architectural change. More importantly, the percentage of this specific subpopulation is fixed. This points out that MDA-MB-231 is composed of heterogeneous subpopulations. The almost identical morphological distribution across multiple conditions also indicate that the morphological changes are more likely dominated by the

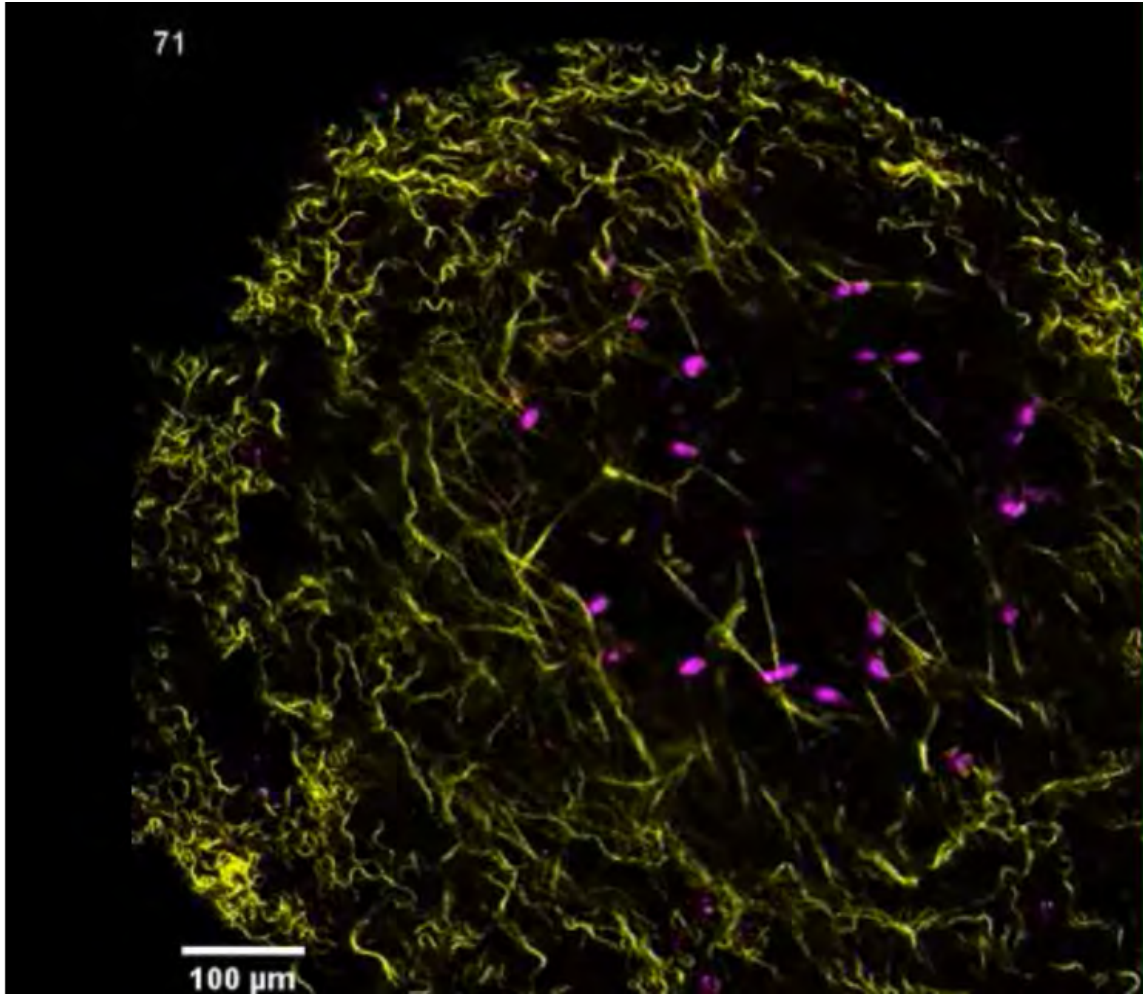


Figure 4.38: **Straightened collagen in vivo** Combined SHG and two-photon imaging of intradermal tumor. Yellow shows collagen SHG, magenta shows tumor cell nuclei (DAPI). Movie shows z-plane series, z distance from top plane shown in upper left, scale bar shown in lower left. Figure adopted from paper[46]

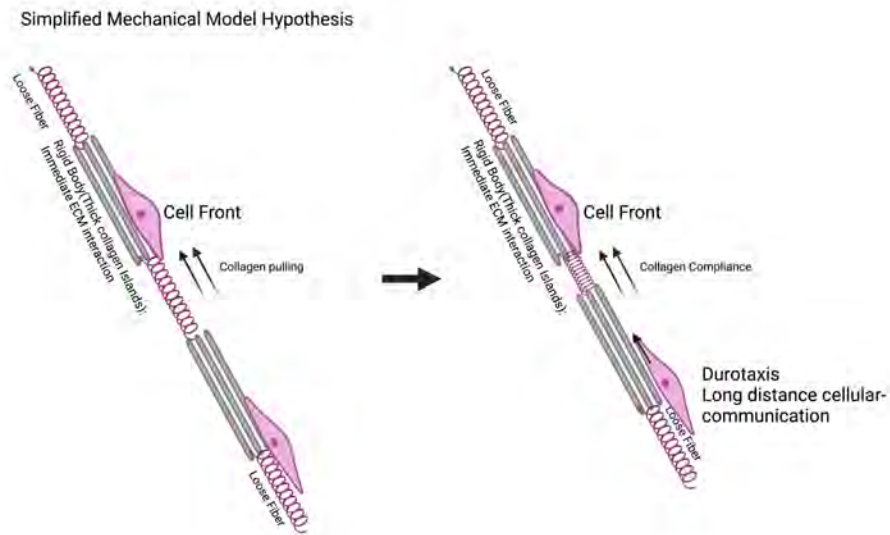


Figure 4.39: **Graphic abstract**

global mechanical feature shared by every single well, instead of the microscale local heterogeneity. In the coculture experiment, we notice that MDA-MB-231 when cocultured with NHLF migrate much more in thick collagen. In the nest of MDA-NHLF cells, NHLF quickly stretches fibers which trigger the movement of MDA cells(Figure4.28). Similar straightened collagen fiber has been reported before(Figure4.38). MDA cells following behind NHLF cells.Meanwhile we also notice that fibroblast can recruit macrophages by dynamic[38], And fibroblasts are activated by microarchitecture[148, 47]; It is like that this happens in this environment as well. Tensile stretching is important[188, 189]. Thus in the near future, more attention should be focused on mesoscale or global scale mechanical sensing need to investigated and also fabricating ECM not only captures spatial architecture but also restore the adequate mechanical property. Fibrillogenesis intervention may provide a good option.

4.6 Future Directions

The application of the thick collagen is wide. The first and most important direction is to apply thick collagen in wound healing model, as its high similarity with collagen architecture in wounded skin. Besides our unpublished data has shown thick collagen can activate normal fibroblasts which bolster the use of this collagen in wound healing in vitro models. The second direction should go towards the stem cell differentiation. It would be equally interesting to see what type of cell we can induce with such collagen architecture. Thirdly, we can apply this collagen in sparse primary cell culture. The idea is that, if one type of collagen is rigid enough locally to allow cell cytoskeleton rearrangement but also allows long distance force mediated communication, then cell may "sense" each other even sparsely located in a gel. To culture sparse primary cell may facilitate many clinical cell therapy which heavily relies on in vitro amplification of human derived primary cells. Besides the wide application of thick collagen bundles, we are also looking forward to adjusting the protocol to make different collagen that further mimics in vivo collagen through fibrillogenesis. Surface modifications etc can be used afterwards.

Chapter 5

Dictating cell movement and shape by light

5.1 Abstract

Three types of Rho GTPases, RhoA, Rac1 are in the central position in regulating cytoskeleton dynamics and cell migration. Most previous observations on cell migration and movement are through 2D spatial-temporal control of these GTPases. Here we report the role of each these molecules in a 3D fibrillar collagen gel. We notice that RhoA can be activated as long as cell is round and floating in gel. Activation of RhoA causes a "squeezing" effect on cell body. Fast and strong RhoA activation triggers large scale membrane ruffling at the front of cell body. Rac1 instead of RhoA is associated with cell peripheral collagen densification. More observations are shown as below.

5.2 Materials and methods

5.2.1 Cell Culture

MDA-MB-231 cells(ATCC,HTB-26™) or MDA-MB-231 cells(lifeact,mCherry) were cultured in DMEM with 10% fetal bovine serum (FBS) and 1% Pen-Strep. Mel624 were maintained in DMEM supplemented with 10% FBS, 1% Pen-Strep,1% Sodium Pyruvate, 1% Hepes buffer. Cells were all incubated at 37°C and 5% CO₂.

5.2.2 Plasmid Extraction and transfection

Photoactivatable Rac1(22027)), Cdc42(75263) and RhoA(80406 and 80408) plasmids are purchased from Addgene. Plasmids are extracted by Qiagen plasmids Midi kit(12143 and 12145 following standard protocol. Extracted plasmids were DNA sequenced to verify the correctness of target DNA segments before transfection. Lipo3000 were used for plasmids transfection. 48hrs after transfection, cells were harvested and seeded in 2mg/ml neutralized rat tail type I collagen gel same way as previous chapters with 20min gelation. Transfected cells were handled strictly without light exposure. Light activation experiments were conducted after gel embedment and finished within 8hrs post gel embedment.

5.2.3 Local light activation

Local activation is conducted with Leica SP8 confocal microscope. For RhoA study, cells were excited with 1% 488nm laser with time interval of 20 seconds and duration of 5min. Experiments of different excitation patterns were carried out. For the Rac1 study, cells were excited with 1% 488nm laser with time interval of 10 seconds and duration of 10min or 20min. Fluorescent stained collagen is used in Rac1 study to show the collagen wrapping around cell near Rac1 excitation site.

5.2.4 Microchannel fabrication

Device masters were fabricated at the Yale School of Engineering and Applied Science cleanroom. Microfluidic devices were fabricated based on standard photo- and soft-lithography techniques (Li et al., 2017; Mak et al., 2011). The photomask with channel pattern was drawn by Layout Editor. Briefly, SU-8 (SU8-2015, Newton) was spin-coated on a silicon wafer and exposed under the photomask. The wafer was then developed to create a negative pattern. Mixed polydimethylsiloxane (PDMS) (Sylgard 184, Dow Corning) with a weight ratio of 10:1 was poured onto the master. The PDMS mold was then peeled from the wafer and bonded to a glass coverslip.(Microchannel fabrication credited to Xingjian Zhang).

5.2.5 Drug Study

Drugs were reconstituted and stored following manufacturers' recommendation and diluted in culture medium to work concentrations. 5uM CytochalasinD, 30uM Y27632, 10uM ML141(Calbiochem@217708), 50uM CK666(Abcam, ab141231), 100uM NSC23766, 20uM EHT1864(Cayman 17258) were used. In drug study, cells were seeded in around 2mg/ml deep ester dye stained collagen first and drugged medium were added after 1hr gelation. Cells were imaged after 12hrs incubation.

5.3 Results

5.3.1 RhoA activation is linked to cell membrane ruffling in 3D

The first phenomenon that we noticed when locally activating RhoA is that we can control cell shape by controlling excitation patterns as shown by Figure5.3.1. Local F-actin accumulation is colocalized to increased RhoA activation. MDA-MB-231 or Mel624 showed

similar response rate (data not shown). All cells responded to light activation by changing shape within 10 secs (judged by eye). All cells are excitable and demonstrate consistent response to the excitation patterns. While MDA-MB-231 cells were excited, membrane ruffling took place at the "non-squeezing" area, suggesting that the cell contents are pushed outward during "squeezing" and caused the membrane ruffling.

Interestingly, cells respond differently to laser intensity settings. When set to a high laser power (1.5% 488), fast and strong blebbing happens immediately (Figure 5.2.A, Figure 5.3) and the position where blebbing happens seems to be associated with nucleus position (Figure 5.2.B). In addition, cells always restore to their original shape before squeezing, no matter after how many rounds of squeezing. It appears that cells have memory of their original shape (Figure 5.4).

Often, the contraction of the cell rear is accompanied with the movement of the cell front. Thus, it looks like we manage to "push" cells forward by exciting the Local RhoA at the cell rear multiple rounds (Figure 5.5). However, due to the complex collagen architecture and the ensuing physical restraints, we managed to push cells forward consistently but also cell movement is often impeded (Figure 5.5). Polystyrene beads were added in the gel to provide spatial reference to demonstrate how far cells can migrate in each round (Figure 5.6).

When quantifying the diameter of the constriction ring between the opposing squeezing sites, we noticed that Mel624 does not concave as much in comparison with MDA-MB-231 (Figure 5.7). Interestingly, Mel624 does not move as much in thick collagen as described in chapter 34 and also does not increase migration speed when in coculture with NHLF2. I have no idea if anyone is going to read this part of the thesis. But this is an Easter egg. I think Mel624 cell body is more rigid (change shape less in response to RhoA activation, let's assume maximum RhoA activation happens in this experiment for each cell), which also highly suggests Mel624 is less contractile than MDA-MB-231. Cell contractility is ultimately decided by how fast cells can rearrange cytoskeleton. The contractility

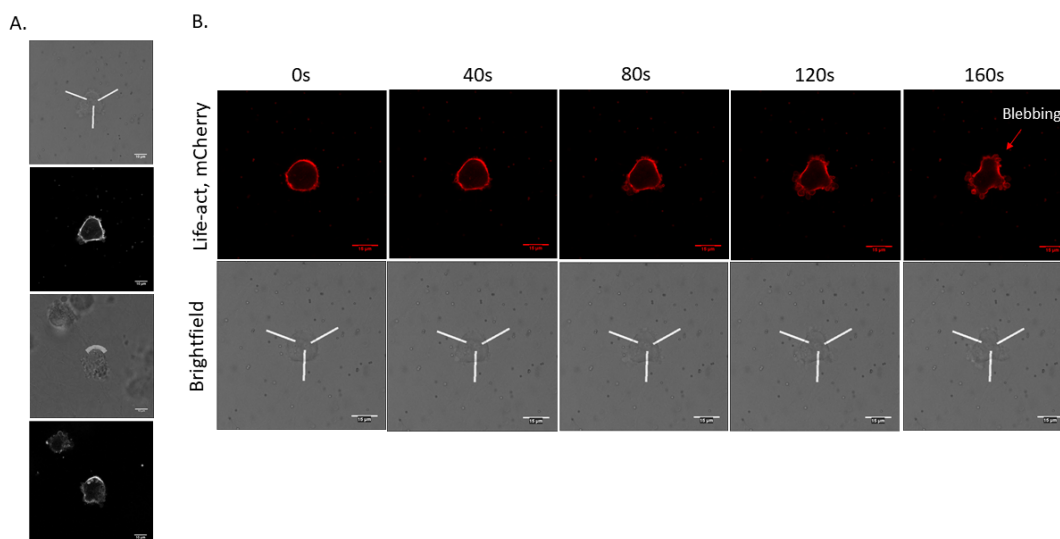


Figure 5.1: **RhoA activation can control cell shape** A. Cell shape can be controlled by adopting different excitation patterns. B. MDA-MB-231 respond to light activation within 20sec. Cell membrane ruffling can be seen at "non-excitation" region.

differences decide MDA-MB-231 is more sensitive to spatial architecture. This experiment also suggests that, this RhoA activation is a potentially good method to test cell body rigidity. However however however, we are not sure how much whether the transfection efficiency influences the interpretation. But in this research, Mel624 has much higher transfection efficiency than MDA-MB-231, which possibly exclude this possibility. In the end, we also tried RhoA activation in microchannels, which is physical limit free. As expected, Mel624 cell thrust forward fast upon rear RhoA activation within first 20 seconds. After cells moved away from excitation beam, cells usually glide on until to a full stop(Figure5.8).

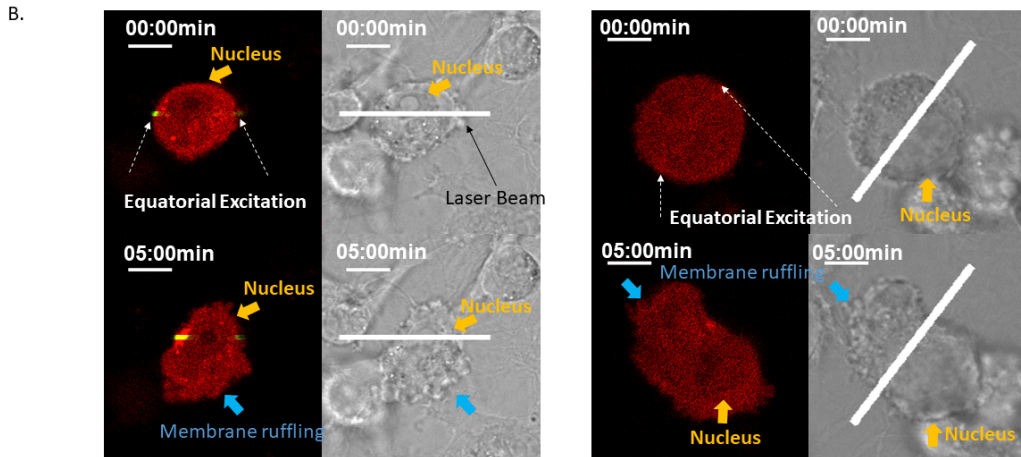
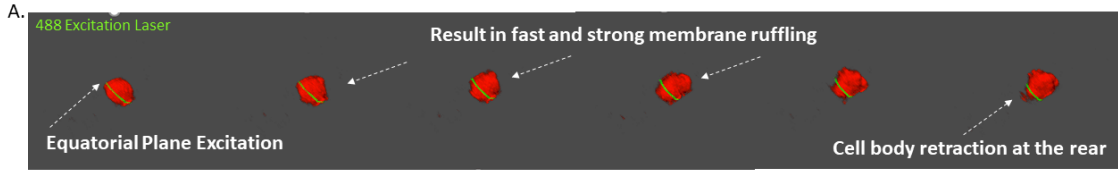


Figure 5.2: **Intensive(1.5%488) RhoA activation induces membrane ruffling at cell front** A. 3D reconstructed video during excitation process. When the laser was set to scan the equatorial plan of the cell, large scale blebbings(membrane ruffling) emerged accompanying fast retraction of cell rear. B. Cell membrane ruffling often takes place on the cell membrane that is opposite direction to nucleus position.

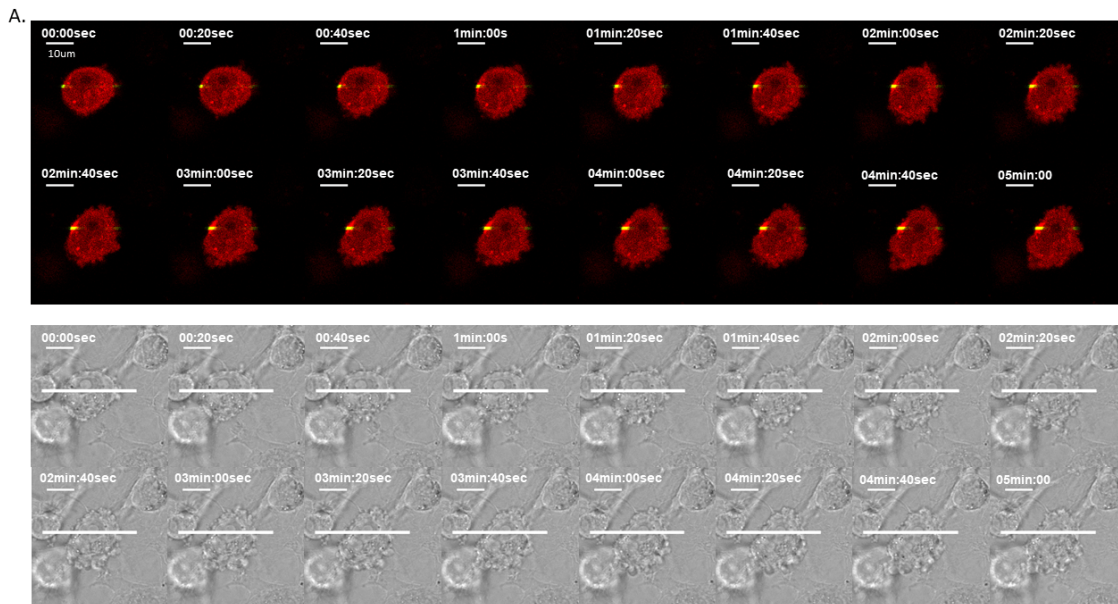


Figure 5.3: **Large scale membrane ruffling take place when RhoA is activated at the cell rear**

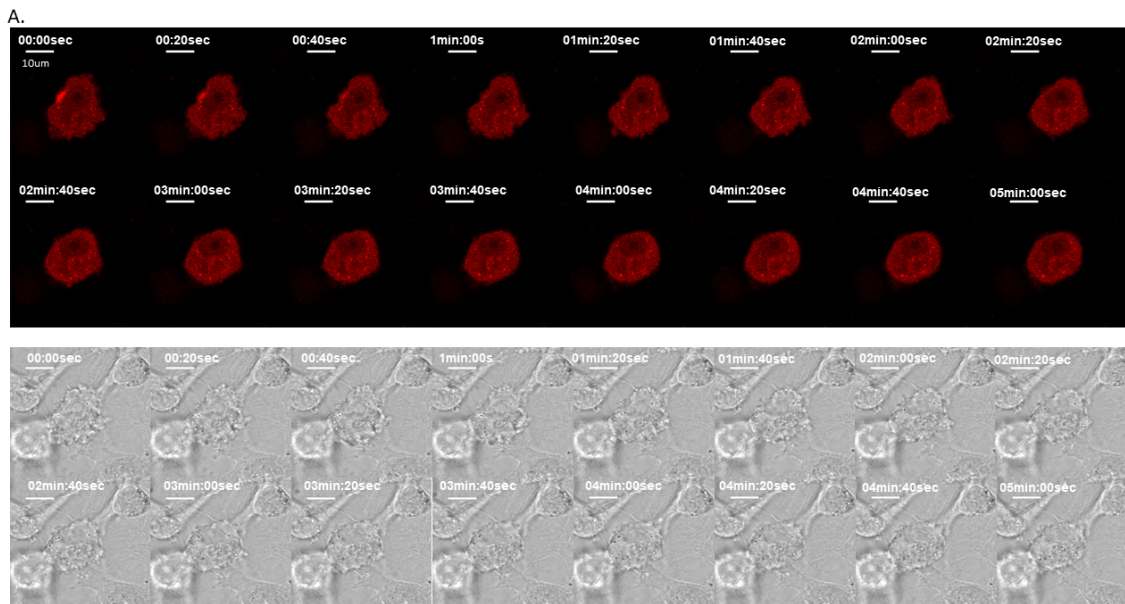


Figure 5.4: Cell shape has memory: Cells restore to its original shape within 1 to 2min after each round excitation

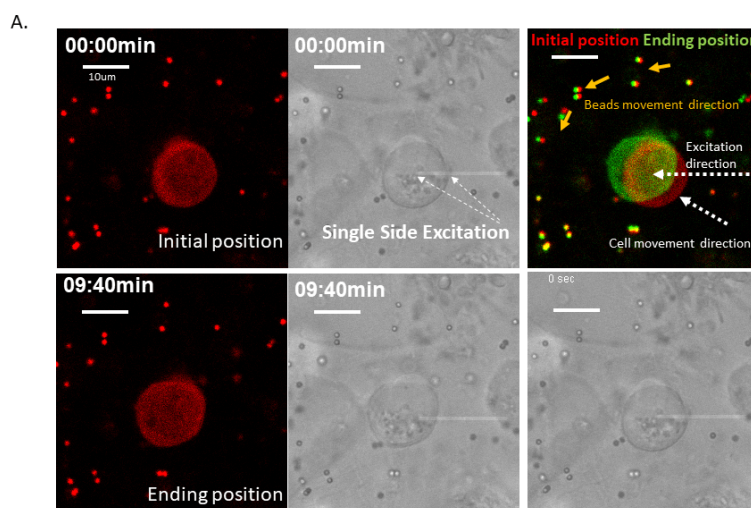


Figure 5.5: RhoA activation at the cell rear pushes cell forward A. When the initial position and ending position is overlaid, we can see clearly how cell position changed before and after squeezing.

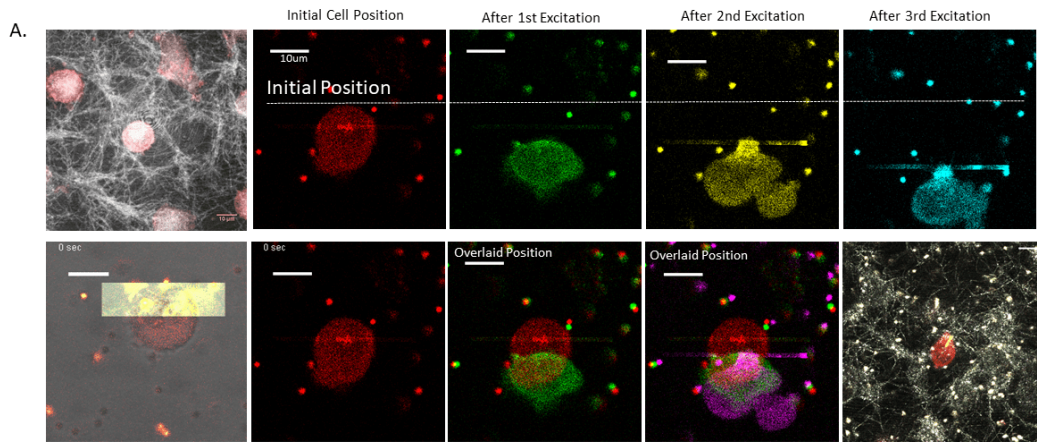


Figure 5.6: **Consistent cell migration after several rounds of squeezing at the cell rear**
 A. Cells can be squeezed forward consistently, though the movement is hindered by the physical restraints imposed by collagen architecture.

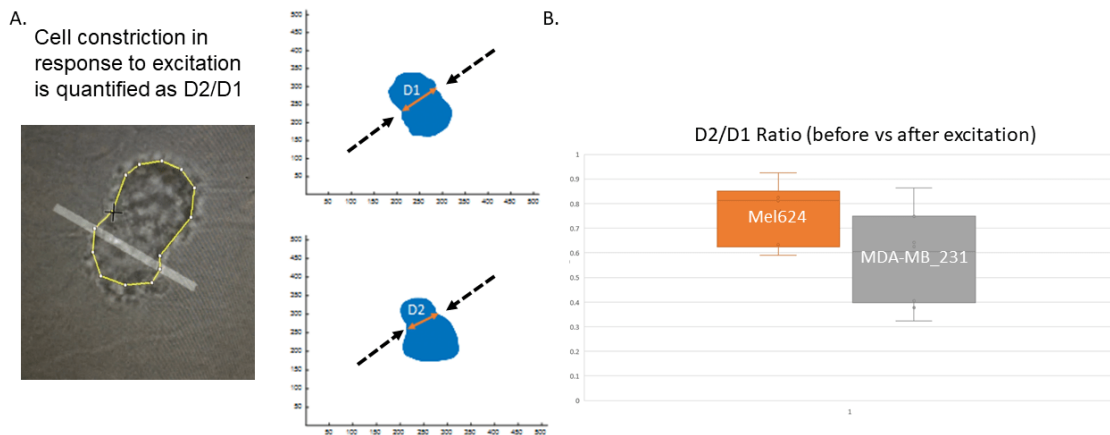


Figure 5.7: **Cell body rigidity varies from cell line to cell line** A. How much cell can be squeezed is quantified by the ratio between D2/D1. MDA-MB-231 can be squeezed more than Mel624 cells.

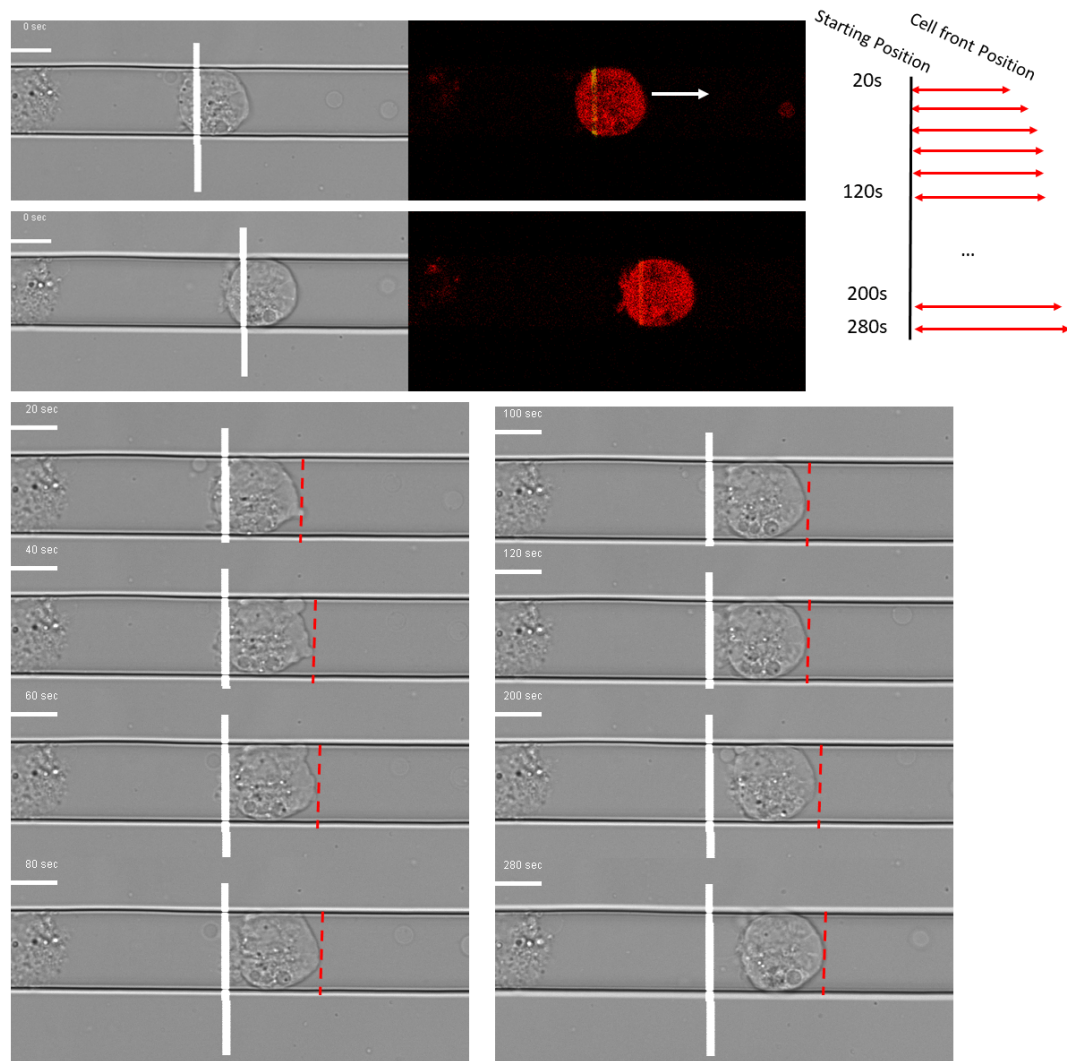


Figure 5.8: **RhoA activation at the cell rear fast push cell forward in microchannel**
 When Mel624 cell is RhoA-activated at the rear, cell body thrust forward suddenly during first 20seconds, moved away from excitation beam, and then slide in the channel until to a full stop.

5.3.2 Rac1 not RhoA activation is associated with cell periphery collagen densification and possibly short-term intercellular communication

After a series of tests on RhoA activation, we then switched to Rac1 activation. We firstly noticed that Rac1 local activation is directly associated with cell periphery collagen densification. Upon Rac1 activation, large scale protrusions emerge from the activated region and grope forward and pulling collagen towards cell body. During this process, the rear of the cell is often fixed without retraction and the whole cell body is stretched due to the forward movement of cell front(Figure5.9.A).The local elevated Rac1 signal is often colocalized with local collagen pulling and densification(Figure5.9.B). Interestingly, as a result of increased Rac1 activity, not only collagen is pulled and becomes perpendicular to cell body, collagen is also wrapped and densified right near cell periphery, which created a wall preventing cell move around(Figure5.9.C). We also notice Rac1 may participate in short-distance cell-cell communications via protrusions. Two paired of cells were shown in Figure5.10.A and Figure5.10.B as examples. In both examples, one cell after activation started generating protrusions, the other cell started to generate protrusions soon after at the nearest site to the light activated cells. In other close paired cells, aligned collagen fibers can be seen between cells. Therefore, we speculated that Rac1 generated protrusions may also participate in intercellular crosstalk. And cells can crosstalk by means of protrusions.

5.3.3 Cdc42 is associated both in protrusions and membrane ruffling

In addition to RhoA and Rac1, we then investigated the last member of the classic trio – Cdc42. However, Cdc42 local activation has shown a very compound yet intriguing pattern in cells. Around half of the cells activated were able to generate protrusions(Figure5.11.A)

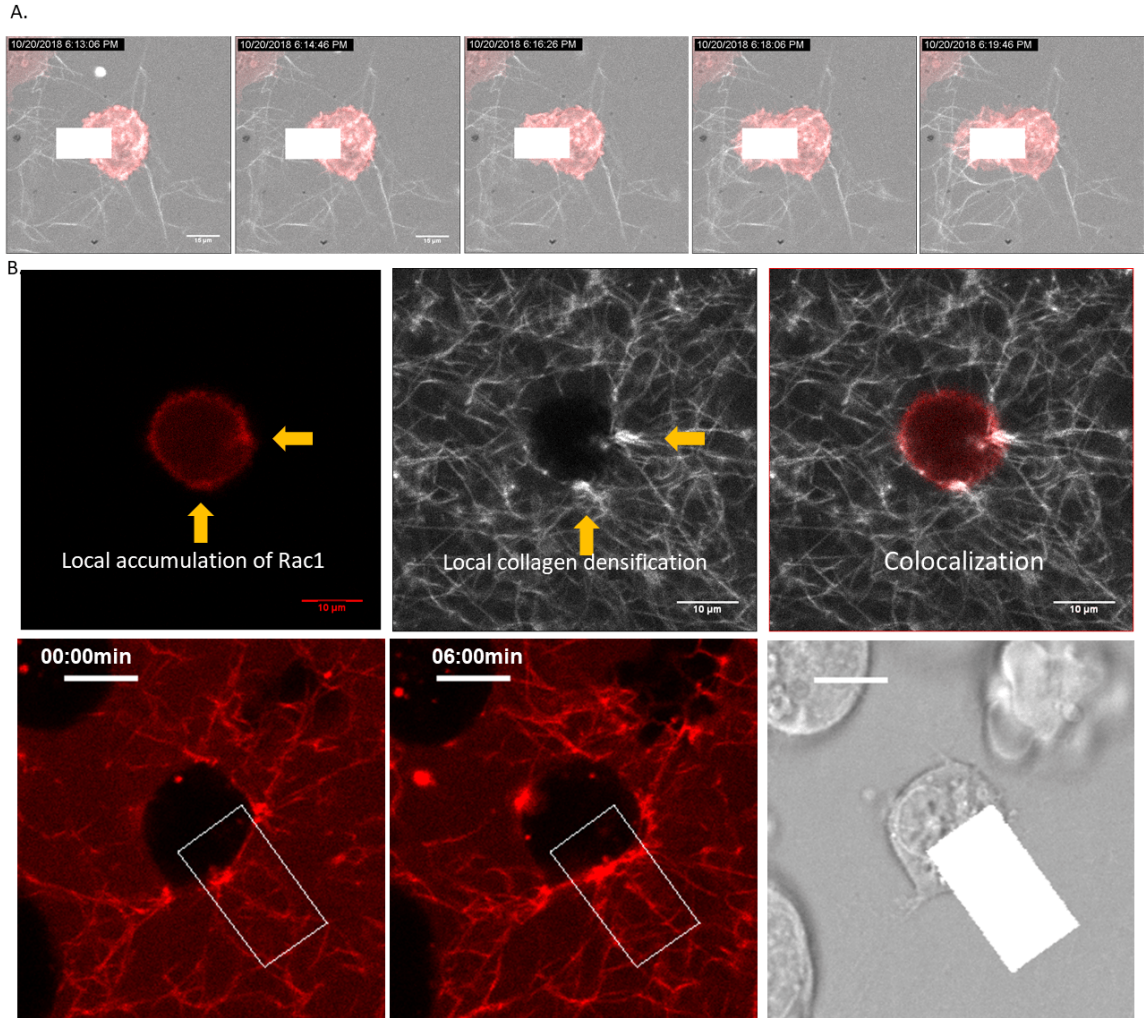


Figure 5.9: Rac1 activation is directly associated with cell periphery collagen densification A. Upon Rac1 excitation(white box), large scale of finger-like protrusions extruded from cell body and pull collagen fibers around. B. The local elevated Rac1 signal is often colocalized with local collagen pulling and densification. C. The densitication of collagen often happens right around cell periphery.

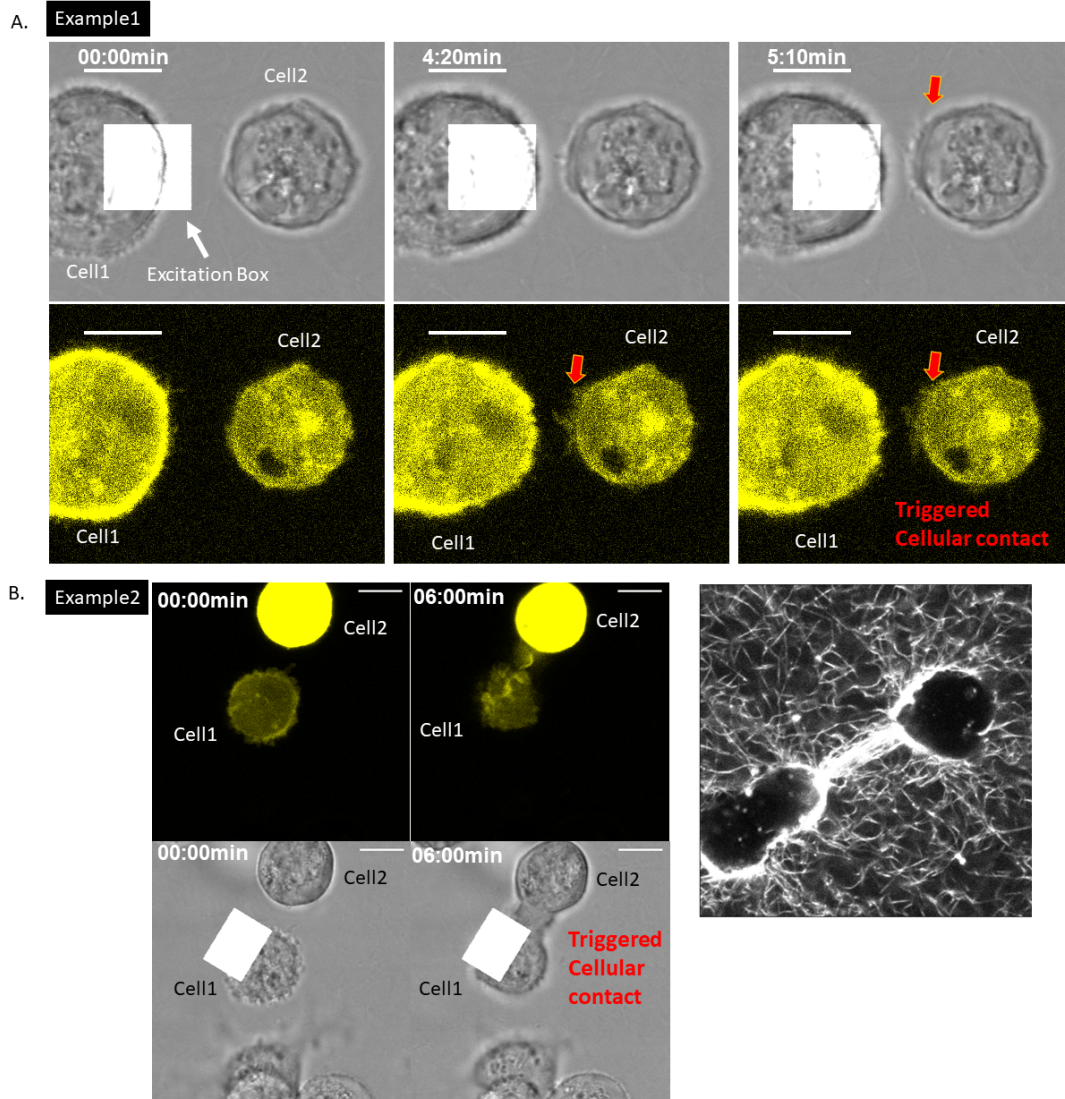


Figure 5.10: **Protrusions induced by Rac1 activation from one cell may trigger protrusions generated from another cell nearby** A. Cell1(left) upon laser activation(shown as white box)generated protrusions. In the meantime, cell2(right) without excitation, also generated protrusions in response to cell1's protrusion. B. Another example when cell1 is activated, cell2 responded by generating large scale of protrusions. In other close-paired cells, aligned collagen fiber can be seen.

but the protrusions are not as in large scale as Rac1 induced ones. And the protrusions induced from Cdc42 is less capable of collagen pulling. Very different with Rac1 activation that cell body usually remain fixed, Cdc42 activation usually result in a fast sloop movement(Figure5.11.C). Along with the fast sloop movement, cell contents also often leak at the front of the cell. A summarized description for each activated cell is organized in Figure5.12.

5.3.4 Drug study on the fibrosis progression

Based on the roles of each RhoGTPase summarized from previous observation, we then proceeded with drug study and see if specific drug is effective preventing collagen densification as often implicated in fibrosis progression. The result is summarized in Figure5.13.

5.4 Conclusion and future directions

This project is not finished at the time when this thesis is firstly drafted. Due to the strict time restraints, only part of the results are listed. One of the ongoing direction is to examine the role of MyoX in the collagen pulling. However – I am not quite interested in this direction, honestly speaking. The reason is simple, however important MyoX is in the clutching of collagen fiber, it is a big protein complex. Any small components that is interferenced will lead to reduced collagen pulling. Even we can prove MyoX is associated with collagen pulling, I still cannot see any clinical impact of this direction. Therefore my interest towards this direction is very limited. However, one thing that I am interested in is to create a pseudo fluorescence imaging, ie to use 2D PDE to mimic molecule aggregates and propagation such as Cdc42, Rac1 and RhoA as well as the local polymerization of actin monomers. MATLAB simulink is a powerful and simple tool to start with. With it's modular design and ready-to-use GUI. It is possible to "visualize" shape/movement related signaling pathway in a "pseudo" fluorescence imaging. The best part of this idea

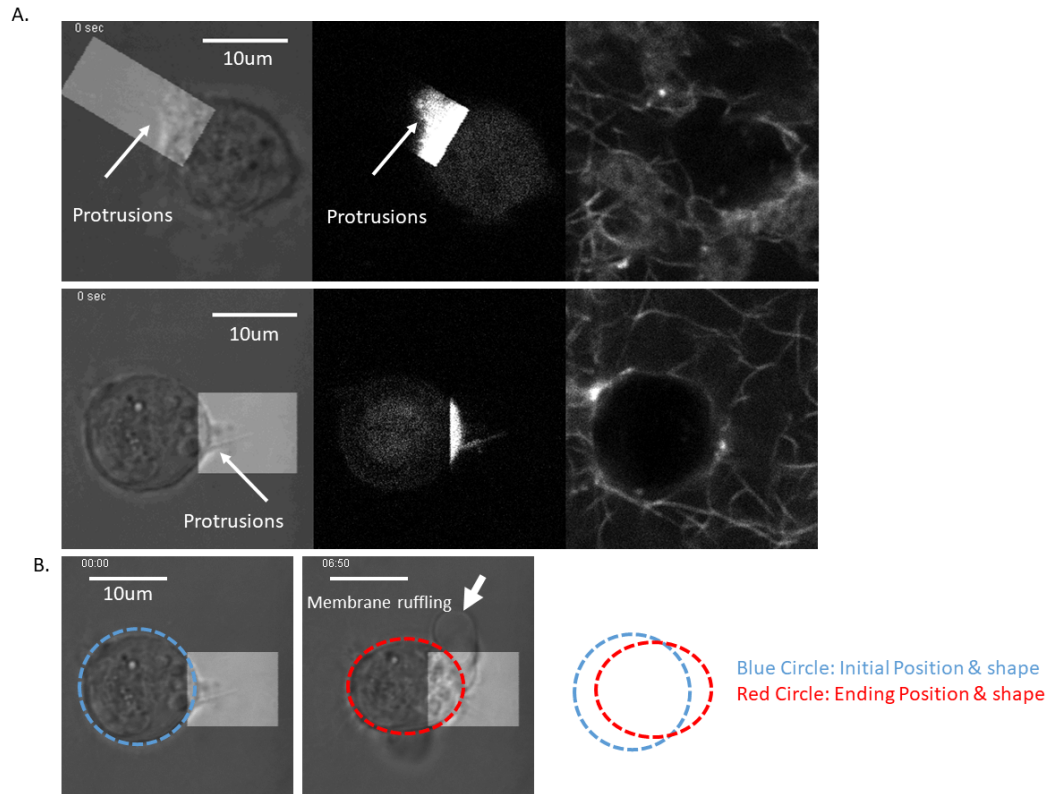


Figure 5.11: **Local Cdc42 activation triggered protrusions from some cells but not all** A. Some MDA-MB-231 cells generated protrusions upon Cdc42 activation but not all(as summarized in Figure5.12). The protrusions from Cdc42 is often less intensive and collagen pulling compared with Rac1 induced protrusions. B. When Cdc42 is activated, cells often fast swoop forward towards the activated region, cell contents leakage often happens at the same time as cell push forward.

Cell ID	+ Clear Protrusions	+ Blebbing in cell front	+ Cell Contraction	+Collagen Wrapping
1	Very few	Yes significant	Yes significant	Yes, slightly
2	Almost none	Yes significant	Yes significant	None
3	No	No	No	None
4	Yes	Yes	Yes	Yes
5	Yes in the beginning long protrusions clearly	Yes significantly	Yes significant	Yes slightly
6	Yes	No	No	Yes (similar to Rac1 data)
7	Yes in the beginning long protrusions clearly	Yes significant	Yes	Yes
8	Yes	Yes	Yes	Yes

Figure 5.12: **Summarized cell responses during Cdc42 activation** Among 8 cells activated, half of the cells generated protrusions while the other half were quiescent. Some cells not only generated protrusions but also experienced cell contents leakage at the cell front.

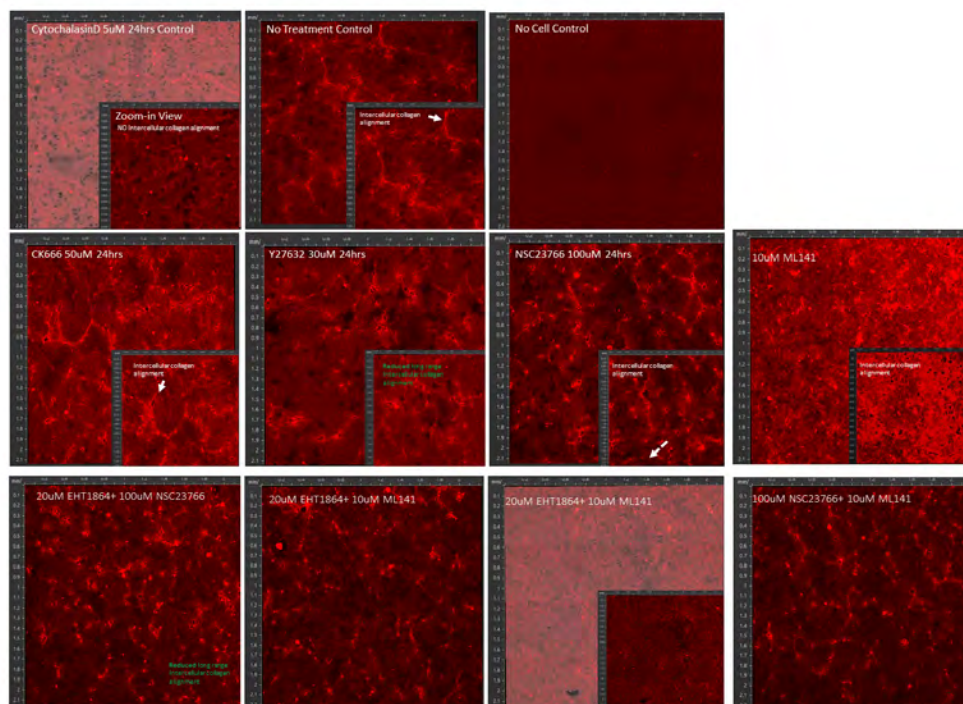


Figure 5.13: **Different drugs' performance on collagen densitization**

is, we already collected real fluorescence imaging, which is the true answer to the simulation. In this case, we can modulate parameters to approach collected data. In addition, because simulink is widely available on campus, such method to visualize signaling pathway instead of simply drawing dots and networks, will help more biologists to think "picturesquely".

Chapter 6

Into the far far future

To tackle the tumor issue, I think in addition to multi-scale simulation and big data enabled prediction, physics-aided tumor therapy will be equally important as conventional cancer therapy. Ultra-thin needles may be a good alternative for precision drug delivery and also fast, non-invasive tumor sampling to facilitate early tumor diagnosis without disturbing original ECM. VR-augmented micro-manipulation can enhance precision surgery and minimize potential harm to surrounding normal tissue. Modern tumor therapy should move towards the direction of "early detection, early control, precision removal and precision therapy". Due to time constraints, I will not discuss each of the subject in detail. Instead, an embryonic idea of "inclusive" data visualization is presented below.

There are three pillar ideas of this modeling strategy. The goal of this modeling is to create an inclusive strategy to link all information together(DNA sequence, epigenetics, RNA sequencing, signal pathway, cell morphology and migration to collective cell behavior and morphogenesis) and create a cross-scale, modular and packable(can be put in black box) platform that allows video visualization, dynamic updates, collaborative contribution.

- The first idea is from "top to bottom", instead of "bottom to top" to model one cell. One can refer to this scale ruler??.Instead of trying to model single cell based on acquired micro-scale information, we may could try acquire inference knowledge

from human body(top) and model a single cell(bottom) based on our observation on human.

- The second idea is that data input/output should be "pseudo-fluorescent" imaging(distribution of molecule aggregates). For each single cell, information of all molecules(physical identities) should be saved as sequential arrays of 2D or even 3D pseudo-fluorescent images. We can use matrix operation to compute the dynamic interaction between channels(each molecule). And the spatial distribution of molecules will be registered to cellular events(mitosis,morphology change, migration) automatically by eye.
- The third idea is circuit design and "black box". To address specific question, there is no need to have thorough knowledge. Instead, we can pack unknown signaling pathways into black boxes, as long as we know with given input, we always get a fixed output. To measure the "black box" output and find the best parameters set, one always can use cytoskeleton protein(highly conserved among all mammalian cells), migration, morphology change, division cycle, as "light bulb".
- The fourth idea is modularization. If pseudo-fluorescent imaging allows visualization and parameter optimization for single cell, then modularization creates an interface between cell to cell, i.e., to model collective cell behaviors such as morphogenesis and embryonic development. The physical entities in one cell can be categorized into different basic function units(will be explained later). Cell-cell talk can be established by creating network between major function units. Organs are simply aggregates of cells populations.

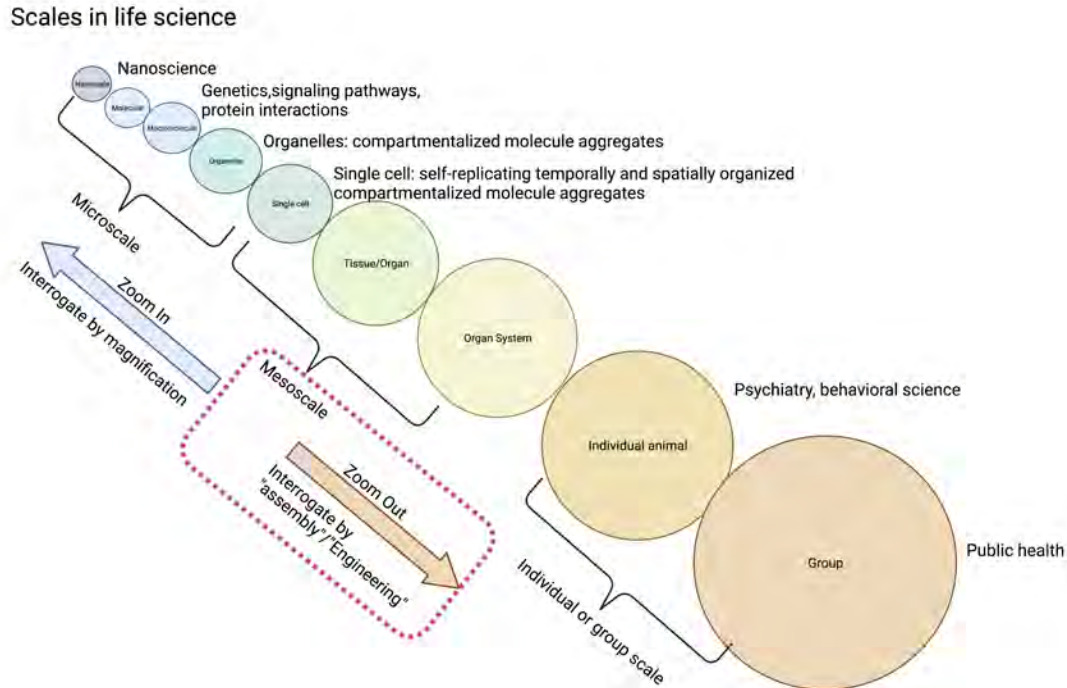


Figure 6.1: "Top to bottom" and "bottom to top": reverse thinking

6.0.1 From human to single cell, starting from fractal imaging

It has been noticed long time ago that the morphogenesis and development of ferns can be accurately simulated by fractal images(Figure6.2). In fact, the growth of advanced plant type such as carpophyte resembles the growth of fractal imaging(Figure6.3).

Animal cell is more complicated than plant cell therefore the morphogenesis process is more complicated. Currently it is unsure whether human embryonic development can be simulated by fractal operation. Here we can make a bold hypothesis that animal embryonic development process involves similar process – that each stand-out features displayed on macro-scale is the functional aggregates of micro-scale function units. In this sense, we can draw a "pseudo-cell" based on reverse "fractal operation" of human body.

The first layer of inference we can start with establishing functional units in a "pseudo-cell". As we can see in Figure6.4), the "pseudo-cell" we inferred from human body can guide us very well on how to categorize existing function units in real cells.

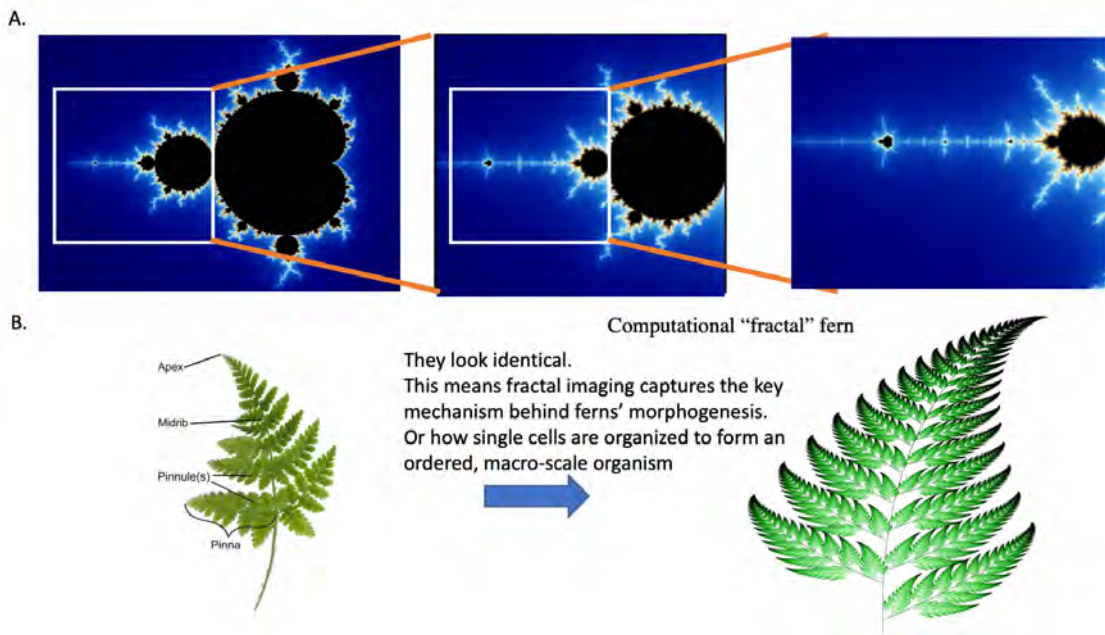


Figure 6.2: Fractal imaging can be used to simulate ferns

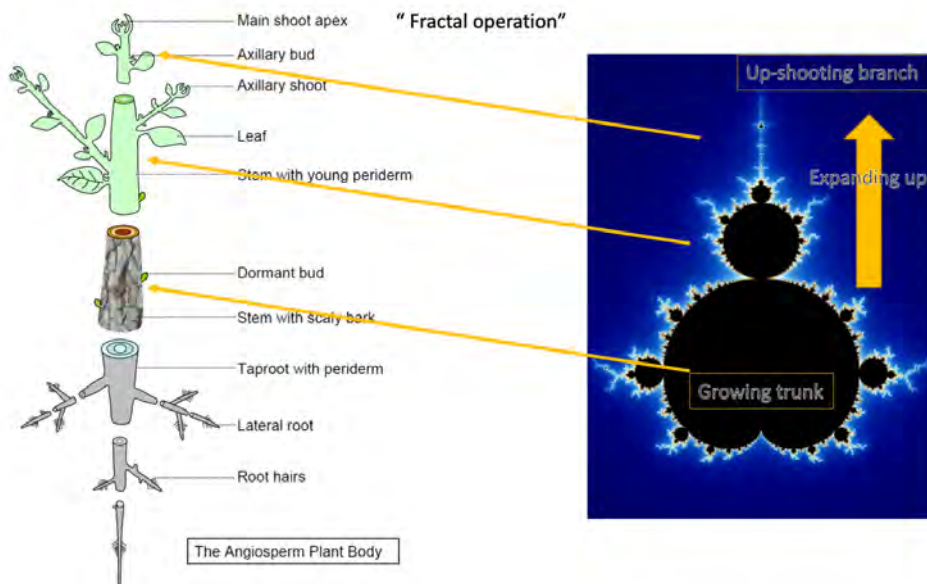


Figure 6.3: The growth of fractal imaging captures the growth of trees

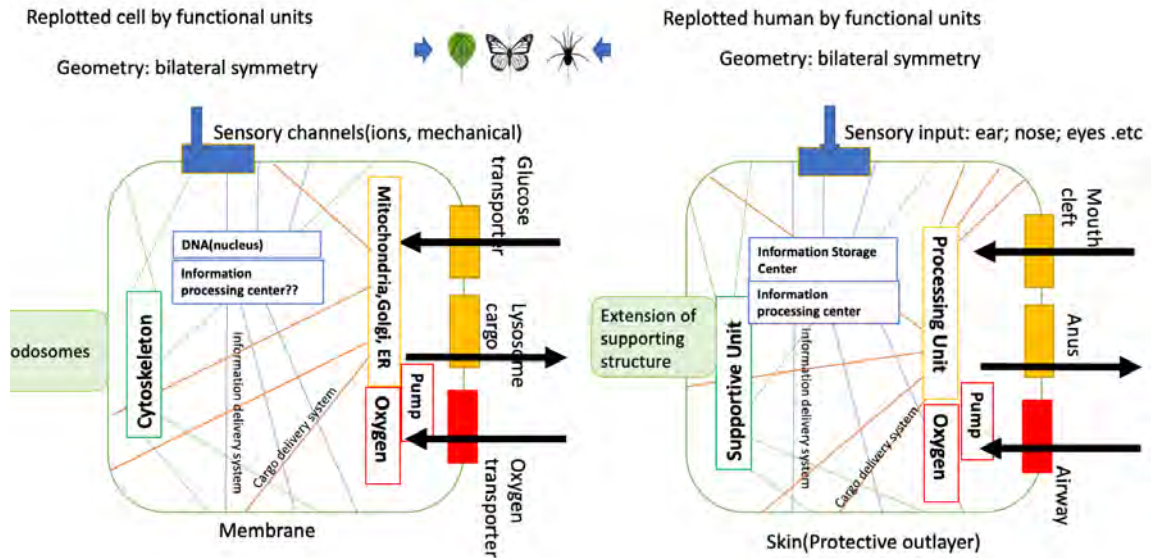


Figure 6.4: **The 1st inference: A pseudo-cell inherits all the basic function units from human body**

Based on the first inference we notice that cell function units correspond to the human function units. From this observation, we can start our second layer of inference, we may establish the projection from human organs to cell apparatus(Figure6.5). In this inference, we think a mechanical pump is necessary and it can be modeled as the joint nexus of a network which has never-ending actin treadmilling and keeps ”pumping” cargos from cell center to cell peripheryFigure6.6. And another type of network, depending on their distribution(central or periphery) and their function, we can name the short and dense network on the cell periphery as ”periphery sensing system”, similar as their counterparts from human(Figure6.7).And one of the central ”neural fiber” functions as cell memory storage. Therefore, three types of cytoskeleton fibers should exist in a ”pseudo-cell” in correspondence to each ”network”-like part in human(Figure6.8). Further, if we make a 3rd round inference and arrange the spatial location of inner cell apparatus according to their counterparts’ location in human body, we may draw a complete and simplified ”pseudo-cell” in following manner(Figure6.9). In this pseudo cell, a cell is always polarized along the

Summary: A rough hypothetical projections from single cell to human(or animal) based on function

Core idea: Single cell is the "scaled-up" version of human. Human organs are "scaled-up" version of single cell apparatus.

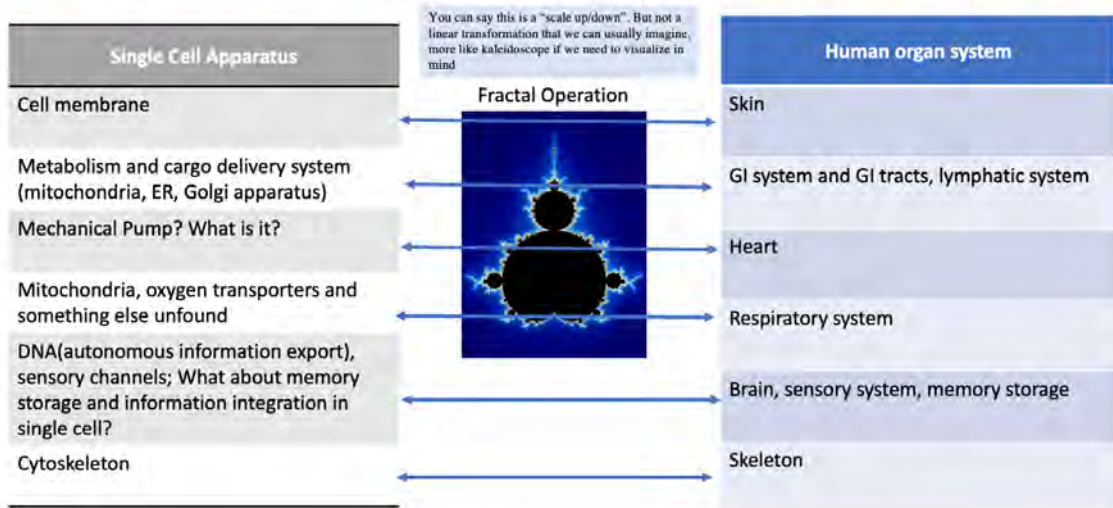


Figure 6.5: **The 2nd inference: projection from human organ to cell apparatus**

major cytoskeleton. One polar of cell is riched in sensory and memory fibers another polar of cell is riched in secretion units. However the branching direction is, there are 4 major protrusions that are responsible for cell gripping and moving. And these protrusions are extensions from a major axis that goes from cell "head" to "bottom". In addition, thin and sensory fibers exists representing hair along human body. Interestingly, the postulated animal from the fractal aggregation of this "pseudo-cell" starts to pick up basic features of quadrupedsalamander for example) as shown in Figure6.10. This suggests that if the morphogenesis process may require additional information on cells change relative position topologically. One good speculation is we may be able to acquire a fourth layer of inference from human body and decide the relative "stiffness/softness", adherens distribution and other basic mechanic properties of one single "pseudo-cell". In this way, we can modulate cell division axis, control cell polarity and alignment.This part can also connect instructive mechanosensing with cell behaviors. Ultimately, we may be able to restore the complete development process from one cell to an ordered cell aggregates.

Play the mind game: from human body to infer single cell details: a series of wild predictions

Human: pumps materials around



What is the cell pump? There has to be a "mechanical pump" that pump cargos around stirring/propelling the materials in the cell.

This structure must fit following requirements

1. One tiny nexus in the middle of cell(not periphery) in the middle of a network with branches
2. Close to ER, mitochondria, Golgi apparatus(Glucose/oxygen center)
3. Non-stopping back and forth movement to pump proteins/enzymes throughout cell body.
4. This nexus is rich in actomyosins.
5. In the middle of a network, in the middle of cargo transport network.

Or the never ending actin treadmilling by itself is the prototype of pumping system? And the nexus is just junction points of thick actin branches?



Figure 6.6: The heart of pseudo cell is the nexus of cytoskeleton that has never-ending actin treadmilling

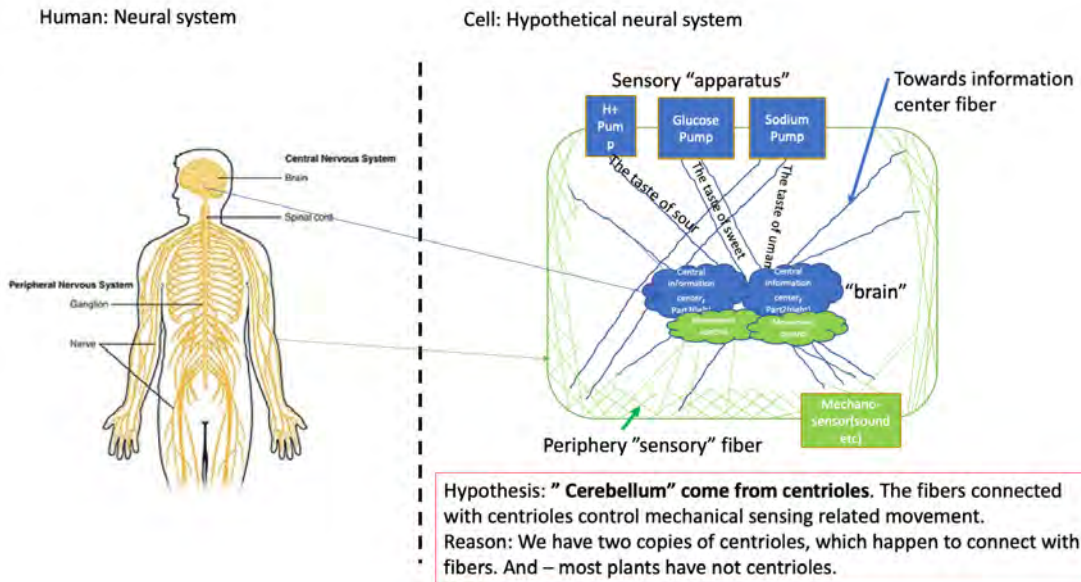


Figure 6.7: The neural system of a pseudo cell:periphery and central cytoskeleton

Revisit cell cytoskeleton: much more than a structural unit

Cell cytoskeleton should be a combination of all "network" like structure and their nexus, and their "scaled-up" aggregation should form following organ system:

1. Heart and blood vessels
2. Muscle and skeleton
3. Neural system

More importantly, I think memory storage is also has something to do with cytoskeleton.

From this angle, there are at least 3 different types of cytoskeleton fibers overlaid with each other but their nexus are at different places. Each type of fiber have its unique role.

One type fiber is responsible to nutrition cargo transport(lysosomes). The nexus of these fibers are almost located in the center of cell.

One type of fiber is for structural support, movement, gripping and contraction.

The third type of fiber is closely associated with type II fiber. But it also connects with other nexus units (Nucleus?) and can pass information around, and storage information.

Figure 6.8: The cytoskeleton of a pseudo cell: different fibers perform specific functions

A simplified single cell model with key features and how it develops into a complete animal

Maybe more predictions if I have time in the future

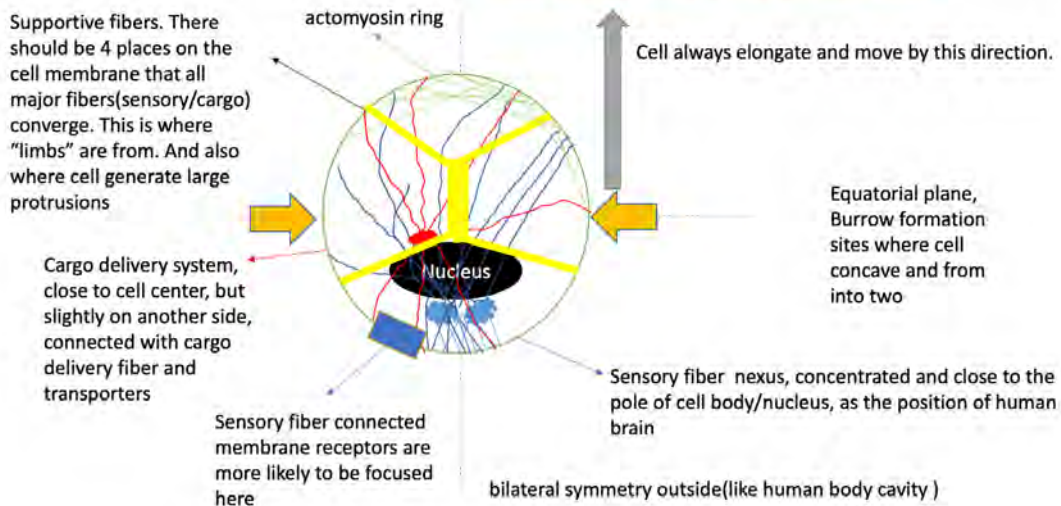


Figure 6.9: The 3rd inference: from the spatial distribution of human organs to single cell apparatus locations

Run the fractal operation: from one single cell architecture to a human being architecture

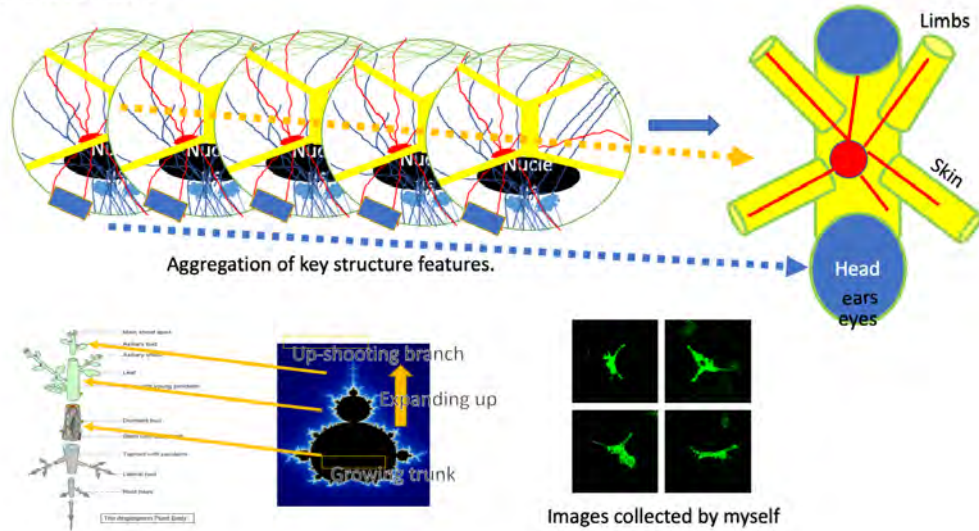


Figure 6.10: **The 3rd inference: a "postulated" computational animal after fractal operation of the "pseudo" single cell**

6.0.2 Tumor cells, rabbits, ecology, and mesoscale characterization

In this section, we will try to interrogate tumor issue by benchmarking it as a "pest control" or a "species invasion" issue. In this way, one micro-scale issue is scaled up to a context that we familiar with and helps us to examine the "tumor event" chronologically and spatially.

Figure.6.11 summarized the key features shared by tumor issue with "rabbit invasion" issue. Through this comparison, we can find the surprising similarity between these two issues. Both tumor cell metastasis and species invasion are driven by high proliferation. Tumor cells are hidden on the vast somatic hinterland and remodel surrounding ECM as rabbits hide and build burrows underground. In fact, we can also benchmark tumor related research (see Figure.6.12) and therapy(see Figure.6.13) accordingly.

Imagine if our current goal is to conquer the rabbits invasion issue. Let's see our first solution: using airplanes to spray extreme toxic pesticide from the sky. Under this

Benchmarking tumor invasion with species invasion







 <p>Cancer cell population</p> <ul style="list-style-type: none"> - High/fast proliferation than normal cells - High migration - Population (gene pool) evolution - Heterogeneity within population - Sensitive to environmental cues(Oxygen, glucose, ECM stiffness) - Evade immunosuppression 	 <p>Rabbits population</p> <ul style="list-style-type: none"> - High/fast proliferation than local rabbits species - Run around fast(sporty, active) - Population (gene pool) evolution - Heterogeneity within population (as a result of high genetic recombination) - Sensitive to environmental cues(food, oxygen, water and soil) - Lack of natural enemy
 <p>Tumor Microenvironment</p> <ul style="list-style-type: none"> - Nest of tumor cells - Architecture dynamically rebuilt by tumor cells - Fibroblasts/macrophages/T cells are involved - Evolve over time. 	 <p>Rabbits burrow</p> <ul style="list-style-type: none"> - Nest of rabbits - Architecture dynamically rebuilt by rabbits - Attract wolves, snakes, birds and other species of animals - Evolve over time.
 <p>Tumor Metastasis</p> <ul style="list-style-type: none"> - Metastasize over time - Has preferred metastasis sites - Nests are hidden under normal tissue - Relative small sized compared with human body - Hard to track/notice in the beginning - "Random" occurrence - Relapse - Destroy original tissue function 	 <p>Species invasion</p> <ul style="list-style-type: none"> - Rabbits build more nests as population expand - Rabbits "choose" certain places to build nests - Rabbits' burrows are hidden underground, - Relative small sized compared with the scale of the meadow - Hard to track/notice in the beginning of species invasion - "Random" occurrence - Relapse - Outcompete or outgrow local species leading to species distinctions

Figure 6.11: Benchmarking tumor issue with "Exotic rabbits invasion" issue

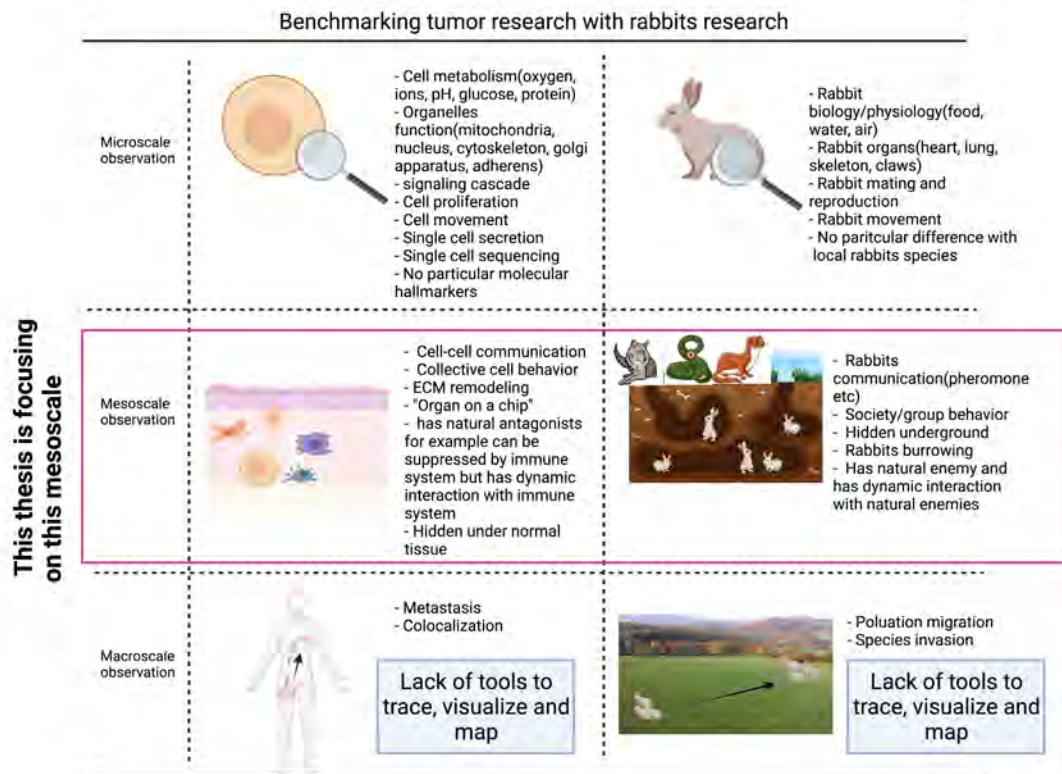


Figure 6.12: **Benchmarking tumor research with rabbit research**

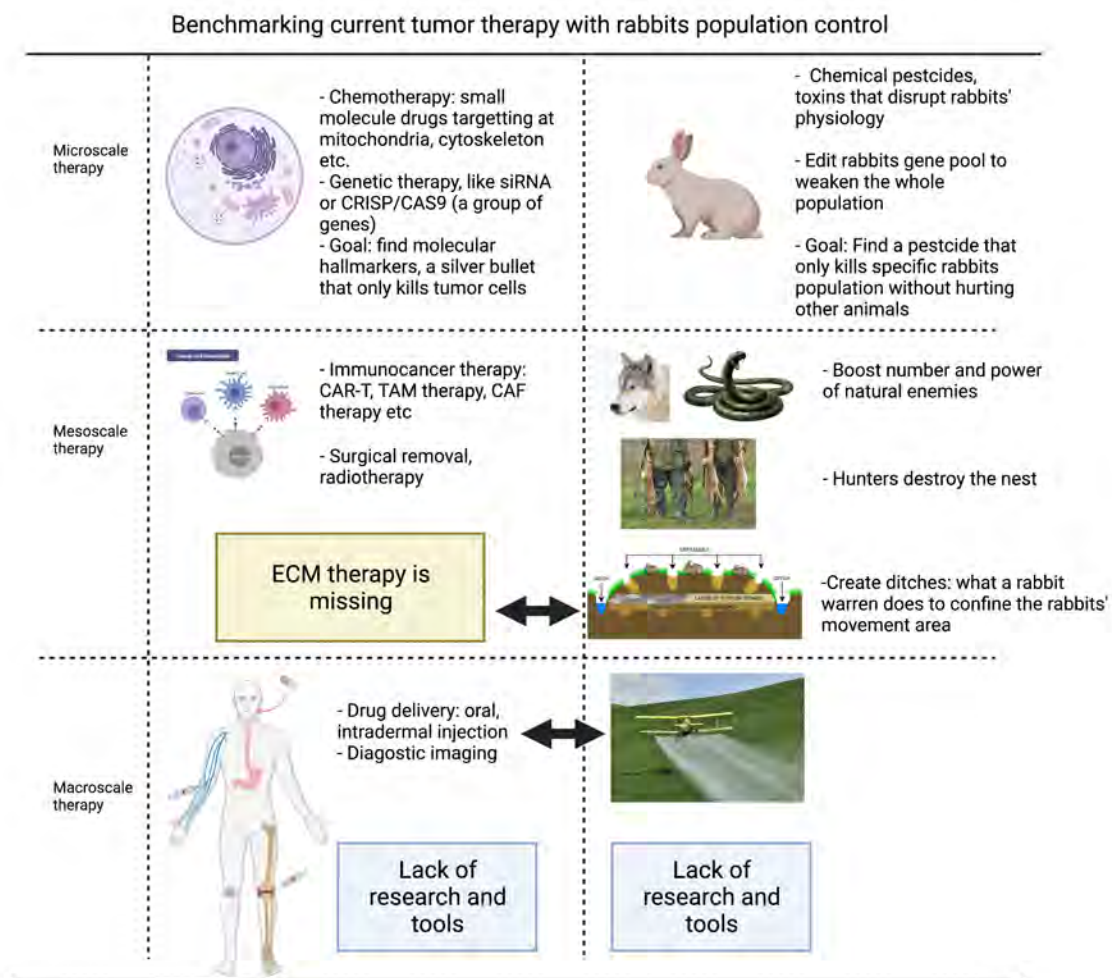


Figure 6.13: **Benchmarking tumor therapy with rabbit population control**

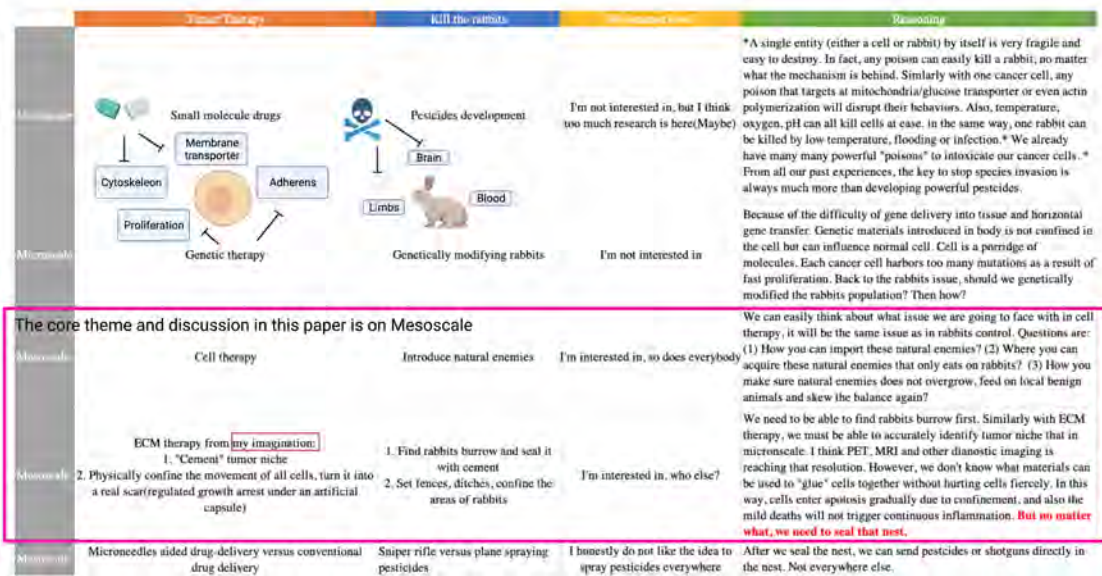
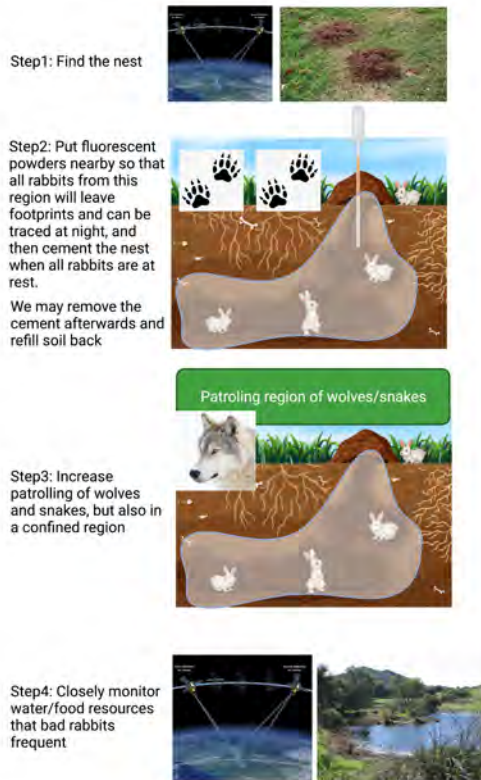


Figure 6.14: What we can learn from "pest control" strategies?

logic, we need to find a pesticide that only kill exotic rabbits not local animals. However, what if the only differences between two types of rabbits are coming from the fact that exotics rabbits reproduce faster and run faster (controlled by hundreds or thousands of genes)? Are we going to genetically modify the exotic rabbit to exterminate them? If we can accurately genetically modify each exotic rabbit, why don't we kill them one by one directly? This method does not sound very correct. However, I think this is exactly what we are trying to do in chemotherapy, by orally taking toxic drugs or intradermal injection. And most patients die of major organ failures. These drugs circulating in our blood are pesticides on the sky above the rabbit holes. Therefore, rationally one would not consider simple pesticides(chemotherapy) as an optimal solution. (Figure6.14)

Under this doubt, naturally, one should come up with a better idea, to introduce natural enemies. In fact, CAR-T has shown extremely good performance on most fluidic cancers. However, CAR-T is limited in solid tumor due to low infiltration rate. Besides, CAR-T is hard to reproduce in large quantity; In vitro culture is subject to accidental con-

Remove the bad rabbit strategy



Remove the bad cell strategy

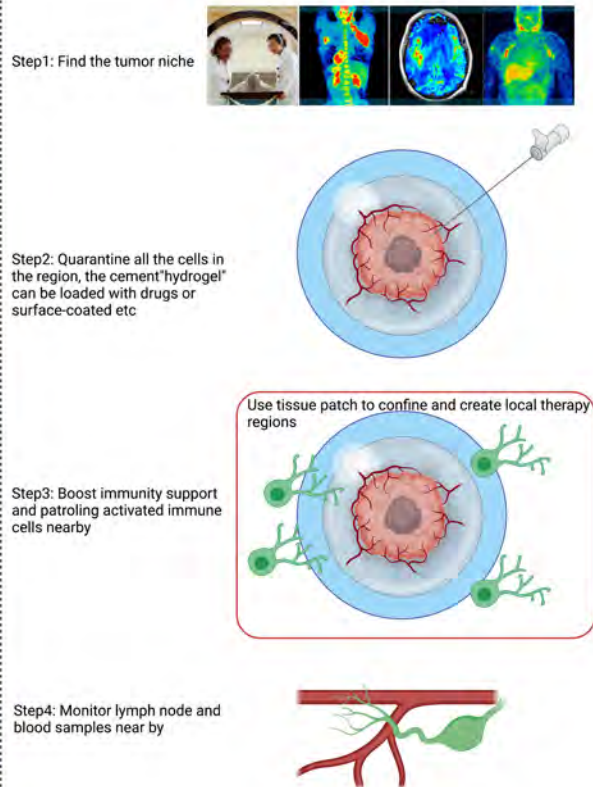


Figure 6.15: **Maybe a better strategy in tumor treatment**

tamination. And too many CAR-T will lead to other health issues like cytokine storm syndromes(CSS). Besides, T cells can work "remotely" shuttle between nearby lymph nodes to distant organs[190]. From our research, we notice that cell and cell has to close enough to communicate. Therefore, how to prolong the retention of T cells in tumor microenvironment is critical. Besides, darwin selection and acquired resistance is another issue[191]. Similarly in rabbit issue, what happens if we put wolves, foxes and snakes into the meadow? Uncontrolled wolves, foxes and snakes will skew the environmental balance and lead to extinction of other animal species again. How to accurately contain wolves, foxes and snakes will become another round of question.

Now let's imagine we are a technical and experienced hunter and focus on the rabbit

issue directly. What would you do? Here is my idea(Figure6.15):

- (1) Firstly, I will use satellite imaging to find any places that look like a bad rabbit burrow
- (2) Secondly, I will confine the activity region of bad rabbits as early as possible, for example creating ditches, as a normal rabbit warren does, or by cementing the burrow. If all the bad rabbits are together in the nest, we then don't have to spray pesticides everywhere. In addition, confinement by itself will gradually lead to the diminish of bad rabbit population due to limited food and water resources.
- (3) Thirdly, I will increase surveillance level and patrolling force by introducing appropriate number of wolves, snakes and other animals.
- (4) Forth, I will use satellite imaging to closely monitor all water resources that bad rabbits rely on. When the number of bad rabbits show up near water resources, we need to repeat (1) and cement/quarantine the burrow again.

If you agree with me that above-mentioned is not a bad idea to deal with invasive rabbits. What if we go back to the tumor issue and think about a similar strategy:

- (1) Improve diagnostic imaging, to identify the tumor nest(ECM signatures – burrow, molecule signatures-confirm the bad rabbit).
- (2) Use a specific tissue glue or a tissue patch to seal the tumor microenvironment as a whole. This tissue glue will result in a “fibrotic capsule” outside but inside none of the tumor cells are able to escape. We can let tumor cells die gradually by themselves, naturally convert to a benign tumor or use a long, ultra-thin needle right deliver the drugs in and kill them all – without killing cells outside the capsule.
- (3) The microneedle should also provide information on the molecule signatures of the tumor cells, which gives us a clue what to monitor. In that sense, we can again

use similar ultra-thin needles to collect sample from nearby lymph nodes and blood and closely monitor the rest of escaped tumor cells.

- (4) With the collected molecule signatures, we then can start engineer CAR-T and other immune cells and increase patrolling and also make sure these enhanced cells are also confined in a local region.
- (5) Keep frequent diagnostic imaging and non-invasive sampling.

The core idea in this therapy strategy is we need to downside the scale of the battlefield from whole body to a quarantined local region. As long as we have good imaging tool to trace cell nest, quarantine the bad guys, and then use high precision guns (ultra-thin needles for example), we have a good chance to win the battle.

Publications

- Xiao, Y., **Liu, C.**, Chen, Z., Blatchley, M. R., Kim, D., Zhou, J., ... Fan, R. (2019). Senescent Cells with Augmented Cytokine Production for Microvascular Bioengineering and Tissue Repairs. *Advanced biosystems*, 3(8), 1900089.
- Gabriela A. Pizzurro, **Chang Liu**, Kathryn Bridges, Amanda F. Alexander, Alice Huang, Janani Baskaran, Julie Ramseier, Marcus W. Bosenberg, Michael Mak*, Kathryn Miller-Jensen*. 3D Model of the Early Melanoma Microenvironment Captures Macrophage Transition into a Tumor-promoting Phenotype. *Cancers*.(Co-first author, 2021)
- Fibroblast-Mediated Uncaging of Cancer Cells and Dynamic Evolution of the Physical Microenvironment. **Chang Liu**, Michael Mak*. (First Author, *Scientific Reports*, 2021)
- Self-Assembly of Mesoscaled Collagen Architectures and Applications in 3D Cell Migration. **Chang Liu**, Ryan Nguyen, Xingjian Zhang, Xiangyu Gong, Gabriela A. Pizzurro, Alejandro Rossello, Michael Mak*. (First Author, *Acta Biomaterialia*, in major revision, 2022)
- A Microfluidic Device for Quantitative Measurements of Physical Occlusion Dynamics in Sickle Cell Disease. Xingjian Zhang, Trevor Chan, Judith Carbonella, Xiangyu Gong, Noureen Ahmed, **Chang Liu**, Farzana Pashankar, Michael Mak*. (Accepted by *Lab On a Chip*, 2022)

Bibliography

- [1] Cristian Tomasetti, Lu Li, and Bert Vogelstein. Stem cell divisions, somatic mutations, cancer etiology, and cancer prevention. *Science*, 355, 2017. 1
- [2] Jingchun Sun, Qiang Wei, Yubo Zhou, Jingqi Wang, Qi Liu, and Hua Xu. A systematic analysis of fda-approved anticancer drugs. *BMC Systems Biology*, 11, 2017. 2
- [3] Steven M. Paul, Daniel S. Mytelka, Christopher T. Dunwiddie, Charles C. Persinger, Bernard H. Munos, Stacy R. Lindborg, and Aaron L. Schacht. How to improve rd productivity: The pharmaceutical industry’s grand challenge. *Nature Reviews Drug Discovery*, 9, 2010. 2
- [4] Bert Vogelstein, Nickolas Papadopoulos, Victor E. Velculescu, Shibin Zhou, Luis A. Diaz, and Kenneth W. Kinzler. Cancer genome landscapes. *Science*, 340, 2013. 2
- [5] Cyriac Kandoth, Michael D. McLellan, Fabio Vandin, Kai Ye, Beifang Niu, Charles Lu, Mingchao Xie, Qunyuan Zhang, Joshua F. McMichael, Matthew A. Wyczalkowski, Mark D.M. Leiserson, Christopher A. Miller, John S. Welch, Matthew J. Walter, Michael C. Wendl, Timothy J. Ley, Richard K. Wilson, Benjamin J. Raphael, and Li Ding. Mutational landscape and significance across 12 major cancer types. *Nature*, 502, 2013. 2
- [6] Fiona M. Behan, Francesco Iorio, Gabriele Picco, Emanuel Gonçalves, Charlotte M. Beaver, Giorgia Migliardi, Rita Santos, Yanhua Rao, Francesco Sassi, Marika Pinnelli, Rizwan Ansari, Sarah Harper, David Adam Jackson, Rebecca McRae, Rachel Pooley, Piers Wilkinson, Dieudonne van der Meer, David Dow, Carolyn Buser-Doepner, Andrea Bertotti, Livio Trusolino, Euan A. Stronach, Julio Saez-Rodriguez, Kosuke Yusa, and Mathew J. Garnett. Prioritization of cancer therapeutic targets using crispr–cas9 screens. *Nature*, 568, 2019. 2, 97
- [7] Christina Philippeos, Stephanie B. Telerman, Bénédicte Oulès, Angela O. Pisco, Tanya J. Shaw, Raul Elgueta, Giovanna Lombardi, Ryan R. Driskell, Mark Soddin, Magnus D. Lynch, and et al. Spatial and single-cell transcriptional profiling identifies functionally distinct human dermal fibroblast subpopulations. *Journal of Investigative Dermatology*, 138(4):811–825, Apr 2018. 3

- [8] Xiyi Chen, Oleg Nadiarynk, Sergey Plotnikov, and Paul J Campagnola. Second harmonic generation microscopy for quantitative analysis of collagen fibrillar structure. *Nature Protocols*, 7(4):654–669, Apr 2012. 3
- [9] P. Schedin and P. J. Keely. Mammary gland ecm remodeling, stiffness, and mechanosignaling in normal development and tumor progression. *Cold Spring Harbor Perspectives in Biology*, 3(1):a003228–a003228, Jan 2011. 4, 5
- [10] Brooke N. Mason, Alina Starchenko, Rebecca M. Williams, Lawrence J. Bonassar, and Cynthia A. Reinhart-King. Tuning three-dimensional collagen matrix stiffness independently of collagen concentration modulates endothelial cell behavior. *Acta Biomaterialia*, 9(1):4635–4644, Jan 2013. 4
- [11] Daniel J. McGrail, Quang Minh N. Kieu, and Michelle R. Dawson. The malignancy of metastatic ovarian cancer cells is increased on soft matrices through a mechanosensitive Rho-ROCK pathway. *Journal of Cell Science*, 2014. 4, 130
- [12] Daniel J. McGrail, Quang Minh N. Kieu, Jason A. Iandoli, and Michelle R. Dawson. Actomyosin tension as a determinant of metastatic cancer mechanical tropism. *Physical Biology*, 2015. 4, 130
- [13] Astrid Slany, Anastasia Meshcheryakova, Agnes Beer, Hendrik Jan Ankersmit, Verena Paulitschke, and Christopher Gerner. Plasticity of fibroblasts demonstrated by tissue-specific and function-related proteome profiling. *Clinical Proteomics*, 11(1):41, Dec 2014. 4
- [14] Antonio Sica and Alberto Mantovani. Macrophage plasticity and polarization: in vivo veritas. *Journal of Clinical Investigation*, 122(3):787–795, Mar 2012. 4
- [15] L. A. Maciel-Barón, S. L. Morales-Rosales, A. A. Aquino-Cruz, F. Triana-Martínez, S. Galván-Arzate, A. Luna-López, V. Y. González-Puertos, N. E. López-Díazguerrero, C. Torres, and Mina Königsberg. Senescence associated secretory phenotype profile from primary lung mice fibroblasts depends on the senescence induction stimuli. *AGE*, 38(1):26, Feb 2016. 4
- [16] Sanya-Eduarda Kuzet and Cedric Gaggioli. Fibroblast activation in cancer: when seed fertilizes soil. *Cell and Tissue Research*, 365(3):607–619, Sep 2016. 4
- [17] David M. Mosser and Justin P. Edwards. Exploring the full spectrum of macrophage activation. *Nature Reviews Immunology*, 8(12):958–969, Dec 2008. 4
- [18] Paolo P Provenzano, David R Inman, Kevin W Eliceiri, Justin G Knittel, Long Yan, Curtis T Rueden, John G White, and Patricia J Keely. Collagen density promotes mammary tumor initiation and progression. *BMC Medicine*, 6(1):11, Dec 2008. 5
- [19] Beatrice Yue. Biology of the extracellular matrix: An overview. *Journal of Glaucoma*, 23:S20–S23, 2014. 5

- [20] Thomas R. Cox and Janine T. Erler. Remodeling and homeostasis of the extracellular matrix: implications for fibrotic diseases and cancer. *Disease Models Mechanisms*, 4(2):165–178, Mar 2011. 5
- [21] Philippe Gascard and Thea D. Tlsty. Carcinoma-associated fibroblasts: orchestrating the composition of malignancy. *Genes Development*, 30(9):1002–1019, May 2016. 6
- [22] Anna Labernadie, Takuya Kato, Agustí Brugués, Xavier Serra-Picamal, Stefanie Derzsi, Esther Arwert, Anne Weston, Victor González-Tarragó, Alberto Elosegui-Artola, Lorenzo Albertazzi, Jordi Alcaraz, Pere Roca-Cusachs, Erik Sahai, and Xavier Trepas. A mechanically active heterotypic E-cadherin/N-cadherin adhesion enables fibroblasts to drive cancer cell invasion. *Nature Cell Biology*, 2017. 6, 11, 16, 23
- [23] Alexandros Glentis, Philipp Oertle, Pascale Mariani, Aleksandra Chikina, Fatima El Marjou, Youmna Attieh, Francois Zaccarini, Marick Lae, Damarys Loew, Florent Dingli, et al. Cancer-associated fibroblasts induce metalloprotease-independent cancer cell invasion of the basement membrane. *Nature communications*, 8(1):1–13, 2017. 6
- [24] Sergei I. Grivennikov, Florian R. Greten, and Michael Karin. Immunity, inflammation, and cancer. *Cell*, 140(6):883–899, Mar 2010. 6
- [25] John Condeelis and Jeffrey W. Pollard. Macrophages: Obligate partners for tumor cell migration, invasion, and metastasis. *Cell*, 124(2):263–266, Jan 2006. 6
- [26] Thomas F Gajewski, Hans Schreiber, and Yang-Xin Fu. Innate and adaptive immune cells in the tumor microenvironment. *Nature Immunology*, 14(10):1014–1022, Oct 2013. 6
- [27] Xu Zhou, Ruth A. Franklin, Miri Adler, Jeremy B. Jacox, Will Bailis, Justin A. Shyer, Richard A. Flavell, Avi Mayo, Uri Alon, and Ruslan Medzhitov. Circuit design features of a stable two-cell system. *Cell*, 172(4):744–757.e17, Feb 2018. 6
- [28] Zhensen Zhu, Jie Ding, Zengshuan Ma, Takashi Iwashina, and Edward E. Tredget. Alternatively activated macrophages derived from thp-1 cells promote the fibrogenic activities of human dermal fibroblasts: M2 macrophages promote fibrogenic activities of fibroblasts. *Wound Repair and Regeneration*, 25(3):377–388, May 2017. 7
- [29] Matthew B. Buechler, Wenxian Fu, and Shannon J. Turley. Fibroblast-macrophage reciprocal interactions in health, fibrosis, and cancer. *Immunity*, 54(5):903–915, May 2021. 7
- [30] Guangwen Ren, Xin Zhao, Ying Wang, Xin Zhang, Xiaodong Chen, Chunliang Xu, Zeng-rong Yuan, Arthur I Roberts, Liying Zhang, Betty Zheng, et al. Ccr2-dependent recruitment of macrophages by tumor-educated mesenchymal stromal

cells promotes tumor development and is mimicked by $\text{tnf}\alpha$. *Cell stem cell*, 11(6):812–824, 2012. 7

- [31] Martin Augsten, Christina Hägglöf, Eleonor Olsson, Claudia Stolz, Panagiotis Tsagozis, Tetyana Levchenko, Mitchell J Frederick, Åke Borg, Patrick Micke, Lars Egevad, et al. Cxcl14 is an autocrine growth factor for fibroblasts and acts as a multi-modal stimulator of prostate tumor growth. *Proceedings of the National Academy of Sciences*, 106(9):3414–3419, 2009. 7
- [32] Pardis Pakshir, Moien Alizadehgiashi, Boaz Wong, Nuno Miranda Coelho, Xingyu Chen, Ze Gong, Vivek B. Shenoy, Christopher A. McCulloch, and Boris Hinz. Author correction: Dynamic fibroblast contractions attract remote macrophages in fibrillar collagen matrix. *Nature Communications*, 10(1):2286, Dec 2019. 7
- [33] Michael Schnoor, Paul Cullen, Julia Lorkowski, Katrin Stolle, Horst Robenek, David Troyer, Jürgen Rauterberg, and Stefan Lorkowski. Production of type vi collagen by human macrophages: A new dimension in macrophage functional heterogeneity. *The Journal of Immunology*, 180(8):5707–5719, Apr 2008. 7
- [34] Tianyi Liu, Linli Zhou, Danni Li, Thomas Andl, and Yuhang Zhang. Cancer-associated fibroblasts build and secure the tumor microenvironment. *Frontiers in Cell and Developmental Biology*, 7:60, Apr 2019. 7
- [35] Lucy MacCarthy-Morrogh and Paul Martin. The hallmarks of cancer are also the hallmarks of wound healing, 2020. 8, 97
- [36] Quanming Shi, Rajarshi P. Ghosh, Hanna Engelke, Chris H. Rycroft, Luke Cassereau, James A. Sethian, Valerie M. Weaver, and Jan T. Liphardt. Rapid disorganization of mechanically interacting systems of mammary acini. *Proceedings of the National Academy of Sciences of the United States of America*, 2014. 9, 134
- [37] Andrew J. Ford and Padmavathy Rajagopalan. Extracellular matrix remodeling in 3D: implications in tissue homeostasis and disease progression. *Wiley Interdisciplinary Reviews: Nanomedicine and Nanobiotechnology*, 2018. 9
- [38] Pardis Pakshir, Moien Alizadehgiashi, Boaz Wong, Nuno Miranda Coelho, Xingyu Chen, Ze Gong, Vivek B. Shenoy, Christopher McCulloch, and Boris Hinz. Dynamic fibroblast contractions attract remote macrophages in fibrillar collagen matrix. *Nature Communications*, 2019. 10, 40, 94, 147
- [39] Yufeng Cheng, Kai Wang, Wei Ma, Xiaomei Zhang, Yipeng Song, Jianbo Wang, Nana Wang, Qingxu Song, Fangli Cao, Bingxu Tan, and Jinming Yu. Cancer-associated fibroblasts are associated with poor prognosis in esophageal squamous cell carcinoma after surgery. *International Journal of Clinical and Experimental Medicine*, 8, 2015. 11

- [40] Susumu Saigusa, Yuji Toiyama, Koji Tanaka, Takeshi Yokoe, Yoshinaga Okugawa, Hiroyuki Fujikawa, Kohei Matsusita, Mikio Kawamura, Yasuhiro Inoue, Chikao Miki, and Masato Kusunoki. Cancer-associated fibroblasts correlate with poor prognosis in rectal cancer after chemoradiotherapy. *International Journal of Oncology*, 38, 2011. 11
- [41] Alessandra Marconi, Marika Quadri, Annalisa Saltari, and Carlo Pincelli. Progress in melanoma modelling in vitro, 2018. 12
- [42] Michelle L. Varney, Sonny L. Johansson, and Rakesh K. Singh. Tumour-associated macrophage infiltration, neovascularization and aggressiveness in malignant melanoma: Role of monocyte chemotactic protein-1 and vascular endothelial growth factor-A. *Melanoma Research*, 2005. 12, 39
- [43] Manesh Chittezhath, Manprit Kaur Dhillon, Jyue Yuan Lim, Damya Laoui, Irina N. Shalova, Yi Ling Teo, Jinmiao Chen, Revathy Kamaraj, Lata Raman, Josephine Lum, Thomas Paulraj Thamboo, Edmund Chiong, Francesca Zolezzi, Henry Yang, Jo A. VanGinderachter, Michael Poidinger, Alvin S.C. Wong, and Subhra K. Biswas. Molecular Profiling Reveals a Tumor-Promoting Phenotype of Monocytes and Macrophages in Human Cancer Progression. *Immunity*, 2014. 12, 39
- [44] Massimo Locati, Graziella Curtale, and Alberto Mantovani. Diversity, Mechanisms, and Significance of Macrophage Plasticity. *Annual Review of Pathology: Mechanisms of Disease*, 2020. 12, 39
- [45] Sarah A. Weiss, Dijana Djureinovic, Shlomit Jessel, Irina Krykbaeva, Lin Zhang, Lucia Jilaveanu, Amanda Ralabate, Barbara Johnson, Neta Shanwetter Levit, Gail Anderson, Daniel Zeltermann, Wei Wei, Amit Mahajan, Ovidiu Trifan, Marcus Bosenberg, Susan M. Kaech, Curtis J. Perry, William Damsky, Scott Gettinger, Mario Sznol, Michael Hurwitz, and Harriet M. Kluger. A phase I study of APX005M and cabiralizumab with/without nivolumab in patients with melanoma, kidney cancer or non-small cell lung cancer resistant to anti-PD-(L)1. *Clinical Cancer Research*, 2021. 12, 39
- [46] Robert S. Fischer, Xiaoyu Sun, Michelle A. Baird, Matt J. Hourwitz, Bo Ri Seo, Ana M. Pasapera, Shalin B. Mehta, Wolfgang Losert, Claudia Fischbach, John T. Fourkas, and Clare M. Waterman. Contractility, focal adhesion orientation, and stress fiber orientation drive cancer cell polarity and migration along wavy ECM substrates. *Proceedings of the National Academy of Sciences of the United States of America*, 2021. 13, 98, 146
- [47] Mahmut Selman Sakar, Jeroen Eyckmans, Roel Pieters, Daniel Eberli, Bradley J. Nelson, and Christopher S. Chen. Cellular forces and matrix assembly coordinate fibrous tissue repair. *Nature Communications*, 2016. 13, 98, 147

- [48] Asja Guzman, Michelle J. Ziperstein, and Laura J. Kaufman. The effect of fibrillar matrix architecture on tumor cell invasion of physically challenging environments. *Biomaterials*, 2014. 13, 98, 143
- [49] Xiangyu Gong, Jonathan Kulwatno, and K. L. Mills. Rapid fabrication of collagen bundles mimicking tumor-associated collagen architectures. *Acta Biomaterialia*, 2020. 13, 98
- [50] Seunghee Oh, Quang Dang Nguyen, Koo-Hyun Chung, and Hyungsuk Lee. Bundling of collagen fibrils using sodium sulfate for biomimetic cell culturing. *ACS Omega*, 5, 2020. 13
- [51] Dominic Kamps, Johannes Koch, Victor O. Juma, Eduard Campillo-Funollet, Melanie Graessl, Soumya Banerjee, Tomáš Mazel, Xi Chen, Yao Wen Wu, Stephanie Portet, Anotida Madzvamuse, Perihan Nalbant, and Leif Dehmelt. Optogenetic tuning reveals rho amplification-dependent dynamics of a cell contraction signal network. *Cell Reports*, 33, 2020. 14
- [52] S. de Beco, K. Vaidžiulytė, J. Manzi, F. Dalier, F. di Federico, G. Cornilleau, M. Dahan, and M. Coppey. Optogenetic dissection of rac1 and cdc42 gradient shaping. *Nature communications*, 2018. 14
- [53] Elizabeth Wagner and Michael Glotzer. Local rhoa activation induces cytokinetic furrows independent of spindle position and cell cycle stage. *Journal of Cell Biology*, 213:641–649, 2016. 14
- [54] Mitsuo Yamauchi, Thomas H. Barker, Don L. Gibbons, and Jonathan M. Kurie. The fibrotic tumor stroma, 2018. 16
- [55] Katarina Wolf, Mariska te Lindert, Marina Krause, Stephanie Alexander, Joost te Riet, Amanda L. Willis, Robert M. Hoffman, Carl G. Figdor, Stephen J. Weiss, and Peter Friedl. Physical limits of cell migration: Control by ECM space and nuclear deformation and tuning by proteolysis and traction force. *Journal of Cell Biology*, 2013. 16, 24, 111, 143
- [56] Peter Friedl and Katarina Wolf. Proteolytic interstitial cell migration: A five-step process, 2009. 16, 24
- [57] Erik Sahai and Christopher J. Marshall. Differing modes for tumour cell invasion have distinct requirements for Rho/ROCK signalling and extracellular proteolysis. *Nature Cell Biology*, 2003. 16
- [58] Jeffrey B. Wyckoff, Sophie E. Pinner, Steve Gschmeissner, John S. Condeelis, and Erik Sahai. ROCK- and Myosin-Dependent Matrix Deformation Enables Protease-Independent Tumor-Cell Invasion In Vivo. *Current Biology*, 2006. 16

- [59] Andrea Malandrino, Xavier Trepas, Roger D. Kamm, and Michael Mak. Dynamic filopodial forces induce accumulation, damage, and plastic remodeling of 3D extracellular matrices. *PLoS Computational Biology*, 2019. 16, 18, 24, 25
- [60] Ehsan Ban, J. Matthew Franklin, Sungmin Nam, Lucas R. Smith, Hailong Wang, Rebecca G. Wells, Ovijit Chaudhuri, Jan T. Liphardt, and Vivek B. Shenoy. Mechanisms of Plastic Deformation in Collagen Networks Induced by Cellular Forces. *Biophysical Journal*, 2018. 16, 24, 100
- [61] Katrina M. Wisdom, Kolade Adebawale, Julie Chang, Joanna Y. Lee, Sungmin Nam, Rajiv Desai, Ninna Struck Rossen, Marjan Rafat, Robert B. West, Louis Hodgson, and Ovijit Chaudhuri. Matrix mechanical plasticity regulates cancer cell migration through confining microenvironments. *Nature Communications*, 2018. 16, 24, 98
- [62] Stefan Münster, Louise M. Jawerth, Beverly A. Leslie, Jeffrey I. Weitz, Ben Fabry, and David A. Weitz. Strain history dependence of the nonlinear stress response of fibrin and collagen networks. *Proceedings of the National Academy of Sciences of the United States of America*, 2013. 16, 25
- [63] Roy M. Bremnes, Tom Dønne, Samer Al-Saad, Khalid Al-Shibli, Sigve Andersen, Rafael Sirera, Carlos Camps, Inigo Marinez, and Lill Tove Busund. The role of tumor stroma in cancer progression and prognosis: Emphasis on carcinoma-associated fibroblasts and non-small cell lung cancer. *Journal of Thoracic Oncology*, 2011. 16
- [64] Kristian Pietras and Arne Östman. Hallmarks of cancer: Interactions with the tumor stroma, 2010. 16
- [65] Sangmyung Rhee and Frederick Grinnell. Fibroblast mechanics in 3D collagen matrices, 2007. 16
- [66] Yu Long Han, Pierre Ronceray, Guoqiang Xu, Andrea Malandrino, Roger D. Kamm, Martin Lenz, Chase P. Broedersz, and Ming Guo. Cell contraction induces long-ranged stress stiffening in the extracellular matrix. *Proceedings of the National Academy of Sciences of the United States of America*, 2018. 16, 24
- [67] Hailong Wang, A. S. Abhilash, Christopher S. Chen, Rebecca G. Wells, and Vivek B. Shenoy. Long-range force transmission in fibrous matrices enabled by tension-driven alignment of fibers. *Biophysical Journal*, 2015. 16, 24
- [68] Matthew W. Conklin, Jens C. Eickhoff, Kristin M. Riching, Carolyn A. Pehlke, Kevin W. Eliceiri, Paolo P. Provenzano, Andreas Friedl, and Patricia J. Keely. Aligned collagen is a prognostic signature for survival in human breast carcinoma. *American Journal of Pathology*, 2011. 16, 24, 98

- [69] Paolo P. Provenzano, David R. Inman, Kevin W. Eliceiri, Steven M. Trier, and Patricia J. Keely. Contact guidance mediated three-dimensional cell migration is regulated by Rho/ROCK-dependent matrix reorganization. *Biophysical Journal*, 2008. 16, 24, 143
- [70] I. Acerbi, L. Cassereau, I. Dean, Q. Shi, A. Au, C. Park, Y. Y. Chen, J. Liphardt, E. S. Hwang, and V. M. Weaver. Human breast cancer invasion and aggression correlates with ECM stiffening and immune cell infiltration. *Integrative Biology (United Kingdom)*, 2015. 16, 24
- [71] G. P. Raeber, M. P. Lutolf, and J. A. Hubbell. Mechanisms of 3-D migration and matrix remodeling of fibroblasts within artificial ECMs. *Acta Biomaterialia*, 2007. 16
- [72] Melinda Larsen, Vira V. Artym, J. Angelo Green, and Kenneth M. Yamada. The matrix reorganized: extracellular matrix remodeling and integrin signaling, 2006. 16
- [73] Christian Frantz, Kathleen M. Stewart, and Valerie M. Weaver. The extracellular matrix at a glance, 2010. 17
- [74] Jay D. Humphrey, Eric R. Dufresne, and Martin A. Schwartz. Mechanotransduction and extracellular matrix homeostasis, 2014. 17
- [75] Stephen F. Badylak, Donald O. Freytes, and Thomas W. Gilbert. Extracellular matrix as a biological scaffold material: Structure and function, 2009. 17
- [76] Xiaohua Yu, John Walsh, and Mei Wei. Covalent immobilization of collagen on titanium through polydopamine coating to improve cellular performances of MC3T3-E1 cells. *RSC Advances*, 2014. 18
- [77] Haeshin Lee, Shara M. Dellatore, William M. Miller, and Phillip B. Messersmith. Mussel-inspired surface chemistry for multifunctional coatings. *Science*, 2007. 18, 100
- [78] Jean-Yves Tinevez, Nick Perry, Johannes Schindelin, Genevieve M Hoopes, Gregory D Reynolds, Emmanuel Laplantine, Sebastian Y Bednarek, Spencer L Shorte, and Kevin W Eliceiri. Trackmate: An open and extensible platform for single-particle tracking. *Methods*, 115:80–90, 2017. 18
- [79] Roman Gorelik and Alexis Gautreau. Quantitative and unbiased analysis of directional persistence in cell migration. *Nature Protocols*, 2014. 19, 103
- [80] Bivash R. Dasgupta, Shang You Tee, John C. Crocker, B. J. Frisken, and D. A. Weitz. Microrheology of polyethylene oxide using diffusing wave spectroscopy and single scattering. *Physical Review E - Statistical Physics, Plasmas, Fluids, and Related Interdisciplinary Topics*, 2002. 19

- [81] Y. Yu, C. H. Xiao, L. D. Tan, Q. S. Wang, X. Q. Li, and Y. M. Feng. Cancer-associated fibroblasts induce epithelial-mesenchymal transition of breast cancer cells through paracrine TGF- β signalling. *British Journal of Cancer*, 2014. 23, 100
- [82] Youmna Attieh, Andrew G. Clark, Carina Grass, Sophie Richon, Marc Pocard, Pascale Mariani, Nadia Elkhatib, Timo Betz, Basile Gurchenkov, and Danijela Matic Vignjevic. Cancer-associated fibroblasts lead tumor invasion through integrin- β 3-dependent fibronectin asse. *Journal of Cell Biology*, 2017. 23
- [83] Cornelis Storm, Jennifer J. Pastore, F. C. MacKintosh, T. C. Lubensky, and Paul A. Janmey. Nonlinear elasticity in biological gels. *Nature*, 2005. 24
- [84] Alireza Labani-Motlagh, Mehrnoush Ashja-Mahdavi, and Angelica Loskog. The Tumor Microenvironment: A Milieu Hindering and Obstructing Antitumor Immune Responses, 2020. 39
- [85] Leire Bejarano, Marta J.C. Jordão, and Johanna A. Joyce. Therapeutic targeting of the tumor microenvironment, 2021. 39
- [86] María Casanova-Acebes, Erica Dalla, Andrew M. Leader, Jessica LeBerichel, Jovan Nikolic, Blanca M. Morales, Markus Brown, Christie Chang, Leanna Troncoso, Steven T. Chen, Ana Sastre-Perona, Matthew D. Park, Alexandra Tabachnikova, Maxime Dhainaut, Pauline Hamon, Barbara Maier, Catherine M. Sawai, Esperanza Agulló-Pascual, Markus Schober, Brian D. Brown, Boris Reizis, Thomas Marron, Ephraim Kenigsberg, Christine Moussion, Philippe Benaroch, Julio A. Aguirre-Ghiso, and Miriam Merad. Tissue-resident macrophages provide a pro-tumorigenic niche to early NSCLC cells. *Nature*, 2021. 39, 92
- [87] Paul C. Tumeh, Christina L. Harview, Jennifer H. Yearley, I. Peter Shintaku, Emma J.M. Taylor, Lidia Robert, Bartosz Chmielowski, Marko Spasic, Gina Henry, Voicu Ciobanu, Alisha N. West, Manuel Carmona, Christine Kivork, Elizabeth Seja, Grace Cherry, Antonio J. Gutierrez, Tristan R. Grogan, Christine Mateus, Gorana Tomasic, John A. Glaspy, Ryan O. Emerson, Harlan Robins, Robert H. Pierce, David A. Elashoff, Caroline Robert, and Antoni Ribas. PD-1 blockade induces responses by inhibiting adaptive immune resistance. *Nature*, 2014. 39
- [88] Padmanee Sharma and James P. Allison. The future of immune checkpoint therapy. *Science*, 2015. 39
- [89] Vinit Kumar, Laxminarasimha Donthireddy, Douglas Marvel, Thomas Condamine, Fang Wang, Sergio Lavilla-Alonso, Ayumi Hashimoto, Prashanthi Vonteddu, Reeti Behera, Marlee A. Goins, Charles Mulligan, Brian Nam, Neil Hockstein, Fred Dentman, Shanti Shakamuri, David W. Speicher, Ashani T. Weeraratna, Timothy Chao, Robert H. Vonderheide, Lucia R. Languino, Peter Ordentlich, Qin Liu, Xiaowei Xu, Albert Lo, Ellen Puré, Chunsheng Zhang, Andrey Loboda, Manuel A. Sepulveda,

Linda A. Snyder, and Dmitry I. Gabrilovich. Cancer-Associated Fibroblasts Neutralize the Anti-tumor Effect of CSF1 Receptor Blockade by Inducing PMN-MDSC Infiltration of Tumors. *Cancer Cell*, 2017. 39

- [90] Vasiliki Koliarakis, Ana Henriques, Alejandro Prados, and George Kollias. Unfolding innate mechanisms in the cancer microenvironment: The emerging role of the mesenchyme, 2020. 40, 92
- [91] Amanpreet Kaur, Brett L. Ecker, Stephen M. Douglass, Curtis H. Kugel, Marie R. Webster, Filipe V. Almeida, Rajasekharan Somasundaram, James Hayden, Ehsan Ban, Hossein Ahmadzadeh, Janusz Franco-Barraza, Neelima Shah, Ian A. Mellis, Frederick Keeney, Andrew Kossenkov, Hsin Yao Tang, Xiangfan Yin, Qin Liu, Xiaowei Xu, Mitchell Fane, Patricia Brafford, Meenhard Herlyn, David W. Speicher, Jennifer A. Wargo, Michael T. Tetzlaff, Lauren E. Haydu, Arjun Raj, Vivek Shenoy, Edna Cukierman, and Ashani T. Weeraratna. Remodeling of the collagen matrix in aging skin promotes melanoma metastasis and affects immune cell motility. *Cancer Discovery*, 2019. 40, 92, 98
- [92] Frances Y. McWhorter, Tingting Wang, Phoebe Nguyen, Thanh Chung, and Wendy F. Liu. Modulation of macrophage phenotype by cell shape. *Proceedings of the National Academy of Sciences of the United States of America*, 2013. 40, 94
- [93] Nikhil Jain and Viola Vogel. Spatial confinement downsizes the inflammatory response of macrophages. *Nature Materials*, 2018. 40
- [94] Anne Mette H. Larsen, Dorota E. Kuczek, Adrija Kalvisa, Majken S. Siersbæk, Marie-Louise Thorseth, Astrid Z. Johansen, Marco Carretta, Lars Grøntved, Ole Vang, and Daniel H. Madsen. Collagen Density Modulates the Immunosuppressive Functions of Macrophages. *The Journal of Immunology*, 2020. 40
- [95] Jessica Y. Hsieh, Mark T. Keating, Tim D. Smith, Vijaykumar S. Meli, Elliot L. Botvinick, and Wendy F. Liu. Matrix crosslinking enhances macrophage adhesion, migration, and inflammatory activation. *APL Bioengineering*, 2019. 40
- [96] Alba Nicolas-Boluda, Javier Vaquero, Lene Vimeux, Thomas Guilbert, Sarah Barin, Chahrazade Kantari-Mimoun, Matteo Ponzo, Gilles Renault, Piotr Deptula, Katarzyna Pogoda, Robert Bucki, Ilaria Cascone, José Courty, Laura Fouassier, Florence Gazeau, and Emmanuel Donnadieu. Tumor stiffening reversion through collagen crosslinking inhibition improves T cell migration and anti-PD-1 treatment. *eLife*, 2021. 40
- [97] Lea Monteran and Neta Erez. The dark side of fibroblasts: Cancer-associated fibroblasts as mediators of immunosuppression in the tumor microenvironment, 2019. 40

- [98] Manuela Liguori, Graziella Solinas, Giovanni Germano, Alberto Mantovani, and Paola Allavena. Tumor-associated macrophages as incessant builders and destroyers of the cancer stroma, 2011. 40
- [99] Curtis J. Perry, Andrés R. Muñoz-Rojas, Katrina M. Meeth, Laura N. Kellman, Robert A. Amezcua, Durga Thakral, Victor Y. Du, Jake Xiao Wang, William Damsky, Alexandra L. Kuhlmann, Joel W. Sher, Marcus Bosenberg, Kathryn Miller-Jensen, and Susan M. Kaech. Myeloid-targeted immunotherapies act in synergy to induce inflammation and antitumor immunity. *Journal of Experimental Medicine*, 2018. 40, 51, 52, 95
- [100] Diletta Di Mitri, Michela Mirenda, Jelena Vasilevska, Arianna Calcinotto, Nicolas Delaleu, Ajinkya Revandkar, Veronica Gil, Gunther Boysen, Marco Losa, Simone Mosole, Emiliano Pasquini, Rocco D'Antuono, Michela Masetti, Elena Zagato, Giovanna Chiorino, Paola Ostano, Andrea Rinaldi, Letizia Gnetti, Mariona Graupera, Ana Raquel Martins Figueiredo Fonseca, Ricardo Pereira Mestre, David Waugh, Simon Barry, Johann De Bono, and Andrea Alimonti. Re-education of Tumor-Associated Macrophages by CXCR2 Blockade Drives Senescence and Tumor Inhibition in Advanced Prostate Cancer. *Cell Reports*, 2019. 40
- [101] Sean P. Arlauckas, Christopher S. Garris, Rainer H. Kohler, Maya Kitaoka, Michael F. Cuccarese, Katherine S. Yang, Miles A. Miller, Jonathan C. Carlson, Gordon J. Freeman, Robert M. Anthony, Ralph Weissleder, and Mikael J. Pittet. In vivo imaging reveals a tumor-associated macrophage-mediated resistance pathway in anti-PD-1 therapy. *Science Translational Medicine*, 2017. 40, 94
- [102] David Argyle and Takanori Kitamura. Targeting macrophage-recruiting chemokines as a novel therapeutic strategy to prevent the progression of solid tumors, 2018. 40
- [103] Justyna Mazurkiewicz, Aleksandra Simiczyjew, Ewelina Dratkiewicz, Marcin Ziętek, Rafał Matkowski, and Dorota Nowak. Stromal cells present in the melanoma niche affect tumor invasiveness and its resistance to therapy, 2021. 40
- [104] Russell W. Jenkins, Amir R. Aref, Patrick H. Lizotte, Elena Ivanova, Susanna Stinson, Chensheng W. Zhou, Michaela Bowden, Jiehui Deng, Hongye Liu, Diana Miao, Meng Xiao He, William Walker, Gao Zhang, Tian Tian, Chaoran Cheng, Zhi Wei, Sangeetha Palakurthi, Mark Bittinger, Hans Vitzthum, Jong Wook Kim, Ashley Merlino, Max Quinn, Chandrasekar Venkataramani, Joshua A. Kaplan, Andrew Portell, Prafulla C. Gokhale, Bart Phillips, Alicia Smart, Asaf Rotem, Robert E. Jones, Lauren Keogh, Maria Anguiano, Lance Stapleton, Zhiheng Jia, Michal Barzily-Rokni, Israel Cañadas, Tran C. Thai, Marc R. Hammond, Raven Vlahos, Eric S. Wang, Hua Zhang, Shuai Li, Glenn J. Hanna, Wei Huang, Mai P. Hoang, Adriano Piris, Jean Pierre Eliane, Anat O. Stemmer-Rachamimov, Lisa Cameron, Mei Ju Su, Parin Shah, Benjamin Izar, Manisha Thakuria, Nicole R. LeBoeuf, Guilherme Rabinowits, Viswanath Gunda, Sareh Parangi, James M. Cleary, Brian C.

- Miller, Shunsuke Kitajima, Rohit Thummalapalli, Benchun Miao, Thanh U. Barbie, Vivek Sivathanu, Joshua Wong, William G. Richards, Raphael Bueno, Charles H. Yoon, Juan Miret, Meenhard Herlyn, Levi A. Garraway, Eliezer M. Van Allen, Gordon J. Freeman, Paul T. Kirschmeier, Jochen H. Lorch, Patrick A. Ott, F. Stephen Hodi, Keith T. Flaherty, Roger D. Kamm, Genevieve M. Boland, Kwok Kin Wong, David Dornan, Cloud Peter Paweletz, and David A. Barbie. Ex vivo profiling of PD-1 blockade using organotypic tumor spheroids. *Cancer Discovery*, 2018. 41
- [105] S. Di Blasio, G. F. van Wigcheren, A. Becker, A. van Duffelen, M. Gorris, K. Verrijp, I. Stefanini, G. J. Bakker, M. Bloemendal, A. Halilovic, A. Vasaturo, G. Bakdash, S. V. Hato, J. H.W. de Wilt, J. Schalkwijk, I. J.M. de Vries, J. C. Textor, E. H. van den Bogaard, M. Tazzari, and C. G. Figdor. The tumour microenvironment shapes dendritic cell plasticity in a human organotypic melanoma culture. *Nature Communications*, 2020. 41, 92, 95
- [106] Fabrizio Fontana, Monica Marzagalli, Michele Sommariva, Nicoletta Gagliano, and Patrizia Limonta. In vitro 3D cultures to model the tumor microenvironment, 2021. 41, 92
- [107] Katrina Meeth, Jake Xiao Wang, Goran Micevic, William Damsky, and Marcus W. Bosenberg. The YUMM lines: a series of congenic mouse melanoma cell lines with defined genetic alterations. *Pigment Cell and Melanoma Research*, 2016. 42, 50, 59
- [108] Jake Wang, Curtis J. Perry, Katrina Meeth, Durga Thakral, William Damsky, Goran Micevic, Susan Kaech, Kim Blenman, and Marcus Bosenberg. UV-induced somatic mutations elicit a functional T cell response in the YUMMER1.7 mouse melanoma model. *Pigment Cell and Melanoma Research*, 2017. 42, 50
- [109] Virginie Trouplin, Nicolas Boucherit, Laurent Gorvel, Filippo Conti, Giovanna Mottola, and Eric Ghigo. Bone marrow-derived macrophage production. *Journal of visualized experiments : JoVE*, 2013. 42
- [110] Andrés R. Muñoz-Rojas, Ilana Kelsey, Jenna L. Pappalardo, Meibin Chen, and Kathryn Miller-Jensen. Co-stimulation with opposing macrophage polarization cues leads to orthogonal secretion programs in individual cells. *Nature Communications*, 2021. 45, 51, 52
- [111] Kevin R. Moon, David van Dijk, Zheng Wang, Scott Gigante, Daniel B. Burkhardt, William S. Chen, Kristina Yim, Antonia van den Elzen, Matthew J. Hirn, Ronald R. Coifman, Natalia B. Ivanova, Guy Wolf, and Smita Krishnaswamy. Visualizing structure and transitions in high-dimensional biological data. *Nature Biotechnology*, 2019. 45
- [112] Jacob H. Levine, Erin F. Simonds, Sean C. Bendall, Kara L. Davis, El Ad D. Amir, Michelle D. Tadmor, Oren Litvin, Harris G. Fienberg, Astraea Jager, Eli R. Zunder,

- Rachel Finck, Amanda L. Gedman, Ina Radtke, James R. Downing, Dana Pe'er, and Garry P. Nolan. Data-Driven Phenotypic Dissection of AML Reveals Progenitor-like Cells that Correlate with Prognosis. *Cell*, 2015. 45
- [113] Andrea Malandrino, Xavier Trepap, Roger D. Kamm, and Michael Mak. Dynamic filopodial forces induce accumulation, damage, and plastic remodeling of 3d extracellular matrices. *PLoS Computational Biology*, 2019. 46
- [114] Deok Ho Kim, Andrew J. Ewald, Jin Seok Park, Kshitiz, Moonkyu Kwak, Ryan S. Gray, Chia Yi Su, Jayhyun Seo, Steven S. An, and Andre Levchenko. Biomechanical interplay between anisotropic re-organization of cells and the surrounding matrix underlies transition to invasive cancer spread. *Scientific Reports*, 2018. 47
- [115] Yao Lu, Jonathan J. Chen, Luye Mu, Qiong Xue, Yu Wu, Pei Hsun Wu, Jie Li, Alexander O. Vortmeyer, Kathryn Miller-Jensen, Denis Wirtz, and Rong Fan. High-throughput secretomic analysis of single cells to assess functional cellular heterogeneity. *Analytical Chemistry*, 2013. 51
- [116] Kim R.M. Blenman, Jake Wang, Shawn Cowper, and Marcus Bosenberg. Pathology of spontaneous and immunotherapy-induced tumor regression in a murine model of melanoma. *Pigment Cell and Melanoma Research*, 2019. 59, 60
- [117] Yosuke Kumamoto, Joao Paulo G. Camporez, Michael J. Jurczak, Marya Shanabrough, Tamas Horvath, Gerald I. Shulman, and Akiko Iwasaki. CD301b+ Mononuclear Phagocytes Maintain Positive Energy Balance through Secretion of Resistin-like Molecule Alpha. *Immunity*, 2016. 92
- [118] Josh M. Morganti, Lara Kirstie Riparip, and Susanna Rosi. Call off the dog(ma): M1/M2 polarization is concurrent following traumatic brain injury. *PLoS ONE*, 2016. 92
- [119] Matthew M. Gubin, Ekaterina Esaulova, Jeffrey P. Ward, Olga N. Malkova, Daniele Runci, Pamela Wong, Takuro Noguchi, Cora D. Arthur, Wei Meng, Elise Alspach, Ruan F.V. Medrano, Catrina Fronick, Michael Fehlings, Evan W. Newell, Robert S. Fulton, Kathleen C.F. Sheehan, Stephen T. Oh, Robert D. Schreiber, and Maxim N. Artyomov. High-Dimensional Analysis Delineates Myeloid and Lymphoid Compartment Remodeling during Successful Immune-Checkpoint Cancer Therapy. *Cell*, 2018. 92
- [120] Lei Zhang, Ziyi Li, Katarzyna M. Skrzypczynska, Qiao Fang, Wei Zhang, Sarah A. O'Brien, Yao He, Lynn Wang, Qiming Zhang, Aeryon Kim, Ranran Gao, Jessica Orf, Tao Wang, Deepali Sawant, Jiajinlong Kang, Dev Bhatt, Daniel Lu, Chi Ming Li, Aaron S. Rapaport, Kristy Perez, Yingjiang Ye, Shan Wang, Xueda Hu, Xianwen Ren, Wenjun Ouyang, Zhanlong Shen, Jackson G. Egen, Zemin Zhang, and Xin Yu. Single-Cell Analyses Inform Mechanisms of Myeloid-Targeted Therapies in Colon Cancer. *Cell*, 2020. 92

- [121] Elke Pach, Jürgen Brinckmann, Matthias Rübsam, Maike Kümper, Cornelia Mauch, and Paola Zigrino. Fibroblast mmp14-dependent collagen processing is necessary for melanoma growth. *Cancers*, 2021. 92
- [122] Matthew A. Lakins, Ehsan Ghorani, Hafsa Munir, Carla P. Martins, and Jacqueline D. Shields. Cancer-associated fibroblasts induce antigen-specific deletion of CD8 + T Cells to protect tumour cells. *Nature Communications*, 2018. 92
- [123] Tamás Roszer. Understanding the mysterious M2 macrophage through activation markers and effector mechanisms, 2015. 92
- [124] Adrian A. Shimpi and Claudia Fischbach. Engineered ECM models: Opportunities to advance understanding of tumor heterogeneity, 2021. 92
- [125] Ilana Berger Fridman, James Kostas, Michal Gregus, Somak Ray, Matthew R. Sullivan, Alexander R. Ivanov, Smadar Cohen, and Tania Konry. High-throughput microfluidic 3D biomimetic model enabling quantitative description of the human breast tumor microenvironment. *Acta Biomaterialia*, 2021. 92
- [126] Barbara Maier, Andrew M. Leader, Steven T. Chen, Navpreet Tung, Christie Chang, Jessica LeBerichel, Aleksey Chudnovskiy, Shrisha Maskey, Laura Walker, John P. Finnigan, Margaret E. Kirkling, Boris Reizis, Sourav Ghosh, Natalie Roy D'Amore, Nina Bhardwaj, Carla V. Rothlin, Andrea Wolf, Raja Flores, Thomas Marron, Adeeb H. Rahman, Ephraim Kenigsberg, Brian D. Brown, and Miriam Merad. A conserved dendritic-cell regulatory program limits antitumour immunity. *Nature*, 2020. 92
- [127] Xu Zhou, Ruth A. Franklin, Miri Adler, Jeremy B. Jacox, Will Bailis, Justin A. Shyer, Richard A. Flavell, Avi Mayo, Uri Alon, and Ruslan Medzhitov. Circuit Design Features of a Stable Two-Cell System. *Cell*, 2018. 93, 94
- [128] Richard Lee Barrett and Ellen Pure. Cancer-associated fibroblasts and their influence on tumor immunity and immunotherapy. *eLife*, 2020. 93
- [129] Daniel Hargbøl Madsen, Henrik Jessen Jürgensen, Majken Storm Siersbæk, Dorota Ewa Kuczek, Loretta Grey Cloud, Shihui Liu, Niels Behrendt, Lars Grøntved, Roberto Weigert, and Thomas Henrik Bugge. Tumor-Associated Macrophages Derived from Circulating Inflammatory Monocytes Degrade Collagen through Cellular Uptake. *Cell Reports*, 2017. 94
- [130] Ran Afik, Ehud Zigmond, Milena Vugman, Mordehay Klepfish, Elee Shimshoni, Metsada Pasmanik-Chor, Anjana Shenoy, Elad Bassat, Zamir Halpern, Tamar Geiger, Irit Sagi, and Chen Varol. Tumor macrophages are pivotal constructors of tumor collagenous matrix. *Journal of Experimental Medicine*, 2016. 94
- [131] Kati Räsänen and Antti Vaheri. Activation of fibroblasts in cancer stroma, 2010. 94

- [132] Thuy U. Luu, Shannon C. Gott, Bryan W.K. Woo, Masaru P. Rao, and Wendy F. Liu. Micro- and Nanopatterned Topographical Cues for Regulating Macrophage Cell Shape and Phenotype. *ACS Applied Materials and Interfaces*, 2015. 94
- [133] Emeline Van Goethem, Renaud Poincloux, Fabienne Gauffre, Isabelle Maridonneau-Parini, and Véronique Le Cabec. Matrix Architecture Dictates Three-Dimensional Migration Modes of Human Macrophages: Differential Involvement of Proteases and Podosome-Like Structures. *The Journal of Immunology*, 2010. 94
- [134] Erica J. Hoffmann and Suzanne M. Ponik. Biomechanical Contributions to Macrophage Activation in the Tumor Microenvironment, 2020. 94
- [135] Antoine Leimgruber, Cedric Berger, Virna Cortez-Retamozo, Martin Etzrodt, An-dita P. Newton, Peter Waterman, Jose Luiz Figueiredo, Rainer H. Kohler, Na-talie Elpek, Thorsten R. Mempel, Filip K. Swirski, Matthias Nahrendorf, Ralph Weissleder, and Mikael J. Pittet. Behavior of endogenous Tumor-associated macrophages assessed in vivo using a functionalized nanoparticle. *Neoplasia*, 2009. 94
- [136] Thomas A. Hamilton, Chenyang Zhao, Paul G. Pavicic, and Shyamasree Datta. Myeloid colony-stimulating factors as regulators of macrophage polarization. *Frontiers in Immunology*, 2014. 94
- [137] Jan Korbecki, Donata Simińska, Klaudyna Kojder, Szymon Grochans, Izabela Gutowska, Dariusz Chlubek, and Irena Baranowska-Bosiacka. Fractalkine/cx3cl1 in neoplastic processes, 2020. 94
- [138] Kim M. van Pul, Marieke F. Fransen, Rieneke van de Ven, and Tanja D. de Gruijl. Immunotherapy Goes Local: The Central Role of Lymph Nodes in Driving Tumor Infiltration and Efficacy, 2021. 95
- [139] Sean P. Arlauckas, Seth B. Garren, Chris S. Garris, Rainer H. Kohler, Juhyun Oh, Mikael J. Pittet, and Ralph Weissleder. Arg1 expression defines immunosuppressive subsets of tumor-associated macrophages. *Theranostics*, 2018. 95
- [140] H F Dvorak. Tumors: wounds that do not heal. Similarities between tumor stroma generation and wound healing. *The New England journal of medicine*, 1986. 97
- [141] Esther N. Arwert, Esther Hoste, and Fiona M. Watt. Epithelial stem cells, wound healing and cancer, 2012. 97
- [142] Meilang Xue and Christopher J. Jackson. Extracellular Matrix Reorganization Dur-ing Wound Healing and Its Impact on Abnormal Scarring. *Advances in Wound Care*, 2015. 98
- [143] Thomas R. Cox and Janine T. Erler. Remodeling and homeostasis of the extracel-lular matrix: Implications for fibrotic diseases and cancer, 2011. 98

- [144] Arseniy E. Yuzhalin, Su Yin Lim, Anton G. Kutikhin, and Alex N. Gordon-Weeks. Dynamic matrixome: ECM remodeling factors licensing cancer progression and metastasis, 2018. 98
- [145] Nathalie Théret, Orlando Musso, Bruno Turlin, Dominique Lotrian, Paulette Bioulac-Sage, Jean Pierre Campion, Karim Boudjéma, and Bruno Clément. Increased extracellular matrix remodeling is associated with tumor progression in human hepatocellular carcinomas. *Hepatology*, 2001. 98
- [146] Steven L. Wood, Maria Pernemalm, Philip A. Crosbie, and Anthony D. Whetton. The role of the tumor-microenvironment in lung cancer-metastasis and its relationship to potential therapeutic targets, 2014. 98
- [147] Ankur Chakravarthy, Lubaba Khan, Nathan Peter Bensler, Pinaki Bose, and Daniel D. De Carvalho. TGF- β -associated extracellular matrix genes link cancer-associated fibroblasts to immune evasion and immunotherapy failure. *Nature Communications*, 2018. 98
- [148] Bo Ri Seo, Xingyu Chen, Lu Ling, Young Hye Song, Adrian A. Shimpi, Siyoung Choi, Jacqueline Gonzalez, Jiranuwat Sapudom, Karin Wang, Roberto Carlos Andresen Eguiluz, Delphine Gourdon, Vivek B. Shenoy, and Claudia Fischbach. Collagen microarchitecture mechanically controls myofibroblast differentiation. *Proceedings of the National Academy of Sciences of the United States of America*, 2020. 98, 147
- [149] Liv Kalbitzer and Tilo Pompe. Fibril growth kinetics link buffer conditions and topology of 3D collagen I networks. *Acta Biomaterialia*, 2018. 98
- [150] Jiranuwat Sapudom, Stefan Rubner, Steve Martin, Tony Kurth, Stefanie Riedel, Claudia T. Mierke, and Tilo Pompe. The phenotype of cancer cell invasion controlled by fibril diameter and pore size of 3D collagen networks. *Biomaterials*, 2015. 98, 111
- [151] Ya Li Yang, Stéphanie Motte, and Laura J. Kaufman. Pore size variable type I collagen gels and their interaction with glioma cells. *Biomaterials*, 2010. 98, 110
- [152] Brooke N. Mason, Alina Starchenko, Rebecca M. Williams, Lawrence J. Bonassar, and Cynthia A. Reinhart-King. Tuning three-dimensional collagen matrix stiffness independently of collagen concentration modulates endothelial cell behavior. *Acta Biomaterialia*, 2013. 98
- [153] Kristin M. Riching, Benjamin L. Cox, Max R. Salick, Carolyn Pehlke, Andrew S. Riching, Susan M. Ponik, Benjamin R. Bass, Wendy C. Crone, Yi Jiang, Alissa M. Weaver, Kevin W. Eliceiri, and Patricia J. Keely. 3D collagen alignment limits protrusions to enhance breast cancer cell persistence. *Biophysical Journal*, 2015. 98

- [154] Jenna A. Mosier, Aniqua Rahman-Zaman, Matthew R. Zanotelli, Jacob A. Vander-Burgh, Francois Bordeleau, Brenton D. Hoffman, and Cynthia A. Reinhart-King. Extent of Cell Confinement in Microtracks Affects Speed and Results in Differential Matrix Strains. *Biophysical Journal*, 2019. 98, 143
- [155] Guannan Chen, Yao Liu, Xiaoqin Zhu, Zufang Huang, Jianyong Cai, Rong Chen, Shuyuan Xiong, and Haishan Zeng. Phase and Texture Characterizations of Scar Collagen Second-Harmonic Generation Images Varied with Scar Duration. *Microscopy and Microanalysis*, 2015. 98, 105, 106
- [156] Norbert Kiss, Dóra Haluszka, Kende Lőrincz, Enikő Kuroli, Judit Hársing, Balázs Mayer, Sarolta Kárpáti, György Fekete, Róbert Szipőcs, Norbert Wikonkál, and Márta Medvecz. Ex vivo nonlinear microscopy imaging of Ehlers–Danlos syndrome-affected skin. *Archives of Dermatological Research*, 2018. 98, 105, 107
- [157] Celeste M. Nelson and Joe Tien. Microstructured extracellular matrices in tissue engineering and development, 2006. 98
- [158] Karl E. Kadler, Adele Hill, and Elizabeth G. Canty-Laird. Collagen fibrillogenesis: fibronectin, integrins, and minor collagens as organizers and nucleators, 2008. 98, 110
- [159] Jayanta Debnath, Senthil K. Muthuswamy, and Joan S. Brugge. Morphogenesis and oncogenesis of MCF-10A mammary epithelial acini grown in three-dimensional basement membrane cultures, 2003. 100
- [160] Robert Matthew Kottmann, Jesse Sharp, Kristina Owens, Peter Salzman, Guang Qian Xiao, Richard P. Phipps, Patricia J. Sime, Edward B. Brown, and Seth W. Perry. Second harmonic generation microscopy reveals altered collagen microstructure in usual interstitial pneumonia versus healthy lung. *Respiratory Research*, 2015. 105
- [161] Jiranuwat Sapudom, Liv Kalbitzer, Xiancheng Wu, Steve Martin, Klaus Kroy, and Tilo Pompe. Fibril bending stiffness of 3D collagen matrices instructs spreading and clustering of invasive and non-invasive breast cancer cells. *Biomaterials*, 2019. 110, 111
- [162] Frederick H. Silver and David E. Birk. Kinetic Analysis of Collagen Fibrillogenesis: I. Use of Turbidity-Time Data. *Topics in Catalysis*, 1983. 110
- [163] G. C. WOOD. The formation of fibrils from collagen solutions. 2. A mechanism of collagen-fibril formation. *The Biochemical journal*, 1960. 110
- [164] Jieling Zhu and Laura J. Kaufman. Collagen i self-assembly: Revealing the developing structures that generate turbidity. *Biophysical Journal*, 2014. 110

- [165] Joel Rosenblatt, Brian Devereux, and D. G. Wallace. Injectable collagen as a pH-sensitive hydrogel. *Biomaterials*, 1994. 110
- [166] Martijn De Wild, Wim Pomp, and Gijsje H. Koenderink. Thermal memory in self-assembled collagen fibril networks. *Biophysical Journal*, 2013. 110
- [167] Xiaofeng Dai, Hongye Cheng, Zhonghu Bai, and Jia Li. Breast cancer cell line classification and Its relevance with breast tumor subtyping, 2017. 111
- [168] Jacob A.M. Nuhn, Anai M. Perez, and Ian C. Schneider. Contact guidance diversity in rotationally aligned collagen matrices. *Acta Biomaterialia*, 2018. 111
- [169] Weijing Han, Shaohua Chen, Wei Yuan, Qihui Fan, Jianxiang Tian, Xiaochen Wang, Longqing Chen, Xixiang Zhang, Weili Wei, Ruchuan Liu, Junle Qu, Yang Jiao, Robert H. Austin, and Liyu Liu. Oriented collagen fibers direct tumor cell intravasation. *Proceedings of the National Academy of Sciences of the United States of America*, 2016. 111
- [170] Florian Geiger, Daniel Rüdiger, Stefan Zahler, and Hanna Engelke. Fiber stiffness, pore size and adhesion control migratory phenotype of MDA-MB-231 cells in collagen gels. *PLoS ONE*, 2019. 111
- [171] Paula D. Bos, Xiang H.F. Zhang, Cristina Nadal, Weiping Shu, Roger R. Gomis, Don X. Nguyen, Andy J. Minn, Marc J. Van De Vijver, William L. Gerald, John A. Foekens, and Joan Massagué. Genes that mediate breast cancer metastasis to the brain. *Nature*, 2009. 111
- [172] Yibin Kang, Peter M. Siegel, Weiping Shu, Maria Drobnjak, Sanna M. Kakonen, Carlos Córdón-Cardo, Theresa A. Guise, and Joan Massagué. A multigenic program mediating breast cancer metastasis to bone. *Cancer Cell*, 2003. 111
- [173] Andy J. Minn, Yibin Kang, Inna Serganova, Gaorav P. Gupta, Dilip D. Giri, Mikhail Doubrovin, Vladimir Ponomarev, William L. Gerald, Ronald Blasberg, and Joan Massagué. Distinct organ-specific metastatic potential of individual breast cancer cells and primary tumors. *Journal of Clinical Investigation*, 2005. 111
- [174] Bojana Gligorijevic, Aviv Bergman, and John Condeelis. Multiparametric Classification Links Tumor Microenvironments with Tumor Cell Phenotype. *PLoS Biology*, 2014. 116, 143
- [175] Miguel Vicente-Manzanares, Xuefei Ma, Robert S. Adelstein, and Alan Rick Horwitz. Non-muscle myosin II takes centre stage in cell adhesion and migration, 2009. 122
- [176] Erick O. Fuentes, Jost Leemhuis, G. Björn Stark, and Eva M. Lang. Rho kinase inhibitors Y27632 and H1152 augment neurite extension in the presence of cultured Schwann cells. *Journal of Brachial Plexus and Peripheral Nerve Injury*, 2008. 122

- [177] Erdem D. Tabdanov, Vikram V. Puram, Zaw Win, Ashab Alamgir, Patrick W. Alford, and Paolo P. Provenzano. Bimodal sensing of guidance cues in mechanically distinct microenvironments. *Nature Communications*, 2018. 123
- [178] Sebastian W. Hofbauer, Peter W. Krenn, Sylvia Ganghammer, Daniela Asslaber, Ulrike Pichler, Karin Oberascher, Reinhard Henschler, Michael Wallner, Hubert Kerschbaum, Richard Greil, and Tanja N. Hartmann. Tiam1/Rac1 signals contribute to the proliferation and chemoresistance, but not motility, of chronic lymphocytic leukemia cells. *Blood*, 2014. 123, 130
- [179] Yuan Gao, J. Bradley Dickerson, Fukun Guo, Jie Zheng, and Yi Zheng. Rational design and characterization of a Rac GTPase-specific small molecule inhibitor. *Proceedings of the National Academy of Sciences of the United States of America*, 2004. 129
- [180] Adam Shutes, Cercina Onesto, Virginie Picard, Bertrand Leblond, Fabien Schweighoffer, and Channing J. Der. Specificity and mechanism of action of EHT 1864, a novel small molecule inhibitor of Rac family small GTPases. *Journal of Biological Chemistry*, 2007. 129, 130
- [181] Yiqun Wang, Jinkang Gong, and Yuan Yao. Extracellular nanofiber-orchestrated cytoskeletal reorganization and mediated directional migration of cancer cells. *Nanoscale*, 2020. 130
- [182] John K. Cowell, Jeffrey LaDuca, Michael R. Rossi, Tania Burkhardt, Norma J. Nowak, and Sei Ichi Matsui. Molecular characterization of the t(3;9) associated with immortalization in the MCF10A cell line. *Cancer Genetics and Cytogenetics*, 2005. 130
- [183] Sirio Dupont, Leonardo Morsut, Mariaceleste Aragona, Elena Enzo, Stefano Giullitti, Michelangelo Cordenosi, Francesca Zanconato, Jimmy Le Digele, Mattia Forcato, Silvio Bicciato, Nicola Elvassore, and Stefano Piccolo. Role of YAP/TAZ in mechanotransduction. *Nature*, 2011. 137
- [184] Muhammad H. Zaman, Linda M. Trapani, Alisha Siemeski, Drew MacKellar, Haiyan Gong, Roger D. Kamm, Alan Wells, Douglas A. Lauffenburger, and Paul Matsudaira. Migration of tumor cells in 3D matrices is governed by matrix stiffness along with cell-matrix adhesion and proteolysis. *Proceedings of the National Academy of Sciences of the United States of America*, 2006. 143
- [185] Stephanie I. Fraley, Pei Hsun Wu, Lijuan He, Yunfeng Feng, Ranjini Krisnamurthy, Gregory D. Longmore, and Denis Wirtz. Three-dimensional matrix fiber alignment modulates cell migration and MT1-MMP utility by spatially and temporally directing protrusions. *Scientific Reports*, 2015. 143
- [186] Farideh Sabeh, Ichiro Ota, Kenn Holmbeck, Henning Birkedal-Hansen, Paul Soloway, Milagros Balbin, Carlos Lopez-Otin, Steven Shapiro, Masaki Inada,

Stephen Krane, Edward Allen, Duane Chung, and Stephen J. Weiss. Tumor cell traffic through the extracellular matrix is controlled by the membrane-anchored collagenase MT1-MMP. *Journal of Cell Biology*, 2004. 143

- [187] Barbara Fingleton. MMP inhibitor clinical trials - The past, present, and future. In *The Cancer Degradome: Proteases and Cancer Biology*. 2008. 143
- [188] Saeid Ansaryan, Mohammad Ali Khayamian, Mohammad Saghafi, Shahriar Shalileh, Mohammad Saied Nikshoar, Fereshteh Abbasvandi, Morteza Mahmoudi, Farideh Bahrami, and Mohammad Abdolahad. Stretch Induces Invasive Phenotypes in Breast Cells Due to Activation of Aerobic-Glycolysis-Related Pathways. *Advanced Biosystems*, 2019. 147
- [189] Brandon D. Riehl, Eunju Kim, Tasneem Bouzid, and Jung Yul Lim. The Role of Microenvironmental Cues and Mechanical Loading Milieus in Breast Cancer Cell Progression and Metastasis, 2021. 147
- [190] Hayley A. McNamara and Ian A. Cockburn. Resident t cells seek the perfect place to work from home. *Nature Immunology*, 22(9):1076–1078, Sep 2021. 178
- [191] Nicholas P. Restifo, Mark J. Smyth, and Alexandra Snyder. Acquired resistance to immunotherapy and future challenges. *Nature Reviews Cancer*, 16(2):121–126, Feb 2016. 178